Galaxy Clustering with Pan-STARRS1 and GAMA

DANIEL JOSEPH FARROW

Galaxy Clustering with Pan-STARRS1 and GAMA

Daniel Joseph Farrow

A thesis submitted to Durham University
in accordance with the regulations for
admittance to the Degree of Doctor of Philosophy.

Institute of Computational Cosmology
Department of Physics
University of Durham
England

September 2013

For Dad

Galaxy Clustering with Pan-STARRS1 and GAMA

Daniel J. Farrow

Abstract

The first theme of this thesis is preparing for the exploitation of a new photometric galaxy survey, Pan-STARRS1 (PS1). The second is measuring projected galaxy clustering in the Galaxy and Mass Assembly (GAMA) survey, and using these measurements to constrain models of galaxy formation.

The PS1 survey is obtaining imaging in 5 bands ($g_{\rm P1}$, $r_{\rm P1}$, $i_{\rm P1}$, $z_{\rm P1}$ and $y_{\rm P1}$) for the 3π steradian survey, the largest optical survey ever conducted. The finished survey will have spatially varying depth, due to the survey strategy. We present a method to correct galaxy number counts and clustering for this based on a simplified signal-to-noise ratio. A star/galaxy separation method calibrated using synthetic images is also presented. By using our techniques on a 69 deg.^{2} region of science verification data, we show PS1 measurements of the two point angular correlation appear reliable down to $r_{\rm P1} < 22.5$. This work lays the foundations for exploiting 3π data for large scale structure.

The GAMA survey is a multi-wavelength, spectroscopic survey of galaxies, covering 180 deg.^{2}. We measure the projected correlation function and its redshift evolution as a function of luminosity, mass and colour. We find redder, more massive and more luminous galaxies are more clustered in three redshift slices over the range $0.0 < z < 0.5$. We find that these trends are reproduced in the galaxy formation model of Bower et al. (2006). We also find redder galaxies have steeper correlation functions; a trend which is also reproduced by the model. However, we find that red galaxies in the model are too clustered, particularly on small scales. Our measurements are new constraints on theories of galaxy formation.

Declaration

The work in this thesis is based on research carried out by the author between 2009 and 2013 under the supervision of Prof. Shaun Cole, Dr. Nigel Metcalfe and Dr. Peder Norberg at the Department of Physics, University of Durham, England. No part of this thesis has been submitted elsewhere for any other degree or qualification.

Parts of this thesis were the author's contributions to the following publications:

- Chapter 2: Metcalfe, N.; Farrow, D. J. et al., 2013, MNRAS, 435, 1825
- Chapter 3: Farrow, Daniel J. et al., 2014, MNRAS, 437, 748

We additionally intend to submit parts of Chapter 4 for publication.

All figures in this thesis were produced by the author except where stated otherwise in the figure captions.

Acknowledgements

Firstly, I would like to thank my family: Mum, Dad, Matthew and Bryan for their support throughout my studies. Without their support, both material and emotional, I probably would not have made it.

In the Department I received lots of help from many people. Firstly, my (official and unofficial) supervisors: Shaun Cole, Nigel Metcalfe and Peder Norberg have been an excellent and patient source of sagely advice. Peter Draper has also offered a great deal of programming wisdom and debugging assistance. I have also made lots of new friends in astronomy, who have made the PhD process much more pleasant. The names that come to mind are Rachael "Ariel" Livermore, Ben Lowing, Mark Lovell, Alice Danielson, Tamsyn McNaught-Roberts, the unmeasurable Stephen Hamer, Sarah Hutton, Chris Harrison and Rachel Kennedy, but many other people in the Department have brightened up my days. I must also acknowledge Lynne Wall, our Senior Dehydration Elimination Specialist, for providing tea, snacks and sympathy twice a day.

During my 8 years in Durham I have met many people who have provided lots of support, kindness and entertainment. My thanks go to all of them, but I would particularly like to acknowledge the people with whom I have been close to for nearly all of those years: Dora Fohring, Oliver Hall, Elizabeth Robinson and Phil Nuttall. I hope to stay close to them forever.

Contents

Abstract iii

Declaration iv

Acknowledgements v

1 Introduction 1

1.1 The expansion of the Universe 1

1.2 Distances 4

1.3 Measuring Hubble's Constant Directly 6

1.4 Type 1a Supernovae 8

1.5 The Cosmic Microwave Background 8

1.6 Large Scale Structure 12

1.7 Correlation Functions 13

1.8 The growth of perturbations in linear theory 14

1.9 Beyond linear theory 18

1.10 Galaxy Formation 21

1.11 Galaxy Clustering 23

1.12 Cosmology from Large Scale Structure 25

1.13 Integrated Sachs Wolfe Effect 27

2 Testing Pan-STARRS1 with Synthetic Images 31

2.1 The Pan-STARRS1 Telescope 31

2.2 The 3π Survey Strategy 33

2.2.1 The PS1 Small Area Survey 2 33

2.3 Detrended Exposures, Warps and Stacks . . . 33
2.4 Coverage Maps and Image Masks . . . 36
2.4.1 IPP Source Detection and Magnitude Measurement . . . 38
2.4.2 Galaxy profiles . . . 40
2.5 Generating Synthetic Objects . . . 41
2.6 Synthetic Image Server . . . 45
2.7 Testing Detrended Exposures with Synthetic Data . . . 45
2.8 Testing Warped Images with Synthetic Data . . . 52
2.9 Testing Stacks with Synthetic Data . . . 55
2.10 Image Background Power Spectra . . . 61
2.11 Estimating the Window Function . . . 65
2.12 The Effect of Warping on Image Backgrounds . . . 67
2.13 Magnitude Dispersions . . . 68
2.14 Summary . . . 71

3 Galaxy Clustering with PS1 72

3.1 Comparison Data . . . 72
3.1.1 SDSS magnitudes and flags . . . 72
3.1.2 PS1 Medium Deep Data . . . 76
3.2 Angular Masks . . . 77
3.2.1 Creating the mask . . . 77
3.2.2 Masks for bright stars . . . 78
3.2.3 Masks for regions of low quality data . . . 79
3.2.4 The effects of masking . . . 82
3.3 Star/Galaxy Separation . . . 85
3.3.1 A morphological separator . . . 85
3.3.2 Comparison to VVDS Spectroscopic Star and Galaxy Classification . . . 90
3.4 Variable Depth . . . 95
3.5 Results and Tests . . . 103
3.5.1 Number Counts . . . 103
3.5.2 Angular Clustering . . . 105

3.5.3 Clustering of Stars and False Positives . . . 117
3.6 Discussion and Conclusions . . . 126

4 Projected Galaxy Clustering in GAMA 129
4.1 Introduction . . . 129
4.2 Data and theory . . . 131
4.2.1 The Galaxy and Mass Assembly survey . . . 131
4.2.2 k-corrections and evolution corrections . . . 132
4.2.3 Mock catalogues . . . 133
4.3 Methodology . . . 135
4.3.1 Sample selection . . . 135
4.3.2 Random catalogues . . . 141
4.3.3 Finding P and Q . . . 144
4.3.4 Projected clustering . . . 150
4.3.5 Integration tests . . . 153
4.4 Results . . . 155
4.4.1 Comparison to literature results . . . 155
4.4.2 Tests of jack-knife error estimates . . . 158
4.4.3 Colour dependent clustering . . . 160
4.4.4 Luminosity dependent clustering . . . 163
4.4.5 Stellar mass dependent clustering . . . 167
4.5 Discussion and Conclusions . . . 169

5 Conclusions 173
5.1 Pan-STARRS1 . . . 173
5.2 GAMA-II . . . 176
5.3 Future Prospects . . . 177

List of Figures

1.1 The temperature power spectrum, as measured by the *Planck* satellite. Grey points represent data, blue represent binned averages of the data and the red line is Planck's best-fitting ΛCDM model. This figure is reproduced from Planck Collaboration et al. (2013). 10

1.2 The positions of galaxies in 2dFRGS. Large scale structure is apparent. The figure is from http://www2.aao.gov.au/2dFGRS/, accessed 04/05/13. 15

1.3 The distribution of dark matter in the Millennium Simulation, with panels showing different scales. dark matter haloes and filaments can be clearly seen. Figure from Springel et al. (2005). 20

1.4 Multiple measurements of the power spectra, transformed to redshift zero using a Lamba CDM transfer function. Figure from Tegmark & Zaldarriaga (2002). 26

1.5 *Top:* A model power spectrum, from CAMB (Lewis & Bridle (2002)). *Bottom:* The correlation function computed by Fourier transforming the power spectrum. The baryonic acoustic peak can clearly be seen. 28

1.6 Initially a photon falls into a potential well, caused by an overdense region of the Universe. Dark energy causes the expansion of the Universe to accelerate, making the potential well shallower, the photon therefore escapes the potential well with more energy than when it entered. 29

2.1 The coverage, i.e. the number of input exposures, of a typical 26 by 26 arcminute SAS2 stack skycell. Black areas correspond to 11 input exposures for that pixel, white corresponds to no input exposures (a blank pixel). The grid pattern arises from the gaps between cells in individual exposures. The elliptical regions correspond to the masking of some spurious reflected light (called ghosts). 37

2.2 The curve of growth of a PS1 PSF model profile, compared to that of a Gaussian with the same FWHM of 0.85″ and the same integrated flux. The top panel gives the enclosed fraction of flux, the bottom panel gives the intensity as a function of radius. We see PS1 PSFs have more extended wings. 39

2.3 A comparison of a real 5 arcminute by 3 arcminute region of the SAS2 r_{P1}-band warp 454105 (above), to the same region in a simulated version of the warp (below). 44

2.4 Screenshots from the synthetic image server. Panel (a) shows the page where the user submits requests, panel (b) shows the queue page where the user can download the finished images. 46

2.5 The input magnitude versus the recovered magnitude for galaxies (above) and stars (below), for synthetic objects placed on synthetic detrended exposures. The red stars mark the median values, the error bars mark the upper and lower quartiles. 48

2.6 The fraction of stars (stars) and galaxies (filled circles) recovered from 4 synthetic detrended exposures as a function of input magnitude. The dashed lines give the recovered fraction of stars on the real images, as calculated from IPP's own synthetic objects. The dotted line gives the 5σ magnitude. 51

2.7 The input magnitude versus the recovered magnitude for galaxies (above) and stars (below), for synthetic objects placed on a synthetic warp. The red stars mark the median values, the error bars mark the upper and lower quartiles. 53

2.8 The fraction of synthetic stars detected as a function of their input magnitude, for the 4 detrended exposures and the warped created from them. Curves have been corrected for fraction of the images masked. 54

2.9 The input magnitude verus the recovered Kron magnitude for galaxies (above) and stars (below), for synthetic objects placed on real warps and then stacked. The red stars mark the median values, the error bars mark the upper and lower quartiles. 56

2.10 The fraction of synthetic stars (above) and galaxies (below) detected as a function of their input magnitude, for a stack with added synthetic objects (red). The grey region gives the region between the detected fractions for the deepest and shallowest of the warps input into the stack. The arrow gives the expected scaling of depth between the warps and the stacked warps. 59

2.11 The predicted $n(z)$ of PS1 3π data, created by applying the estimates of finished 3π depth to our mock catalogue. The legend gives the different combinations of bands in which a detection is required. The $g_{\rm P1}$ and $y_{\rm P1}$-bands are the shallowest, and seem to cause the greatest decrease in depth. 60

2.12 The 2D power spectrum of a PS1 SAS2 detrended exposure. The vertical feature relates to noise perpendicular to the rows of pixels, so we believe it is related to the row-by-row bias issues. The peaks at around 30 degrees from the vertical are thought to be caused by radio interference in the electronics. 63

2.13 The power spectra for a real PS1 detrended exposure, a synthetic PS1 image and an SDSS tile. Different lines in each panel refer to different sizes of mask to remove sources from the images. The legend indicates which line refers to a certain mask size, expressed as a percentage of the measured source size. 64

2.14 The measured power spectrum of a synthetic image with a ramp offset added, i.e. a offset from zero proportional to the x-axis position in the image. The lines show the recovered power spectrum after different masks have been applied to the image, as indicated in the legend. . . 66

2.15 The power spectra of background pixels, for a PS1 SAS2 detrended exposure, a warp and an SDSS tile. We see the turnover in the warped image spectra caused by the convolution kernel smoothing out noise on small scales. The amplitude of the spectra here have been shifted such that they overlap with the warp spectra, for easier comparison. . 67

2.16 The rms scatter between different apertures placed onto image backgrounds, as a function of aperture diameter. The dashed lines give the prediction from integrating the measured power spectra. 70

3.1 The difference between r-band SDSS Stripe 82 Petrosian magnitudes and $r_{\rm P1}$-band PS1 Kron magnitudes, for all objects in an overlap region. Points with error bars show the median values along with upper and lower quartiles. The two magnitudes are fairly well matched, with a small median offset that varies slightly with magnitude. 73

3.2 A colour magnitude diagram of Stripe 82 galaxies, using Stripe 82 apparent model magnitudes. The red dashed line marks our separator between red and blue galaxies. 75

3.3 *(Top)* The correlation of false positive detections with bright stars in the UCAC4 catalogue. The lines show the ratio of the number of false to UCAC4 pairs to the number of false to random pairs as a function of R and V magnitudes from the UCAC4 catalogue. Using two different bands is necessary as the astrograph measuring R magnitudes saturates for very bright stars. We see a clear correlation between false positives and UCAC4 sources. The level at which there are 10 times as many UCAC4 to false pairs as random to false pairs is marked with a horizontal dashed line. *(Bottom)* The largest separation corresponding to this level for each bin, multiplied by 1.5. A fit to these points (blue curve) sets the size of the bright source mask as a function of R and V magnitude. 80

3.4 A histogram of the lowest coverage values, i.e. fewest exposures per stack pixel, in each of our binned up coverage map pixels for the central area of SAS2. 81

3.5 *(Top)* A plot of all detections in SAS2, binned into 0.3 square arcminute pixels. *(Bottom)* The same plot after masking and applying the flags specified in Section 2.2. We can see the circular star masks, the areas near the edge masked due to our cut on low coverage and the square area masked by hand where the data reduction failed. Over-densities caused by stars are removed; the remaining darker regions are caused by variable image depth or genuine over-densities in the object distribution. 83

3.6 The fraction of unmatched objects as a function of magnitude, error bars show Poisson noise. The improvement gained from applying the flags and applying the masking is clear. 84

3.7 Kron minus PSF $r_{\rm P1}$-band magnitudes for all synthetic objects (black), synthetic stars (green dashed) and synthetic galaxies (red dashed) placed into the SAS2 skycell 1315.028, which has a PSF FWHM typical of SAS2 data. Also plotted are the real sources from that skycell (blue) and all sources in SAS2 (grey shaded area); the latter is normalised to the area of skycell.1315.028. The vertical dashed line shows the position of the star and galaxy separation cut for the 98% separator, the dotted vertical line shows the position of the extreme Kron minus PSF magnitude cut. 86

3.8 Galaxy (filled points) and extreme Kron minus PSF cuts (open circles) in the $r_{\rm P1,raw} - r_{\rm P1,PSF,raw}$ versus $r_{\rm P1,raw}$ plane, with colours indicating their completeness as found by the simulations shown in Fig. 6. The points are fitted with second order polynomials (Eq. 3.3.5) (dashed lines). 87

3.9 The probability of correctly classifying a source as a galaxy using the 98% cut (black) and the probability of misclassifying a star as a galaxy (red solid), as predicted using our synthetic objects in Fig. 3.7. Also plotted is the predicted amount of stellar contamination as a fraction of the 98% galaxy sample (red dashed), found from scaling the probability of misclassifying a star with power law fits to the bright end of the observed star and galaxy number counts. The dashed line marks 98%, whilst the dotted line shows our completeness before applying the extreme Kron minus PSF cut. The points with error bars are estimates based on our comparison to the spectroscopic classifications of VVDS sources, as explained in Section 3.3.2 89

3.10 Colour-colour and colour-magnitude diagrams, using Kron magnitudes, of SAS2 objects falling on the star side and galaxy side of our chosen star/galaxy separator (section 3.3.1). The greyscale bar gives the number of objects in each colour-magnitude bin. We see the characteristic stellar features highlighted in Finlator et al (2000), such as the upturn in the colour-colour diagram. In support of our classification we see no evidence of these features in the galaxy sample. 91

3.11 The fraction of Pan-STARRS objects in VVDS as a function of PS1 magnitude: for all VVDS sources (black), VVDS sources targeted for spectroscopy (green-dashed) and VVDS sources with good redshift flags as described in the text (red dashed). 92

3.12 The fraction of Stripe 82 objects detected as a function of fiducial SNR (Eq. 3.4.7). Overlap between magnitude bins implies the fiducial SNR can be used as an estimator of the probability of source detection. The red line shows this quantity as measured from the synthetic galaxies added into real PS1 images and processed by the standard IPP. The dashed line shows the best-fitting relation of Eq. 3.4.8, the dotted line marks SNR = 5.0. Error bars are from 100 bootstrap re-samplings. 97

3.13 The $r_{P1,raw}$ magnitude corresponding to 50% galaxy completeness as predicted by our fiducial SNR method. SAS2 is shallower near the edges where there are fewer exposures, while the pattern of deeper areas across the central region is more representative of of what we expect from the whole 3π survey. 99

3.14 The number density of galaxies, binned by right ascension and declination and corrected for variable depth. We claim over-densities in this plot are genuine, except those caused by Poisson noise in pixels nearer the edges of the field which have small numbers of galaxies. . . 101

3.15 The detected fraction of Stripe 82 galaxies, separated into red and blue by Stripe 82 colours. We see little evidence that red and blue galaxies have different detection efficiency properties, despite the fact that their morphology is expected to be different. 102

3.16 Number counts in the $r_{\rm P1}$-band before (blue) and after (red) the depth correction for galaxies, along with the number counts of objects classed as stars by our adopted separator (green). We do not correct the stars, or the galaxies fainter than $r_{P1} = 23.7$ for completeness. The dashed lines are power law fits to the number counts. Example r-band literature galaxy counts have been included, as indicated in the legend. PS1 Kron magnitudes have been corrected to total using our adopted correction of 0.2 magnitudes. 104

3.17 The differential number magnitude counts for stars (green stars) and galaxies (open triangles) for different PS1 bands matched to the $r_{\rm P1}$-band, in which the star and galaxy separation cut was applied (section 3.3.1). These counts have been uncorrected for image depth. Matching to $r_{\rm P1}$-band data has some contribution to the turnover in each band. However, only the depth of the $i_{\rm P1}$-band is greatly affected, as this band is the only one deeper than the $r_{\rm P1}$-band. 106

3.18 Angular clustering of galaxies in PS1 (connected, open circles) and in the same region of SDSS DR8 (star-shaped symbols), both measured for this paper using the sample selection described in the text. This shows good agreement between PS1 and SDSS DR8. The dashed line is a reference line included in all of our clustering plots. Different measurements have been offset horizontally for clarity, the brightest galaxies are at the true x-axis position for all of the measurements. . 108

3.19 Angular clustering of galaxies over the full SAS2 area in PS1 (connected, open circles) and measurements from a much larger area of SDSS DR7 (filled stars) from Wang et al. 2013. The dashed line is the same reference power law as in Fig. 3.18. Different measurements have been offset horizontally for clarity, with the brightest PS1 and SDSS samples showing the positions of the true angular bins. 109

3.20 Angular clustering of faint galaxies before (dashed lines with points) and after (solid lines with points) applying our spatially varying depth correction. The dashed line is the same reference power law as Fig. 3.18. Different measurements have been offset horizontally for clarity. The uncorrected clustering of the brightest galaxy sample is at the true x-axis position for all of the measurements. 110

3.21 The angular correlation function of a random catalogue that has detection efficiency corrections applied to it, in effect measuring the clustering of the detection-weighted randoms relative to a uniform set of randoms. This gives an estimate of the clustering signal introduced into the data by the spatially varying depth. The clustering here is much weaker than the clustering of the galaxies, indeed for most magnitude bins there is no significant clustering. The faintest magnitude range shows a clear clustering signal, introduced by our modulation of the randoms to correct for spatially varying incompleteness. The dashed line is a reference power law added to all of our clustering plots, the dotted line marks no clustering. 112

3.22 Angular clustering for $22.0 < r_{\rm P1} < 22.5$ galaxies in sub-areas satisfying different fiducial SNR cuts, as indicated in the key. We see that more conservative estimates of the clustering are in agreement with measures which use less deep data with a larger correction applied. For the brighter magnitude bin we also plot the clustering uncorrected for spatially varying depth from a region where the depth is fairly uniform. The points for the different curves have been artificially displaced along the x-axis for clearer viewing, the top curve in the legend shows the true x-axis position for all curves. The dashed grey line is a reference power law added to all of our clustering plots. 113

3.23 As in Fig. 3.22 but for $22.5 < r_{\rm P1} < 23.0$. The solid grey line is the power law we use to roughly estimate the effects of the integral constraint, which is necessary as the sub-areas in the faintest magnitude bin can be very small. 114

3.24 A comparison of our measurements (in red) to Hudon & Lilly (1996), Roche & Eales (1999) and the PS1 MD07 measurements of Foucaud et al (in preparation), before (dashed) and after (solid) our depth correction. The depth correction brings our results into closer agreement with the other measurements, which are from deeper and more uniform surveys than the PS1 SAS2 data. No attempt has been made to correct for the differences between the Hudon & Lilly (1996) or Roche & Eales (1999) R-band filters and our $r_{\rm P1}$-band filter. Corrections for stellar contamination have been applied to all of the measurements. The dashed grey line is a reference power law added to all of our clustering plots. 116

3.25 The lines and open points with error bars show the angular clustering of PS1 galaxies in the SAS2 region, for different magnitude ranges as indicated by the legend. Clustering measurements from Christodoulou et al. (2012). for similar magnitude ranges from the full area of SDSS DR7 are plotted as triangles. The stars with error bars are measurements of clustering from the MD07 fields for Foucaud et al. (in preparation). Error bars on our measurements are estimated with 9 jack-knife re-samplings. Our results and the Foucaud et al. (in preparation) have been corrected for stellar contamination. The Christodoulou et al. (2012) are assumed not to suffer from stellar contamination. The dashed line is a reference power law added to all of our clustering plots. 118

3.26 The angular correlation of objects classed as stars by our adopted star and galaxy separator, split by magnitude, as indicated by the key. The dashed line is a reference power law added to all of our clustering plots, the dotted line marks no clustering. 119

3.27 Measurements of the angular correlation function for the magnitude range indicated. Dashed lines show the clustering of objects classed as stars, for measurements with either extinction corrections (EXT), detection efficiency corrections (DE) or both (DE+EXT) applied as indicated in the legend. The solid line shows the clustering of galaxies, with detection efficiency corrections and extinction corrections applied. The straight, grey dashed line is the reference power law added to all of our clustering plots. 121

3.28 Measurements of the angular correlation function for the magnitude range indicated. Dashed lines show the clustering of objects classed as stars, for measurements with either extinction corrections (EXT), detection efficiency corrections (DE) or both (DE+EXT) applied as indicated in the legend. The solid line shows the clustering of galaxies, with detection efficiency corrections and extinction corrections applied. The dotted line gives the power law used to correct the clustering for the integral constraint. Extinction corrections and detection efficiency corrections combined greatly enhance the clustering, as the extinction correction results in a fainter apparent magnitude sample which receives greater detection efficiency corrections. These detection efficiency corrections enhance the clustering of stars as they are designed for galaxies, which are harder to detect. 123

3.29 The angular correlation of objects cut by the extreme Kron minus PSF magnitude threshold given in Table 3.1, split by magnitude (see key). These objects are mostly false positives. Bins where one or more of the jack-knife regions have undefined clustering measurements, due to zero data-random or random-random pairs at that separation, have been omitted. The dashed line is a reference power law added to all of our clustering plots. 125

4.1 A restframe colour-magnitude diagram for the real GAMA galaxies (left) and for the mock galaxies (right). The red dashed line shows our cuts to define red and blue samples of galaxies. 135

4.2 *(Top)* The redshift distribution of GAMA-II galaxies (solid) and our randoms (dashed) for multiple iterations of the Cole (2011) random catalogue generating approach, as explained in Section 4.3.2. The redshift distribution of the randoms is a good match to the data. *(Bottom)* Our estimates of the galaxy over-density as a function of redshift, from the ratio of the galaxy and random redshift distributions. The solid, black line in the lower panel shows how the mean density increases with respect to $z = 0$, given a value of the density evolution parameter of $P = 1.6$, (i.e. it is $\phi^*(z)/\phi^*(z = 0)$). 143

4.3 The reduced χ^2 of the random catalogue $n_{\rm r}(z)$, given the data. The star indicates the Loveday et al. (2012) value of P and Q for GAMA-I data. The χ^2 we estimated here ignores covariance between the redshift bins in the data, so is likely an underestimate. Nonetheless, we can still see a clear degeneracy between Q and P. 146

4.4 The reduced χ^2 of the random catalogue $n_{\rm r}(z)$, given the mock. The star indicates the Loveday et al. (2012) value of P and Q for GAMA-I data. The triangle indicates the Q and P adopted to produce randoms for the mock catalogue. The χ^2 we estimated here ignores covariance in the data, so is likely an underestimate. 147

4.5 The redshift distribution of the data (solid lines) compared to the redshift distribution of the randoms (dashed lines), for different samples as indicated in the legend. Vertical dotted lines mark the positions of our redshift cuts. The randoms provide an excellent fit to the data. 148

4.6 The redshift distribution of the mock catalogue (solid lines) compared to the redshift distribution of the randoms (dashed lines), for different samples as indicated in the legend. Vertical dotted lines mark the positions of our redshift cuts. The randoms provide an excellent fit to the mock data. 149

4.7 The 2-point correlation function of red (top row) and blue (bottom row) galaxies, for the redshift slices indicated. The elongation of the correlation function on small scales, caused by redshift space distortions, can be seen more clearly in the red sample, as one might expect since these galaxies tend to be in clusters. 151

4.8 The projected two point correlation function of our low redshift, $-20 < M_r - 5\log_{10}h < -19$ galaxy sample, for different values of $\pi_{\rm max}$, as indicated in the legend. Adjacent measurements have been offset by 0.01 dex along the x-axis, with the highest $\pi_{\rm max}$ in its original position. The measurements are divided by the reference power law defined in Section 4.3.4. 153

4.9 The projected two point correlation function of our low redshift, $-20 < M_r - 5\log_{10}h < -19$ galaxy sample, for different approaches to binning the 2D correlation function, as indicated in the legend. Adjacent measurements have been offset by 0.01 dex along the x-axis, with the linear binning line in its original position. The measurements are divided by the reference power law defined in Section 4.3.4. 154

4.10 The $-22.0 < M_r^{0.1} - 5\log_{10}h < -21.0$ clustering measurement from Zehavi et al.(2011) (black), along with our measurement of clustering for the same magnitude and redshift cuts. The dashed line is the reference power law defined in Section 4.3.4. 156

4.11 The $-22.0 < M_r^{0.1} - 5\log_{10}h < -21.0$ clustering measurement from Zehavi et al.(2011) (black), along with our measurement of clustering for the same magnitude and redshift cuts. The different coloured lines indicate measurements from excluding different GAMA regions, as indicated in the legend. The dashed line is the reference power law defined in Section 4.3.4. 157

4.12 The projected clustering of real red galaxies (red solid line) and mock red galaxies for multiple different mock catalogues, as indicated by the legend, for our low redshift slice. We see considerable scatter between the different mock catalogues. The dashed line is the reference power law defined in Section 4.3.4. 159

4.13 The projected correlation function of red galaxies (red solid lines and circles) and blue galaxies (blue solid lines and circles) in different redshift slices. Also shown is the clustering of mock galaxies from the Bower et al. (2006) model (stars and dotted lines with darker shades of blue and red). The Bower et al. (2006) model does a good job reproducing the clustering of blue galaxies but is less successful in reproducing the clustering of red galaxies, particularly on smaller scales. The dashed line is the reference power law defined in Section 4.3.4. . 161

4.14 The relative bias of the red and blue galaxy samples, for different redshift slices as indicated in the legend. 162

4.15 The relative bias of the red and blue mock galaxy samples, for different redshift slices as indicated in the legend. 164

4.16 The projected two-point correlation function of real (top) and mock (bottom) galaxies as a function of redshift (different columns) and luminosity (different colours, as indicated in the legend). The measurements are divided by the reference power law defined in Section 4.3.4. 166

4.17 The projected two-point correlation function of real (top) and mock (bottom) galaxies as a function of redshift (different columns) and stellar mass (different colours, as indicated in the legend). The measurements are divided by the reference power law defined in Section 4.3.4. 167

4.18 Measurements of the correlation length, r_0, for galaxy samples of different mass as indicated in the legend. The stars show our measurements, while the circles show measurements from the VIPERS survey from Marulli et al. (2013). Values are plotted at the median redshift of each sample. 170

List of Tables

2.1 The median and interquartile range of the difference between total input synthetic magnitude and the recovered Kron magnitude, for synthetic objects on synthetic detrended exposures. At faint magnitudes the bright offset in the median recovered value is simply a selection effect, objects scattered fainter are not detected by the software. 49

2.2 The median and interquartile range of the difference between total input synthetic magnitude and the recovered Kron magnitude, for synthetic objects on synthetic detrended exposures that have been warped. 52

2.3 The median and interquartile range of the difference between total input synthetic magnitude and the recovered Kron magnitude on a stack. Measured from synthetic objects placed on real warps and then stacked. 57

3.1 Coefficients for the star, galaxy and false positives separator. Percentages represent the percentage of objects would be included in the sample. The upper or lower limit column defines the direction of the cut, e.g. an upper limit indicates only taking values below the given $r_{\mathrm{P1,raw}} - r_{\mathrm{P1,PSF,raw}}$ line. 88

3.2 The second column gives the probability of a redshift measurement being correct for different ZFLAGS values, taken from Le Fèvre et al. (2005). The third and forth columns give the fraction of the full sample and discrepant sample that have certain ZFLAGS values. The final column gives an estimate of the total fraction of PS1 objects with incorrect VVDS estimates of redshift. 94

4.1 Different galaxy samples in the low redshift region ($0.02 < z < 0.14$), with their average number density, size and median properties. 138

4.2 Different galaxy samples in the medium redshift region ($0.14 < z < 0.24$), with their average number density, size and their median properties. 139

4.3 Different galaxy samples in the high redshift region ($0.24 < z < 0.5$), with their average number density, their size and their median properties. 140

Chapter 1

Introduction

This thesis is focused around two galaxy surveys. The first, Pan-STARRS1, is a survey of galaxies across almost the whole sky. Data from Pan-STARRS1 consists only of measurements of galaxy brightnesses, shapes and positions on the sky. The Pan-STARRS1 sections of this thesis will focus on preparing for the finished survey. In contrast, the work we carry out with the second survey in this thesis, the Galaxy and Mass Assembly Survey, will be focused on exploiting the survey for galaxy formation studies. The GAMA survey measures galaxy redshifts, allowing one to map out the positions of galaxies in 3D. Before all this however, we will cover some important preliminary information.

We shall begin by introducing the standard model of cosmology and models of galaxy formation, along with the observational evidence for these models. Among the most important pieces of evidence is the large scale structure of the Universe: the pattern of how galaxies are distributed across the Universe. This chapter will stress the importance of these observations, giving the motivation for the rest of the research presented in this thesis.

1.1 The expansion of the Universe

Arguably one of the most impressive discoveries of 20th century physics was that the Universe is expanding. The observational evidence for such a conclusion is traditionally allocated to Edwin Hubble Hubble (1929), though as stressed in Peacock

(2013) some cosmologists believe Vesto Slipher (Slipher, 1917) played an even bigger role in this discovery. Regardless, it was found that the redshift, z, of the emission and absorption lines in a galaxy's spectra were correlated with the galaxy's distance. Galaxies further away from Earth were found to be receding faster,

$$\mathbf{v} = H(t)\mathbf{d}, \tag{1.1.1}$$

where $\mathbf{v}$ is the recession velocity, $\mathbf{d}$ is the proper distance to a galaxy and $H(t)$ is known as Hubble's parameter. If we invoke the assumptions of statistical homogeneity and statistical isotropy, that the Universe looks the same wherever you are and no matter what direction you look, this observation leads to the conclusion that the Universe itself is expanding. The traditional way of describing such an expansion is to define the vector between two points, $\mathbf{r}$, at time t to be some factor, $a(t)$, multiplying a fixed reference separation $\mathbf{x}$ thus

$$\mathbf{d} = a(t)\mathbf{x}. \tag{1.1.2}$$

The fixed reference separation is called the comoving distance and is defined to be $\mathbf{d}$ at the present epoch, such that $a = 1$ today. For convenience we will not write the time dependence of $a(t)$ explicitly from now on i.e. $a = a(t)$. It can be easily shown that Hubble's parameter is related to a via

$$H(t) = \frac{\dot{a}}{a}. \tag{1.1.3}$$

By considering the definition of redshift and by considering light being stretched by a factor a, one can also conclude

$$a = \frac{1}{1+z}. \tag{1.1.4}$$

Before the discovery of the Universe's expansion a theoretical framework to describe such a universe was already in place. The Friedmann equation describes the time evolution of a and can be derived from considering a uniform expanding medium with classical mechanics (see e.g. Liddle, 2003) or with General Relativity (GR) (see e.g. Foster & Nightingale, 1995). In a Universe of uniform density ρ the Friedmann equation is

$$\left(\frac{\dot{a}}{a}\right)^2 = \frac{8\pi G}{3}\rho + \frac{k}{c^2 a^2}. \tag{1.1.5}$$

Where k is a constant related to the total energy of the Universe in the classical derivation, and the overall curvature of space in the GR derivation. Note that ρ varies with the expansion factor a; the time variation of ρ is described by an equation called the "fluid equation" which can be derived from classical thermodynamics or GR (see e.g. Liddle, 2003)

$$\dot{\rho} + 3\frac{\dot{a}}{a}\left(\rho + \frac{p}{c^2}\right) = 0 \tag{1.1.6}$$

where p is the pressure of the fluid. A closely related equation to the fluid equation is the acceleration equation (see e.g. Liddle, 2003), given by

$$\frac{\ddot{a}}{a} = -\frac{4\pi G}{3}\left(\rho + \frac{3p}{c^2}\right). \tag{1.1.7}$$

As explained in many textbooks (here we follow Coles & Lucchin, 2002) we can define an equation of state for fluids in our Universe as

$$p = w\rho c^2. \tag{1.1.8}$$

Substituting Equation 1.1.8 into 1.1.6 we gain the a evolution of ρ

$$\rho a^{3(1+w)} = \text{const} \tag{1.1.9}$$

$$\therefore \rho = \frac{\rho_0}{a^{3(1+w)}}. \tag{1.1.10}$$

Where ρ_0 refers to the value of ρ at the present epoch where $a = 1$. For non-relativistic materials $\rho << \rho c^2$ and $w = 0$ and so $\rho = \rho_0/a^3$. This can physically be seen as the density simply diluting with increasing volume as a increases. For relativistic species and radiation $w = 1/3$ and $\rho = \rho_0/a^4$. Physically this can be seen as volume dilution with an added decrease in density caused by the energy loss as the wavelength of the particles are stretched by the Universe's expansion. For the special case of $w = -1$ the density ρ remains constant, such a fluid is labelled the "cosmological constant".

In the currently favoured model of cosmology the Universe's total density is made up of contributions from several different fluids. The most easily observed of these is normal matter, which in a cosmological context is treated as effectively pressureless as it is non-relativistic. Adding to the normal matter component is another component which does not interact with light, known as "dark matter". Dark matter

was first proposed by Zwicky (1933) to explain the high velocities of galaxies in the Coma cluster. Later, work studying the rotation of nearby galaxies demonstrated a need for a large unseen component of matter in order to explain the non-Keplerian rotation curve of galaxies (Rubin & Ford, 1970). In order to distinguish normal matter from dark matter, normal matter is often labelled "baryonic matter" even though this is not the correct use of the word in the particle physics sense (i.e. because this definition includes leptons).

The density of the dark matter, $\rho_{\rm DM}$, and baryonic matter, $\rho_{\rm b}$, components evolve in the same way with the expansion factor, and together they are sometimes labelled as the matter density, $\rho_{\rm m}$. Radiation density, $\rho_{\rm r}$, and relativistic neutrinoes, ρ_ν also contribute to the total density. In practice the relativistic neutrino contribution ρ_ν is counted as a part of ρ_r. Note that at some point during the expansion of the Universe, the neutrinos become non-relativistic, we will discuss what effects this has in Section 1.8. A further contribution is from a component known as "dark energy" labelled $\rho_{\rm DE}$, which is a component with an equation of state parameter very close to or equal to -1. The true value of w for dark energy, whether or not it is a cosmological constant, is an unsolved question of cosmology.

The values of these density parameters are elegantly expressed as fractions of the critical density $\rho_{\rm c}$. The critical density is the value of the density such that $k = 0$ in Equation 1.1.5. These fractions are

$$\Omega_{\rm x} = \frac{8\pi G}{3H^2(t)}\rho_{\rm x} \tag{1.1.11}$$

where x denotes the different density contributions, m, r, ν, DE for matter, radiation, neutrinos and dark energy respectively. One can also express the value of k in an analogous way as

$$\Omega_k = -\frac{kc^2}{a^2H^2}. \tag{1.1.12}$$

1.2 Distances

A vital piece of information, connecting this theory to observations, is understanding how to measure distance. We briefly review the key distance measures in cosmology, here we use Coles & Lucchin (2002) as a reference but many other pedagogical

introductions exist (e.g. Hogg, 1999; Liddle, 2003). The geometry of space and time in the Universe can be described by the Robertson-Walker metric

$$\mathrm{d}s^2 = (-(c\mathrm{d}t)^2 + a^2(t)\left((\mathrm{d}R)^2 + S_\mathrm{k}(R)(\mathrm{d}\theta^2 + \sin^2\theta\mathrm{d}\phi^2)\right) \tag{1.2.13}$$

where θ, ϕ and R are comoving $\mathbf{x}$ expressed in polar coordinates. The function $S_\mathrm{k}(R)$ varies between a universe with open geometry $k > 0$, closed geometry $k < 0$ or flat geometry $k = 0$. It is defined as

$$S_\mathrm{k}(R) = \begin{cases} \frac{\sinh\sqrt{|k|}R}{\sqrt{|k|}} & \text{if } k < 0 \\ R & \text{if } k = 0 \\ \frac{\sin\sqrt{k}R}{\sqrt{k}} & \text{if } k > 0 \end{cases} \tag{1.2.14}$$

To use this with observational data we must connect the comoving distance r to an object's measured redshift z. Consider a beam of light travelling radially along $\mathrm{d}R$, the distance it traverses, in time t, in an expanding Universe will be

$$r = \int_0^t \frac{c}{a(t)}\mathrm{d}t. \tag{1.2.15}$$

Using Equations 1.1.5, 1.1.3 and 1.1.4 to change variables one can show that

$$r = \int_o^z \frac{c\mathrm{d}z}{H_0 E(z)} \tag{1.2.16}$$

where H_0 is Hubble's Constant, which is Hubble's parameter at the present epoch and $E(z)$ gives the redshift evolution of H_0 such that $H(t) = H_0 E(z)$. Integrating this from the start of the Universe (i.e. $z = \infty$) to a redshift, z, gives the maximum distance light could have travelled in the Universe by z, known as the light horizon of the Universe. The function $E(z)$ can be derived from Equations 1.1.5, 1.1.9, 1.1.11 and 1.1.12 to be

$$E(z) = \left[\Omega_{\mathrm{m},0}(1+z)^3 + \Omega_{\mathrm{r},0}(1+z)^4 + \Omega_{\mathrm{DE},0}(1+z)^{3(1+w)} + \Omega_{k,0}(1+z)^2\right]^{0.5} \tag{1.2.17}$$

where the w here is from the equation of state for dark energy, and is constant, and the $\Omega_{\mathrm{X},0}$ values refer to the Ω_X values at $a = 1$. We can see that the relationship between redshift and distance encloses a large amount of information about the contents (i.e. the values of $\Omega_{\mathrm{X},0}$) and the curvature of the Universe. Before we

begin our discussion on how these parameters are observationally constrained we will present two other important distances in cosmology. The first is known as the angular diameter distance, d_A, defined such that an object of length l is observed to subtend an angle θ_A thus

$$\theta_A = \frac{l}{d_A}. \tag{1.2.18}$$

This distance can be shown to be

$$d_A = \frac{S_k(r)}{1+z}. \tag{1.2.19}$$

Additionally, one can define the luminosity distance, d_L, which is defined such that the flux, F, received from an isotropically emitting source of luminosity L is

$$F = \frac{L}{4\pi d_L^2}. \tag{1.2.20}$$

The flux received from a source is decreased by the expansion of the Universe, both as the photons arrive less frequently and their energies are lower as their wavelengths have been stretched (see e.g. Coles & Lucchin, 2002). This leads to a decrease in flux by a factor of a^2. The relation between luminosity distance and angular diameter distance is therefore

$$d_L = d_A(1+z)^2 \tag{1.2.21}$$

(see e.g. Coles & Lucchin, 2002). With these distance measures explained, we are almost ready to introduce the large scale structure of the Universe and how it can act as a probe for cosmology and galaxy formation. Before this, however, we will briefly review some of the other sources of observations important for cosmology.

1.3 Measuring Hubble's Constant Directly

Determining Hubble's constant directly via equation 1.1.3 requires the measurement of a galaxy's distance. The most important method of doing this in the local Universe is to utilize the relationship between the period and luminosity of Cepheid variable stars discovered by Henrietta Leavitt. Brighter Cepheid variable stars have longer periods, due to a well understood physical process involving pulsations of the star's atmosphere (e.g. Zeilik & Gregory, 1998). By measuring the period of a Cepheid

variable and using this to estimate its intrinsic luminosity, the Cepheid variable's luminosity distance can be measured. In the local Universe, this luminosity distance is almost equal to the distance used in equation 1.1.3. This method can therefore provide a simple way of measuring H_0.

The difficulty in measuring stars in other galaxies restricts using Cepheid distances to the local Universe. As explained in Freedman et al. (2001), using these local measurements alone cannot give an accurate measure of Hubble's constant as the recession velocity of local galaxies due to the Universe's expansion is small, so the peculiar motions of galaxies, deviations from the Hubble flow caused by density inhomogeneities, can influence measurements. One of the most accurate and commonly used measurements of H_0 is from a *Hubble Space Telescope* (HST) Key Project (Freedman et al., 2001, and references therein). They used the Cepheid variable distances to calibrate other distance measures, such as type 1a supernovae, the Tully-Fisher relation and the fundamental plane of elliptical galaxies (Freedman et al., 2001, and references therein). This approach of calibrating more distant probes of the distance-redshift relation with Cepheid variables, which themselves are calibrated using parallax measurements, forms what is known as a "distance ladder". In this distance ladder overlaps between the different calibrators allow them to be mutually calibrated to probe higher redshift parts of the distance-redshift relation. This distance ladder allows higher redshift galaxies to be used to measure Hubble's constant.

The dominant source of error in measuring Hubble's constant comes from finding the intrinsic luminosity of Cepheid variables (Freedman et al., 2001). The Leavitt relation only gives the predicted relative brightnesses of different Cepheids, one still requires measurements of Cepheid variables' intrinsic luminosities, which requires measurements of their distance. The distance to galactic Cepheid variables has been measured using parallax, but the low numbers of observed galactic Cepheid variables means Cepheid variables from the nearby galaxies like the Large Magnellic Cloud (LMC) or NGC4258 are also used when measuring the Leavitt relation (Riess et al., 2011; Freedman et al., 2012). The galaxy NGC4258 is particularly useful as a source of Cepheids as its distance has been measured using maser emitting regions

around its central black hole (see e.g. Riess et al., 2011). The most accurate direct measurement of H_0 is from Freedman et al. (2012) who measured $H_0 = 74.3 \pm 2.3$ km s^{-1}Mpc^{-1}.

1.4 Type 1a Supernovae

The approach of using "standard candles" like Cepheid variables to measure luminosity distance has also been used with higher redshift data to constrain cosmological parameters. Another choice of standard candle is type 1a supernovae; they are luminous enough to be seen at high redshift and have an intrinsic luminosity that can be accurately inferred from measurements of how their observed flux changes with time (e.g. Riess et al., 1998).

It was by observing type 1a supernovae magnitudes that Riess et al. (1998) and Perlmutter et al. (1999) discovered that the expansion of the Universe was accelerating, as supernovae magnitudes were too faint for their redshifts in other models. By adopting the prior that the Universe is flat[1] and that any dark energy is in the form of a cosmological constant, $w = -1$, Riess et al. (1998) and Perlmutter et al. (1999) both found that dark energy must dominate the Universe's density, with the (Perlmutter et al., 1999) best fit cosmology being $\Omega_{\rm m} = 0.28^{+0.09}_{-0.08}$, $\Omega_\Lambda = 0.72^{+0.08}_{-0.09}$.

Type 1a supernovae data are often combined with other cosmological probes in order to break degeneracies between measurements of different cosmological parameters. In order to do this large samples of type 1a supernovae have been produced and their luminosity distance and redshift measured, such as the Union 2.1 sample of 580 (Suzuki et al., 2012).

1.5 The Cosmic Microwave Background

The observation that the Universe is expanding leads to the idea that at some point it must have been much smaller, denser and hotter. At one point the Universe would have been fully ionised and photons would have been trapped by scattering

[1] We shall see in Section 1.5 this has very strong observational evidence.

off electrons. At a later time when the Universe was cool enough for the electrons to be incorporated in neutral atoms, an epoch known as recombination, these photons would have been free to propagate producing a background of photons which would be red-shifted into microwaves by the present day (see e.g. Coles & Lucchin, 2002; Liddle, 2003). The observation of a "cosmic microwave background" (CMB) by Penzias & Wilson (1965) was a key piece of evidence that the Universe was once much denser and hotter, in support of the so called "big bang theory".

The measured temperature of the CMB, $T = 2.7255 \pm 0.0006$K (Fixsen, 2009) gives a measurement of the value of the radiation density parameter $\Omega_{\rm r}$, but far more cosmological information can be extracted from the CMB from its "anisotropies", the measurement of temperature variations across the sky. The COBE satellite was the first satellite to detect these anisotropies, which represent a deviation only of the order of 10^{-5} (Fixsen et al., 1996, and references therein). These anisotropies are thought to be first generated from quantum processes translated to a larger scale by a process known as inflation (Guth, 1981). These initial anisotropies were then processed though the plasma of the early Universe before being emitted as the CMB. A statistical way of describing these anisotropies is with their power spectra, $P(k)$, which are the squared amplitudes of modes with wavenumber k in a Fourier decomposition of the temperature field.

A detailed review of the physics of the early-Universe which influenced the CMB is well beyond the scope of this thesis, and unnecessary for understanding the research presented here. We will, however, highlight some of the important processes in order to explain how one can use CMB observations to constrain cosmological parameters. In the plasma before recombination the anisotropies can be Fourier decomposed into oscillating standing waves, with gravity acting to compress the plasma and photon pressure acting as a restoring force (see e.g. Coles & Lucchin, 2002; Hu & Dodelson, 2002; Liddle, 2003). In configuration space these oscillations would look like spherical sound waves in the plasma emanating from multiple over-densities (e.g Eisenstein et al., 2007). The longest wavelength oscillation possible in this plasma before recombination is equal to the integral of the sound speed of the plasma over the age of the Universe at recombination (see e.g. Hu & Dodelson,

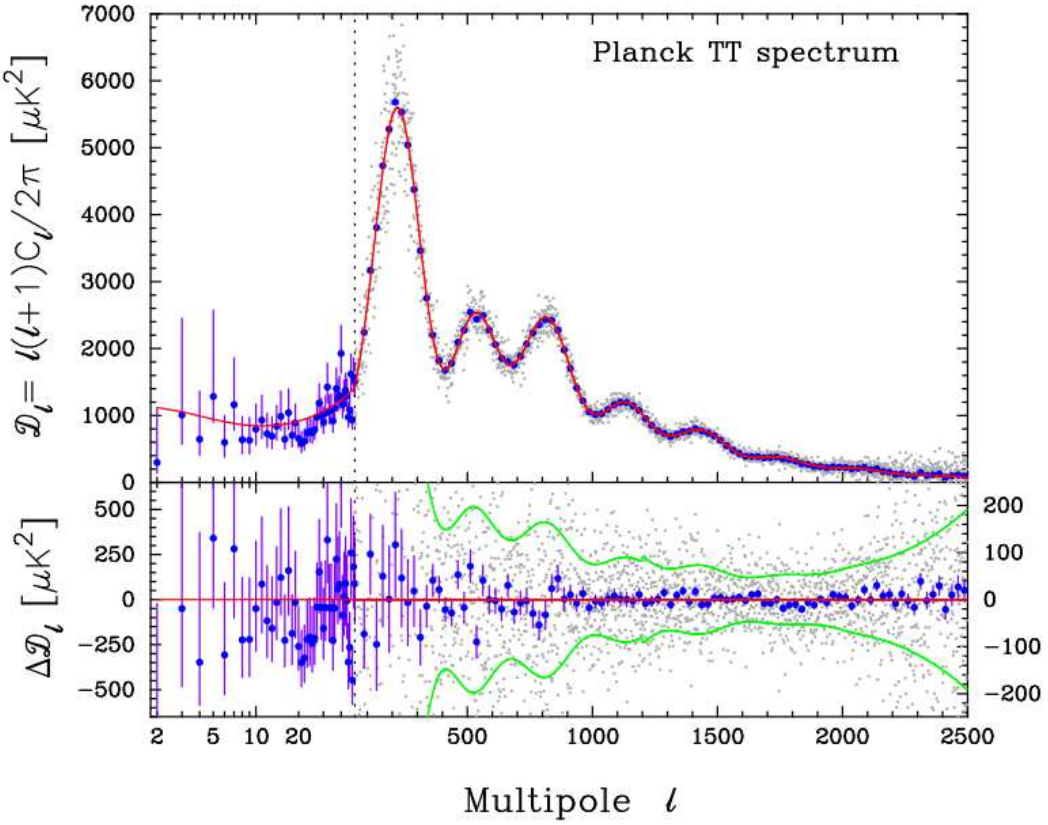

Figure 1.1: The temperature power spectrum, as measured by the *Planck* satellite. Grey points represent data, blue represent binned averages of the data and the red line is Planck's best-fitting ΛCDM model. This figure is reproduced from Planck Collaboration et al. (2013).

2002). Higher frequency oscillations also occurred, in Fourier space standing waves at their most compressed or most rarefied state at recombination produce peaks in the power spectra of the CMB (see e.g. Hu & Dodelson, 2002). In configuration space this can be seen as the sound waves constructively or destructively interfering with the perturbations in the dark matter (e.g Eisenstein et al., 2007). The latest measurement of the CMB, from the Planck consortium, is reproduced in Fig. 1.1.

The precise positions of the peaks can be used to constrain cosmology. Consider the position of the first peak (largest wavelength), its angular scale at recombination depends upon the time of recombination and the sound speed before recombination. The sound speed mainly depends on the relative numbers of photons and baryons,

set by $\Omega_{\rm b}h^2$, whilst the time of recombination is set by the expansion rate of the Universe (e.g Percival et al., 2002; Eisenstein et al., 2007). The Universe's expansion rate changes between the matter dominated and radiation dominated eras, and this results in the matter density, $\Omega_{\rm m}h^2$, being the most important cosmological parameter when setting the recombination time (e.g Percival et al., 2002; Eisenstein et al., 2007). However, the strongest influence on the observed position is spatial curvature, which allows it to be used to constrain curvature (e.g. Hu & Dodelson, 2002). The observed position of the first peak sets a strong constraint on the Universe being flat, i.e. $\Omega_k = 0$, or close to flat (e.g. de Bernardis et al., 2000). Of course, with CMB data alone a degeneracy exists between smaller amounts of curvature and the combination of $\Omega_{\rm b}h^2$ and $\Omega_{\rm m}h^2$ (e.g. Percival et al., 2002). Helpfully, this degeneracy can be broken by large scale structure measurements we will introduce later in this chapter.

Observations of the first peak alone also give very degenerate estimates of the other cosmological parameters, but, helpfully, peaks at smaller scales also contain valuable cosmological information. To give one example the density of baryons in the early Universe affects how compressed the oscillations become by adding additional gravitational mass, analogous to adding more mass to a spring. This effect, known as baryon loading, enhances the power of waves in their compression phase. This leads to odd numbered peaks in the power spectrum appearing higher than they otherwise would (see e.g. Hu & Dodelson, 2002). In addition, the gravitational lensing of the CMB and its polarisation can also help constrain cosmology (e.g. Planck Collaboration et al., 2013).

The latest CMB data, from the *Planck* satellite, is able to accurately constrain all of the parameters we have mentioned so far of the standard ΛCDM model with a cosmological constant ($w = -1$) (Planck Collaboration et al., 2013). In addition, the *Planck* satellite measured the initial power spectrum of the CMB anisotropies, showing the initial anisotropies are a power law, $P(k) \propto k^n$, with a slight scale dependence with $n = 0.959 \pm 0.007$. In addition to this, the measured shape and amplitude of the power spectrum allows the calculation of σ_8, the variance of mass with an $8\,{\rm Mpc}\,h^{-1}$ sphere (see e.g. Coles & Lucchin, 2002). This is a useful parameter

as it quantifies how clumpy the distribution of matter is. It is calculated from the spherically averaged power spectrum via

$$\sigma_8^2 = \frac{1}{2\pi^2}\int_0^R P(k)\left(\frac{3(\sin(kR) - kR\cos(kR))}{(kR)^3}\right)^2 k^2 \mathrm{d}k. \tag{1.5.22}$$

Here the trigonometric terms are the Fourier transform of the spherical top-hat function (see e.g. Coles & Lucchin, 2002) and $R = 8\,\mathrm{Mpc}\,h^{-1}$. The value of σ_8 is also often used to define the normalisation of the power spectra. In Chapter 4 we will further discuss how the value of σ_8 could affect galaxy clustering predictions.

For extensions to the standard cosmological model, for example dark energy with an equation of state with $w \neq -1$, CMB data alone offers less of a constraint. CMB data is therefore often combined with other cosmological data sets, such as the supernovae, measurements of Hubble's constant and measurements from large scale structure. Combining Planck data with direct measurements of Hubble's constant or supernovae data suggests $w < -1.0$ at a significance of greater than 2σ. However one interpretation of this is that the latter two measurements suffer from systematic errors (Planck Collaboration et al., 2013).

Large scale structure has the opportunity to add vital new information to these studies. We shall see it also offers, when combined with CMB data, the best measurements of w. A key gain of using large scale structure data is that it overcomes a major limitation of the CMB, which is that it only offers a single distance projection, i.e. all of the CMB signal is from a shell of plasma at roughly the same luminosity distance. Measurements of large-scale structure can overcome this by offering measurements from different redshifts with different distance projections. We will now move on to introduce the fundamentals of what large scale structure is and how it arises. This will include an introduction to the theories of galaxy formation and the observations that constrain these theories. Near the end of the chapter we will return to how large scale structure can constrain cosmology.

1.6 Large Scale Structure

The large scale structure of the Universe is how galaxies are distributed across the Universe, i.e. whether they are scattered uniformly throughout space or whether

their positions have some structure. An important milestone in the search for such structures was the production of the Lick galaxy catalogue (Shane & Wirtanen, 1967), which counted the number of galaxies in $10'$ by $10'$ cells over two thirds of the sky (Peebles, 1980). This catalogue demonstrated that the galaxies were distributed in filaments, high density regions like "clusters" and low density regions called "voids" (Coles & Lucchin, 2002). More recently, surveys such as the 2dF Galaxy Redshift Survey (2dFGRS) (Colless et al., 2001) and the Sloan Digital Sky Survey (SDSS) (York et al., 2000) have made detailed maps of the positions of galaxies in three dimensions, by measuring the radial distance to galaxies using their redshift. We show in Fig. 1.2 the positions of galaxies in the 2dFRGS survey, clearly showing the clusters, voids and filaments formed by the pattern of galaxies.

1.7 Correlation Functions

An often used statistic to measure how galaxies are clustered is the two-point correlation function. As explained in Peebles (1980) the two point correlation function, ξ, is related to the probability δP of finding a galaxy in each of two volumes δV_1 and δV_2 at a separation of r_{12} thus

$$\delta P = n^2 \delta V_1 \delta V_2 [1 + \xi(r_{12})] \tag{1.7.23}$$

where n is the mean number density of galaxies. For $\xi = 0$ the probability of finding two galaxies simply becomes the product of the mean number of galaxies in each volume, meaning the galaxies are uncorrelated. For $\xi > 0$ the probability of finding two galaxies is enhanced over random and so the galaxies are clustered, for $\xi < 0$ the galaxies are anti-correlated. A value of $\xi = -1$ means finding galaxies in both volumes is impossible.

We can also give an alternative definition of the 2-point correlation function by first defining the over-density, δ, as a fluctuation in density $\rho(\mathbf{x})$ over the mean density $\langle\rho\rangle$ thus

$$\delta = \frac{\rho(\mathbf{x}) - \langle\rho\rangle}{\langle\rho\rangle}. \tag{1.7.24}$$

One can then define ξ in terms of over-density as

$$\xi(r) = \langle \delta(\mathbf{x})\delta(\mathbf{x}+\mathbf{r}) \rangle \tag{1.7.25}$$

(e.g. Coles & Lucchin, 2002). We can relate the correlation function to the power spectrum by first decomposing the over-density field $\delta(\mathbf{x})$ into its Fourier components $\delta_{\mathbf{k}}$ thus

$$\delta(\mathbf{x}) = \Sigma_{\mathbf{k}} \delta_{\mathbf{k}} \exp(i\mathbf{k}\cdot\mathbf{x}). \tag{1.7.26}$$

Using Equations 1.7.25 and 1.7.26 one yields the Wiener-Khintchine theorem (see e.g. Coles & Lucchin, 2002), that the correlation function is the Fourier transform of the power spectrum,

$$\xi(r) = \frac{1}{(2\pi)^3} \int P(k) \exp(-i\mathbf{k}\cdot\mathbf{r}) \mathrm{d}\mathbf{k}. \tag{1.7.27}$$

The correlation function is often measured by counting pairs of galaxies, n_{gg}, with separation, $\mathbf{r}$, and comparing them to the number of pairs of points distributed randomly over the region in question, n_{rr}. The most intuitive estimate of $\xi(\mathbf{r})$ is then

$$\xi(\mathbf{r}) = 1 + \frac{n_{\mathrm{gg}}}{n_{\mathrm{rr}}}. \tag{1.7.28}$$

Whilst this is the most intuitively simple estimator, usually other combinations of random-random, random-galaxy and galaxy-galaxy pairs are used which give lower variance estimates of $\xi(\mathbf{r})$. The most popular of these are the Hamilton (1993) and Landy & Szalay (1993) estimators, which will be used in later chapters of this thesis.

1.8 The growth of perturbations in linear theory

To understand how these filaments, clusters and voids of galaxies formed one needs to track the small, almost scale-free perturbations in the CMB to later times. Gravity, pressure, the expansion of the Universe and the velocities of gas particles all play a role. A detailed mathematical study of this is beyond the scope of this thesis, and not required to understand the research presented here. We will, however, highlight a few results. A much more thorough introduction is available in Peebles (1980).

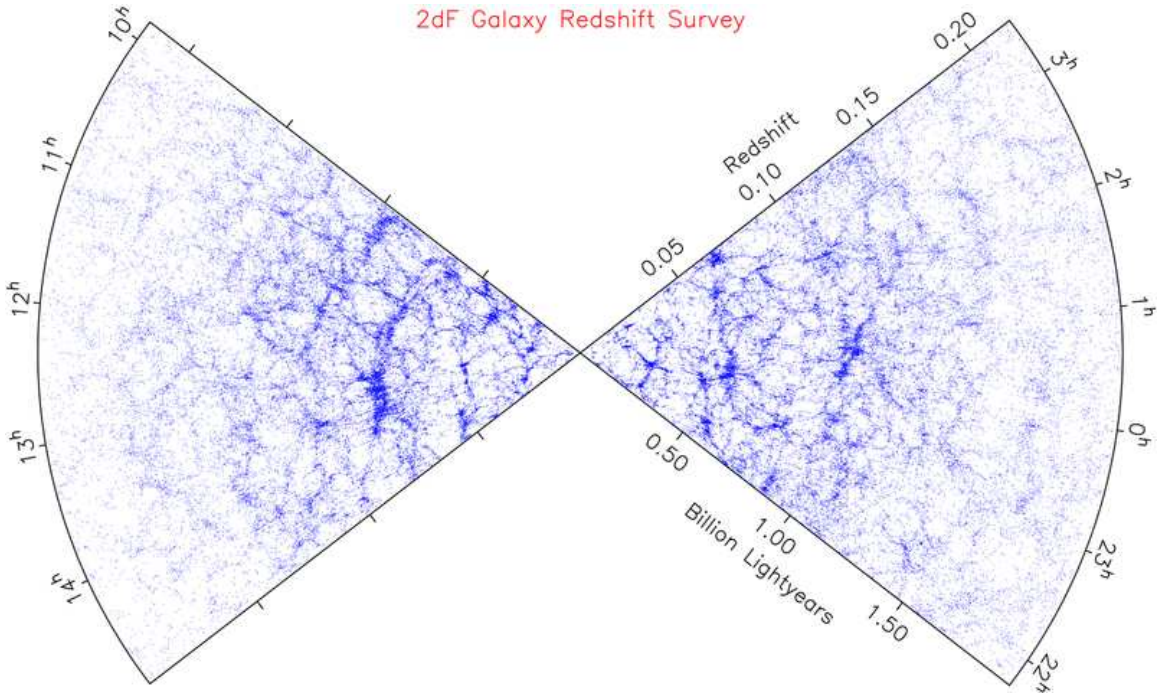

Figure 1.2: The positions of galaxies in 2dFRGS. Large scale structure is apparent. The figure is from http://www2.aao.gov.au/2dFGRS/, accessed 04/05/13.

By combining the continuity equation, the Euler equation and the Poisson equation one can derive an equation for the evolution of δ, for perturbations within the horizon (see Section 1.1), in a non-relativistic fluid as

$$\frac{\partial^2\delta}{\partial t^2} + 2\frac{\dot{a}}{a}\frac{\partial\delta}{\partial t} = \frac{\nabla^2\delta p}{a^2\bar{\rho}} + 4\pi\bar{\rho}\delta \tag{1.8.29}$$

where δp is the perturbation to the pressure, p. Here the second term on the LHS represents how the expansion of the Universe slows the growth of perturbations, whilst the first and second terms on the RHS show how pressure and gravity affect the growth of the perturbation. To describe the expansion of dark matter one can remove the pressure term as $p = 0$ for a non-relativistic fluid. By solving this equation one finds that for a flat, matter dominated Universe (where $\Omega_{\rm m} \approxeq \Omega$) perturbations grow like $\delta \propto a$. This solution is applicable from the Universe at the time matter and radiation densities were equal, $a_{\rm eq}$, until close to today where dark energy is beginning to dominate over matter (i.e. $\Omega_\Lambda > \Omega_{\rm m}$). Before $a_{\rm eq}$ the Universe was in the radiation dominated era, to see how perturbations grow in this era one must change variables in Eq. 1.8.29 to $y \equiv a/a_{\rm eq} = \rho_m/\rho_r$ and use Eq. 1.1.5

and Eq. 1.1.7. The result of doing this is the Meszaros equation, the solution of which is

$$\delta \propto 1 + \frac{3}{2}y. \tag{1.8.30}$$

From this we see that for $a < a_{\rm eq}$ the growth of perturbations is frozen. This is because the expansion of the Universe is too fast for over-densities to collapse. As a increases, Equation 1.8.30 tends towards the solution for perturbation growth in the matter dominated regime. We have now seen the two most important regimes of perturbation growth within the horizon. For a full picture we need to understand how perturbations grow outside of the horizon also. We cannot use Eq. 1.8.29 as this is only for perturbations within the horizon. One simple way of determining the growth of super-horizon perturbations is by comparing two model universes: one flat universe and one universe with a small curvature δK, both with the same $\rho(a)$. The Friedmann equation for the slightly curved universe is

$$H_1^2 = \frac{8\pi G}{3}\rho(a) + \frac{\delta K}{a^2} \tag{1.8.31}$$

At some expansion factors a and $a + \delta a$ for the flat and slightly curved universes respectively, the age of these universes would be equal. We find this time by equating the age of both universes, and changing variables to the expansion factor

$$\int_0^a \frac{da'}{a'H(a')} = \int_0^{a+\delta a} \frac{da'}{a'H_1(a')} \tag{1.8.32}$$

rewriting $H_1(a')$ using Equation 1.1.5 and using a Taylor expansion yields

$$\int_0^a \frac{da'}{a'H(a')} = \int_0^{a+\delta a} \frac{da'}{a'H(a')}\left(1 + \frac{\delta K}{2H^2(a)a^2}\right) \tag{1.8.33}$$

$$\approxeq \int_0^a \frac{da'}{a'H(a')} + \frac{\delta a}{aH(a)} + \int_0^a \frac{\delta K}{2H^2(a)a^2} \tag{1.8.34}$$

To yield the second line we drop terms higher than first order perturbative terms. Finally if we use Equation 1.1.9 we can show that $\delta\rho/\rho = \delta a/a$ and

$$\frac{\delta\rho}{\rho} \propto a^{\frac{3}{2}(1+w)} \int_0^a \frac{da'}{a'(1 - \frac{3}{2}(1+w))} \tag{1.8.35}$$

$$\therefore \frac{\delta\rho}{\rho} \propto a^{(1+3w)}. \tag{1.8.36}$$

So, for a universe dominated by radiation, with $w = 1/3$, super-horizon perturbations grow as $\delta \propto a^2$. In contrast, for a matter dominated universe with $w = 0$,

super-horizon perturbations have the same growth rate to perturbations smaller than the horizon, i.e. $\delta = a$. This has an interesting effect, known as the Meszaros effect, in that perturbations smaller than the horizon at $a_{\rm eq}$ are retarded with respect to super horizon perturbations which can continue to grow in the radiation dominated regime. Information such as this can be encapsulated in the transfer function, $T(k)$, which is defined as the actual growth of perturbations divided by the growth expected due only to self-gravity and without the Meszaros effect. In general the transfer function is used to evolve perturbations from inflation to some epoch in the matter dominated era. The transfer function depends on the wavenumber of the perturbation, k, and is expressed mathematically as

$$T(k) = \frac{\delta_k(z=0)}{\delta_k(z)D(z)} \tag{1.8.37}$$

where $D(z)$ is the growth due to self gravity and without the Meszaros effect (e.g. Peacock, 1999). We have shown for a super-horizon perturbation in the radiation dominated era, $D(z) \propto a^2$, whilst perturbations inside the horizon do not grow. This means perturbations with a wavelength less than the horizon size at matter-radiation equality, $l_{\rm H,eq}$, miss out on a factor of

$$\left(\frac{a_{\rm eq}}{a_{\rm enter}}\right)^2 \tag{1.8.38}$$

growth. As the horizon grows like a in the radiation dominated era, and because the horizon size at $a_{\rm enter}$ has to be the wavelength of the perturbation, $2\pi/k$,

$$a_{\rm enter} = \frac{2\pi}{k l_{H,eq}} a_{\rm eq} \tag{1.8.39}$$

$$\therefore \left(\frac{a_{\rm eq}}{a_{\rm enter}}\right)^2 \propto k^{-2} \tag{1.8.40}$$

This results in a transfer function that is close to unity for perturbations with wave numbers that mean they are outside the horizon before matter radiation equality, but is k^{-2} for perturbations which enter the horizon during the radiation dominated era. This results in a curved shape of the $z = 0$ power spectrum, where the turnover is related to the size of the horizon at matter-radiation equality.

Accurate determinations of the transfer function require complex calculations, which depend on other physics not described here. One interesting effect is free

streaming, where particles can escape potential wells due to their thermal velocities. This adds a high k cut off to the transfer function. This can occur for relativistic neutrinos, adding a characteristic damping to the power spectrum on scales smaller than the horizon size when cosmological neutrinos became non-relativistic (Hu et al., 1998). Another important effect is the previously mentioned baryonic acoustic oscillations. By comparing the power spectrum measured from the CMB and the power spectrum of matter, as traced by galaxies, one can constrain $T(k)$ and as such cosmology. Before we explore this in detail, we will first discuss how to follow the evolution of perturbations when δ grows larger and the problem becomes non-linear.

1.9 Beyond linear theory

A first step in understanding the evolution of perturbations in the non-linear regime is to consider over-densities with simple geometry. One such approach is the spherical top hat collapse model (e.g. Coles & Lucchin, 2002). In this analytical approximation one describes the collapse of a spherical top-hat over-density as a closed (i.e. positively curved) universe using the Friedmann equation. The over-density begins by expanding with the Hubble flow, before collapsing. One useful result from this model is it gives an expression for the times that a perturbation begins to collapse, reaches maximal compression and becomes virialised. One can relate these times to over-densities one would predict with linear theory; an often used value is $\delta_{\rm c} = 1.68$ which is the linear theory predicted over-density for the time when a spherical top hat perturbation reaches maximal compression in an $\Omega = \Omega_{\rm m} = 1$ universe (e.g. Coles & Lucchin, 2002). This linear theory value of $\delta_c = 1.68$ turns out to be much smaller than the spherical top hat model prediction of $\delta_c = 180$. The linear theory value is often used as a cut-off to decide when a linear theory over-density can be considered "collapsed", i.e. decoupled from the expansion of the Universe. Press & Schechter (1974) used these linear theory cut-off over-densities to make predictions for the number of collapsed objects as a function of mass. Press & Schechter (1974) model the over-density as a Gaussian field, and integrate the Gaussian to find the

fraction of objects with an over-density past some cut-off value, such as $\delta_c = 1.68$. By smoothing this Gaussian field with kernels of different sizes before integrating, one can predict the number of collapsed structures as a function of mass by considering the mass enclosed within the smoothing kernel. One problem with this approach is that over-densities which may be considered collapsed on one smoothing scale, may also be counted as collapsed on another smoothing scale leading to over-densities being counted multiple times. This was fixed with the revised method of Bond et al. (1991), which calculates the fraction of objects crossing the cut-off over-density for the first time.

Other approaches to predicting large scale structure beyond linear theory also exist. Arguably the most widely used is the N-body simulation approach. For a review of the history and results of N-body simulations see Frenk & White (2012). In this approach one simulates a set of particles, distributed in such a way to conform to the linear theory predictions for the density field at some high redshift (where linear theory is accurate). The motions of these particles are then followed through time, experiencing forces based on the gravitational pull of the other particles. For a collisionless fluid like dark matter, the results of these simulations should be very accurate, at least down to the resolution of the simulation. Perhaps the most famous cosmological simulation is the Millennium Simulation (Springel et al., 2005), which followed 2160^3 particles from $z = 127$ to $z = 0$. An image of the Millennium Simulation is shown in Fig. 1.3, one can see the collapsed structures known as dark matter haloes as well as filaments and voids. Comparing Fig. 1.3 and 1.2 one can already see similarities, pointing to the idea that galaxies trace out the structure of the dark matter. In the next section we build on this idea as we introduce the key concepts of galaxy formation.

Before moving on we will cover one more important concept, this is the idea of "bias". This is the general term used to describe the idea that galaxies or dark matter haloes are not faithful tracers of the underlying mass distribution. For example, the clustering of a subset of dark matter haloes will differ from the clustering of all dark matter. The relationship between the correlation function of the dark matter, $\xi_{\rm DM}$,

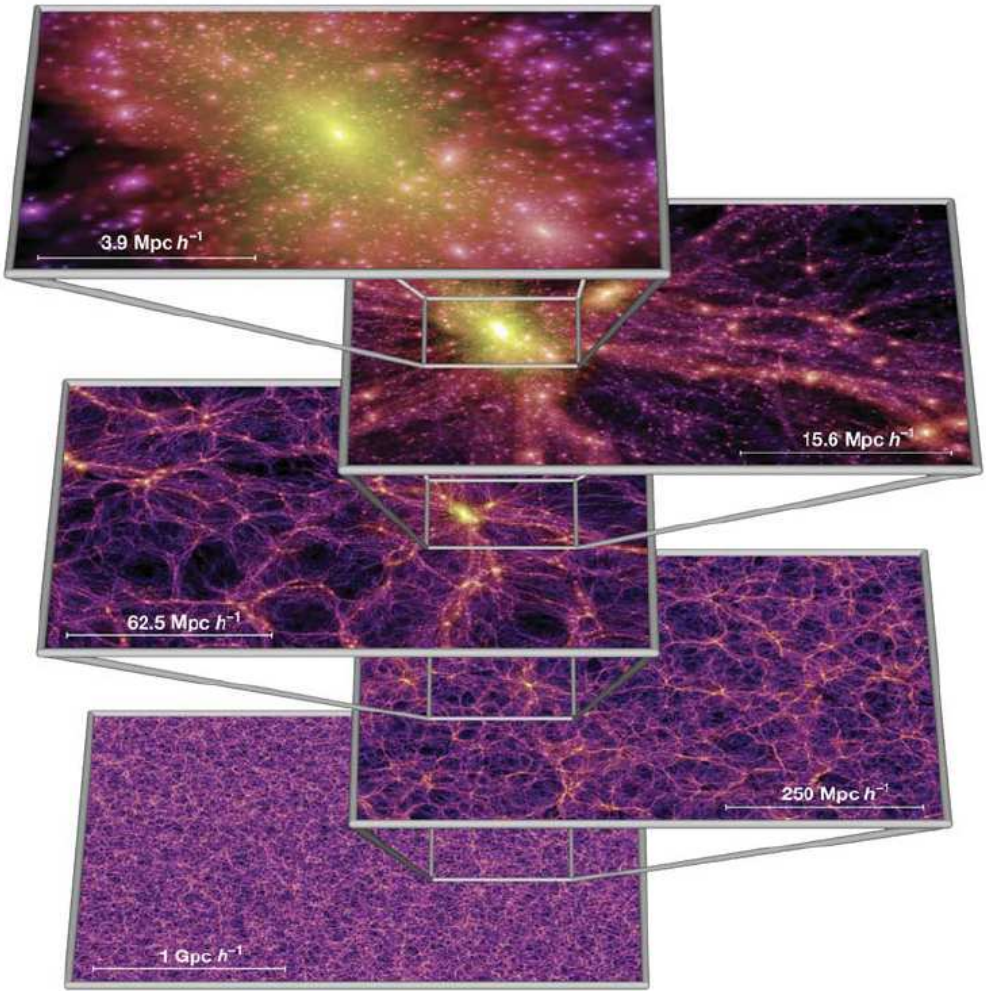

Figure 1.3: The distribution of dark matter in the Millennium Simulation, with panels showing different scales. dark matter haloes and filaments can be clearly seen. Figure from Springel et al. (2005).

and that of a subset of haloes, $\xi_{\rm H}$, can be approximated by the simple relation

$$\xi_{\rm H} = b^2 \xi_{\rm DM} \tag{1.9.41}$$

where b is the bias. More massive, rarer dark matter haloes have a larger bias and so stronger clustering. Work such as Cole & Kaiser (1989) give expressions to relate the mass of dark matter haloes to their bias.

1.10 Galaxy Formation

Observations of dark matter around galaxies (e.g Rubin & Ford, 1970) lead to the idea that all galaxies are surrounded by haloes of dark matter, with the dark matter by far out-weighing the baryonic matter. White & Rees (1978) used this idea to suggest that galaxies formed by gas falling into dark matter haloes, before cooling and forming stars. Stars could form so long as the cooling time of the gas in the dark matter halo was shorter than the age of the Universe. For less massive dark matter haloes White & Rees (1978) used "feedback" from star formation to heat the gas and so decrease star formation rates. This "feedback" from star formation consists of supernovae explosions and winds from young stars. Using a form of Press & Schechter (1974) and simple prescriptions for stellar feedback and the merging of dark matter haloes, White & Rees (1978) predicted the abundance of galaxies as a function of luminosity, known as the "luminosity function". Another observation explained by the White & Rees (1978) was the existence "satellite galaxies", galaxies which orbit larger companions. In White & Rees (1978) these were explained as galaxies contained in smaller dark matter haloes, accreted by a larger halo but not yet merged with the central galaxy. Later work such as White & Frenk (1991), Kauffmann et al. (1993) and Cole et al. (1994) built on this, establishing the "semi-analytic" approach to galaxy formation, where complex processes such as star formation and feedback are approximated with simple analytic prescriptions.

Perhaps the most widely used semi-analytic model is the GALFORM model first presented in Cole et al. (2000). This first version included prescriptions for star formation based on the available cool gas content, the cooling rate of gas in galaxies, the timescales for an accreted halo to merge with the host galaxy and supernovae

feedback as a function of star formation rate. An initial mass function (IMF), the number of stars formed as a function of their mass, needs also to be assumed. Often, observed IMFs of regions in the very local Universe are used (e.g Kauffmann et al., 1993; Cole et al., 2000). Models like GALFORM always involve several free parameters which reflect our lack of understanding and ability to model complex processes such as star formation. The approach generally adopted is to fit these parameters to some observational data set (e.g. the luminosity function) before testing the model using these fitted parameters on other independent data sets (see e.g. Cole et al., 2000).

Later additions to the GALFORM model have brought new insight into the process of galaxy formation. The Baugh et al. (2005) model suggested a modified version of the IMF for galaxies undergoing a burst of star formation, which produced a better fit to the submillimetre luminosity function of galaxies. The Bower et al. (2006) model of galaxy formation invoked feedback from active galactic nuclei (AGN) to stop gas cooling into the most massive haloes, which was found to be necessary to fit the bright end of the luminosity function.

Other approaches to modelling galaxy formation have also been successful. Hydrodynamic simulations attempt to model the baryonic gas more directly, tracing the forces and temperatures affecting the baryons using either particles or by splitting the problem up into a mesh. These simulations range from smaller volume simulations tracing parts of a galaxy (e.g Creasey et al., 2013) or larger volume simulations tracing the evolution of dark matter and gas (e.g. Vogelsberger et al., 2013). These simulations can provide insights that can be incorporated into semi-analytic models (e.g. Creasey et al., 2013).

Semi-analytic models can be combined with N-body simulations to predict the large scale distribution of galaxies, and therefore their clustering. The next section will return to our main topic of large scale structure and review the current predictions and observations of galaxy clustering.

1.11 Galaxy Clustering

It has been known for several decades that galaxies are clustered, with an approximately power law correlation function (e.g. Peebles, 1980). One strength of the galaxy formation models introduced in the previous section is their ability to understand the physics behind this clustering. One observation that these models can explain is that brighter and more massive galaxies are more strongly clustered (e.g. Norberg et al., 2001, 2002; Li et al., 2006; Zehavi et al., 2011; Christodoulou et al., 2012). This observation is explained by galaxy formation models by predicting that galaxies of different properties preferentially reside in haloes of different mass. Brighter, more massive galaxies are predicted to reside in more massive dark matter haloes which are more strongly clustered (see Sec. 1.9). Observations also show that red galaxies, galaxies with elliptical morphologies and galaxies with spectra suggesting little star formation cluster more strongly than their bluer, star forming counterparts (e.g Norberg et al., 2002; Madgwick et al., 2003; Li et al., 2006; Zehavi et al., 2011; Christodoulou et al., 2012). Galaxy formation models can also explain these observations. In the models, red galaxies, with little star formation, which typically have elliptical morphologies are also more strongly clustered. This is due to processes such as AGN feedback arresting star formation in the largest haloes (e.g. Bower et al., 2006).

On smaller scales the clustering signal is primarily thought to arise from multiple galaxies and satellite galaxies in the same dark matter halo, whilst on larger scales the clustering signal is thought to be dominated by pairs of galaxies in different haloes (Benson et al., 2001, e.g). This has lead to the halo occupation distribution (HOD) approach to understanding galaxy clustering, where one assumes the dark matter halo mass is the only important factor in setting a galaxy's properties and characterises a population of galaxies based on the number of them expected within a halo of a given mass (e.g. Berlind & Weinberg, 2002; Peacock & Smith, 2000; Benson et al., 2001; Zheng et al., 2005; Zehavi et al., 2011). From this the small scale, "one-halo" clustering term of galaxies within the same halo is calculated based on a model of the distribution of dark matter sub-haloes within a larger halo. The larger scale, "two-halo" clustering term is calculated from the prediction of the clustering

of dark matter haloes as a function of their mass. The HOD has contributions from central and satellite galaxies. The central term is usually modelled as an error function defining a minimum mass for a central galaxy to appear, plateauing at unity as haloes can only have a maximum of one central galaxy (e.g. Zheng et al., 2005). The satellite term is modelled as a power law, with increasing numbers of satellites in more massive haloes (e.g. Zheng et al., 2005). Approaches like the HOD can be quite powerful in understanding clustering. For example Zehavi et al. (2011) fit HODs to SDSS data and use them to explain the reason why faint, red galaxies are strongly clustered: because these galaxies are mostly satellite galaxies in large haloes. A larger number of satellites in red galaxy samples also explains why observations of red galaxy correlation functions show them to be steeper than blue galaxy correlation functions (e.g Li et al., 2006; Christodoulou et al., 2012). Note that Ross et al. (2011b) finds the large-scale bias of red galaxies continues to decrease with luminosity down to $M_r < -17$. This would suggest that the majority of faint, red galaxies are central galaxies in less massive haloes, with only a minority of them being satellite galaxies in massive haloes.

Whilst the general predictions of galaxy formation models have been qualitatively confirmed by observations, detailed comparisons show disagreement and as such point towards new physics in galaxy formation. For example, Kim et al. (2009) compared the GALFORM models of Bower et al. (2006) and Font et al. (2008) to the competing semi-analytic model of De Lucia & Blaizot (2007). Kim et al. (2009) found the De Lucia & Blaizot (2007) model could fit some galaxy samples' clustering perfectly but could not match the trends of clustering with luminosity; the GALFORM models conversely could not match the detailed shape of the correlation function but could match the trends with luminosity. Kim et al. (2009) found the GALFORM models had too much small scale clustering, a problem which they successfully remedied by introducing new physical processes that remove satellite galaxies from the model, and so lower the amplitude of the "one-halo" term. Another example comes from Gonzalez-Perez et al. (2011) who found the Bower et al. (2006) model could reproduce the clustering of objects with red $(R-K)$ colours but under-predicted clustering of the objects with red $(i-K)$ colours. In Chapter 4 we

will use the GAMA survey to further test the clustering predictions of semi-analytic models.

1.12 Cosmology from Large Scale Structure

Now galaxy clustering and large scale structure have been introduced, we can return to the issue of using them to constrain cosmology. The power spectrum of galaxy clustering is thought to be an evolved version of that observed in the CMB. To demonstrate this we show figure 1 of Tegmark & Zaldarriaga (2002) in Fig. 1.4. To produce this figure, Tegmark & Zaldarriaga (2002) transformed all of the power spectrum measurements to $z = 0$ using a ΛCDM transfer function. As a demonstration of the utility this has in testing cosmological models, Tegmark & Zaldarriaga (2002) showed that using a transfer function with a high baryonic fraction, $\Omega_{\rm b}h^2 = 0.07$, resulted in the CMB measurements and galaxy measurements disagreeing. More recent measurements of the galaxy and CMB power spectra have greatly decreased the size of the errors on the measurements shown in Fig. 1.4. The galaxy power spectrum can be modelled, and from it cosmological parameters derived. This approach, however, has different challenges to that of using the CMB power spectrum. Galaxy formation physics, non-linear structure formation and the effect of galaxy peculiar velocities on redshifts all modify the shape of the galaxy power spectrum and thus need to be modelled (e.g. Parkinson et al., 2012).

One feature in the galaxy power spectrum, which is arguably less influenced by the effects described above, is the measurement of the "baryonic acoustic oscillation" (BAO) scale. The BAO are the imprint of the CMB acoustic oscillations in the matter power spectrum, they arise from the same process as the CMB oscillations but represent fluctuations in galaxies and matter rather than the CMB photons. First detected by Cole et al. (2005) and Eisenstein et al. (2005), they are a strong piece of evidence that the large scale structure of galaxies really was formed by gravitational effects on perturbations in the early Universe. Like the first peak in the CMB, their comoving size is set by the sound speed before recombination and only changes slightly with different cosmological models. The position of the BAO

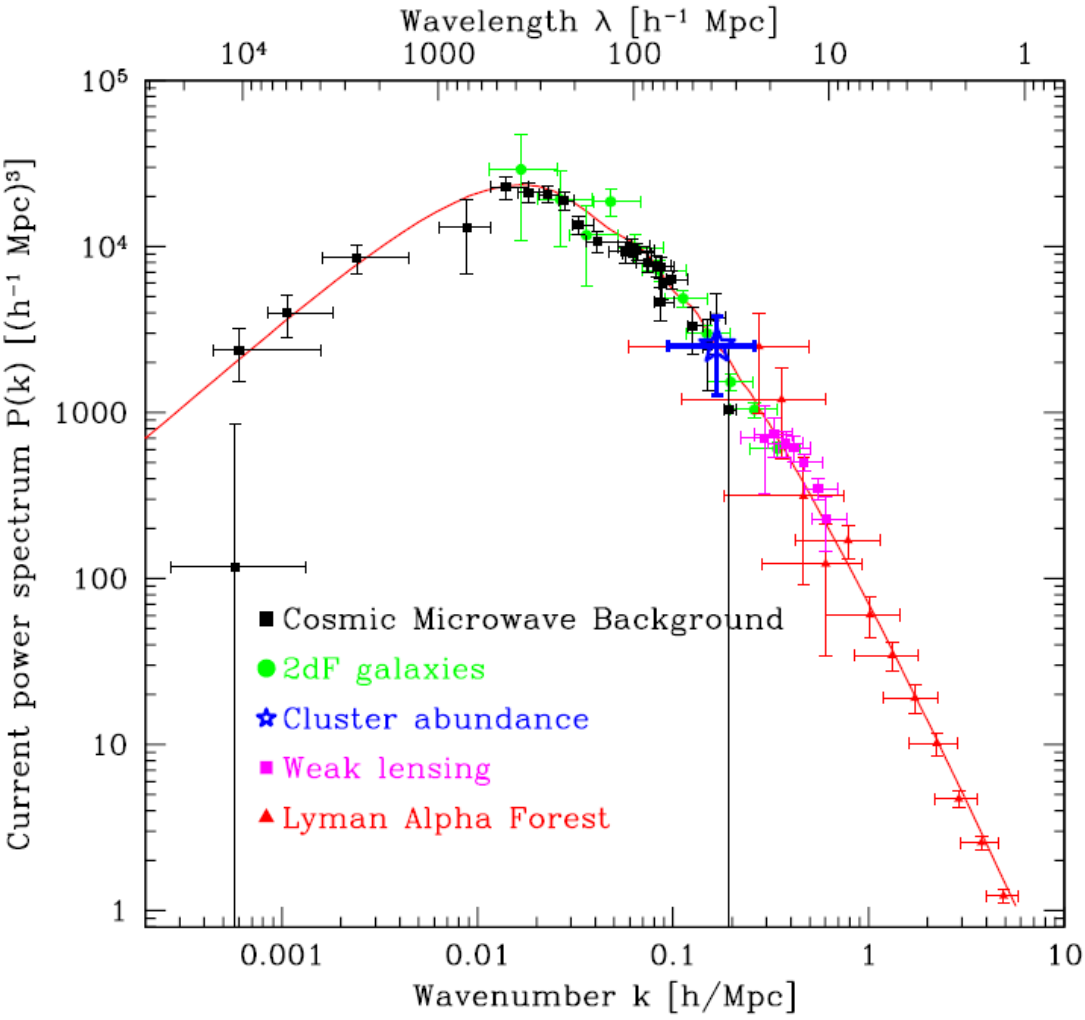

Figure 1.4: Multiple measurements of the power spectra, transformed to redshift zero using a Lamba CDM transfer function. Figure from Tegmark & Zaldarriaga (2002).

peak can therefore act as a standard ruler with which to measure the size of the Universe at different epochs, by measuring its location in the correlation function of galaxy samples at different redshifts. These measurements of the size of the Universe can be used to constrain cosmological models.

The BAO can be seen in both the galaxy power spectrum and the galaxy correlation function. To demonstrate this, and the connection between $P(k)$ and $\xi(r)$, we computed both functions for the same cosmological model. For this we used software called 'Code for Anisotropies in the Microwave Background' (Lewis & Bridle, 2002) to generate a theoretical power spectrum at $z = 0$ using cosmological parameters from Planck Collaboration et al. (2013) (we modified parameter files supplied by Adrian Jenkins). We then solved Eq. 1.7.27 by numerical integration to compute the predicted correlation function. The result of this is given in Fig. 1.5, we see that the baryonic acoustic oscillations in the power spectrum (at scales of $k \sim 0.1\,h$ Mpc^{-1}) appear in the correlation function as a single peak.

Combining other cosmological probes with the galaxy power spectrum and BAO data can help break degeneracies that exist when considering them in isolation. As an example, measurements of the BAO scale help break the degeneracy between $w \neq -1$ and small amounts of curvature in the CMB data (e.g Parkinson et al., 2012). So far the combined measurements of all cosmological probes are consistent with a ΛCDM model (e.g Percival et al., 2010; Anderson et al., 2012; Parkinson et al., 2012; Planck Collaboration et al., 2013).

1.13 Integrated Sachs Wolfe Effect

One remaining effect predicted by the existence of dark energy, but not yet detected with high statistical significance, is the "Integrated Sachs-Wolfe" (ISW) effect. This is predicted to occur when CMB photons fall into a gravitational well that has a decaying potential; such wells are expected to exist if the expansion of the Universe is accelerating. As the CMB photon falls into the well it gains energy, but does not lose all of that energy when it climbs out of the evolved, now shallower potential (see Fig. 1.6). It therefore emerges with more energy than when it fell into the well.

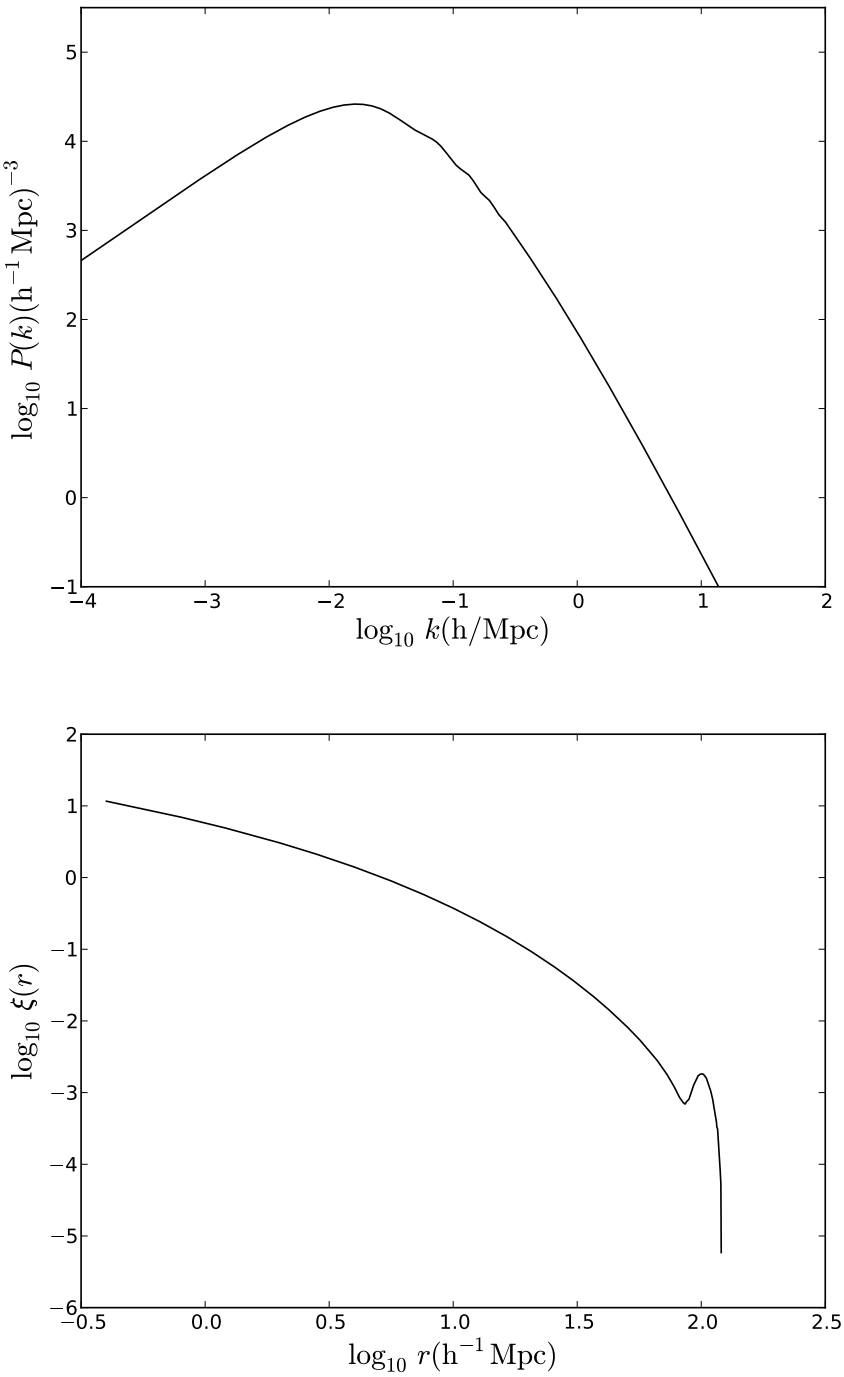

Figure 1.5: *Top:* A model power spectrum, from CAMB (Lewis & Bridle (2002)). *Bottom:* The correlation function computed by Fourier transforming the power spectrum. The baryonic acoustic peak can clearly be seen.

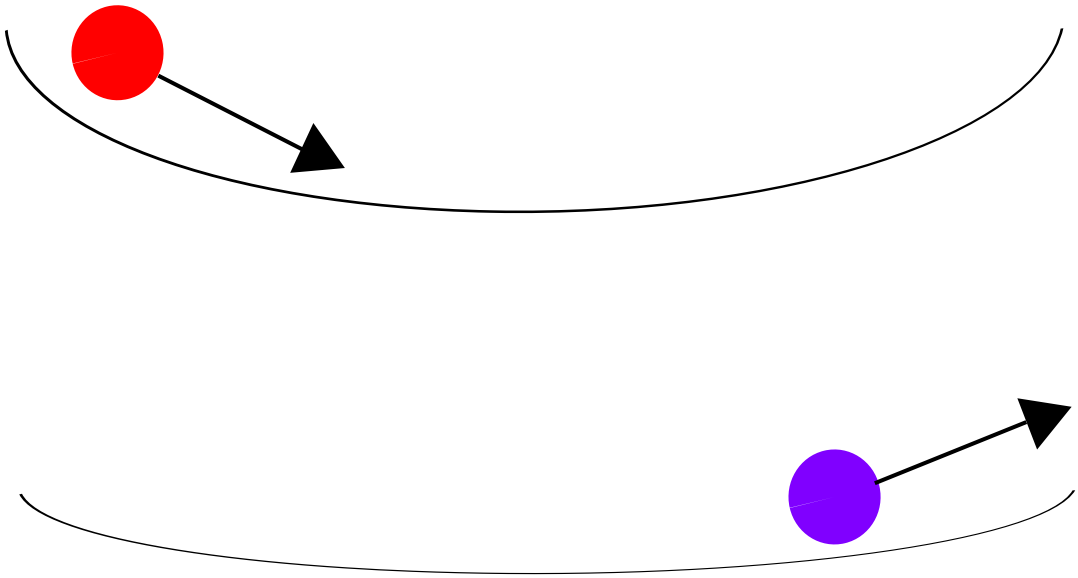

Figure 1.6: Initially a photon falls into a potential well, caused by an overdense region of the Universe. Dark energy causes the expansion of the Universe to accelerate, making the potential well shallower, the photon therefore escapes the potential well with more energy than when it entered.

Large area galaxy surveys can be cross-correlated with the CMB to detect this effect, as overdensities in matter should cause hotter regions in the CMB. Goto et al. (2012) measured this, by cross-correlating a subregion of the WISE galaxy survey with WMAP CMB data, and detected a cross-correlation signal with a significance of 3.3σ. Curiously their measured amplitude is 2σ above the level expected for ΛCDM (Goto et al., 2012). However, more recently Kovács et al. (2013) measured the ISW using the same method but the full-sky WISE data, they detected a cross correlation signal at a level consistent with standard ΛCMD, but with little statistical significance (only 1σ). They found the difference between the results was entirely consistent with sample variance, highlighting the need for large area surveys when measuring the ISW. As well as WISE, several other galaxy surveys have also been used to measure the ISW, for example Giannantonio et al. (2012) combines data from three different surveys to yield a 4.4σ detection of a CMB and galaxy cross-correlation signal.

The Pan-STARRS1 3π survey has the chance to detect the ISW at a higher

significance than previously measured, due to its large area and relatively deep photometry. In Cabré et al. (2007) the significance of an ISW detection through the cross-correlation method is shown to scale with the square root of the area of the survey. In SDSS DR8 data Giannantonio et al. (2012) detected a cross-correlation signal with a significance of 2.2σ using 25% of the sky. The 3π survey will have similar or greater depth than SDSS (see Chapter 2), so to forecast the significance of future ISW detections with Pan-STARRS1, one could scale up the SDSS significance for the larger 3π area. After masking the galactic plane, the 3π should cover around 50% of the sky, which would result in a 3.1σ detection based on the SDSS DR8 result. As mentioned however, these calculations may not be accurate, as sample variance may mean that SDSS DR8 has a particularly enhanced ISW amplitude.

As well as ISW, Pan-STARRS1 should also yield new measurements of the galaxy power spectra and BAO. The next few chapters will introduce Pan-STARRS1, and the work carried out to prepare Pan-STARRS1 for measuring large scale structure.

Chapter 2

Testing Pan-STARRS1 with Synthetic Images

In this chapter we introduce the Pan-STARRS1 (PS1) telescope, its camera, its planned surveys and a region of verification data we used in this thesis. PS1 has the potential to yield new information on galaxy formation and large scale structure. In order to do this however it is important that the magnitudes it measures from objects are accurate and free from systematic errors. It is also important to check that the telescope software is processing the raw data in an optimal way. We will therefore produce synthetic images and use them to test the PS1 telescope and software. The tests with synthetic images in this chapter represent the author's contribution to a larger paper testing PS1, Metcalfe et al. (2013), which we will refer to as Paper I in this thesis. Sections of the introduction to PS1 given in this chapter are from Farrow et al. (2014).

2.1 The Pan-STARRS1 Telescope

PS1 is a 1.8m telescope on Haleakala, Maui (Hodapp et al., 2004). Its unique selling point is its high *etendue*, the product of its collecting area and field of view, which allows it to survey large areas of sky quickly (Kaiser et al., 2002). It was designed as a prototype of PS4, an array of four identical telescopes scanning the whole sky in relatively short intervals for potentially threatening Near Earth Objects (NEOs)

(Kaiser et al., 2002). The multi-epoch nature of PS1 observations is not only good for the detection of moving and transient objects but also provides the redundancy necessary for highly accurate zero point calibration (Schlafly et al., 2012; Magnier et al., 2013), which is important for large scale structure analysis. Zero points should be accurate to 10 mmag from the calibration described in Schlafly et al. (2012) and Tonry et al. (2012)

To fully utilise its large etendue PS1 has a huge camera (GPC1), with 1.4 Gpixels. This camera is described in Tonry et al. (2008), but we will briefly introduce it here. CCD cells, 600 by 600 pixels in size, are arranged into 8 by 8 groupings called Orthogonal Transfer Arrays (OTAs). The whole camera is made from a mosaic of 60 OTAs, in an 8 by 8 grid with no OTAs in the four corners. PS1 pixels are 10μm or 0.256$''$ in size, such that each CCD cell is 2.6' on a side. Between individual CCD cells there is a 6 to 8 arcsecond gap, and between each OTA a 36 arcsecond gap or a 70 arcsecond gap depending on direction. This leads to masked regions in individual PS1 exposures. Overall the camera field of view is around 8.5 square degrees in size.

The finished PS1 survey will have two major co-added data products. The 3π survey with 31,500 square degrees of imaging and ten deeper 8.5 square degree (i.e. the telescope footprint) fields known as the "Medium Deeps". Each will have coverage in all 5 of the PS1 bands: $g_{\rm P1}$, $r_{\rm P1}$, $i_{\rm P1}$, $z_{\rm P1}$ and $y_{\rm P1}$. The 3π survey will be deeper and have a larger area than its predecessors, and is unique amongst existing optical surveys in having, $y_{\rm P1}$, a near infrared band. For more details on the 3π survey please refer to Chambers et al. (in preparation) and to Section 2.2.

As well as the main goal of detecting NEOs, it has always been envisaged that PS1 will meet a wide variety of science goals, including comets, extra-solar planets, supernovae, AGNs and large scale structure. PS1 does not have a spectrograph but photometric redshifts will be available from a dedicated pipeline (Saglia et al., 2012). As of March 2013, PS1 has been successful in detecting many new solar system objects[2], as well as supernovae (e.g. Valenti et al., 2010), variable AGN (e.g. Ward et al., 2011) and satellite galaxies around Andromeda (Martin et al., 2013).

[2]http://www.minorplanetcenter.org/iau/mpc.html

It has also been successfully used as a source of optical data for other surveys to measure the clustering of Extremely Red Galaxies (Kim et al. in preparation). In this chapter we test the PS1 system and software, with specific attention to whether it is ready to measure large scale structure.

2.2 The 3π Survey Strategy

The focus of this thesis is exploiting the 3π survey for large scale structure. Each region of sky in the 3π survey will be visited by the telescope twice a year in each band; during each visit two exposures will be taken. Individual exposures will last 43, 40, 45, 30 and 30 seconds in $g_{\rm P1}$, $r_{\rm P1}$, $i_{\rm P1}$, $z_{\rm P1}$ and $y_{\rm P1}$ respectively. The whole survey should last three years, so that when finished there will be 12 exposures of each sky position. These exposures will be stacked to produce the final image of the sky.

2.2.1 The PS1 Small Area Survey 2

The Small Area Survey 2 (SAS2) is a subset of the 3π survey roughly covering the region of $327.5 < \alpha(\text{deg.}) < 338.5$ and $-5.5 < \delta(\text{deg.}) < 5.5$. It is designed to be representative of the finished 3π survey. A large number of individual exposures were taken, co-added and mosaiced to form around 69 square degrees of imaging. It has a median $r_{\rm P1}$-band point spread function (PSF) FWHM of 0.94″, which has an rms scatter of less than 0.05″across the field. PS1 has a raw pixel scale of 0.256″. A careful study of the depth of this data set can be found in Paper I, which reports 50% of stars are recovered at magnitudes in the $g_{\rm P1}$, $r_{\rm P1}$, $i_{\rm P1}$, $z_{\rm P1}$and $y_{\rm P1}$-bands of 23.4, 23.4, 23.2, 22.4 and 21.3 respectively. All magnitudes in this thesis are measured in the AB system.

2.3 Detrended Exposures, Warps and Stacks

PS1 data reduction, from the initial processing of images through to stacking and source detection is carried out by the PS1 Image Processing Pipeline (IPP) (Magnier,

2006). In this section we will introduce the different steps of image processing that occur between taking the exposure and the final stacked images. The first step is detrending, where standard astronomical image processing such as flat fielding, background and dark image subtraction is carried out by the IPP (Magnier, 2006). An additional important correction that occurs at the stage is the correction for "row-by-row bias"[4]. Each row of pixels on the CCD has a "bias" added to the charge produced from photons falling onto the CCD row. This bias is simply a DC offset that ensures the signal is always positive when it is fed into further electronics to generate a digital signal. This bias is usually removed in two ways. Firstly a bias frame can be used, which is a read-out from the CCD when it has not been exposed to light. The second method estimates the bias from special regions of the CCD that do not get exposed to light when an image is taken. Unfortunately, in PS1, this offset changes from pixel row to pixel row and can vary with time, even changing as a row is read. This is a result of unintended problems with the CCD electronics. As a result neither of the two usual methods are entirely successful in removing the bias. In order to correct for this, a polynomial is fit to the read-out of each row of pixels, and subtracted. Unfortunately an unintended consequence of this subtraction is to over-subtract flux from around bright objects; this correction is therefore only applied to the worst affected CCDs. We will called the resultant images from these initial image processing steps "detrended exposures". For each image PS1 also produces "variance maps" which record the variance of the noise in each image pixel. This variance includes contributions from sources of astronomical noise including sky background, read noise and Poisson noise, and how they scale with the weighting of exposures in a stack.

The next step of processing is known as "warping". Here detrended exposures are translated from the CCD coordinates to the stack pixel coordinate system, and the pixel scale is changed from $0.256''$ to $0.25''$. Warping introduces correlations between the image pixels on scales of less than around $1''$. It also affects the variance of the image pixels (see Section 2.12). We will refer to these warped images as "warps".

[4]http://www.ifa.hawaii.edu/users/chambers/Astr735.html

The image, I, the variance map of that image, V, and the warp, I', and warped variance, V', are related by a warping kernel, k, thus

$$I'(x,y) = \sum_{u,v} k(u,v) I(x-u, y-v) \tag{2.3.1}$$

$$V'(x,y) = \sum_{u,v} k(u,v)^2 V(x-u, y-v), \tag{2.3.2}$$

where x and y are image pixel indices and u and v are kernel pixel indices. Here the kernel has been normalised so it sums to unity. This warping process converts some variance into covariance, such that $V'(x,y)$ no longer represents all of the noise on a pixel. To measure a warped pixel's total noise one needs to use a covariance matrix which accounts for the correlations between the pixels in the image. Storing the full covariance matrix would require a prohibitive amount of space so a much smaller matrix, known as the "covariance pseudo-matrix" is stored per image.

The covariance pseudo-matrix, $\tilde{C}(i,j)$, describes the covariance of a single pixel with each of the pixels in its neighbourhood, with relative pixel coordinate (i,j). For initially uncorrelated data this matrix is simply a function of the warping kernel,

$$\tilde{C}(i,j) = \sum_{u,v} k(u-i, v-j) k(u,v) K. \tag{2.3.3}$$

Where $K = (\sum_{u,v} k^2(u,v))^{-1}$, such that $\tilde{C}(0,0) = 1$ and $K = \sum_{i,j} \tilde{C}(i,j)$. The latter property follows from the normalisation of kernel, k. When making measurements which combine many pixels the effect of covariance on the overall variance of the measurement can be approximated by simply boosting individual variances by the factor K and otherwise ignoring covariance. This approximation is asymptotically exact for apertures much larger than the kernel size. The value of K changes from place to place on the sky but has an approximately Gaussian distribution with a mean of 1.379 with an rms of 0.006 for SAS2 $r_{\rm P1}$-band. We show that the warping process has little or no effect on the depth of images in Section 2.8, but we will revisit the covariance pseudo-matrix in a later chapter.

The final step is stacking the warps. A description of the IPP stacking procedure is given in the PS1 document PSDC-430-012 available from the IPP engineering

documents webpage[5], but we will highlight key features here. The warps are all scaled to a common zeropoint, based on the photometry of objects in each warp, before being stacked together. Pixels from individual warps are sigma clipped to remove outliers, before their mean value is computed for the stack. When computing the mean, warp pixels are weighted by their inverse variance.

2.4 Coverage Maps and Image Masks

The resultant stacks will potentially have different numbers of input warps contributing to each pixel. This is down to the observing strategy, which means exposures in a stack are not always coincident on each other. Additionally around 25% of individual exposures are masked, which is mainly due to the gaps between CCD cells and OTAs (Section 2.1), as well as defective CCD cells and other regions.

We will refer to the number of input exposures to a pixel as the "coverage" throughout this thesis. To illustrate this Fig. 2.1 gives the "coverage map", i.e. an image recording the number of exposures stacked for each pixel, in a $26'$ by $26'$ region. A typical SAS2 stacked image has an average coverage of around 8.9 exposures per pixel, with a standard deviation of around 3 exposures per pixel. In the stacks this gives rise to a spatially varying noise level. This noise is tracked in the stack's variance map. Naturally the spatially varying image noise leads to different depths at different positions on the sky. We will develop ways to address this issue when measuring clustering in Chapter 3.

In addition to coverage maps and variance maps the PS1 IPP (Magnier, 2006) also produces image masks. These image masks track pixel quality and highlight pixels which have been flagged as suspicious (e.g. likely to be cosmic rays or image artifacts) by the pipeline. Images, image masks, coverage maps and variance maps are all supplied in approximately $26'$ by $26'$ units called "skycells". These skycells do not represent unique areas on the sky but overlap, and in these overlap regions pixels from different skycells are not necessarily the same, since decisions on which exposures to reject from a stack are made on a skycell by skycell basis.

[5]http://svn.pan-starrs.ifa.hawaii.edu/trac/ipp/wiki/IPP_Engineering

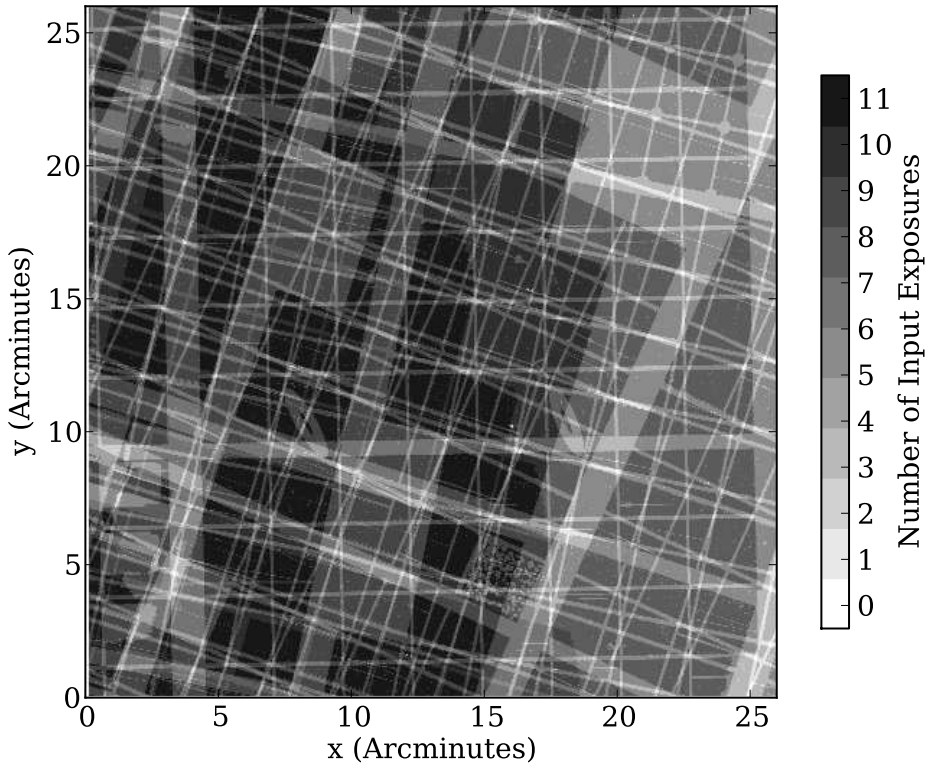

Figure 2.1: The coverage, i.e. the number of input exposures, of a typical 26 by 26 arcminute SAS2 stack skycell. Black areas correspond to 11 input exposures for that pixel, white corresponds to no input exposures (a blank pixel). The grid pattern arises from the gaps between cells in individual exposures. The elliptical regions correspond to the masking of some spurious reflected light (called ghosts).

2.4.1 IPP Source Detection and Magnitude Measurement

Source detection on the images is carried out by the IPP code PSPHOT (Magnier, 2006); we will give a basic overview of this code here. First an image is convolved with a filter, chosen to maximise the signal-to-noise ratio (SNR), before being divided by the variance map to produce an image giving the SNR for each pixel. The code then uses the covariance pseudo-matrix to decide where significant peaks are in the SNR image.

Due to the atmosphere and telescope optics galaxy light profiles appear convolved by the point spread function (PSF) of the instrument and atmosphere. Another task of PSPHOT is to fit a model of the PSF to the image. In the PS1 IPP stars are fitted with a PSF model, called the PS_v1 model, of the form

$$I = \frac{I_0}{1 + kz + z^{3.33/2}}, \tag{2.4.4}$$

$$\text{where } z = \frac{x^2}{2\sigma_x^2} + \frac{y^2}{2\sigma_{y^2}} + xy\sigma_{xy}, \tag{2.4.5}$$

where I_0 is the central intensity, x and y are the x-axis and y-axis distances from the centre, k is a free parameter and σ_x, σ_y, σ_{xy} are free parameters that represent the x-axis width, the y-axis width and a cross term respectively. Typically PS1 PSFs, and indeed real PSFs in general, have more extended wings than Gaussian PSFs of the same full width half max (FWHM). To show this we numerically integrate Eq. 2.4.4, using a PSF model fit to a typical SAS2 OTA with $k = -0.12$ and $\sigma_x = 1.64$. We force the model to be circular by artificially setting $\sigma_x = \sigma_y$ and $\sigma_{xy} = 0$. The result of this integration, compared to a Gaussian with the same FWHM is shown in Fig. 2.2; the more extended wings and less peaked central surface brightness can be seen.

Skycells are split 3 by 3 during the PSF fitting, and the best-fitting model parameters are found for bright, unsaturated stars in each of the 9 cells. The final PSF model interpolates between these parameters such that the PSF model varies smoothly across a skycell.

PSPHOT is also responsible for measuring magnitudes. In this thesis we use Kron magnitudes (Kron, 1980) as measured by PSPHOT. Kron magnitudes measure flux in an aperture with a radius called the "Kron radius", which is some multiple (2.5

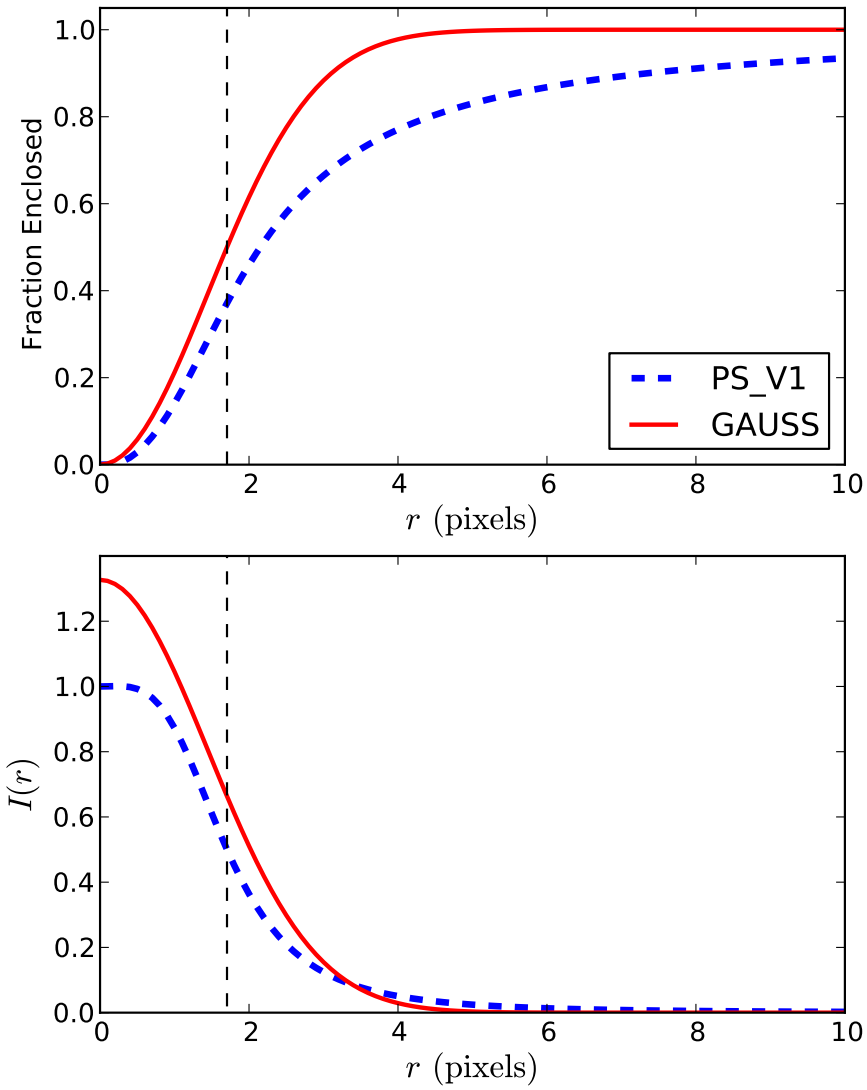

Figure 2.2: The curve of growth of a PS1 PSF model profile, compared to that of a Gaussian with the same FWHM of 0.85″ and the same integrated flux. The top panel gives the enclosed fraction of flux, the bottom panel gives the intensity as a function of radius. We see PS1 PSFs have more extended wings.

for PS1) of the first moment radius of the flux (Kron, 1980). Kron magnitudes are designed to contain the majority of flux for a given source profile regardless of size, but a small, profile dependent correction term is required to account for flux outside the Kron radius. For galaxies with the same light profile this fraction is theoretically the same, regardless of the apparent size of the galaxy.

In this thesis we also use point spread function (PSF) magnitudes as measured by PSPHOT, which are magnitudes based on extrapolating the magnitude from a small aperture, chosen to maximise SNR, using the IPP PSF model. We shall label these magnitudes with the suffix "PSF" to contrast with the Kron magnitudes which we label simply using the name of the filter, i.e. $g_{\rm P1}$, $r_{\rm P1}$, $i_{\rm P1}$, $z_{\rm P1}$ and $y_{\rm P1}$.

Finally, in this thesis we also refer to 'input' or 'total' magnitudes when talking about synthetic objects. These are simply the magnitude corresponding to the sum of all of the flux of the synthetic object.

The code PSPHOT also produces flags for each object which indicate how reliable it is. We use these flags and all objects with FITFAIL, SATSTAR, BADPSF, DEFECT, SATURATED, CR_LIMIT, MOMENTS_FAILURE, SKY_FAILURE, SKYVAR_FAILURE OR SIZE_SKIPPED set are removed. Further discussion of these flags can be found in Paper I.

The last feature of PSPHOT we will mention is its synthetic star generation. PSPHOT adds synthetic stars, using its own PSF model, to images. It can return the detected fraction of these stars as a function of magnitude along with the difference between their input and recovered magnitudes. We also require synthetic galaxies, in order to test the measurements of galaxy magnitudes and how well PS1 recovers galaxies. Unfortunately PSPHOT does not produce galaxies; so we have produced our own synthetic sources. In addition, our synthetic sources can be added to images and then these images can be warped and stacked. PSPHOT does not put synthetic images through the warping and stacking procedure.

2.4.2 Galaxy profiles

Before describing our method of generating synthetic images, we first review the basic properties of galaxy light profiles. Galaxies have light profiles well fitted by

the famous Sérsic functions (Sérsic, 1963). For a review see Graham & Driver (2005). In flux this can be expressed as

$$F(R) = F_{\rm eff} \exp\left(-b_n \left[\frac{R}{R_{\rm eff}}\right]^{\frac{1}{n}} - 1\right), \tag{2.4.6}$$

where R is the distance to the centre, $F_{\rm eff}$ is the flux at $R_{\rm eff}$ and b_n is a scaling constant that depends on the index, n, defined such that $R_{\rm eff}$ is the half light radius. A value of $n = 1$ and $b_n = 1.678$ gives an exponential profile, typical of the discs of spiral galaxies while a value of $n = 4$ and $b_n = 7.669$ gives the de Vaucouleurs profile typical of elliptical galaxies (see Graham & Driver, 2005; de Vaucouleurs, 1948).

2.5 Generating Synthetic Objects

To generate a synthetic star one needs to simply choose a magnitude and a position and then evaluate the PSF model. Generating a galaxy is harder as several parameters must be chosen, namely: the position, the bulge to disc ratio, the Sérsic index, the size, the ellipticity and the orientation on the sky. The last of these is chosen at random. As the clustering of the synthetic sources is not important here a position is also randomly assigned.

When choosing the Sérsic index we approximate the Universe as being made up entirely of de Vaucouleurs profiles for elliptical type galaxies and bulges, or exponential profiles for discs. This follows the classic bi-modality in Sérsic index between elliptical galaxies and discs. In reality galaxies follow a distribution of Sérsic indices, with elliptical galaxies displaying a positive correlation between luminosity and Sérsic index (see e.g. Ferrarese et al., 2006). We also treat bulges in disc galaxies in the same way as elliptical galaxies, which is a common approximation adopted in the literature (Bertin & Arnouts, 1996; Shen et al., 2003). A major goal of these tests is to see how well PS1 recovers faint galaxies, and how accurate magnitude measurements from them are. As these faint galaxies will tend to have small angular sizes, and because the synthetic galaxies are convolved with a PSF, our approximations should have little effect on our results.

For the axis ratios of discs we choose a random inclination angle, i, distributed uniformly in $\cos(i)$ and assuming circular flat discs with a thickness which is some

fraction, t, of the radius we calculate the apparent axis ratio, $e_{\rm sky}$, using simple geometry as

$$e_{\rm sky} = \cos(i) + t\sin(i). \tag{2.5.7}$$

We take $t = 0.1$ for our disc height to scale-length ratio. The resulting distribution is flat and a reasonable fit to the observations in Padilla & Strauss (2008). For bulges we select a major to minor axis ratio, e, between 0.3 and 1.0, corresponding to the classical elliptical types of E0 to E7 (see e.g. Mo et al., 2010). Within this range we select e from a truncated Gaussian distribution of mean $\mu = 0.75$ and variance of $\sigma^2 = 0.1$, which we chose to give a reasonable fit to the data in figure 4 of Padilla & Strauss (2008).

For physical galaxy sizes we use the empirically measured relation and its scatter given in equations 14, 15 and 16 of Shen et al. (2003). We adopt parameters measured in Shen et al. (2003) for galaxies separated into late and early types by Sérsic index (figure 6 of that paper). It was reported in Dutton et al. (2011) that using the Shen et al. (2003) measurements would result in discs too small by a factor of around 1.4, due to not factoring in the effects of inclination which decreases the size by the square root of the apparent axis ratio. We therefore increase the size of our disc galaxies by this factor. We also correct the empirical bulge size relation for this effect, adopting a correction of 1.2, calculated from the typical bulge ellipticity μ. For bulges and elliptical galaxies we choose not to extrapolate the relation from Shen et al. (2003) to fainter magnitude bins than measured in that paper. Instead, we keep the sizes of bulges and elliptical galaxies fixed fainter than $M_r = -19$; this is motivated by observations that dwarf elliptical galaxies have a nearly constant size regardless of magnitude (see e.g. Shen et al., 2003; Mo et al., 2010).

We now have a relation between physical size and absolute magnitude, therefore we need a redshift and an absolute magnitude to predict angular sizes. One could generate these using observed luminosity functions and redshift distributions, but here we use data from the mock catalogues produced for Merson et al. (2013) using a recent version of the GALFORM galaxy formation model presented in Lagos et al. (2011). Using these catalogues gives us the potential to extend this work to generate synthetic images with realistic galaxy clustering. For the purposes of this

work, however, we use random angular positions. The model adopts a concordance cosmology of $\Omega_{\rm m} = 0.25, \Omega_\Lambda = 0.75, \Omega_{\rm b} = 0.045, h = 0.73$; we use this cosmology for the whole of this work. The GALFORM model gives magnitudes and redshift distributions in good agreement with observations at low redshift (e.g. Bower et al., 2006). We split the total flux of the model galaxy into a bulge component and a disc component by randomly sampling bulge to total ratios from table 3 of Simard et al. (2011), which gives an observational estimate of bulge to total ratios for around a million SDSS galaxies.

Once we have the galaxy morphological properties we evaluate Equation 2.4.6 on a pixel grid of a linear scale three times smaller than PS1 warped pixel scale of $0.25''$ before binning up. This is to minimise the effect of gradients in the profile across pixels. Pixels on the finer grid whose centres are closer than $0.1''$ to the profile centre are further subdivided 3 by 3 to take into account the steeper profile near the centre. If any of these subdivided fine pixels are on the centre of a de Vaucouleurs profile, an analytic integral is used to approximate the flux required, as de Vaucouleurs profiles asymptote to infinity at zero radius. Stars, conversely, are evaluated directly on to the native pixel scale as this is the scale at which the model is measured. Galaxy profiles are convolved with the PSF using the C-library FFTW (Frigo & Johnson, 2005). The grid dimensions are chosen to ensure that the finished, convolved galaxy image contains more than 99.8% of the flux. Stars are evaluated on a grid of $36''$ by $36''$ which contains more than 99.9% of the flux for PS1 SAS2 PSFs.

In Fig. 2.3 we show an example of a synthetic warp, next to the real warp from which we took the PSF model, the background noise and the mask. The colour scale of Fig. 2.3 is the same for both panels. We see our fake images look realistic, although we do not model the image artifacts visible in the real image. The most notable of these image artifacts are the horizontal lines caused by the row-by-row bias issues.

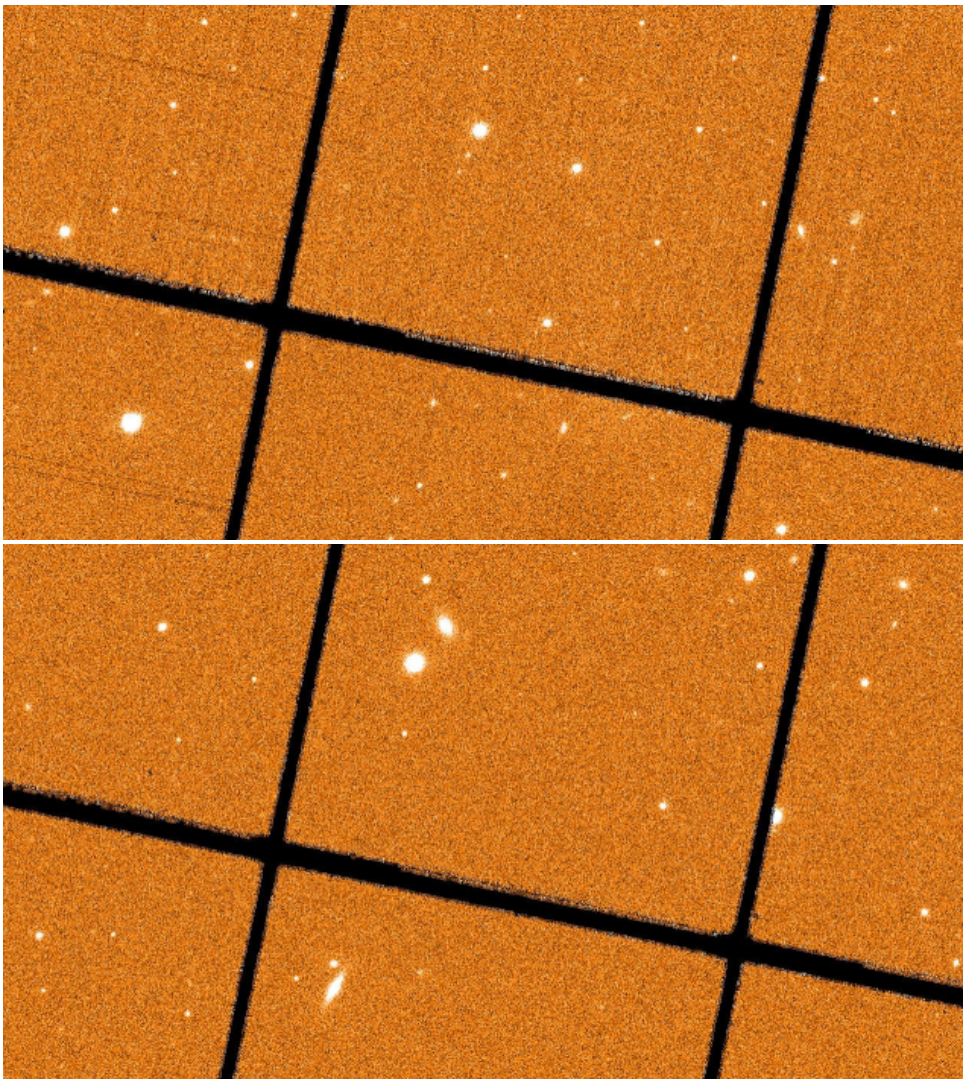

Figure 2.3: A comparison of a real 5 arcminute by 3 arcminute region of the SAS2 r_{P1}-band warp 454105 (above), to the same region in a simulated version of the warp (below).

2.6 Synthetic Image Server

Whilst our use of the synthetic images is for the testing and development of PS1 data generally, other users of PS1 data may find synthetic images useful if they want detailed tests of a particular region of PS1. For example, if they wished to know the chance of detecting an object with a particular morphology in a certain PS1 image. We have therefore produced the "PS1 Fake Image Server". This is essentially a web interface to the synthetic image code we have developed. The user is given a webpage, as displayed in Fig. 2.4(a), into which the user inputs the zeropoint and stack ID of a particular PS1 stack they wish to insert images into. The user must also upload a source file, which is an ASCII file containing the pixel positions, magnitudes and morphological properties of the objects they wish to simulate. On submission of the form, a PHP script downloads the source file to the fake image server's hard drive and uploads the other supplied information to a MySQL database. The list of currently uploaded requests, the "queue page" is available to the user from another webpage which queries that MySQL database, see Fig. 2.4(b).

On the server a Python script is run which regularly checks the MySQL database for new requests. On receiving a new request it downloads the required PS1 images from the PS1 Postage Stamp Server and then produces the required fake images. These are placed into a folder on the server, and the Python script updates the MySQL server to mark the request as complete. The queue page then includes a link to the folder where the user can download their requested images, see Fig. 2.4.

2.7 Testing Detrended Exposures with Synthetic Data

With the synthetic images introduced, we will now describe the tests we carried out with them on PS1. The first test we conducted with synthetic images was the most simple. We produced synthetic detrended exposures, which are as close to raw PS1 data as we study. To produce these detrended exposures we used four real SAS2 detrended exposures as a template, namely from the cells XY21, XY22, XY31,

Figure 2.4: Screenshots from the synthetic image server. Panel (a) shows the page where the user submits requests, panel (b) shows the queue page where the user can download the finished images.

XY32 from the 40 second $r_{\rm P1}$-band exposure o5745g0448o. We copied the pixel rms as measured from the real detrended exposures, used the real image zeropoint, used the PSPHOT measured PSF models and adopted the same image masks. We chose the magnitudes and numbers of stars and galaxies to place on the OTA from power-law fits to the number counts of stars and galaxies for the whole of SAS2 (see Chapter 3). If the noise in an image is dominated by sky noise or source noise, the pixel rms is simply the square root of the image and variance maps are simply the images without any background subtraction. To approximate the level of the sky background, we assume that the measured rms is mainly caused by Poisson fluctuations in the sky background. We therefore estimate the sky background by squaring the measured rms value. This value is then added to the image to form the variance map.

In order to improve statistics whilst maintaining a realistic number-density of objects we produced multiple synthetic realisations of the same detrended exposure, with different objects for each realisation. The resultant images and variance images were fed into PSPHOT along with the mask images from the real detrended exposures.

Fig. 2.5 gives the difference between the magnitude of the input object and the measured Kron magnitude as a function of input magnitude. The red points and error bars mark medians, along with upper and lower quartiles. The median values and interquartile range, i.e. the difference between the upper and lower quartiles, are given in Table 2.1. As expected the Kron magnitude is slightly fainter than the input magnitude for stars and galaxies, with the offset being larger for galaxies. The magnitude offset for galaxies of 0.1 to 0.2 magnitudes is slightly larger than theoretical expectations. For example one would expect an offset of 0.1 magnitudes for de Vaucouleurs profiles and 0.04 magnitudes for exponential disks (e.g Graham & Driver, 2005). We note in Paper I that the offset between PSPHOT Kron magnitudes and SDSS estimates of total real galaxy magnitudes, found from fitting Sérsic models, are also larger than the theoretical expectations. The simple theoretical expectations assume that the first moment radius can be measured perfectly for a galaxy which consists of a single Sérsic profile. Our simulated galaxies come from composites of two Sérsic profiles, have noise and have been convolved with the PSF.

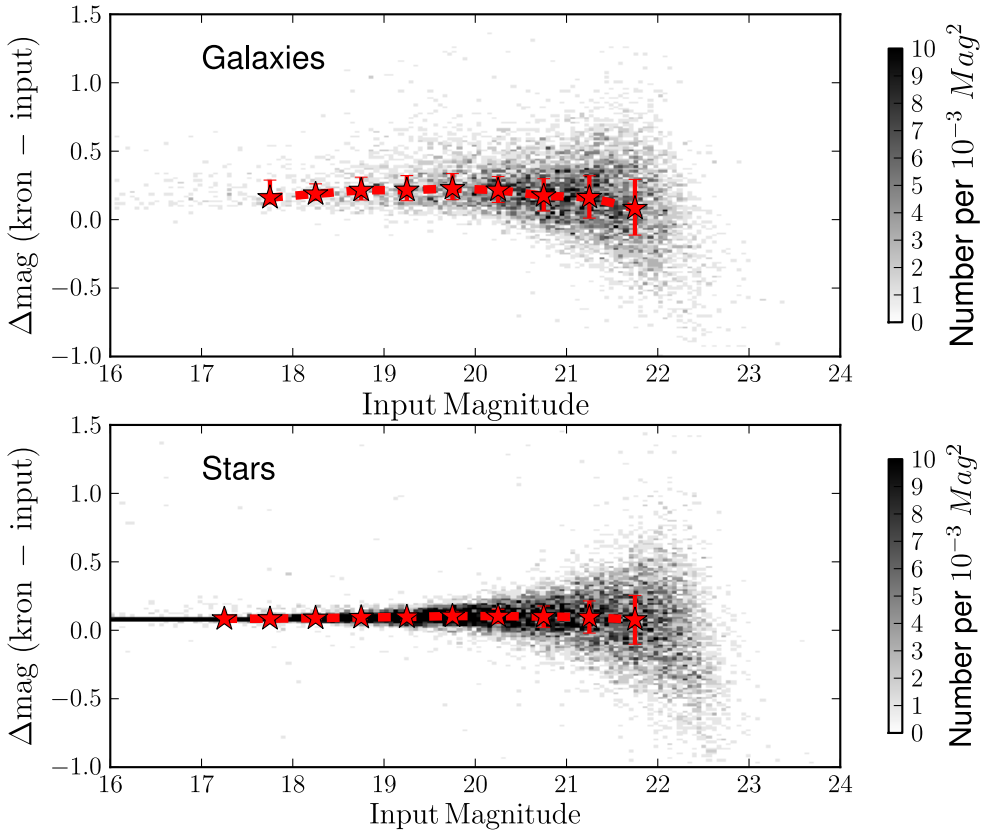

Figure 2.5: The input magnitude versus the recovered magnitude for galaxies (above) and stars (below), for synthetic objects placed on synthetic detrended exposures. The red stars mark the median values, the error bars mark the upper and lower quartiles.

Table 2.1: The median and interquartile range of the difference between total input synthetic magnitude and the recovered Kron magnitude, for synthetic objects on synthetic detrended exposures. At faint magnitudes the bright offset in the median recovered value is simply a selection effect, objects scattered fainter are not detected by the software.

Magnitude	Star Median	ΔQuartile	Galaxy Median	ΔQuartile
17.2	0.08	0.01	0.18	0.14
17.8	0.08	0.02	0.16	0.17
18.2	0.09	0.02	0.19	0.12
18.8	0.09	0.03	0.21	0.17
19.2	0.10	0.05	0.22	0.18
19.8	0.10	0.07	0.23	0.19
20.2	0.10	0.10	0.22	0.19
20.8	0.10	0.16	0.17	0.24
21.2	0.10	0.23	0.16	0.31
21.8	0.08	0.36	0.08	0.41

All of these extra observational effects are likely to contribute to the slightly higher than expected offset. At faint magnitudes the bright offset in the median recovered value is simply a selection effect, objects scattered fainter are not detected by the software. We see no evidence of any systematic trends with magnitude in Fig. 2.5 and overall PSPHOT seems to recover the magnitudes successfully from these synthetic detrended exposures.

We can use these measurements when comparing total magnitudes from synthetic galaxies to observed quantities and when comparing to literature measurements. In this thesis we adopt an average correction of $mag_{\rm Total} = mag_{\rm Kron} - 0.2$ to convert from Kron magnitude to total magnitudes for galaxies; we will state explicitly wherever we apply this correction throughout this thesis.

Fig. 2.6 gives the fraction of synthetic objects recovered from the detrended exposures for synthetic stars (stars) and galaxies (circles) as a function of magnitude. We shall refer to this detected fraction as "detection efficiency" in this thesis. The error bars represent the scatter between the multiple realisations of the detrended exposures. The dashed line represents the fraction of detected synthetic stars placed on the real detrended exposures by the IPP's own synthetic star software. We see excellent agreement in terms of detection efficiency between our synthetic detrended exposures and the real detrended exposures. Fig. 2.6 also demonstrates galaxies are harder to detect, with the detection fraction turning over around 0.5 magnitudes brighter for the galaxies than for the stars.

A commonly used statistic in astronomy is the 5σ limiting magnitude, the magnitude corresponding to an SNR of 5.0. Using the pixel rms, we calculated the total stellar magnitude which gave an SNR of 5 within an aperture with a diameter equal to that of the measured FWHM of the PSF. We plot this 5σ limiting magnitude as a vertical line in Fig. 2.6. We see this magnitude corresponds to a fraction of 50%-60% for synthetic stars. This value can be useful as the 5σ limiting magnitude can be quickly estimated for PS1 images; Paper I shows one can make reasonably accurate estimates of σ for a PS1 image from tabulated measurements of the sky brightness, read noise, dark current and exposure time.

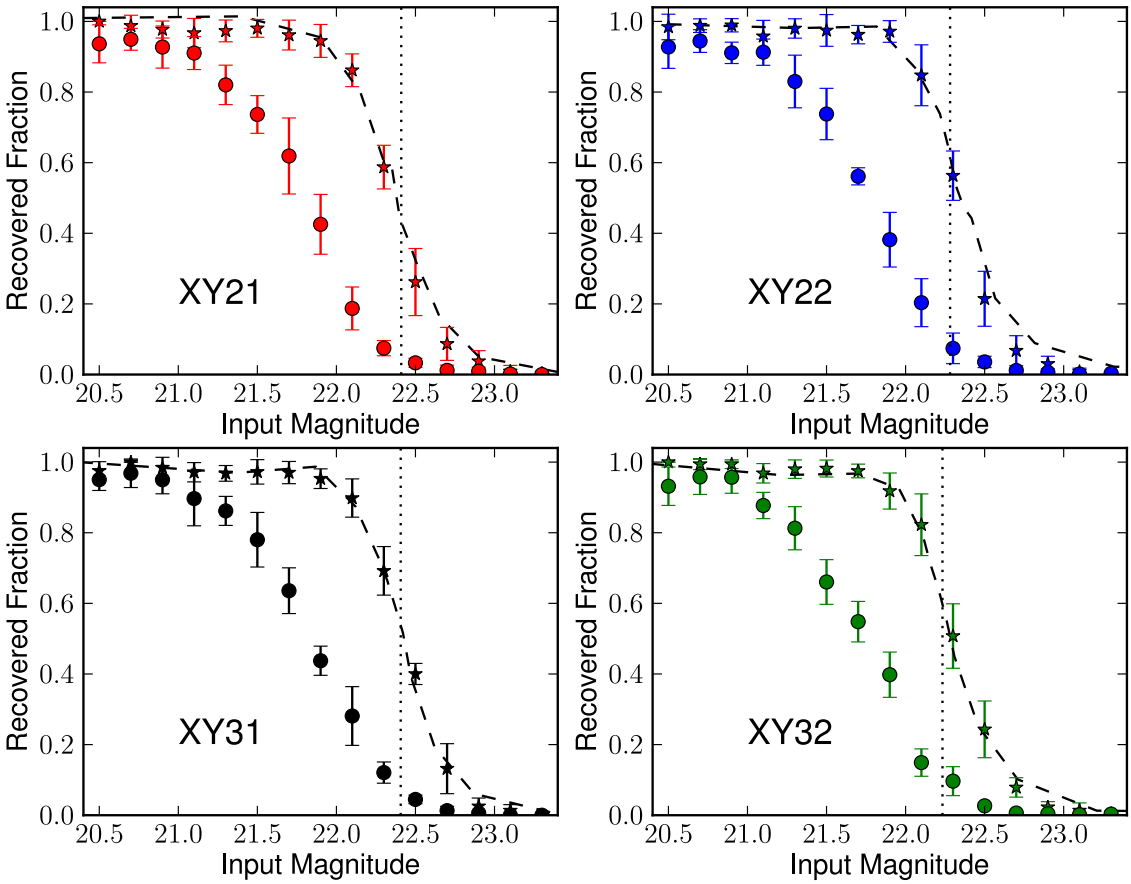

Figure 2.6: The fraction of stars (stars) and galaxies (filled circles) recovered from 4 synthetic detrended exposures as a function of input magnitude. The dashed lines give the recovered fraction of stars on the real images, as calculated from IPP's own synthetic objects. The dotted line gives the 5σ magnitude.

Table 2.2: The median and interquartile range of the difference between total input synthetic magnitude and the recovered Kron magnitude, for synthetic objects on synthetic detrended exposures that have been warped.

Magnitude	Star Median	ΔQuartile	Galaxy Median	ΔQuartile
17.2	0.08	0.01	0.19	0.19
17.8	0.09	0.01	0.14	0.17
18.2	0.09	0.02	0.18	0.10
18.8	0.09	0.03	0.25	0.23
19.2	0.10	0.05	0.21	0.19
19.8	0.11	0.07	0.23	0.22
20.2	0.11	0.10	0.22	0.21
20.8	0.12	0.15	0.18	0.23
21.2	0.10	0.23	0.16	0.31
21.8	0.07	0.37	0.07	0.42

2.8 Testing Warped Images with Synthetic Data

The detrended exposures we produced for the previous section were fed into the IPP routine PSWARP, which warped the detrended exposures to produce synthetic versions of the warp with warp id 454105. We produced each warp from a unique set of synthetic OTA images. Note that the warp covers a smaller area of sky than the detrended exposures so the synthetic warps have fewer synthetic objects than the combined detrended exposures. The IPP routine PSWARP produced variance images and masks for the resultant synthetic warp. We ran PSPHOT on the warp with these masks and variance maps, to test for systematic errors arising in the warping process.

Fig. 2.7 gives the difference between the input and recovered magnitudes for our synthetic warps. We see PSPHOT on the warps also successfully recovers the input magnitude. The medians and interquartile ranges are given in Table 2.2. From comparing Table 2.1 to Table 2.2 we see no evidence of the warping significantly modifying the scatter or offset from total of the recovered magnitudes. The only

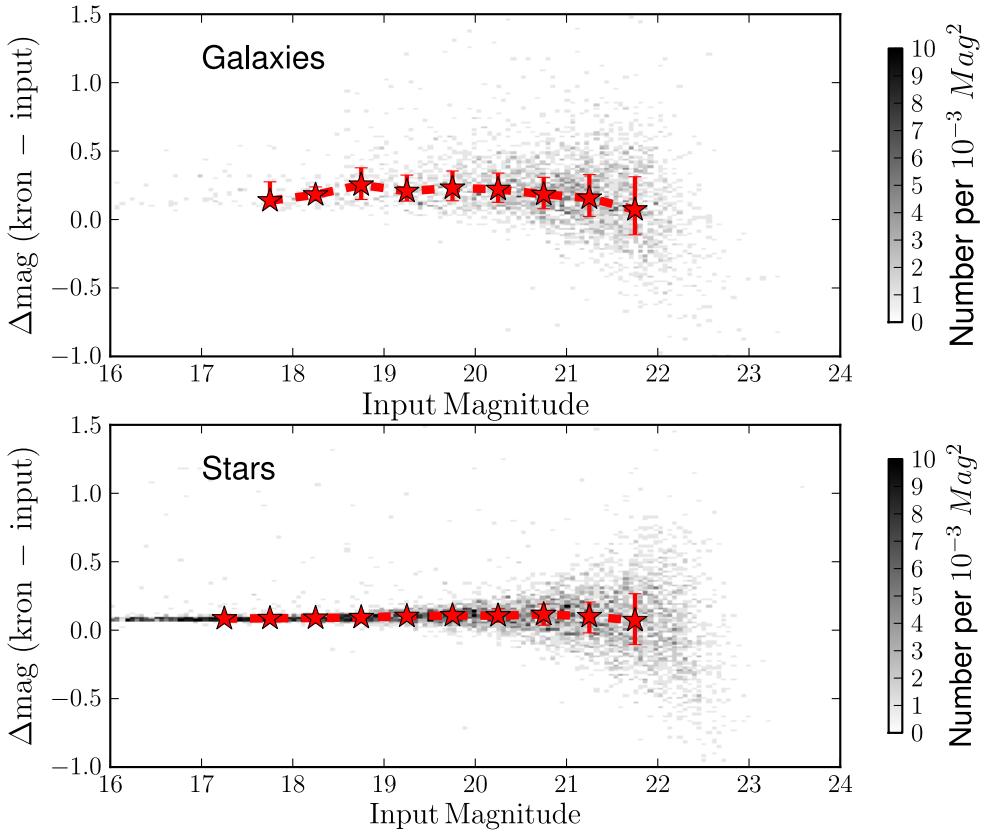

Figure 2.7: The input magnitude versus the recovered magnitude for galaxies (above) and stars (below), for synthetic objects placed on a synthetic warp. The red stars mark the median values, the error bars mark the upper and lower quartiles.

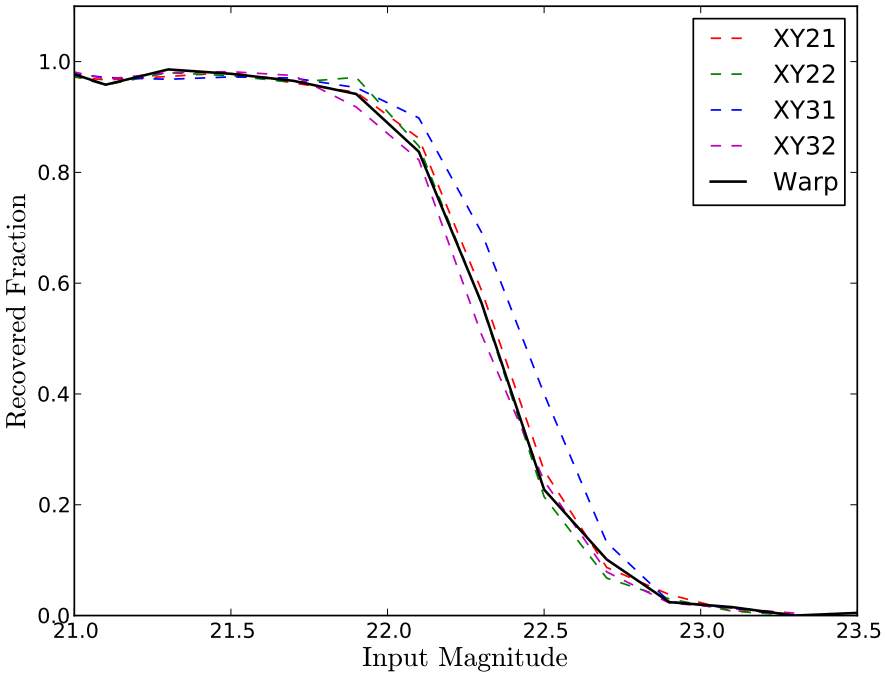

Figure 2.8: The fraction of synthetic stars detected as a function of their input magnitude, for the 4 detrended exposures and the warped created from them. Curves have been corrected for fraction of the images masked.

difference larger than 0.02 magnitudes is for the brightest galaxies in a magnitude range where we have few objects and the scatter is large. The few objects on the detrended exposures that are not within the field of view of the warp could explain this difference.

We also wished to test if warping has any affect on image depth. Fig. 2.8 compares the depth of the warp with those of the four detrended exposures. The warp depth is greater than the shallowest OTA. Given that different detrended exposures contribute varying amounts of area to the warp, Fig. 2.8 shows no evidence that warping is modifying depth. Again this is the expected result, since the covariance pseudo-matrix should track any changes to the noise introduced by warping.

Overall these results indicate the warping process does not introduce systematic errors in the magnitudes or probability of detection of PS1 objects.

2.9 Testing Stacks with Synthetic Data

The stacking process is perhaps where systematic errors are most likely to arise, as it is a more complex procedure than warping. Warping is an image transform which, if carried out correctly, should conserve flux. Stacking, on the other hand, involves averaging multiple images, with different backgrounds and PSFs, and applying statistical outlier rejection (such as median clipping). The resultant stack should have a higher signal-to-noise ratio than the individual images and will have a complex variable noise pattern, owing to the variable coverage. In order to test the stacking process we change our approach slightly and add synthetic objects to real warps. This saves us from producing the large number of detrended exposures which combine to make one stack, it also has the added benefit of using real image backgrounds complete with any sources of noise or systematics unmodeled by our synthetic images.

We do not model the effect of the warping procedure on a synthetic object's flux, beyond ensuring we use the appropriate pixel scale and zeropoint for the warps. Since we already convolved the synthetic objects by the PSF, this extra convolution by the much smaller warping kernel is unlikely to affect our results. When generating synthetic objects we still draw their morphological characteristics from our realistic distributions, but we simply add a set number of synthetic objects which is much less than the observed number density. This is because real objects are already present on the image, and to duplicate their number would result in excessive crowding and so excessive overlaps between objects.

Fourteen real warps with our added synthetic images were stacked using the IPP routine ppStack, which is the same set of software that is used to produce the real stacks. The routine produces images, masks, coverage maps and variance maps complete with spatially varying background noise from our warps. The end product is a version of the $r_{\rm P1}$-band, 540 second exposure SAS2 stack with id 1034502, complete with synthetic objects.

Fig. 2.9 shows the difference between the input magnitude of the synthetic objects and their measured magnitude from the stack. As before the medians and interquartile ranges are given, in Table 2.3. We see again that psphot does a good

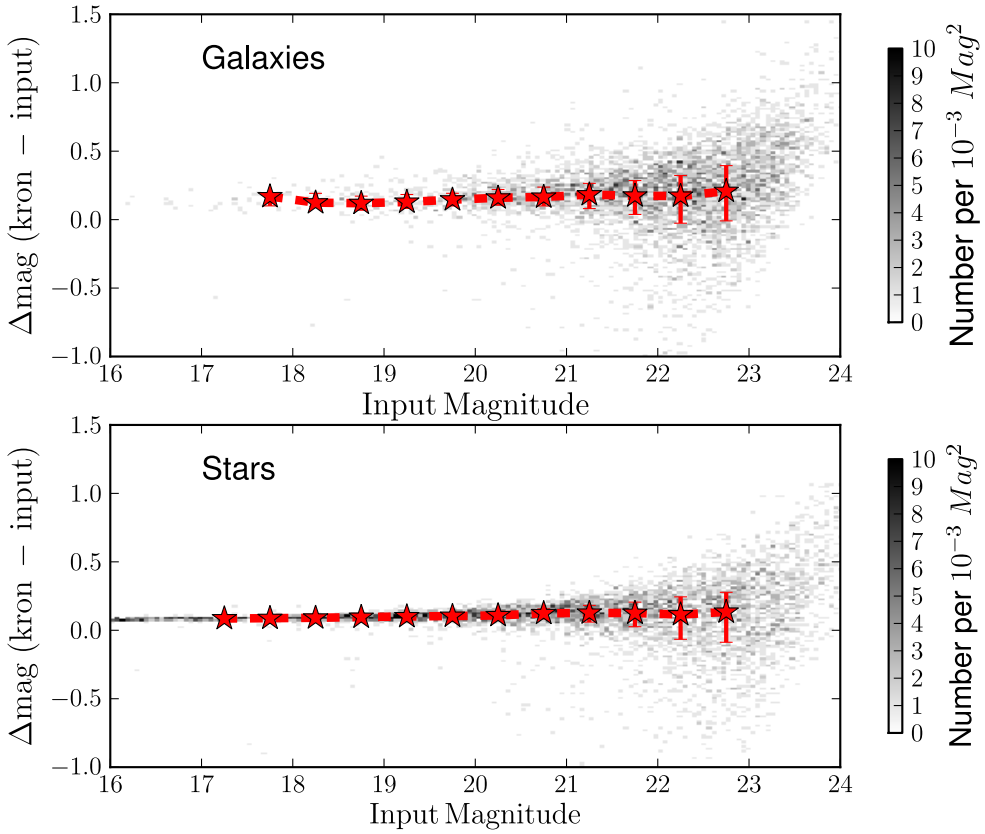

Figure 2.9: The input magnitude verus the recovered Kron magnitude for galaxies (above) and stars (below), for synthetic objects placed on real warps and then stacked. The red stars mark the median values, the error bars mark the upper and lower quartiles.

Table 2.3: The median and interquartile range of the difference between total input synthetic magnitude and the recovered Kron magnitude on a stack. Measured from synthetic objects placed on real warps and then stacked.

Magnitude	Star Median	ΔQuartile	Galaxy Median	ΔQuartile
17.2	0.09	0.01	0.08	0.08
17.8	0.09	0.01	0.17	0.08
18.2	0.09	0.02	0.12	0.09
18.8	0.10	0.03	0.12	0.10
19.2	0.10	0.03	0.13	0.10
19.8	0.10	0.04	0.15	0.09
20.2	0.11	0.06	0.16	0.11
20.8	0.12	0.07	0.17	0.14
21.2	0.13	0.12	0.18	0.18
21.8	0.13	0.18	0.17	0.25
22.2	0.11	0.31	0.17	0.35
22.8	0.13	0.37	0.21	0.40

job at recovering the correct magnitudes: the magnitudes offsets on the stacks are in accord with those on the warps and detrended exposures. We can also see the stacking procedure decreases the scatter on the recovered magnitudes, particularly for faint stars and for galaxies. This suggests that the stacking and the spatially varying number of input warps does not introduce systematics into the magnitude measurements.

The top panel of Fig. 2.10 shows the area between the detection efficiency curves for synthetic stars on the deepest and shallowest warps, in the grey region, and the stellar detection efficiency curve from the resultant stack, in red. If a certain SNR corresponds to a certain detection fraction, and the stacking procedure lowers the noise by the square root of the number of input warps, $\sqrt{N}$, then the image should get deeper by $-2.5\log_{10}(\sqrt{N})$ magnitudes. The mean number of input warps for any pixel on this stack is $N = 8.8$, as measured from the coverage maps. We therefore expect a 1.18 magnitude increase in depth; this value is indicated by the arrow on Fig. 2.10. We can see the stacking procedure successfully increases the depth by the expected amount.

The bottom panel of Fig. 2.10 gives the difference in warp and stack depth for galaxies. We can see that the improvement in galaxy depth is arguably greater than expected from the simple $\sqrt{N}$ scaling argument, and is greater than the depth increase of synthetic stars. This could be due to fainter galaxies having smaller angular sizes and as such being easier to detect. Note that Fig. 2.10 still shows that in these stacks galaxies are harder to detect than stars.

So far we have found no evidence that the warping and stacking processes introducing errors into the source magnitudes. We have also shown that the depth scales as expected with stacking. The depth of the typical SAS2 stack presented here is consistent with the Paper I $r_{\rm P1}$-band 'turnover magnitude', which is the magnitude at which number counts begin to decrease. It appears from Fig. 2.10 that the Paper I turnover magnitude of $r_{\rm P1} = 22.8$ corresponds to a detected fraction of around 80%. The benefit of the turnover magnitude is that it is easily measured across multiple bands, Paper I found its value to be 23.0, 22.8, 22.5, 21.7, 20.8 in the $g_{\rm P1}$, $r_{\rm P1}$, $i_{\rm P1}$, $z_{\rm P1}$ and $y_{\rm P1}$-bands respectively. Paper I suggests that the turnover magnitudes for

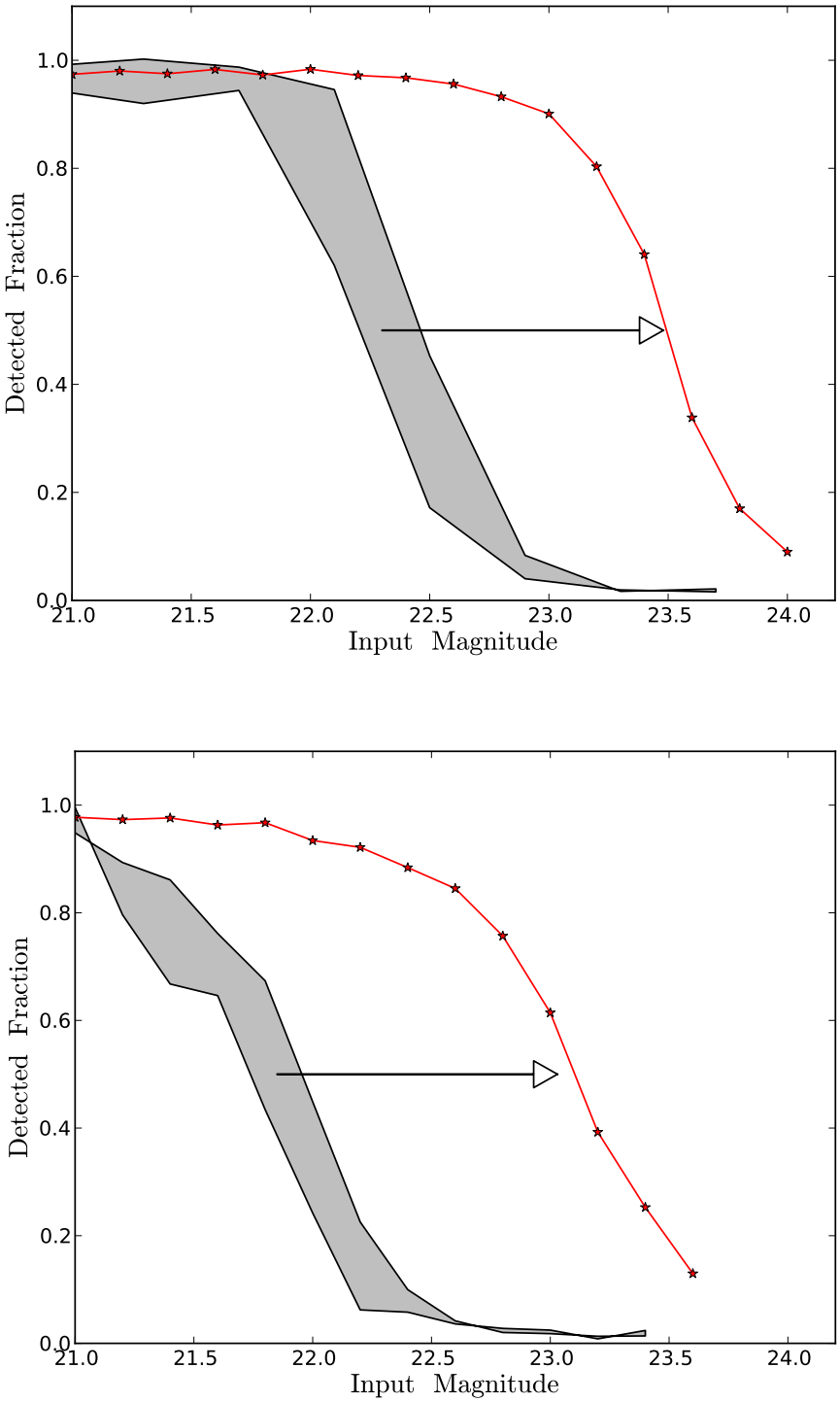

Figure 2.10: The fraction of synthetic stars (above) and galaxies (below) detected as a function of their input magnitude, for a stack with added synthetic objects (red). The grey region gives the region between the detected fractions for the deepest and shallowest of the warps input into the stack. The arrow gives the expected scaling of depth between the warps and the stacked warps.

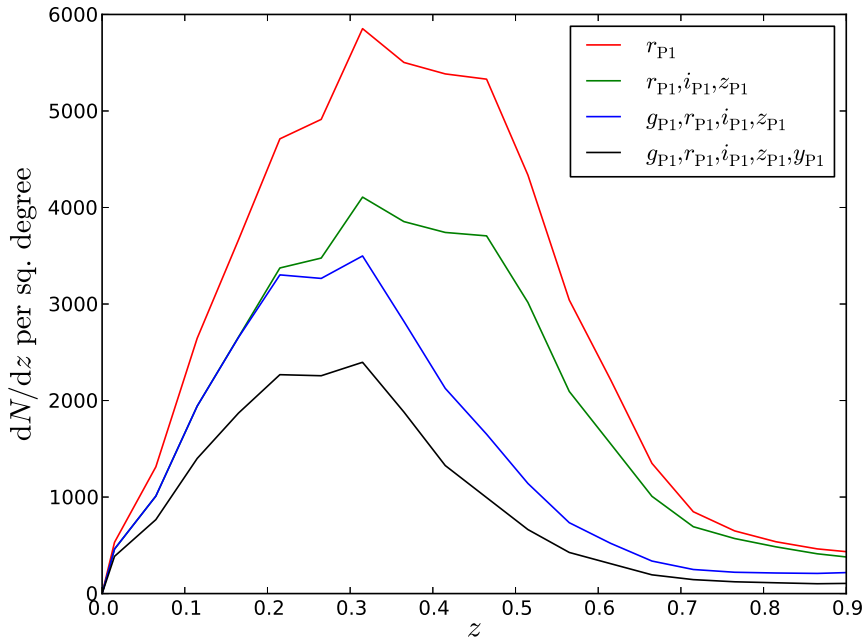

Figure 2.11: The predicted $n(z)$ of PS1 3π data, created by applying the estimates of finished 3π depth to our mock catalogue. The legend gives the different combinations of bands in which a detection is required. The g_{P1} and y_{P1}-bands are the shallowest, and seem to cause the greatest decrease in depth.

the full 3π data will be 0.4 mags brighter due to the poorer seeing when compared to SAS2. We can use these brightened limits to predict the redshift distribution of 3π galaxies, by applying them to our mock catalogue.

In Fig. 2.11 we show the predicted $n(z)$ from applying the predicted 3π magnitude limits to the mock catalogue, applying the cut on each galaxy in different combinations of bands. The g_{P1} and y_{P1}-bands are the shallowest, and seem to cause the greatest decrease in depth. Clearly to yield the deepest data set one would not require a detection in these bands. However, for photometric redshifts these bands may be needed. Now we have studied the depth of PS1 data, we will analyse magnitude dispersions and the background power spectra more closely.

2.10 Image Background Power Spectra

An interesting statistic that one can measure from an image is the power spectrum of the image background pixels. This power spectrum contains information about any features in the noise of the image. To measure power spectra we compute the Fourier transform of the image using the routine FOURIER from the Starlink Kernel Applications Package (KAPPA)[6]. The amplitude of the resultant 2D Fourier transform is squared in order to compute the 2D power spectrum. From the 2D power spectrum the circularly averaged power spectrum, $P(k)$, is measured in circular annuli using the KAPPA routine ELPROF. We measure the power specta of a PS1 SAS2 detrended exposure, an SDSS DR7 tile from around the same region of sky and a synthetic image designed to replicate the real detrended exposure. To test if galaxy clustering affects the results, we use the angular positions of the synthetic objects taken from the Merson et al. (2013) lightcone, so that the galaxy clustering predicted by the Lagos et al. (2011) model is included in the synthetic image. SDSS tiles have a constant offset from zero, called a "soft bias", which was subtracted from the image to avoid adding a large $k = 0$ term to the power spectrum.

SDSS tiles are smaller than PS1 images, additionally we trimmed down the images to square sizes. The final image sizes used were 1000 by 1000 pixels for SDSS, and 4000 by 4000 pixels for PS1. This sets the size of bins, $\Delta k = 2\pi/L$, to be $\Delta k \sim 0.006$ arcseconds^{-1} and $\Delta k \sim 0.02$ arcseconds^{-1} for PS1 and SDSS respectively. This information is important for Section 2.11.

The measurement of the power spectrum of the pixel background is complicated in two ways. Firstly, astronomical images contain sources, the light from which can have a huge effect on the measured power spectrum. The second complication is that masking, and the finite size of the image, results in measurements of the power spectrum that are convolved with a window function of the mask, $W^2_{\rm mask}$, i.e.

$$P(\mathbf{k}) = \int P_{\rm t}(\mathbf{k}')W^2_{\rm mask}(\mathbf{k}-\mathbf{k}')\mathrm{d}^2k' \tag{2.10.8}$$

where $P(\mathbf{k})$ is the measured power spectrum and $W^2_{\rm mask}$ the window function. This

[6]http://www.starlink.ac.uk/docs/sun95.htx/sun95.html, accessed 23/09/13

window function is the square of the Fourier transform of the image mask. We will deal with the issue of astronomical sources in the image first.

To remove the effect of sources on the background power spectrum measurements, we detect all objects on the images using the source detection software SEXTRACTOR (Bertin & Arnouts, 1996) (we use this instead of PSPHOT simply because the software we use to construct a mask requires input from a SEXTRACTOR catalogue). We use this catalogue to produce masks which cover sources, the size of masks is set to be some multiple, S, of the source size as measured by SEXTRACTOR. We will discuss the choice of S later in this section. We additionally mask, by hand, regions of the image that are affected by diffraction spikes and use the IPP masks to remove suspect pixels. Masked pixels are all assigned the value zero.

Dealing with the effects of the masking is more difficult. The masks of differently sized sources, cell gaps, diffraction spikes and suspect pixels are complicated and as such will modify the power spectrum in a scale dependent way. As a first step to dealing with masking we can use of Parseval's theorem,

$$\int_{-\infty}^{\infty} |f(x)|^2 \mathrm{d}x = \int_{-\infty}^{\infty} |F(k)|^2 \mathrm{d}k \tag{2.10.9}$$

where $f(x)$ and $F(k)$ are a function and its Fourier transform. If a certain fraction of $f(x)$ is masked, then the integral on the left hand side of Eq. 2.10.9 will be decreased by the masked fraction. In order for Eq. 2.10.9 to still be true, $|F(k)|^2$ must also decrease by the masking fraction. As $P(k) = \langle |F(K)|^2 \rangle$, the power spectra will also be decreased by the masked fraction. To compensate for this we therefore divide the image power spectra by the fraction of unmasked pixels in the image. This is similar to the f_{sky} approximation commonly used in CMB analysis, where f_{sky} is the fraction of sky imaged. Compensating for the shape of the window function is far more complicated. However, as we shall show in Section 2.11, the window function is similar for the different images and masks we utilise here, so it is fair to compare these measurements. To determine the optimum value of S, we produced masked images with different values of S, and measured their power spectra. An example 2D power spectrum from the real PS1 detrended exposure, with $S = 600\%$, is given in Fig. 2.12. An obvious vertical line, corresponding to pertubations perpendicular to the rows of pixels, can be seen in Fig. 2.12. This vertical line is at the correct

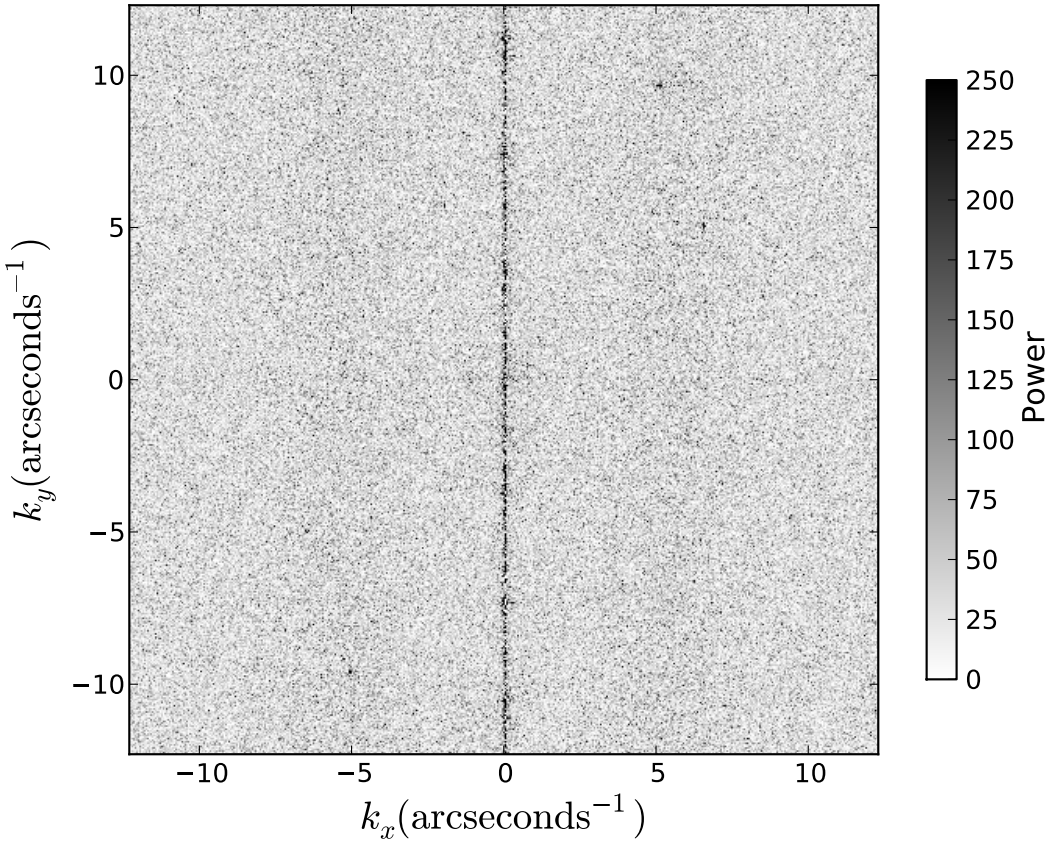

Figure 2.12: The 2D power spectrum of a PS1 SAS2 detrended exposure. The vertical feature relates to noise perpendicular to the rows of pixels, so we believe it is related to the row-by-row bias issues. The peaks at around 30 degrees from the vertical are thought to be caused by radio interference in the electronics.

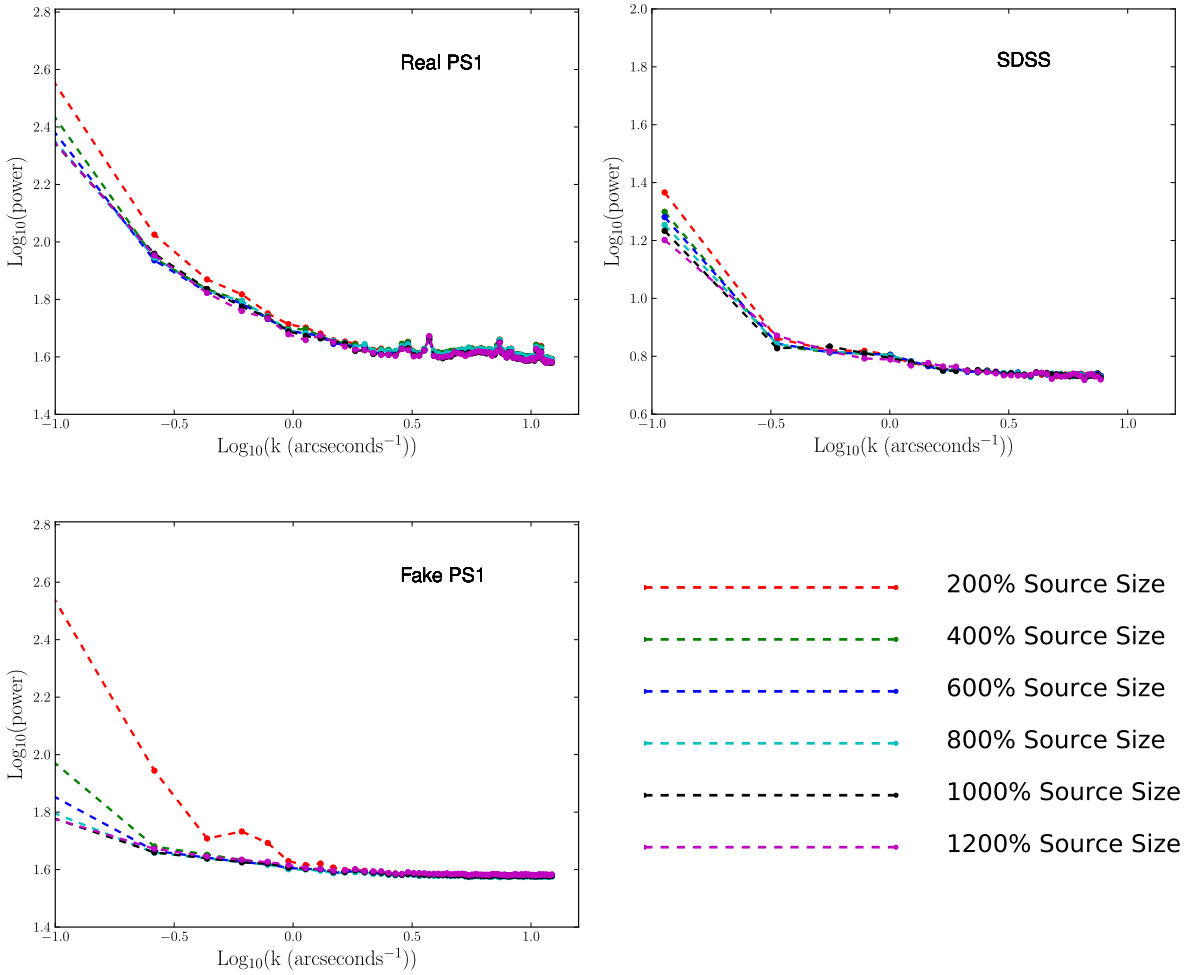

Figure 2.13: The power spectra for a real PS1 detrended exposure, a synthetic PS1 image and an SDSS tile. Different lines in each panel refer to different sizes of mask to remove sources from the images. The legend indicates which line refers to a certain mask size, expressed as a percentage of the measured source size.

orientation to be related to the row-by-row bias mentioned in Section 2.3. An additional feature of the 2D power spectrum are small peaks around 30 degrees from the vertical. These peaks are caused by a regular diagonal noise feature, the only candidate for this type of pattern is radio frequency interference in the detector electronics. The circularly averaged power spectra as a function of S are shown in Fig. 2.13. Whilst changing S may change the shape of the window function, the overlap between different power spectra at small scales suggests this is not a large effect. Increasing the mask size decreases the larger scale power for all of the power spectra. This suggests light leaking from masks can add power on larger scales to

the power spectrum. We choose to adopt a mask size of $S = 600\%$, as the shape of the power spectra changes very little for larger values of S. All of the power spectra show increased power at scales larger than $k \sim 1$, which corresponds to sizes of around 2π arcseconds. This power continues increasing to larger scales regardless of the mask size, suggesting this cannot be attributed to light leaking from masks. As this upturn exists in the synthetic images, some of this excess power may be due to faint, undetected objects which are present in the image background. However, the large scale power is much greater in the SDSS image and the PS1 image than in the synthetic image. This suggests the existence of further, larger contributions to large scale power that are not modelled in the simulated image. Additionally, the PS1 power spectrum appears to have more larger scale power than the SDSS power spectrum. We will test this is not just an effect of the different masks in Section 2.11.

In addition to the large scale power, we can also observe peaks in the power spectrum of real PS1 data in Fig. 2.13. These peaks occur at $\log_{10}\mathrm{k} \sim 0.58$ and $\log_{10}\mathrm{k} \sim 0.87$, corresponding to wavelengths of 1.7 arcseconds and 0.85 arcseconds. The cause of these peaks is bright spots in the vertical line seen in Fig. 2.12. As this vertical line corresponds to noise perturbations between different rows of pixels, the row-by-row biases (Section 2.3) are a likely cause. The radio frequency interference peaks in Fig. 2.12 are too small to be visible in the circularly averaged power spectrum.

2.11 Estimating the Window Function

To estimate the effects of the window function on our measurements, we begin by producing an unmasked image with a power spectrum comparable to that of our data. We only have measurements of true power spectrum convolved with the window function, so we cannot use these. As a simple test we therefore generate a random image of noise with a ramp across it, i.e. an offset in the pixel value that increases linearly across the x-axis. Adding this ramp is designed to emulate the large wavelength elements of the noise we see in the real image power spectra. We

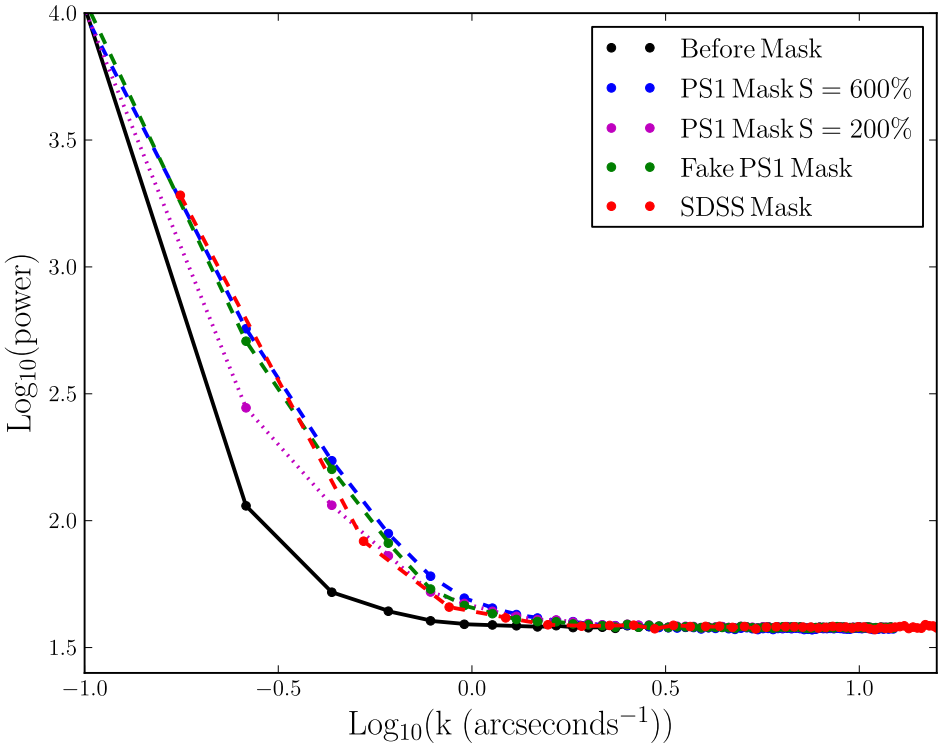

Figure 2.14: The measured power spectrum of a synthetic image with a ramp offset added, i.e. a offset from zero proportional to the x-axis position in the image. The lines show the recovered power spectrum after different masks have been applied to the image, as indicated in the legend.

generate this image with a pixel rms equal to the synthetic PS1 image, which was measured from empty regions of the real image. Fig. 2.14 shows the power spectrum of this test image, with and without our masks applied. We also show the same for a synthetic SDSS image with no sources and a ramp. For the SDSS image we increased the pixel variance and ramp amplitude by the area difference, and ensured the ramp had the same slope in arcseconds as for the PS1 image. We see that the effect of the window function is to spread power from larger scales to smaller scales, which is to be expected from the convolution in Eq. 2.10.8. We do however see that the SDSS and PS1 window functions have a similar effect on the power spectrum, suggesting that PS1 does genuinely have more larger scale power than the SDSS image, i.e. it is not just a result of differences in the window function. Fig. 2.14 also shows the difference in the window function between masks with two different sizes, we see

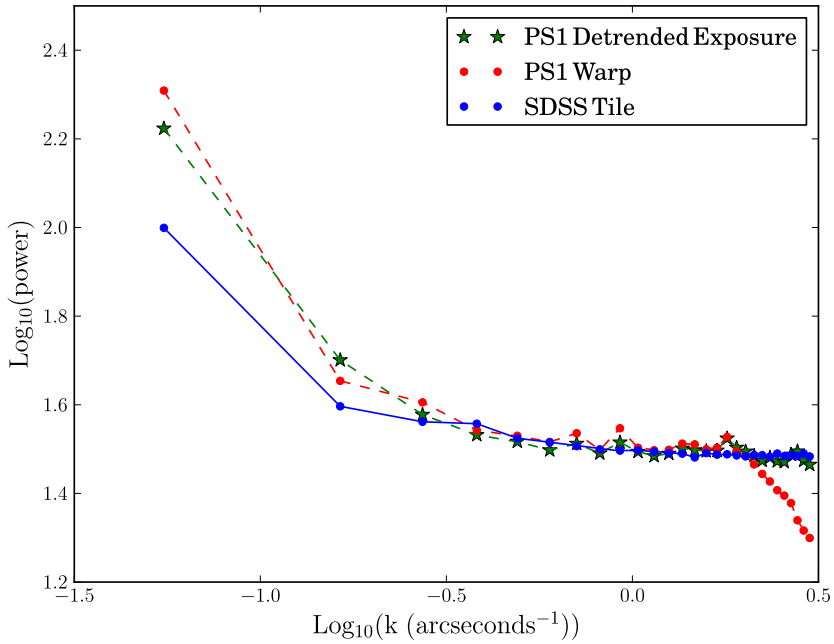

Figure 2.15: The power spectra of background pixels, for a PS1 SAS2 detrended exposure, a warp and an SDSS tile. We see the turnover in the warped image spectra caused by the convolution kernel smoothing out noise on small scales. The amplitude of the spectra here have been shifted such that they overlap with the warp spectra, for easier comparison.

that there are some differences, but these differences are far less then the difference in the power spectra for different mask sizes seen in Fig. 2.13. This supports our previous conclusion that the difference seen in the power spectra for different mask sizes is due to removing different amounts of light from sources.

2.12 The Effect of Warping on Image Backgrounds

To see the effect of the warping process on noise, we study the pixel power spectra of the image background of a PS1 detrended image and a warp partially made from that detrended exposure. Note that multiple detrended exposures produce one warp so the warping process is not the only source of difference in the two images.

We show the circularly averaged power spectra for a PS1 OTA and the warp

resulting from it in Fig. 2.15. As a comparison we show the power spectrum we measured from our SDSS DR7 tile. The SDSS tile has a different background pixel rms to that of the PS1 images, we have therefore arbitrarily normalised the power spectra to overlap for easier comparison. This removes information about noise in absolute terms in Fig. 2.15, but still allows us to see the relative contribution to the background noise from different wavenumbers.

Small scale noise is clearly removed from the warp with a turnover visible in its power spectrum at around $1''$. This suggests the warping process will decrease the pixel rms but should not affect measurements from larger apertures which are more sensitive to larger scale noise. Note that, even in this case, to estimate noise within apertures from the variance map one still needs to use the covariance pseudo matrix.

On larger scales, the warping process leaves the power spectrum unaffected. The OTA and the warp both have more excess power on large scales than the SDSS data; this excess appears at the scale, $k \cong 0.2$ arcseconds^{-1}. Note that this k may be an overestimate, as the window function acts to spread power from larger scales to smaller scales of the power spectrum.

2.13 Magnitude Dispersions

So far we have studied the many different noise contributions to PS1 images. We will now try and understand how these noise contributions affect a more practical issue: the measurement of magnitudes. To investigate this we study the rms of the total flux recovered from differently sized apertures placed onto the image backgrounds. Neglecting source noise, these measurements of rms should be representative of the scatter in recovered magnitude measurements. Using SEXTRACTOR we put down apertures on the backgrounds on the masked SDSS, PS1 detrended exposure and synthetic PS1 images. Apertures are placed on a grid to avoid overlaps, and apertures are only placed on unmasked regions. To avoid complications we do not fit a background to the image in SEXTRACTOR. For each aperture size, 150, 350 and 950 apertures where placed on the SDSS, real PS1 and synthetic PS1 images respectively. The different number of apertures arises due to the difference in size between

the SDSS tile and the PS1 images, as well as the difference in the fraction of the images masked. The rms of the sum of the pixels enclosed by the different apertures is measured. For white noise this should scale like

$$rms = \sqrt{\pi R^2 \sigma^2} \tag{2.13.10}$$

where R is the radius of the aperture and σ^2 the pixel variance. We therefore expect a linear relation between aperture radius and the rms scatter of measurements of the background between different apertures. Fig. 2.16 shows the results of our measurements. The SDSS image and the synthetic PS1 image follow the expected linear relation. The real PS1 data breaks from the linear relation for larger apertures. An explanation for this could be the large scale noise in the power spectra, which would act to enhance the noise measurements for larger apertures. To study if this is the case we will now use our measurements of the background pixel power spectra to estimate the rms between apertures.

The integral of the power spectrum of an image gives it variance. Imagine convolving an image with a circular aperture, e.g.

$$f_{\rm c}(r) = \begin{cases} \frac{1}{\pi R^2} & \text{if } r < R \\ 0 & \text{otherwise} \end{cases} \tag{2.13.11}$$

with $r = \sqrt{x^2 + y^2}$, and then measuring the rms of the resultant image. This rms would be the rms of the sums of pixels within different the apertures placed on the unconvolved image. We can use this to estimate what this rms would be from the power spectrum, by recalling that a convolution in real space is a product in Fourier space. Also recall from the physics of optics that the square of the Fourier transform of a circular aperture, called the Airy Pattern, is given by

$$F_{\rm Airy}(k) = \left(\frac{2\pi J_1(kR)}{k} \right)^2 \tag{2.13.12}$$

where J_1 is the first Bessel Function. We can then predict the rms, $\sigma_{\rm aper}$, in apertures of radius, R, from the measured power spectrum via

$$\sigma^2_{\rm aper} = 2\pi \int_0^\infty P(k) F_{\rm Airy}(k) k {\rm d}k. \tag{2.13.13}$$

In practice we only integrate up to the Nyquist frequency of the FFT estmate of $P(k)$. For the apertures we show here, this is beyond the point where the Airy

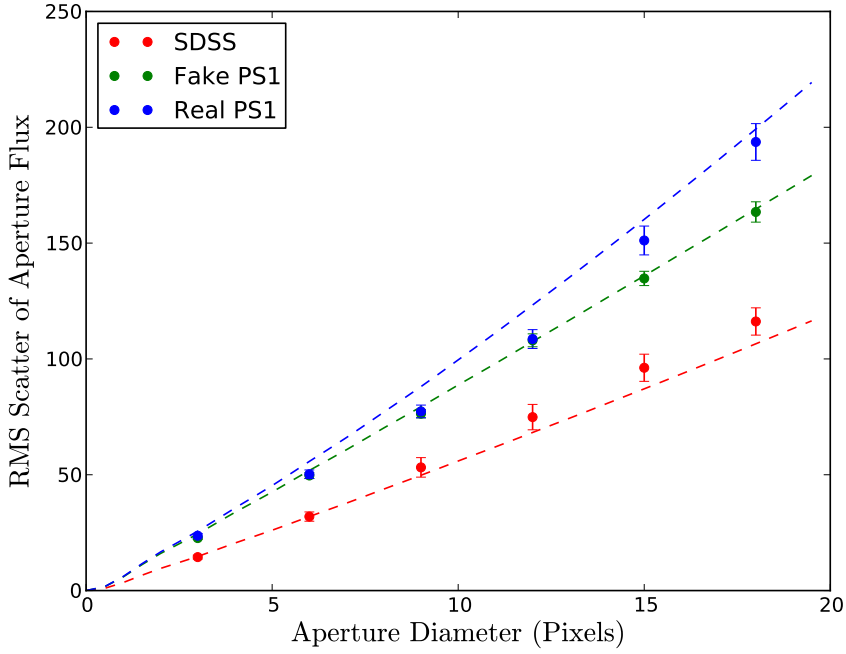

Figure 2.16: The rms scatter between different apertures placed onto image backgrounds, as a function of aperture diameter. The dashed lines give the prediction from integrating the measured power spectra.

function falls to a small amplitude and, as such, including the larger values of k would make a negligible contribution to the integral. We see that the estimates from integrating the power spectra agree with the SDSS data and synthetic data but not with the real PS1 image. This is likely to be related to the effect of the window function. Power in the power spectrum is shifted to smaller scales by the convolution with the window function, so the predicted magnitude dispersions would be artificially increased for smaller apertures. It does however seem convincing from Fig. 2.16 that the larger scale power in the power spectra does lead to the observed enhancement in scatter for larger apertures. When estimating magnitude errors, e.g. for photometric redshift estimates, one therefore needs to be careful to account for this. We leave this to later work, when tests like this can be extended to the full 3π survey.

2.14 Summary

This chapter has introduced PS1 and our technique of producing synthetic images, in addition to testing various parts and features of PS1 images and the IPP. Our synthetic images use a combination of galaxy formation models and empirical relations to generate realistic galaxy magnitudes, shapes and sizes. The IPP PSF model is utilised, along with de Vaucouleurs and exponential profiles to produce synthetic images of stars and galaxies. Synthetic image backgrounds are also produced using real masks and measured background noise.

We have utilized these synthetic images to demonstrate that IPP can successfully recover the magnitudes of galaxies for detrended exposures, warps and stacks. Also using our synthetic images, we have confirmed that the image depth scales as expected from stacking the images.

By studying the background pixel power spectra of SDSS and PS1 images, we find that both contain non-Gaussian features. Both have excess power on larger scales, though the PS1 image we studied has significantly more than SDSS. PS1 also has spikes in its pixel power spectrum, which we believe are caused by the row-by-row biases affecting the read-out from the CCDs. The excess larger scale noise may be increasing the rms scatter in the background, as measured in larger apertures, beyond what one would expect from scaling up the rms measured in smaller apertures. This effect would need to be taken into account if one wanted to accurately model magnitude dispersions, which is useful for measuring photometric redshifts.

Chapter 3

Galaxy Clustering with PS1

The finished 3π survey will have spatially varying depth, due to the nature of the camera and the survey strategy. This chapter presents a method to correct galaxy number counts and galaxy clustering for this potential systematic based on a simplified SNR measurement. A star and galaxy separation method calibrated using our realistic synthetic images is also presented, along with an approach to mask bright stars. Overall, this chapter will build on the work of Chapter 2 and of Paper I to prepare for measuring galaxy clustering in PS1 3π. To begin, we will introduce the comparison data we use to test our measurements of clustering and calibrate our SNR based, spatially varying depth correction method.

3.1 Comparison Data

3.1.1 SDSS magnitudes and flags

The SAS2 field overlaps with SDSS DR8 and is partially covered by the SDSS Stripe 82 co-added data (Annis et al., 2011). The size of the Stripe 82 overlap region is around 16 square degrees (see figure 1 of Paper I). We compare PS1 to both of these. Stripe 82 comparisons are particularly useful as Stripe 82 is deeper than PS1.

SDSS measures magnitudes in an asinh magnitude system (Lupton et al., 1999). We adjust this to the standard Pogson system using the formula available on the

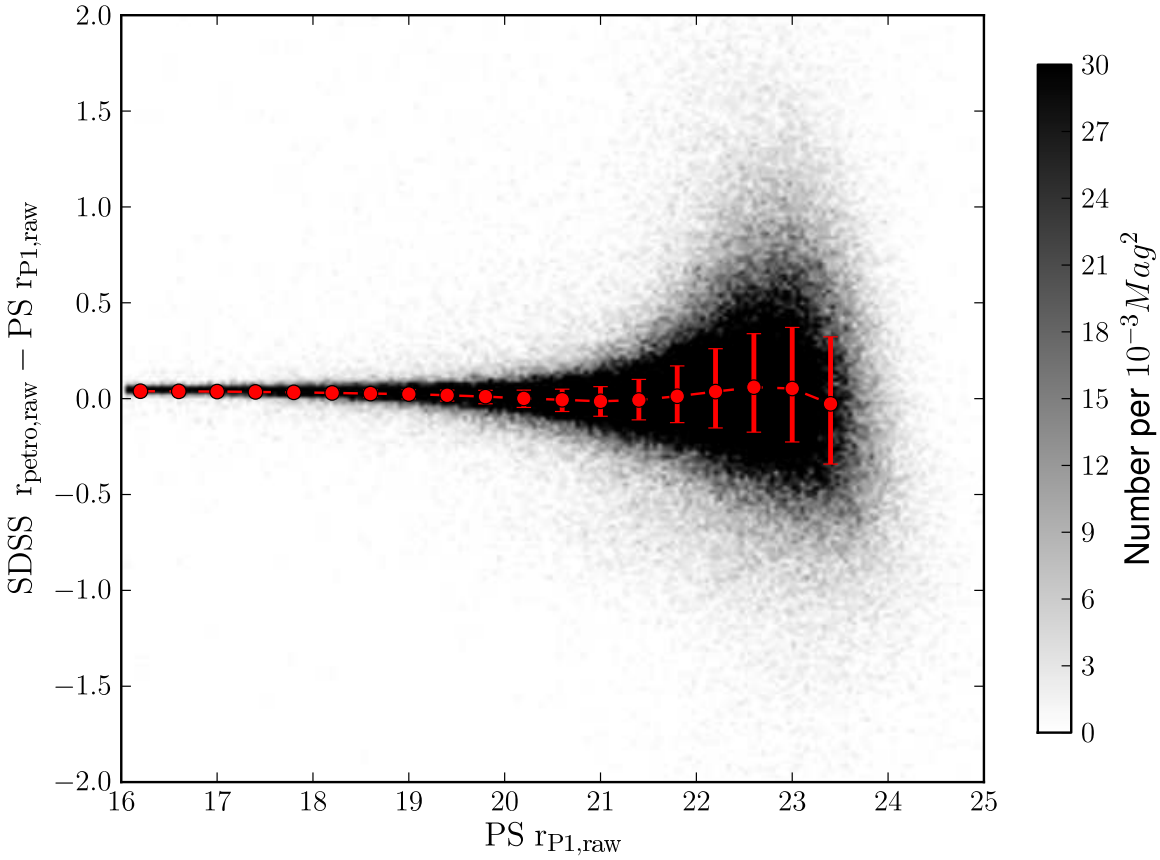

Figure 3.1: The difference between r-band SDSS Stripe 82 Petrosian magnitudes and $r_{\rm P1}$-band PS1 Kron magnitudes, for all objects in an overlap region. Points with error bars show the median values along with upper and lower quartiles. The two magnitudes are fairly well matched, with a small median offset that varies slightly with magnitude.

SDSS website[1]. This adjustment is very small, at its maximum value, at $r = 23.0$, it is only 0.04 magnitudes in size. The SDSS bands are slightly different to those of PS1, transformations are given in Tonry et al. (2012). These transformations in our comparison band, $r_{\rm P1}$, are very small, less than 0.01 magnitudes for a wide range of colours in figure 6 of Tonry et al. (2012), and hence are neglected.

SDSS DR8 and SDSS Stripe 82 do not provide Kron magnitudes. Whilst the SDSS magnitudes measured using model fits, so called "modelMags", give an estimate of the total magnitude of a galaxy, we want to select a magnitude estimator

[1]http://www.sdss3.org/dr8; accessed 27/07/2012

most similar to our Kron magnitudes (see Paper I for PS1 Kron and SDSS modelMag comparisons). Petrosian magnitudes (Petrosian, 1976), a modified form of which are provided by SDSS (see Blanton et al., 2001; Yasuda et al., 2001) measure flux within an aperture of a size determined by the ratio of a surface brightness in an annulus around a source to the average surface brightness of the region interior to that annulus. In theory the fraction of flux enclosed by a Kron magnitude and a Petrosian magnitude could differ. A comparison of PS1 measured Kron magnitudes and SDSS DR8 Petrosian magnitudes (Fig. 3.1) shows that these two magnitude measures are fairly well matched in the $r_{\rm P1}$-band and r-band for objects in SDSS.

To define SDSS galaxies we use the Strauss et al. (2002) star-galaxy separator,

$$r_{\rm psf} - r_{\rm model} > 0.3, \tag{3.1.1}$$

where $r_{\rm psf}$ is the SDSS PSF magnitude and $r_{\rm model}$ is the SDSS model magnitude. We use SDSS flags to remove false positives in SDSS DR8. Following the spectroscopic target selection of Strauss et al. (2002) we reject SDSS objects with SATURATED or BRIGHT flags, and require the BINNED1 flag to be set for the r-band (i.e. a 5σ detection). To remove low surface brightness false positives, following Strauss et al. (2002), we apply to the DR8 data a Petrosian half light surface brightness cut of

$$\mu_{50} = m_{\rm petro} + 2.5{\rm log}_{10}(\pi R^2_{50,{\rm petro}}) < 24.0, \tag{3.1.2}$$

where $m_{\rm petro}$ is the Petrosian magnitude and $R_{50,{\rm petro}}$ is the radius enclosing 50% of the Petrosian flux. Strauss et al. (2002) adopted a similar cut to remove low surface brightness false positives; though they used a slightly more complicated cut than this, which was dependent on sky values and fibre magnitudes. We adopt our simplified, less conservative cut (that of Strauss et al. (2002) could be as bright as $\mu_{50} < 23.0$) as we find it is sufficient to remove SDSS false (unmatched to PS1) detections from the magnitude ranges we consider. Applying this surface brightness cut limits SDSS DR8 depth faintward of $r = 20.0$, so we do not compare to SDSS DR8 faintward of this value. With more work it is likely to be possible to measure SDSS DR8 clustering over SAS2 for galaxies fainter than this, but we choose instead to use PS1 Medium Deep data for faint clustering comparisons as it is much deeper than both 3π SAS2 and SDSS DR8.

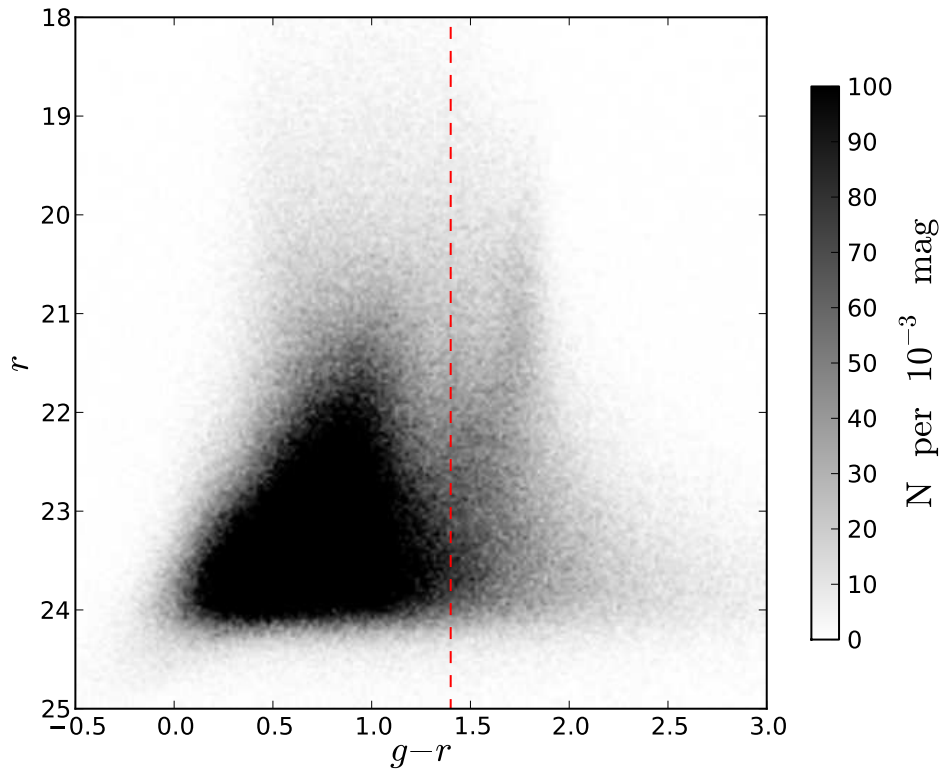

Figure 3.2: A colour magnitude diagram of Stripe 82 galaxies, using Stripe 82 apparent model magnitudes. The red dashed line marks our separator between red and blue galaxies.

We do not apply any surface brightness cut to Stripe 82 data as our main use of Stripe 82 is to estimate PS1 depth and these cuts could limit Stripe 82 depth. How Stripe 82 false detections affect this work will be discussed in Section 3.4. Stripe 82 does not have a publicly available mask for the co-added data, so we created our own by visual inspection of the area. This masks defines areas with no Stripe 82 imaging and removes a satellite trail in Stripe 82.

A further use for Stripe 82 is to test how strongly detection efficiency depends on apparent colour. A galaxy's colour is correlated with its morphology, red galaxies tend to be ellipticals and blue galaxies tend to be spirals. Galaxies with different morphologies have different surface brightness distributions and as such may have a different chance of being detected. Since galaxy clustering is a function of colour and morphology, with red ellipticals being more clustered (see e.g. Chapter 4), this

effect could modify our clustering result as depth corrections are based soley on apparent magnitude. Fig. 3.2 shows a colour magnitude diagram using Stripe 82 model magnitudes for objects classed as galaxies by Stripe 82's own morphological star and galaxy separator, TYPE = 3. We separate galaxies on the red sequence from those in the blue cloud using the cut indicated on Fig. 3.2, $(g - r) = 1.4$. We will use this sample of red and blue galaxies when testing the dependence of detection efficiency on apparent colour and hence morphology.

3.1.2 PS1 Medium Deep Data

When comparing our faint galaxy clustering to other measurements we both compare to literature data and to results from the much deeper and more spatially homogeneous PS1 Medium Deep survey. Foucaud et al. (in preparation) have produced their own stacks of Medium Deep field 7 (MD07) using PS1 exposures and reduced them using SExtractor (Bertin & Arnouts, 1996). The MD07 stack consists of more than 100 exposures, each of which are longer than 3π exposures. The longer exposure time makes it more likely that the noise in the exposures is dominated by the sky, making them less subject to noise features from the CCD electronics. The limiting magnitude of the MD07 stack is around $r_{\rm P1} = 25$. Unfortunately, MD07 does not overlap with SAS2, but instead is roughly centered on $\alpha = 213$ deg. and $\delta = 53.0$ deg. Foucaud et al. (in preparation) measure the Kron magnitudes of galaxies, using SExtractor MAG_AUTO, and star/galaxy separate using a combined morphological and SED fitting approach. They also adopt a mask to remove bright stars and poorer quality data. After masking, MD07 has an area of 7 square degrees, much smaller than the SAS2 field. For more details on these stacks see Jian et al. (2013) and Foucaud et al. (in preparation).

Now the comparison data has been introduced, we will move on to explain how we create angular masks.

3.2 Angular Masks and False Positives

3.2.1 Creating the mask

To create a set of random points suitable for measuring clustering and to remove regions of low data quality we define a new set of angular masks. These masks differ from IPP image masks in that a single, unique mask covers the whole region of interest. In IPP two overlapping skycells will have two different masks, one for each skycell. As well as masks we produce variance maps and coverage maps binned-up to the same resolution as our mask pixels. We take variance maps at the native pixel scale and compute their mean on a grid of 12000^2, $3.3'' \times 3.3''$ equal area pixels, which covers the whole SAS2 area. The binned up pixels are a grid with separations defined in arcseconds, not IPP pixels. Within this grid, it is possible for individual IPP pixels not to align with the boundaries of the binned-up pixels. In such cases, rather than resampling, we simply take a "nearest-neighbour" approach and assign the IPP pixel to the nearest binned-up pixel. Our binned up pixel grid has the same rotation as the IPP pixels. For our coverage maps we take the lowest value of any IPP pixel contributing to our binned-up pixel, rather than the mean. This is in order to be conservative in our estimates of low coverage areas. Our binned-up pixel size was chosen to preserve the fine structure in the variance whilst still yielding a mask of manageable size. Experimenting with different mask and map pixels sizes and different mask and map tessellations is left for later work.

Only taking into account the variance recorded in the variance maps would result in underestimating the noise, as we would be ignoring the covariance. We therefore multiply the variance values from IPP variance maps by the sum of the elements of their associated covariance pseudo-matrix (see Section 2.2.1). This is almost the same as multiplying all of the variance map values by a constant, as the rms of this scaling factor, given in Section 2.2.1, is only around 0.5% across the SAS2 field. We carry this scaling out to allow easier comparison to the work of Chapter 2, which works with uncorrelated noise measurements. We also apply this scaling now as it could become more important if the warping kernel were to change.

Where data from two skycells overlap we take data from the skycell whose centre

is closest to the overlapping data. We do this for both the pixels and the object detections to ensure the catalogues, masks and maps are consistent.

As well as defining the basic geometry of the survey, we also use angular masks to avoid two other types of potential problem: deblending and image artifacts.

3.2.2 Masks for bright stars

In common with a large amount of image reduction software (see e.g Bertin & Arnouts, 1996), PSPHOT can mistakenly split bright objects and diffraction spikes into multiple detections. To avoid this we mask out regions around bright stars. To define a bright star sample we use photometry from the UCAC4 catalogue (Zacharias et al., 2013) rather than PS1, since PS1 saturates at around $r_{\rm P1} < 15.0$. We use R-band photometry from the UCAC astrograph up to a bright limit of $R = 10.0$, where the astrograph becomes saturated. To mask even brighter objects we use V-band data from Hipparcos, FK6 and Tycho-2. These data are already included in the UCAC4 catalogue. Zacharias et al. (2013) states that the UCAC4 catalogue is a complete catalogue of stars down to $R < 16$.

We identify the required mask sizes as follows. We find likely candidates for false positives by identifying objects in the $r_{\rm P1}$-band that are not in the $i_{\rm P1}$-band catalogue, with a $0.5''$ matching radius. To eliminate objects that are not detected in both bands due to image depth, we remove objects with $r_{\rm P1} > 20.0$. We assume these candidate false positives trace the spatial distribution of all false positives caused by bright stars. Selecting the central, deeper region of SAS2 we count "false positive" and UCAC4 pairs as a function of angular separation, $FU(\theta)$, as well as pairs of "false-positive" and random points uniformly distributed across the area, $FR(\theta)$. We calculate the ratio of these pairs

$$\frac{N_{\rm FU}(\theta)}{N_{\rm FR}(\theta)} = \frac{FU(\theta)}{FR(\theta)} \frac{n_{\rm R}}{n_{\rm D}} \tag{3.2.3}$$

where $n_{\rm D}$ is the number of UCAC4 objects and $n_{\rm R}$ is the number of random points. This technique is very similar to that used to compute a cross-correlation function. This technique can be used to map out the scale out to which one finds false positives around stars of different magnitudes. In Fig. 3.3(top) we plot the results for

various UCAC4 R magnitude and V magnitude ranges. Note that the brightest bin contains only one $V = 2.33$ magnitude star. From Fig. 3.3(top) we can see brighter objects cause false positives out to a larger spatial extent than fainter ones. We also see a relative deficit of false positives at smaller separations. This is due to masked, saturated regions closer into the bright object. Note that false positives are preferentially found near brighter objects all the way down to the magnitude limit of $R = 15.0$. The ratio $\frac{FU(\theta)}{FR(\theta)}$ is an indicator of how much more likely one is to detect a false positive at a given separation from an object of a given magnitude, over a finding a false positive at that same distance from a random position. Whilst Fig. 3.3(top) shows one is ten times more likely to find false positives at a separation of $3''$ from objects with $14 < R < 15$, it does not imply that all of these objects cause false positives, and in real terms the number of bright false positives is very small. To decide on the size of mask to put on bright objects as a function of R and V magnitude, we use the last crossing of the $\log 10(N_{FU}(\theta)/N_{FR}(\theta)) = 1.0$ line as a reference separation and increase this distance by 50%. The curve describing mask size is smooth across the V-band to R-band boundary, see Fig. 3.3(bottom). We fit these sizes with a simple power law, truncated such that mask size cannot be less than one mask pixel (i.e. $3.3''$),

$$r_{\rm mask} = \begin{cases} 7.26(13.0 - m)^{1.65} & \text{if } r_{\rm mask} \geq 3.3 \\ 3.3 & \text{otherwise} \end{cases} \tag{3.2.4}$$

where $r_{\rm mask}$ is the mask radius in arcseconds, and m is the stellar magnitude. We use this to mask down to $R < 15$ and $V < 10$.

3.2.3 Masks for regions of low quality data

The second potential issue we combat with masks is that certain regions of PS1 images have instrumental signatures (i.e. image artifacts) caused by scattered light and electronic noise. This is particularly noticeable in regions of low coverage where we do not have sufficient numbers of exposures to remove these image defects statistically, i.e. by median filtering or outlier rejection in the stacking procedure. We therefore simply mask regions with a coverage of three exposures or fewer. In the fin-

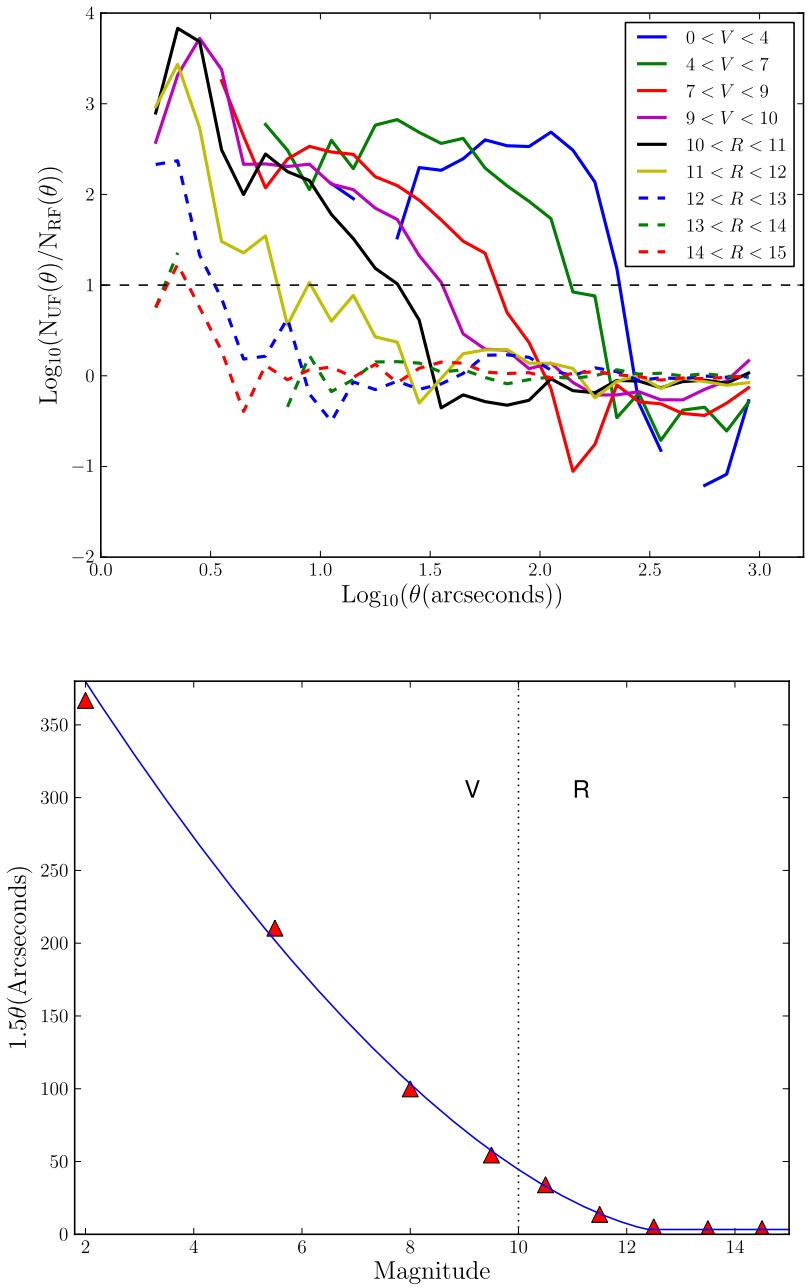

Figure 3.3: *(Top)* The correlation of false positive detections with bright stars in the UCAC4 catalogue. The lines show the ratio of the number of false to UCAC4 pairs to the number of false to random pairs as a function of R and V magnitudes from the UCAC4 catalogue. Using two different bands is necessary as the astrograph measuring R magnitudes saturates for very bright stars. We see a clear correlation between false positives and UCAC4 sources. The level at which there are 10 times as many UCAC4 to false pairs as random to false pairs is marked with a horizontal dashed line. *(Bottom)* The largest separation corresponding to this level for each bin, multiplied by 1.5. A fit to these points (blue curve) sets the size of the bright source mask as a function of R and V magnitude.

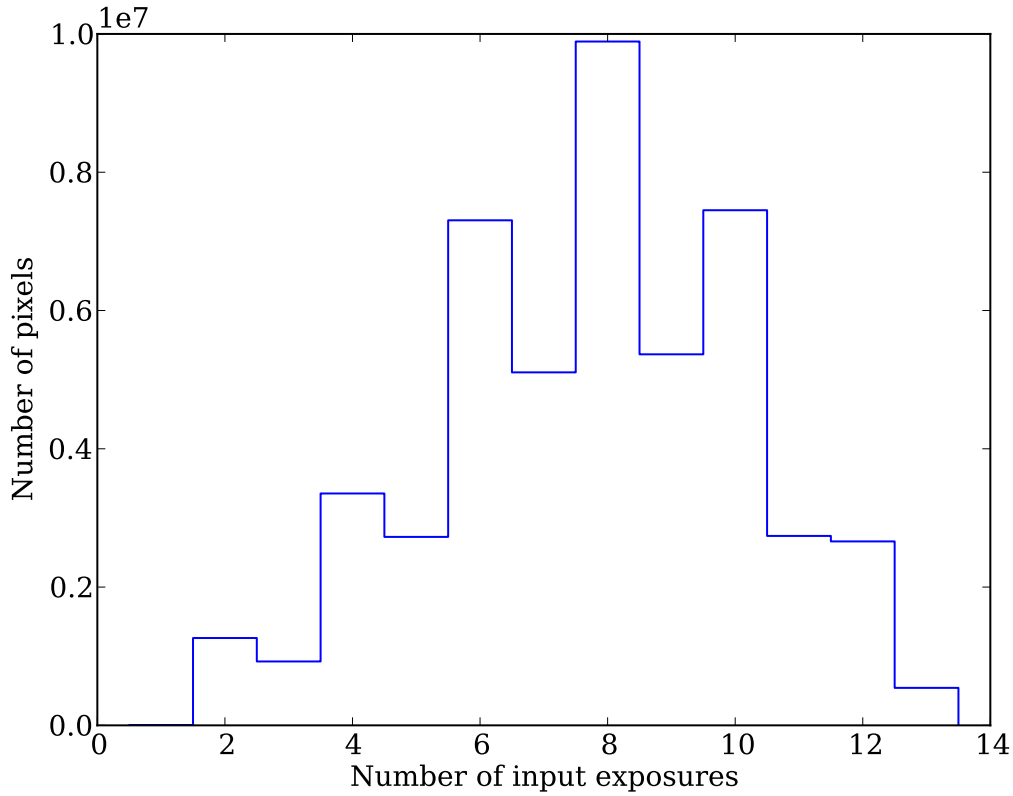

Figure 3.4: A histogram of the lowest coverage values, i.e. fewest exposures per stack pixel, in each of our binned up coverage map pixels for the central area of SAS2.

ished survey the area with coverage this low should be very small. To estimate this value we took the central area, $331.0 < \alpha(\text{deg.}) < 336.0$ and $-3.0 < \delta(\text{deg.}) < 3.0$, of our binned up version of the coverage map and produced Fig. 3.4. The central area of SAS2 should be representative of the finished 3π data and, as such, we can estimate from Fig. 3.4 that only about 4% of the full survey area should be lost by this cut.

All of the masked regions are expanded by a one binned-up mask pixel border in order to exclude from the catalogue objects with unreliable measurements caused by being on the edge of the mask. This is similar to using cuts in the IPP value PSF_QF_PERFECT, which quantifies the fraction of masked or suspicious pixels in a source (for more details on these cuts see Paper I).

3.2.4 The effects of masking

The source detections before and after applying the final mask are shown in Fig. 3.5; the regions of fewer objects on the outskirts of the masked field are not caused by depth variations but simply the larger number of masked pixels caused by a lower coverage in these areas. The grid like patterns are also caused by our masking of low coverage regions; the grid pattern in coverage is caused by gaps between individual chips on the detector. One can see from Fig. 3.5 how our angular mask removes peaks of false positives caused by bright objects. Finally we have to mask, by hand, a square region in SAS2 where the data reduction process failed, an issue that will hopefully be rectified for the final survey.

A quantitative measure of how our mask removes false detections was made by cross matching the Stripe 82 and PS1 catalogues after applying our SDSS Stripe 82 mask (see Section 3.1.1) to PS1 data and the PS1 mask to Stripe 82 data. Fig. 3.6 shows the fraction of PS1 objects with no match to Stripe 82, for an ~ 8 square degrees overlap region and a matching radius of $1''$, before and after applying the masking and flags to PS1.

Fig. 3.6 shows a decrease in the fraction of false positives once flags have been applied and masking conducted. In particular brighter false positives associated with bright stars are almost entirely removed. Some unmatched objects do remain, but at magnitudes brighter than ~ 21 these are mostly real objects missed by Stripe 82 or objects with proper motions. Fainter than this false positives can be caused by the previously mentioned instrumental signatures. Note that Paper I achieves similarly low numbers of false positives by applying the PSF_QF_PERFECT flag; however the use of this flag, which depends on the number of masked or suspect pixels near a source, can change the angular selection function. The approach using masks presented here deals with these false positives in a way that keeps track of this, which is more appropriate for clustering studies.

Now the mask has been introduced, we will introduce another vital requirement to measure galaxy clustering: star/galaxy separation.

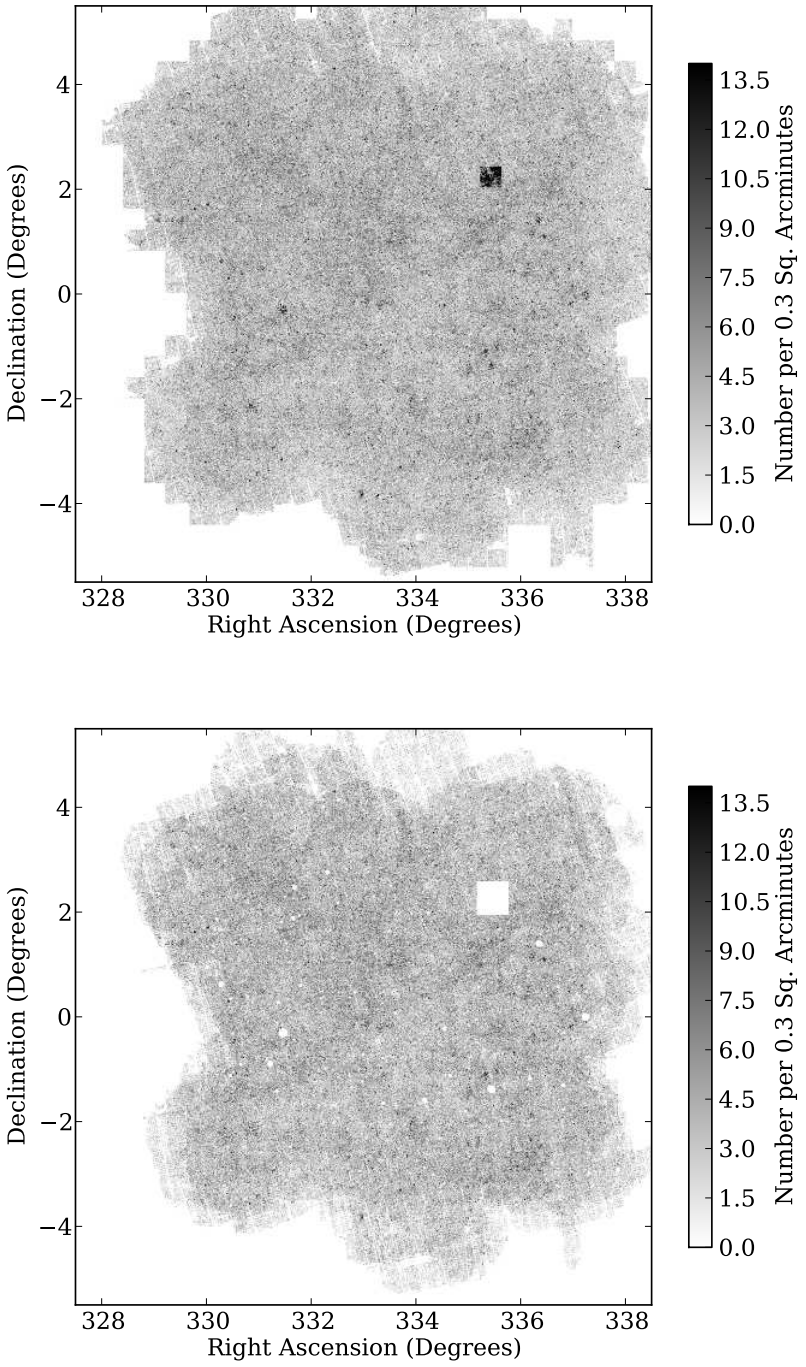

Figure 3.5: *(Top)* A plot of all detections in SAS2, binned into 0.3 square arcminute pixels. *(Bottom)* The same plot after masking and applying the flags specified in Section 2.2. We can see the circular star masks, the areas near the edge masked due to our cut on low coverage and the square area masked by hand where the data reduction failed. Over-densities caused by stars are removed; the remaining darker regions are caused by variable image depth or genuine over-densities in the object distribution.

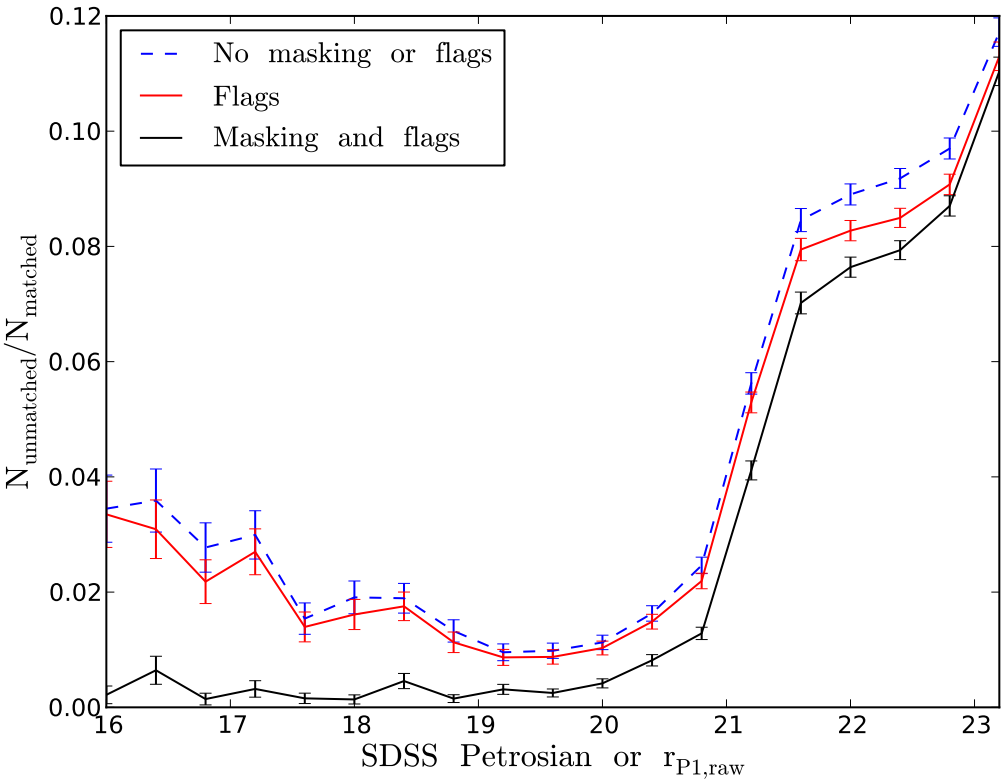

Figure 3.6: The fraction of unmatched objects as a function of magnitude, error bars show Poisson noise. The improvement gained from applying the flags and applying the masking is clear.

3.3 Star/Galaxy Separation

3.3.1 A morphological separator

The PS1 SAS2 $r_{\rm P1}$-band skycell 1315.028 was taken as an example and 286 synthetic galaxies and 300 synthetic stars down to a limit of $r_{\rm P1} \leq 23.5$ were inserted into it, created as described in Section 2.5. This skycell was chosen as it has a PSF FWHM typical of SAS2. The PS1 photometry code PSPHOT was run on this skycell and this process was repeated 40 times yielding data from 11,440 synthetic galaxies and 12,000 synthetic stars. Motivated by the often used star/galaxy separator of a PSF magnitude minus an aperture-like magnitude (e.g. Strauss et al., 2002), we show in Fig. 3.7 a histogram of the PSPHOT measured Kron minus PSF magnitude for the synthetic sources, the real sources in this skycell and for sources over the whole of SAS2. The number of synthetic galaxies and stars are scaled to the observed number of objects in each magnitude bin. We can see from Fig. 3.7 that the synthetic stars and galaxies follow the distribution of the real sources. This indicates we are justified in using the synthetic objects to define cuts in Kron minus PSF magnitude, with the synthetic stars following a peaked, stellar locus and the synthetic galaxies following a broader, more negative locus.

We use our synthetic objects to define cuts in Kron minus PSF magnitude ($\Delta_{\rm kron-psf}$ hereafter) that define samples of stars or galaxies. We also adopt a smallest allowed value of $\Delta_{\rm kron-psf}$ for galaxy samples; this removes objects with extremely negative $\Delta_{\rm kron-psf}$ which are likely to be false positives. We place this extreme $\Delta_{\rm kron-psf}$ cut at a value where only 0.5% of synthetic galaxies are to the left of this cut. Fig. 3.8 shows cuts in $\Delta_{\rm kron-psf}$ that define galaxy samples of a given completeness. These cuts were measured from the histograms in Fig 3.7. The cut defines a minimum $\Delta_{\rm kron-psf}$ for stars or a maximum value for galaxies. The dashed lines are fits to the cuts using a second order polynomial of the form

$$r_{\rm P1,raw} - r_{\rm PSF,raw} = \sum_{i=0}^{2} a_i (r_{\rm P1,raw} - 21)^i. \tag{3.3.5}$$

Table 3.1 gives the values of the coefficients of this equation for different samples. We use the 98% cut to define galaxies throughout this work. For this cut we use

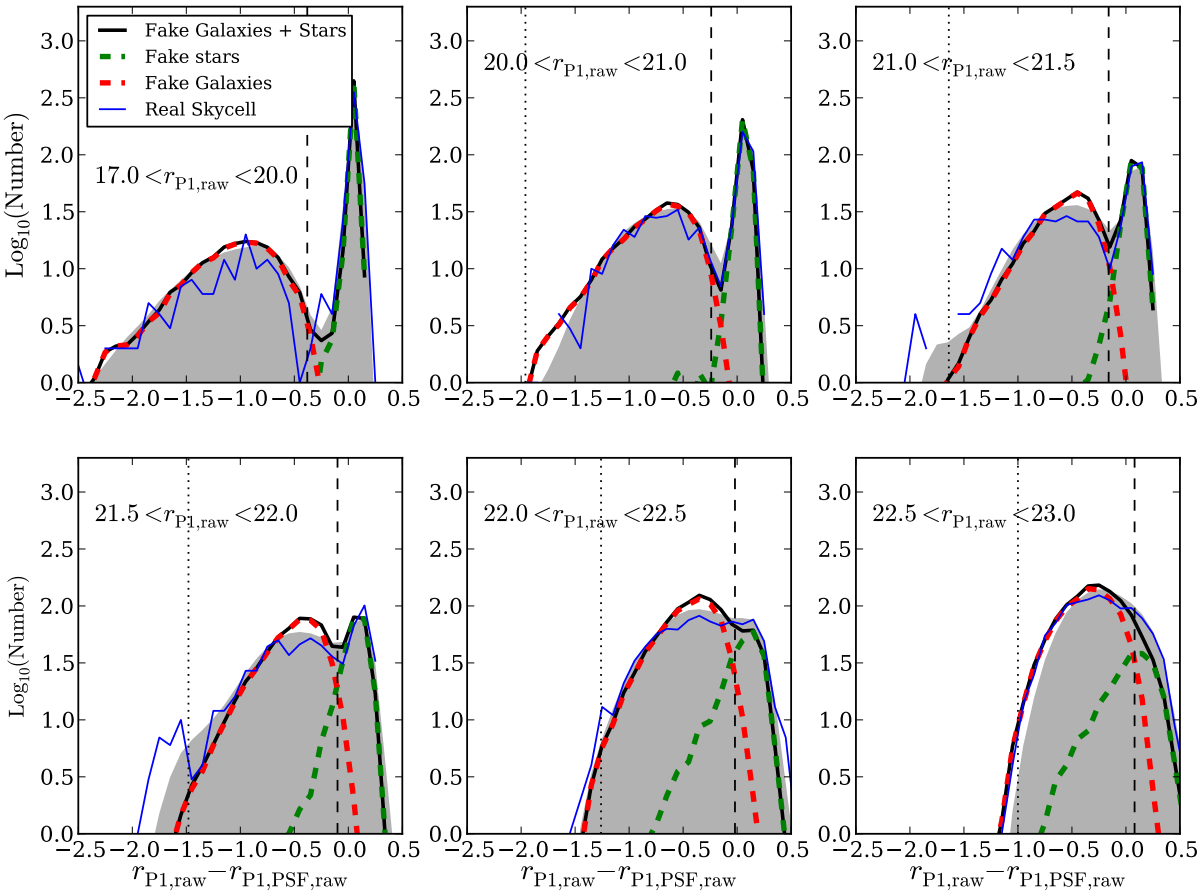

Figure 3.7: Kron minus PSF $r_{\rm P1}$-band magnitudes for all synthetic objects (black), synthetic stars (green dashed) and synthetic galaxies (red dashed) placed into the SAS2 skycell 1315.028, which has a PSF FWHM typical of SAS2 data. Also plotted are the real sources from that skycell (blue) and all sources in SAS2 (grey shaded area); the latter is normalised to the area of skycell.1315.028. The vertical dashed line shows the position of the star and galaxy separation cut for the 98% separator, the dotted vertical line shows the position of the extreme Kron minus PSF magnitude cut.

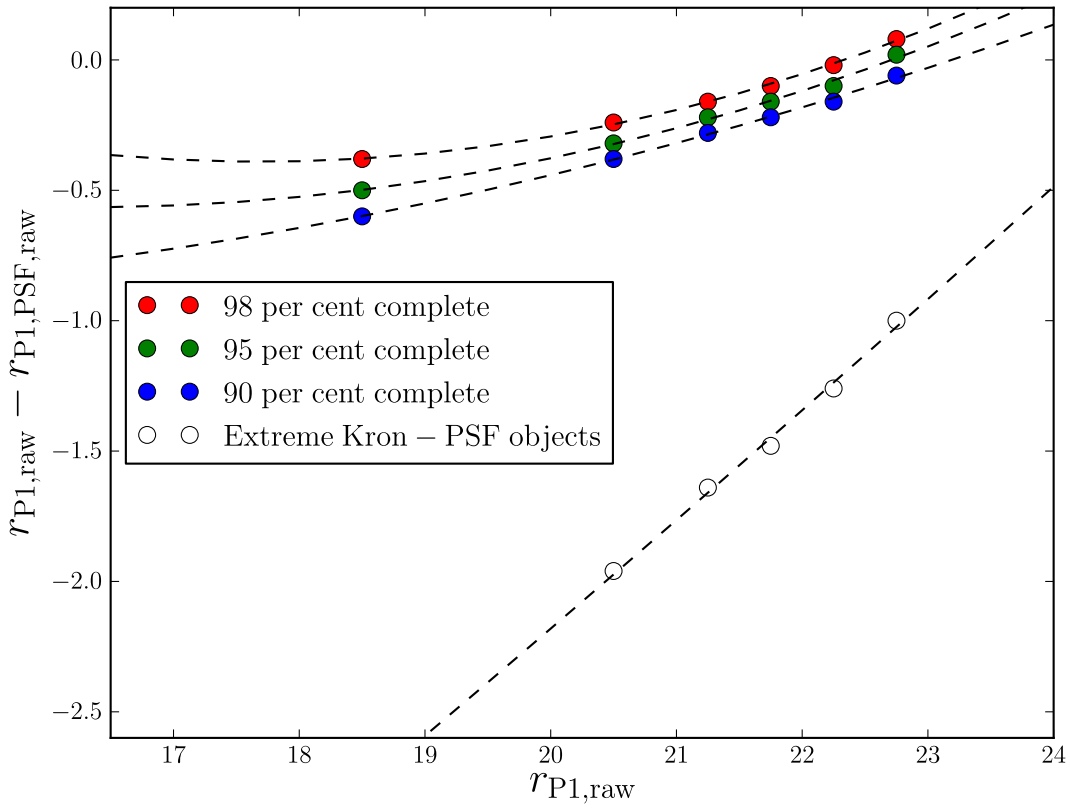

Figure 3.8: Galaxy (filled points) and extreme Kron minus PSF cuts (open circles) in the $r_{\rm P1,raw} - r_{\rm P1,PSF,raw}$ versus $r_{\rm P1,raw}$ plane, with colours indicating their completeness as found by the simulations shown in Fig. 6. The points are fitted with second order polynomials (Eq. 3.3.5) (dashed lines).

Table 3.1: Coefficients for the star, galaxy and false positives separator. Percentages represent the percentage of objects would be included in the sample. The upper or lower limit column defines the direction of the cut, e.g. an upper limit indicates only taking values below the given $r_{\rm P1,raw} - r_{\rm P1,PSF,raw}$ line.

Sample	a_2	a_1	a_0	Upper or Lower Limit
98% Galaxies	0.018	0.120	−0.192	Upper
95% Galaxies	0.014	0.129	−0.261	Upper
90% Galaxies	0.007	0.129	−0.319	Upper
Extreme $\Delta_{\rm kron-psf}$	–	0.417	−1.759	Lower

our synthetic objects, along with fits to the observed SAS2 bright star and galaxy number counts (shown in Fig. 3.16), to predict completeness and stellar contamination rates. Note that our contamination is one minus what some authors define as 'purity'. In Fig. 3.9 the predicted galaxy completeness line follows the 98% line (solid, black), by construction, down to a faint magnitude limit. Near the end of this magnitude range the completeness does drop very slightly and this suggests our fits with Eq. 3.3.5 cannot be used beyond a faint magnitude limit of $r_{\rm P1,kron} = 23.0$. The dotted line in Fig. 3.9 shows the completeness of the sample before applying the extreme $\Delta_{\rm kron-psf}$. This cut, again by construction, has very little effect on the completeness of real galaxies.

Fig. 3.9 also gives the probability of misclassifying a star as a galaxy (solid red) and the predicted stellar contamination as a fraction of the galaxy sample (dashed red). The latter were calculated from our power law fits to the observed SAS2 bright star and galaxy number counts (Fig. 3.16). We see stellar contamination stays below 10% for all magnitude ranges.

In order to further test our star/galaxy separator, we match our $r_{\rm P1}$-band data to the $i_{\rm P1}$-band and $g_{\rm P1}$-band and plot the colour-colour and colour-magnitude diagrams for stars and galaxies classified via our 98% cut in the $r_{\rm P1}$-band. The diagrams in Fig. 3.10 follow those for SDSS objects seen in Finlator et al. (2000). In Finlator et al. (2000) the shape of the distribution of stars in these plots is explained as being driven by different spectral types, with M dwarfs causing the upturn in the

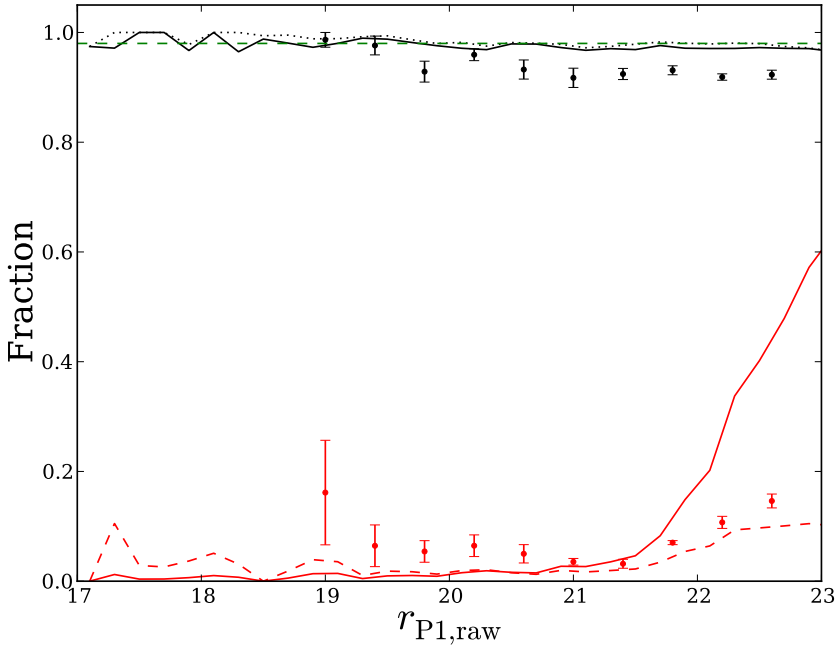

Figure 3.9: The probability of correctly classifying a source as a galaxy using the 98% cut (black) and the probability of misclassifying a star as a galaxy (red solid), as predicted using our synthetic objects in Fig. 3.7. Also plotted is the predicted amount of stellar contamination as a fraction of the 98% galaxy sample (red dashed), found from scaling the probability of misclassifying a star with power law fits to the bright end of the observed star and galaxy number counts. The dashed line marks 98%, whilst the dotted line shows our completeness before applying the extreme Kron minus PSF cut. The points with error bars are estimates based on our comparison to the spectroscopic classifications of VVDS sources, as explained in Section 3.3.2

colour-colour diagram and F and G disc stars along with fainter, bluer halo stars causing the locus at $g_{\rm P1} - r_{\rm P1} \sim 0.4$. We see no evidence of these features in objects classified as galaxies, which gives further support to the effectiveness of our star/galaxy separator.

3.3.2 Comparison to VVDS Spectroscopic Star and Galaxy Classification

As a final test of our star/galaxy separator, we compare to the spectral classifications from the F22 field VIMOS VLT Deep Survey (VVDS) (Le Fèvre et al., 2005), which we downloaded from the CeSAM website[3]. The VVDS survey is an $I_{\rm AB}$ selected sample of objects. Objects targeted for redshifts are purely selected on apparent $I_{\rm AB}$ magnitude to be $17.5 < I_{\rm AB} < 22.5$, though the full photometric catalogue is deeper than PS1 (McCracken et al., 2003; Le Fèvre et al., 2005). F22 and SAS2 overlap by 4 square degrees. We match the two catalogues using a $1''$ matching radius. From the matched catalogue we select objects which have been targeted for spectroscopy based on the value of the column ZFLAGS, taking ZFLAGS=99 to mean the object was not targeted. Following Ilbert et al. (2005) we also use ZFLAGS to select objects with secure redshifts, by requiring the last digit of ZFLAGS to be greater than or equal to 2. Objects with these ZFLAGS are expected to have the correct redshift 80-99% of the time, depending on their value of ZFLAGS (Le Fèvre et al., 2005).

In Fig. 3.11 we show the fraction of objects in PS1 matched to VVDS as a function of PS1 raw Kron magnitude. We do not correct for the VVDS mask, which explains why the curve does not reach unity. An $I_{\rm AB}$-band selected sample may have a different morphological mix than an r-band selected sample in the same magnitude range. From Fig. 3.11 we see the fraction of objects targeted for spectroscopy drops brighter than around $r_{\rm P1,raw} = 18.0$ and fainter than $r_{\rm P1,raw} = 22.0$: this is the region where the effects of the VVDS $I_{\rm AB}$-band selection may become important and as such results from these magnitude ranges may be unreliable. Also note from

[3]http://www.lam.fr/cesam/?lang=en

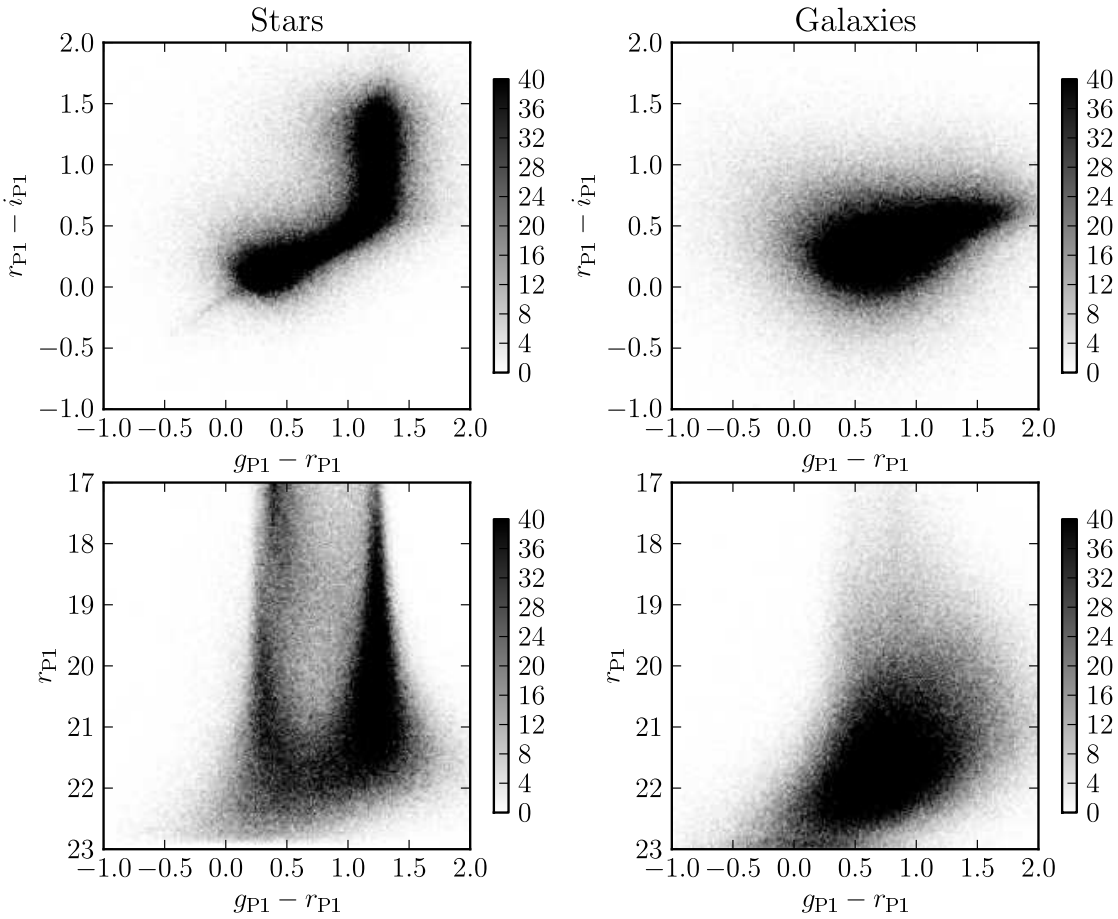

Figure 3.10: Colour-colour and colour-magnitude diagrams, using Kron magnitudes, of SAS2 objects falling on the star side and galaxy side of our chosen star/galaxy separator (section 3.3.1). The greyscale bar gives the number of objects in each colour-magnitude bin. We see the characteristic stellar features highlighted in Finlator et al (2000), such as the upturn in the colour-colour diagram. In support of our classification we see no evidence of these features in the galaxy sample.

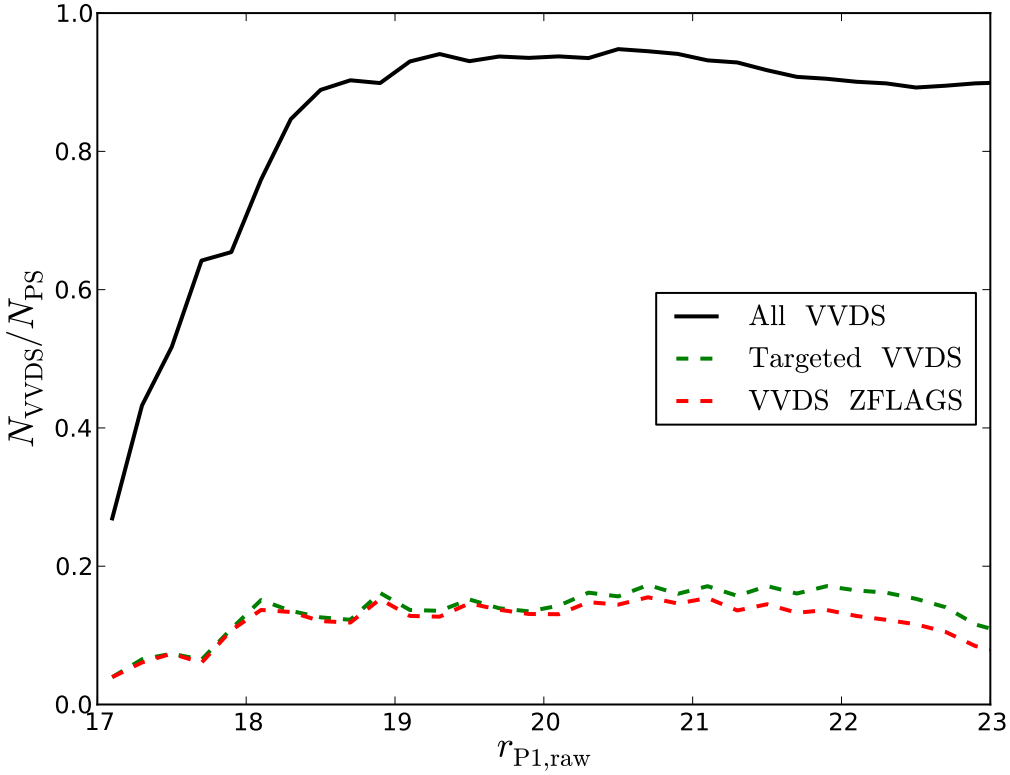

Figure 3.11: The fraction of Pan-STARRS objects in VVDS as a function of PS1 magnitude: for all VVDS sources (black), VVDS sources targeted for spectroscopy (green-dashed) and VVDS sources with good redshift flags as described in the text (red dashed).

Fig. 3.11 that the fraction of objects with secure redshifts decreases with magnitude, as one might expect.

A well reported issue in VVDS is its bias against extended sources. Whilst the targeting criteria is purely based on apparent magnitude the program which allocates VIMOS slits to targets, the Slit Positioning Optimization Code (SPOC) (Bottini et al., 2005), is biased against extended sources as they take up more space on the x-axis of the spectrograph and so decrease the efficiency with which spectra are taken (Bottini et al., 2005). When computing luminosity functions Ilbert et al. (2005) corrected for this incompleteness by weighting galaxies in a way proportional to their x-axis size on VIMOS. For our tests we choose to weight galaxies depending on their $\Delta_{\mathrm{kron-psf}}$. In magnitude and $\Delta_{\mathrm{kron-psf}}$ bins we measure the completeness as the ratio of objects with good ZFLAGS to all objects matched between PS1 and VVDS in the overlap region. The weight of each object is then the inverse of the completeness of its magnitude and $\Delta_{\mathrm{kron-psf}}$ bin.

When comparing to VVDS there are three different cases to consider. The first case is where the object is classed as a galaxy in VVDS and PS1, we label weights for these objects as W_{gg}. The second case is for an object classed as a galaxy in PS1 but has a VVDS stellar spectral classification, we label weights for these objects as W_{gs}. The final case is an object classed as a star in PS1 but with a galaxy spectra in VVDS, these objects are assigned weights labeled W_{sg}. The completeness, C_{m}, and contamination, C_{n}, are estimated using the following weighted sums

$$C_{\mathrm{m}} = \frac{\Sigma W_{\mathrm{gg}}}{\Sigma W_{\mathrm{gg}} + \Sigma W_{\mathrm{sg}}}, C_{\mathrm{n}} = \frac{\Sigma W_{\mathrm{gs}}}{\Sigma W_{\mathrm{gg}}}. \tag{3.3.6}$$

We plot these estimates, along with jack-knife errors from 9 re-samplings of the data, in Fig. 3.9. Estimates of stellar contamination are slightly higher than the estimates based on synthetic images, but this is only a small discrepancy given the size of the errors. Estimates of completeness agree until around $r_{\mathrm{P1}} = 20$ when it looks like our synthetic source estimates are too optimistic. The spectroscopic estimates suggest a completeness of around 91%, as opposed to the predicted 98%.

There are several possible reasons for this difference. A major cause of disagreement could be misclassifications in the VVDS sample. To calculate the fraction of

Table 3.2: The second column gives the probability of a redshift measurement being correct for different ZFLAGS values, taken from Le Fèvre et al. (2005). The third and forth columns give the fraction of the full sample and discrepant sample that have certain ZFLAGS values. The final column gives an estimate of the total fraction of PS1 objects with incorrect VVDS estimates of redshift.

ZFLAGS	$P_{\rm correct}$	$F_{\rm Full}$	$F_{\rm Disagree}$	$F_{\rm Full}(1-P_{\rm correct})$
2	0.80	0.25	0.42	0.05
3	0.91	0.22	0.23	0.02

objects in our sample which could be misclassified by VVDS we use ZFLAGS. The value of ZFLAGS has been related to the probability of having been assigned the correct redshift, $P_{\rm correct}$, by Le Fèvre et al. (2005). We assume this is also the probability of being correctly classified as a star or galaxy. This is the best approach available but is unfortunately not ideal, as the probability of correctly classifying an object as a star or galaxy is not the same as the probability of assigning it the correct redshift. Indeed, it may be easier to obtain a redshift from a galaxy rather than a star, so one should be careful to view the following analysis as giving an upper limit on the misclassification-corrected estimate of completeness.

Table 3.2 gives the different fractions of the full sample, $F_{\rm Full}$, and sample with discrepant star/galaxy classification, $F_{\rm Disagree}$, that have certain values of ZFLAGS. Table 3.2 also gives our estimate of the fraction of objects in the full sample with incorrect VVDS classification, $F_{\rm Full}(1-P_{\rm correct})$. Given that 9% of the full sample have discrepant classifications, $0.09F_{\rm Disagree}$ is the number of objects in the discrepant sample with a certain ZFLAGS value as a fraction of the total matched sample. Taking the minimum of $0.09F_{\rm Disagree}$ or $F_{\rm Full}(1-P_{\rm correct})$ for each ZFLAGS value in Table 3.2 and summing suggests that 6% of our disagreement could be down to misclassified VVDS objects. This would lead to a VVDS misclassification-corrected estimate of completeness of 97%, consistent within random errors with our estimate from synthetic sources.

Another potential explanation is that the synthetic galaxies may be slightly too

extended in their $\Delta_{\mathrm{kron-psf}}$ values. Simplification of modelling galaxies with de Vaucouleurs and exponential profiles, adopting a mean extinction value for the galaxies, using redshifts and magnitudes from GALFORM and only generating synthetic images on one skycell could all contribute to this effect.

From Fig. 3.9 it appears that our classification is around 91%-98% accurate down to faint magnitudes depending on how you estimate classification completeness. Brighter than $r_{\mathrm{P1,raw}} = 22.0$ stellar contamination is below 6%, increasing to around 10% at magnitudes fainter than this. The action of stellar contamination, on smaller scales where the stars are uniformly distributed, is to dilute the clustering by $(1-f)^2$, where f is the fraction of stars in the galaxy sample (e.g. Hudon & Lilly, 1996; Roche & Eales, 1999). We will revisit the effect of stellar contamination in Section 3.5.3.

Classification contamination and completeness can influence galaxy clustering measurements and as such work alternative approaches to star/galaxy separation are being explored by other groups. Classifications based on SED fits along with star/galaxy separators calibrated on other data sets and other morphological measurements will be available to help meet the future PS1 science goals.

3.4 Dealing with Variable Depth

The finished PS1 3π survey will have spatially variable image depth for several reasons. These include spatially varying stack coverage due to masking and greater or fewer visits to any piece of sky (see Fig. 2.1), varying PSFs, varying photometric conditions and varying sky brightness. To measure reliable clustering it is vital to measure the angular incompleteness, otherwise fluctuations in galaxy density caused by changes in depth would contaminate the clustering measurements. Once this angular incompleteness is modelled we can deal with it by introducing the same depth variations into the random distribution of points we use to measure clustering, which we shall refer to from now on as our "random catalogue".

One approach to generate such a random catalogue would be to generate synthetic galaxies, place them randomly on PS1 images, run the source detection software and add them to the random catalogue if they are detected. If this process

were carried out as part of the IPP, then it could be a good approach. However, attempting this outside of IPP, using, for example, the synthetic image server (Section 2.6) would be prohibitively slow as IPP software would have to be run many times on each image. Additionally, results could be sensitive to how realistic the synthetic galaxies are. We therefore adopt a faster, more empirically rooted approach.

We assume that the probability of detecting an object is only dependent on the signal-to-noise ratio. In order to make a simplified estimate of the signal to noise ratio we assume all sources have a Gaussian light distribution. For the stacked data most galaxies near the magnitude limit have small angular sizes so this is a reasonable approximation (we further test this later in this section). Using a PS1 PSF rather than a Gaussian would simply scale our FWHM measurements to different values, an effect that would be removed by the empirical calibration we present later in this section. We define the "fiducial" SNR as

$$\mathrm{SNR} = \frac{F}{\sqrt{\pi d_{\mathrm{FWHM}}^2 \sigma^2}}, \tag{3.4.7}$$

where d_{FWHM} is the FWHM of the PSF in units of pixels, F is the apparent flux of the source (without extinction correction) and σ^2 is the variance according to our variance map. Whilst d_{FWHM} is measured for all PS1 detections, for this work we use the typical FWHM of SAS2 of $0.94''$. As SAS2 has fairly uniform seeing this simplifies our work whilst not significantly affecting our results. The downside of this is that we are unable to test that our method holds for the wide range of seeing conditions experienced over the whole 3π survey. We use our binned-up variance maps to extract σ^2 which results in the loss of some spatial accuracy. This is unavoidable due to the otherwise prohibitively slow process of retrieving the individual variance maps at the native pixel scale.

To calibrate the relationship between our fiducial SNR measurements and source recovery fraction we again make use of the overlap region with Stripe 82. We use the Stripe 82 Petrosian magnitude to calculate the fiducial SNR for all Stripe 82 objects and then match to PS1 SAS2 and see what fraction are recovered. We plot these fractions in Fig. 3.12 in different magnitude bins. The fact that over different magnitude bins the fiducial SNR values have the same detected fraction

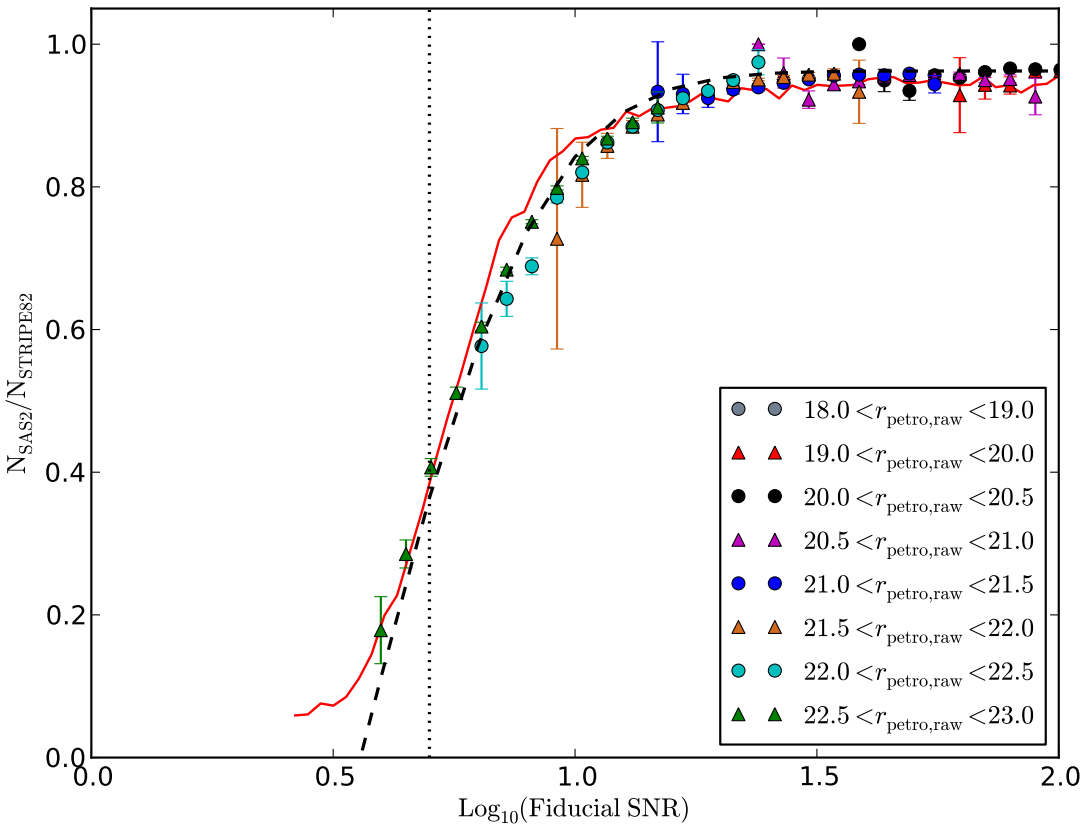

Figure 3.12: The fraction of Stripe 82 objects detected as a function of fiducial SNR (Eq. 3.4.7). Overlap between magnitude bins implies the fiducial SNR can be used as an estimator of the probability of source detection. The red line shows this quantity as measured from the synthetic galaxies added into real PS1 images and processed by the standard IPP. The dashed line shows the best-fitting relation of Eq. 3.4.8, the dotted line marks SNR = 5.0. Error bars are from 100 bootstrap re-samplings.

shows that this measurement can be used to assess the probability of detection. We parameterize this curve with the fitting formula

$$P_{\rm Det}({\rm SNR}) = a\ {\rm erf}(b\ \log_{10}({\rm SNR}) + c), \tag{3.4.8}$$

where a, b and c are constants with best-fitting values $a = 0.962$, $b = 2.446$ and $c = -1.361$. The fact that a is not unity implies there is always some fraction of Stripe 82 objects undetected by PS1. We believe this fraction is caused by false positives in SDSS Stripe 82 and visually inspecting a subset of these objects suggests they are mainly caused by spurious detections in the wings of extended objects. So long as the number of false positives in Stripe 82 remains a constant fraction of the real objects this effect should not bias our results. This seems to be the case, as the curve is flat for large values of fiducial SNR. As a sanity check we also add a curve to Fig. 3.12 showing the detection efficiency (as defined in Chapter 2) estimated from our synthetic galaxies, using the input synthetic object magnitude, corrected to Kron magnitude using a correction of 0.2 magnitudes (explained in Section 2.2.1). Our estimate of detection efficiency from synthetic objects shows a reasonable agreement with the real data on the plot, though the synthetic galaxies seem to suggest the Stripe 82 comparisons slightly underestimate the depth at fiducial SNR values of around 6 to 9. The differences could be due to multiple causes. For example, it could be Stripe 82 false positives or slightly above average seeing in the skycell used in Section 3.3.1. As these differences are only of the order of a few percent we choose to defer further careful studies to the analysis of the full 3π dataset, where a larger amount of deeper comparison data will be available.

We can see in Fig. 3.12 that a 5σ SNR implies a 20-30% detected fraction; this is slightly higher than the detected fraction in Fig. 2.6 for synthetic galaxies on synthetic detrended exposures. This is unsuprising however as fainter galaxies near the stack detection limits tend to appear smaller than galaxies near the detrended exposure detection limits, and so are easier to detect. None the less this highlights the fact that where the curve of Fig. 3.12 is steep small changes in the SNR can lead to large changes in detection fraction. To avoid any problems caused by this we can impose lower limits on the fiducial SNR by excluding spatial regions where

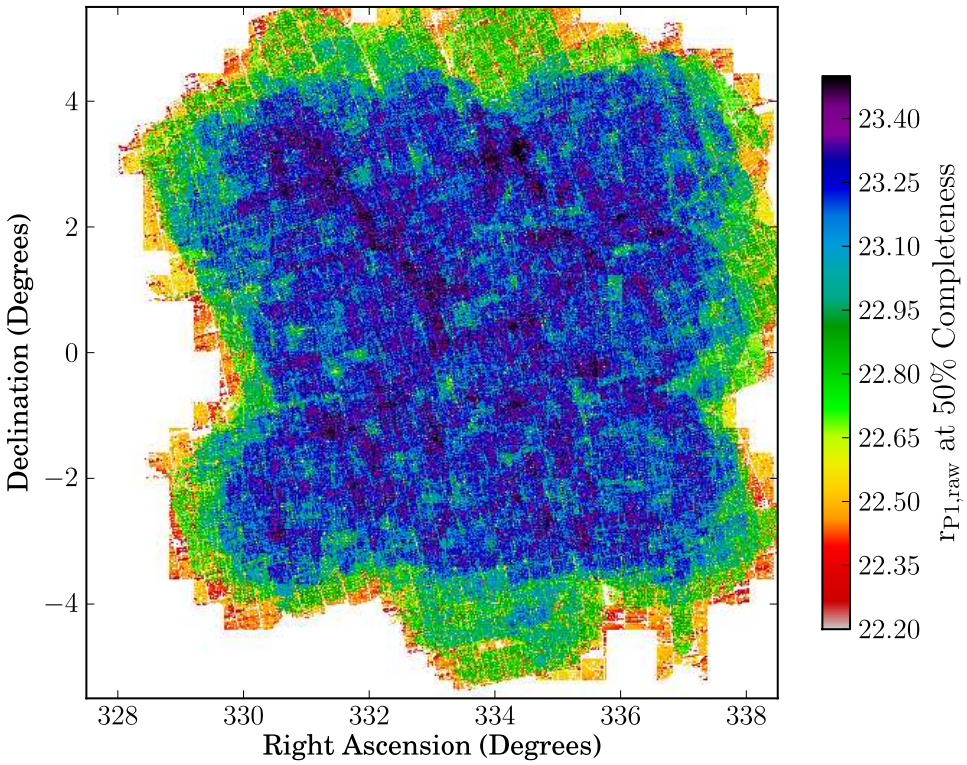

Figure 3.13: The $r_{P1,raw}$ magnitude corresponding to 50% galaxy completeness as predicted by our fiducial SNR method. SAS2 is shallower near the edges where there are fewer exposures, while the pattern of deeper areas across the central region is more representative of of what we expect from the whole 3π survey.

the SNR is less than some value from our clustering samples. By default we impose SNR < 3.0, but we experiment with it in Section 3.5.2 in order to test if our results are sensitive to its value.

Using our binned up variance maps and Eq. 3.4.8 we can produce a map of the magnitude at 50% galaxy recovery, shown in Fig. 3.13. Note we can produce these maps even in SAS2 regions without Stripe 82 overlap, as we only need Stripe 82 to calibrate Eq. 3.4.8. One can clearly see the shallower regions near the edges of the SAS2 field, along with patterns of deeper regions in the central area caused by the overlapping pattern of input exposures. Fig. 3.13 demonstrates our technique produces maps of depth to very high resolution, contrast this with the much lower

resolution depth maps produced using synthetic stars presented in figure 15 of Paper I. Reassuringly, we see common features, including the shallower edge region and the deeper diagonal feature.

We use the curve fitted to Fig. 3.12 to correct our random catalogue by making the chance of placing a random point of a certain magnitude in any region equal to the detected fraction expected for that region, given the random point's fiducial SNR. Magnitudes are assigned to the random points from the observed galaxy counts, uncorrected for extinction. As a first pass we estimate these number counts by fitting the bright end of the galaxy counts with a power law (in Section 3.5.1 we show we can use our method to yield depth corrected number counts, which we use to assign magnitudes to the random points). After assigning magnitudes and deciding if a random is detected, we extinction-correct the random catalogue. This technique results in a random catalogue with the same spatial depth variation as the data.

We plot the depth-corrected density of galaxies in Fig. 3.14. To produce this figure we binned the galaxies and detection efficiency randoms onto the same grid and then divided the galaxy grid by the random grid, normalising by the ratio of the relative numbers of galaxies and randoms. To eliminate noise from regions with very few randoms, generally near the edge of the field, we white-out pixels with fewer than 5 randoms. Comparing Fig. 3.5(bottom) to Fig. 3.14 we see the over-densities caused by varying image depth are removed. There are fewer objects in Fig. 3.14 than Fig. 3.5(bottom) as star/galaxy separation has removed the stars.

One key assumption of our depth correction method is that all galaxies in our sample have the same detection efficiency properties for the same fiducial SNR, i.e. that secondary parameters such as morphology or colour are unimportant in determining how likely objects are to be detected (consider Eq. 3.4.7). We argue that at faint magnitudes galaxies predominantly have small angular sizes and, as such, look similar to one another after being convolved with the PSF. To further test this we plot, in Fig. 3.15, the detection efficiency curves of our Stripe 82 red and blue samples of galaxies. In Fig. 3.15 we see, for the same reasons as in Fig. 3.12, that the curve does not reach unity. We also see that at brighter magnitudes blue galaxies

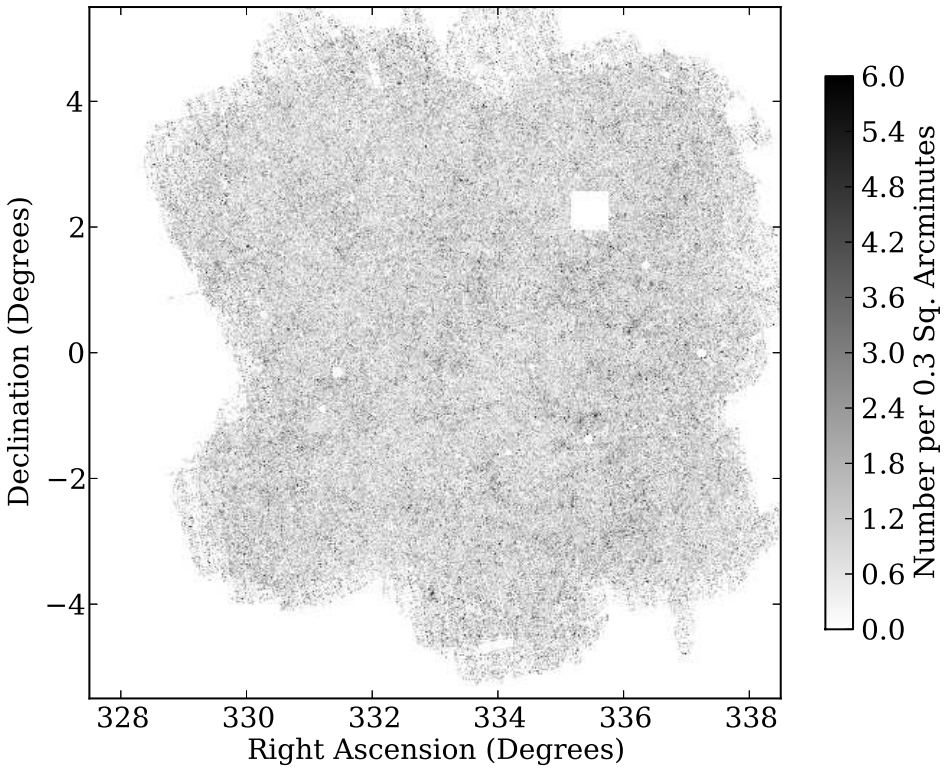

Figure 3.14: The number density of galaxies, binned by right ascension and declination and corrected for variable depth. We claim over-densities in this plot are genuine, except those caused by Poisson noise in pixels nearer the edges of the field which have small numbers of galaxies.

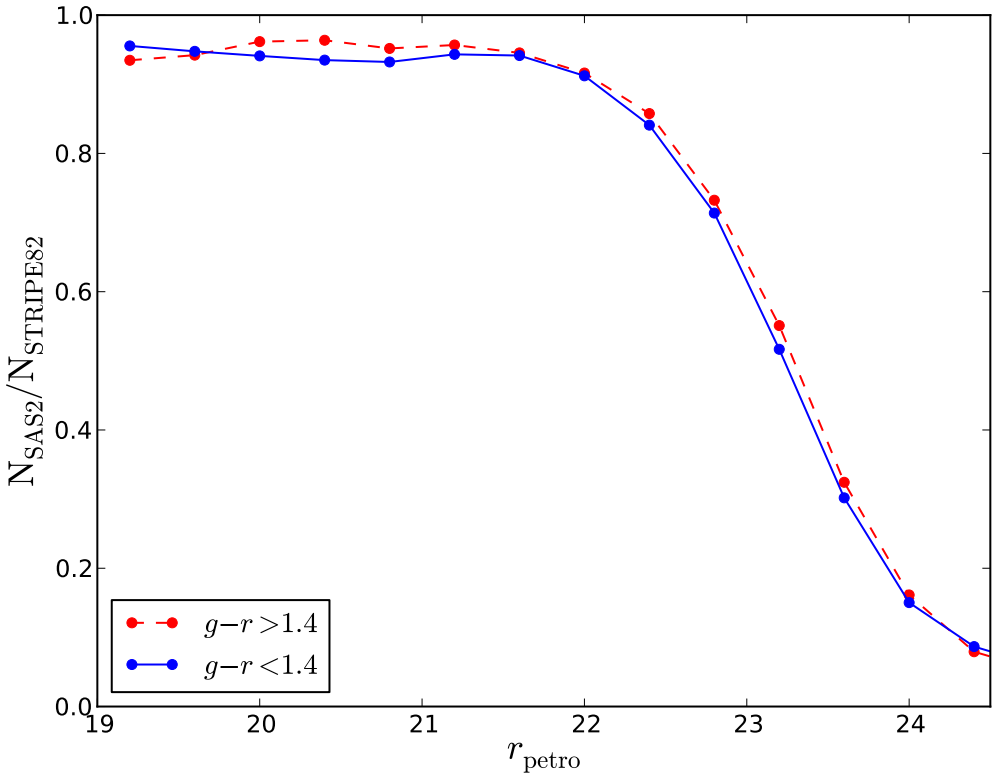

Figure 3.15: The detected fraction of Stripe 82 galaxies, separated into red and blue by Stripe 82 colours. We see little evidence that red and blue galaxies have different detection efficiency properties, despite the fact that their morphology is expected to be different.

have a slightly lower detection efficiency. As this effect is at magnitudes far brighter than our detection limit we attribute this to false positives in Stripe 82 falling on the blue side of our colour cut. The agreement between the red and blue detection efficiency curve at faint magnitudes in Fig. 3.15 suggests that an undetected low surface brightness population of galaxies must either be split equally between our two colour bins or represent a very small fraction of our sample. This supports our assumption that at the limiting magnitude of 3π data detection efficiency depends on a single parameter, SNR. However in small regions of the 3π survey where the limiting magnitude may be much brighter, and galaxies near this magnitude have larger angular sizes, the situation may be more complicated.

3.5 Results and Tests for Systematics

3.5.1 Number Counts

We plot, in Fig. 3.16, the $r_{\rm P1}$-band differential number magnitude counts of galaxies before and after our correction. A Kron to total correction of 0.2 magnitudes is applied to the galaxy counts, as explained in Section 2.2.1. To generate the detection efficiency corrected number counts in Fig. 3.16 we use our extinction corrected random catalogue, from before and after the detection efficiency corrections, to predict the fraction of galaxies detected as a function of extinction corrected magnitude. We then correct the observed number counts by these fractions. We see after the counts have been corrected the turnover no longer occurs, and the counts continue to grow to very faint magnitudes until we stop using our depth correction at $r_{P1} = 23.7$, where the correction is very large (a factor of 70 at this magnitude). We see that our number counts show reasonable agreement with the published data of Huang et al. (2001), Yasuda et al. (2001), McCracken et al. (2003) and Kashikawa et al. (2004). At the faintest magnitude, where our correction is important, our number counts are slightly above the literature measurements. This could be partially due to the 10% false positives at these magnitudes (see Fig. 3.6 and also Paper I). It could also be partially explained by sample variance, as the literature measurements also disagree to a similar extent at these magnitudes.

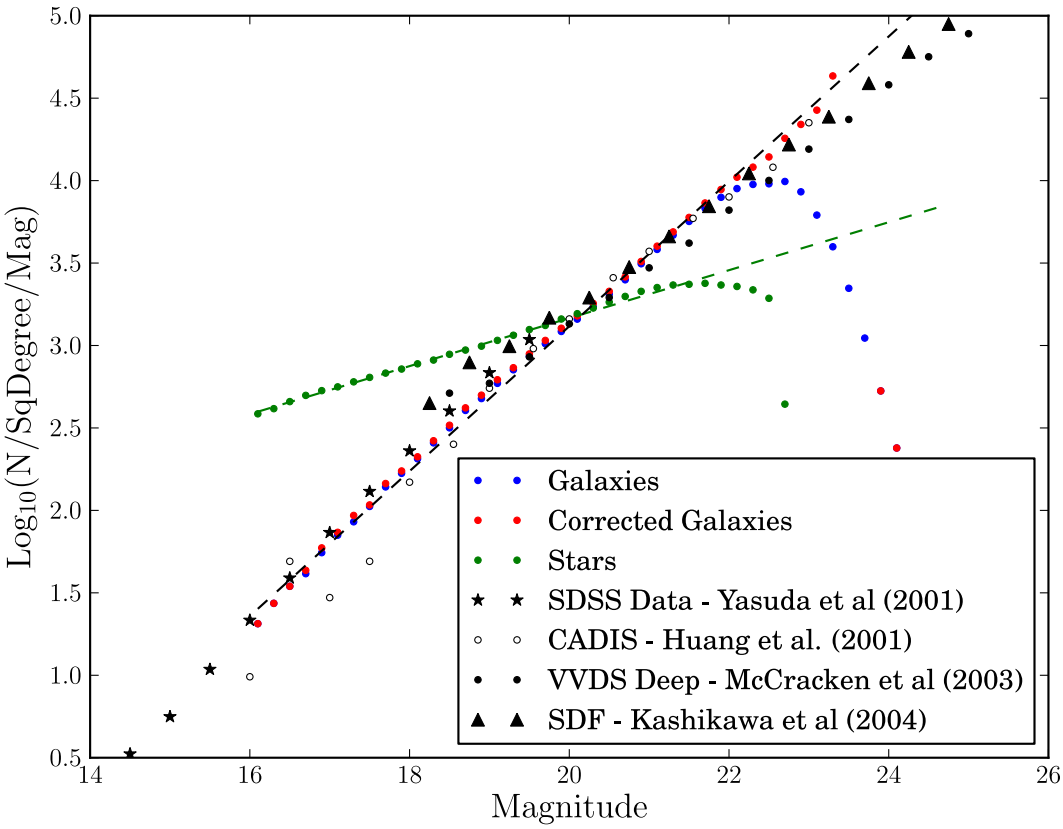

Figure 3.16: Number counts in the $r_{\rm P1}$-band before (blue) and after (red) the depth correction for galaxies, along with the number counts of objects classed as stars by our adopted separator (green). We do not correct the stars, or the galaxies fainter than $r_{P1} = 23.7$ for completeness. The dashed lines are power law fits to the number counts. Example r-band literature galaxy counts have been included, as indicated in the legend. PS1 Kron magnitudes have been corrected to total using our adopted correction of 0.2 magnitudes.

In Fig. 3.17 we show our measured, uncorrected, number counts for different bands. Each band was matched to the $r_{\rm P1}$-band, where the star/galaxy classification was made. The galaxies show a power law trend in good agreement with previous measurements. The stars show a shallower power law trend. The turnover in the samples is caused by the incompleteness and this turnover happens at brighter magnitudes as we move toward redder bands. In redder bands the ratio of stars to galaxies increases, until the $y_{\rm P1}$-band where we see more stars than galaxies at all magnitudes. As these are the same objects as seen in Fig. 3.16 the main purpose of this plot is to check if our $r_{\rm P1}$-band star/galaxy classification gives sensible results for different bands. We leave detailed science analyses using the number counts to later work.

3.5.2 Angular Clustering

In this section we present measurements of angular clustering. To measure this clustering we make use of the GPU code of Bard et al. (2012). We use the Hamilton (1993) estimator, though our results are unchanged if we use the Landy & Szalay (1993) estimator. Error bars for all clustering measurements are from 9 jack-knife re-samplings of the data. We use eight times as many random points as data points throughout. On each clustering plot we draw the same dashed-black reference line, for easier comparisons between plots.

When measuring clustering an effect known as the integral constraint can artificially weaken clustering on scales comparable to the area of the survey (e.g. Roche & Eales, 1999). For SAS2 data, over the scales we measure clustering, this has no effect on our results, except in one case we will discuss later. For the MD07 measurements however the smaller area results in the integral constraint being important on the scales we consider. We therefore estimate the true clustering of the MD07 data on large scales by fitting a power law between scales of 0.002 to 0.165 degrees and then use this fit to estimate the size of the integral constraint, IC, using the standard formula as seen in e.g. Roche & Eales (1999) of

$$IC = \frac{\Sigma RR(\theta) w_{\rm model}(\theta)}{\Sigma RR(\theta)} \tag{3.5.9}$$

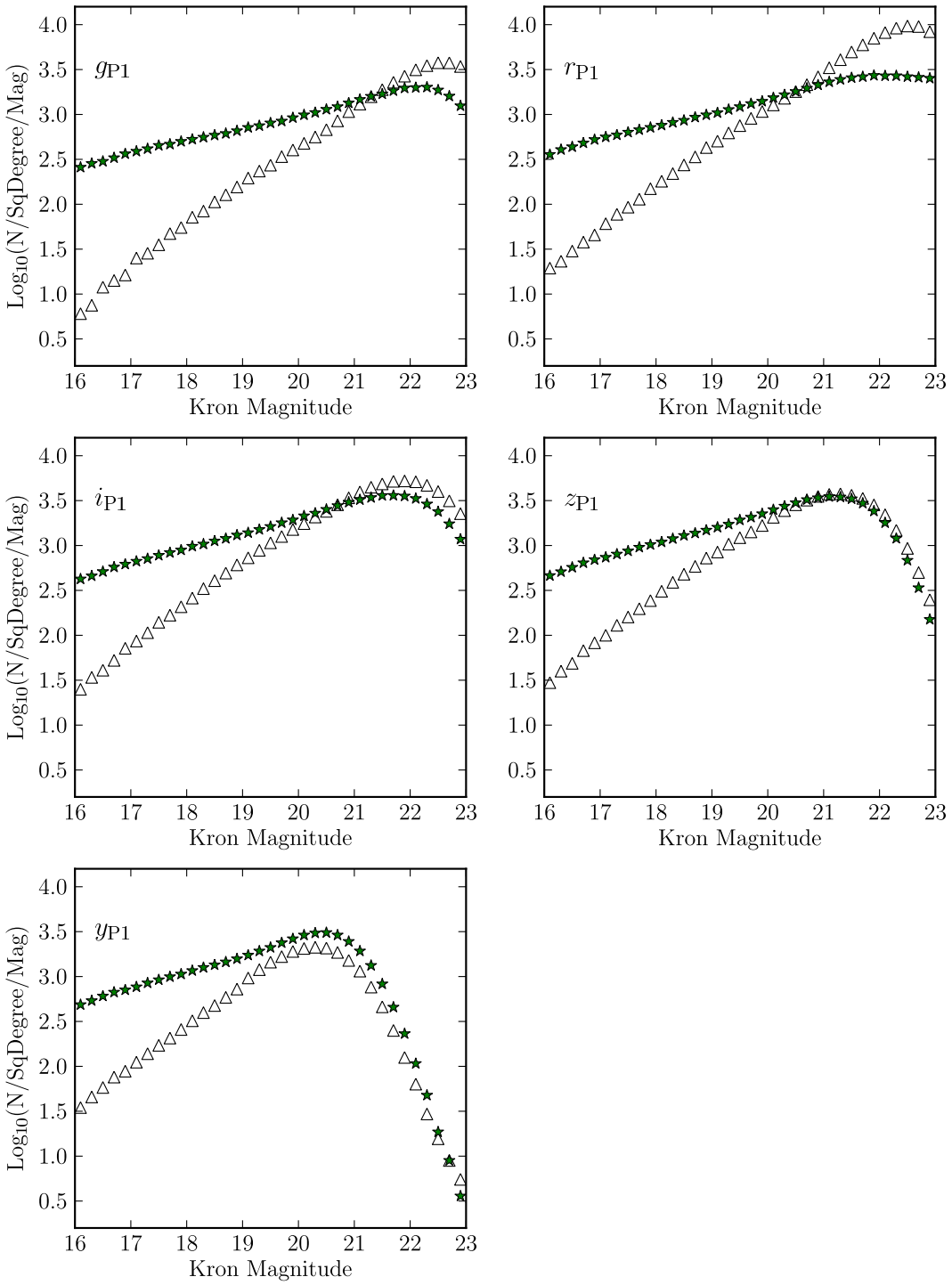

Figure 3.17: The differential number magnitude counts for stars (green stars) and galaxies (open triangles) for different PS1 bands matched to the r_{P1}-band, in which the star and galaxy separation cut was applied (section 3.3.1). These counts have been uncorrected for image depth. Matching to r_{P1}-band data has some contribution to the turnover in each band. However, only the depth of the i_{P1}-band is greatly affected, as this band is the only one deeper than the r_{P1}-band.

where $RR(\theta)$ are the pair counts of the randoms on SAS2 as a function of angular separation and $w_{\rm model}(\theta)$ is our power law correlation function. The value IC is added to the clustering measurements. As an example, for our threshold sample $r_{\rm P1} < 23.0$ the integral constraint is 80% of the signal at the largest separations plotted, dropping to 14% by $\theta \cong 0.1$ deg.

We begin by studying the regime where the spatially varying depth correction has no effect. Fig. 3.18 shows the clustering of PS1 data compared the clustering of DR8 data over the same region, which we measured from our galaxy sample (Section 3.1.1). We see the well-reported effect of clustering being stronger in brighter apparent magnitude bins. This result is caused by two effects. The first is that fainter magnitude bins are projected over larger radial distance ranges so incoherent clustering signals are summed together decreasing the clustering strength. The second cause is that intrinsically fainter galaxies are less clustered, usually interpreted as evidence they lie in less massive dark matter haloes (see Chapter 1). This latter effect is much smaller than the former as apparent magnitude ranges relate to similar absolute magnitude ranges. We see good agreement between the SDSS and PS1 measurements for these ranges, an agreement much closer than the jack-knife error bars as the two data samples are from the same area of sky. We do see some differences, but photometric errors scatter galaxies in and out of the different magnitude bins and so the two samples can contain a significant fraction of galaxies that are not in common. Overall, Fig. 3.18 acts as a detailed test to determine if PS1 is capable of measuring the clustering of galaxies down to $r_{\rm P1} = 20.0$. Fainter than this it becomes more difficult to measure reliable clustering with SDSS DR8 and, as such, we compare to measurements in the literature.

In Fig. 3.19 we compare our angular clustering measurements from PS1 SAS2 to recent angular clustering measurements from Wang et al. (2013) from 8000 square degrees of SDSS DR7 data. In Wang et al. (2013) careful studies are carried out which suggest SDSS DR7 can measure clustering down to $r = 21.0$, Fig. 3.19 demonstrates PS1 data shows reasonable agreement with the SDSS data. Naturally, differences arise due to sample variance in the relatively small SAS2 field, but Fig. 3.19 is a promising indicator that PS1 clustering measurements are capable of match-

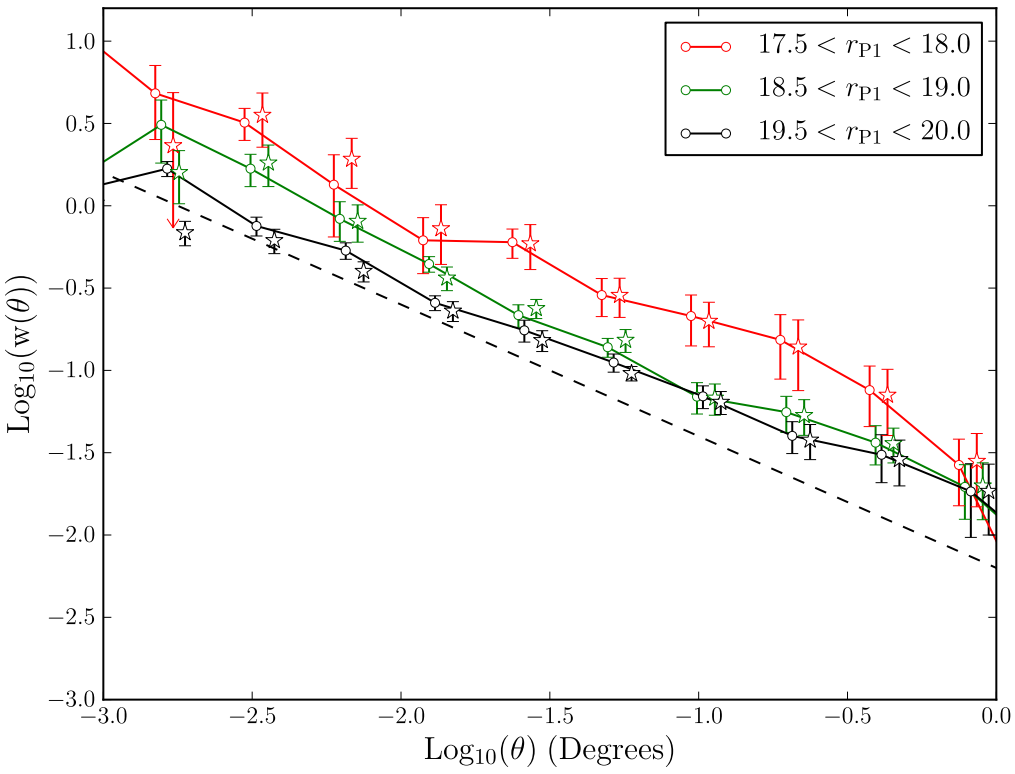

Figure 3.18: Angular clustering of galaxies in PS1 (connected, open circles) and in the same region of SDSS DR8 (star-shaped symbols), both measured for this paper using the sample selection described in the text. This shows good agreement between PS1 and SDSS DR8. The dashed line is a reference line included in all of our clustering plots. Different measurements have been offset horizontally for clarity, the brightest galaxies are at the true x-axis position for all of the measurements.

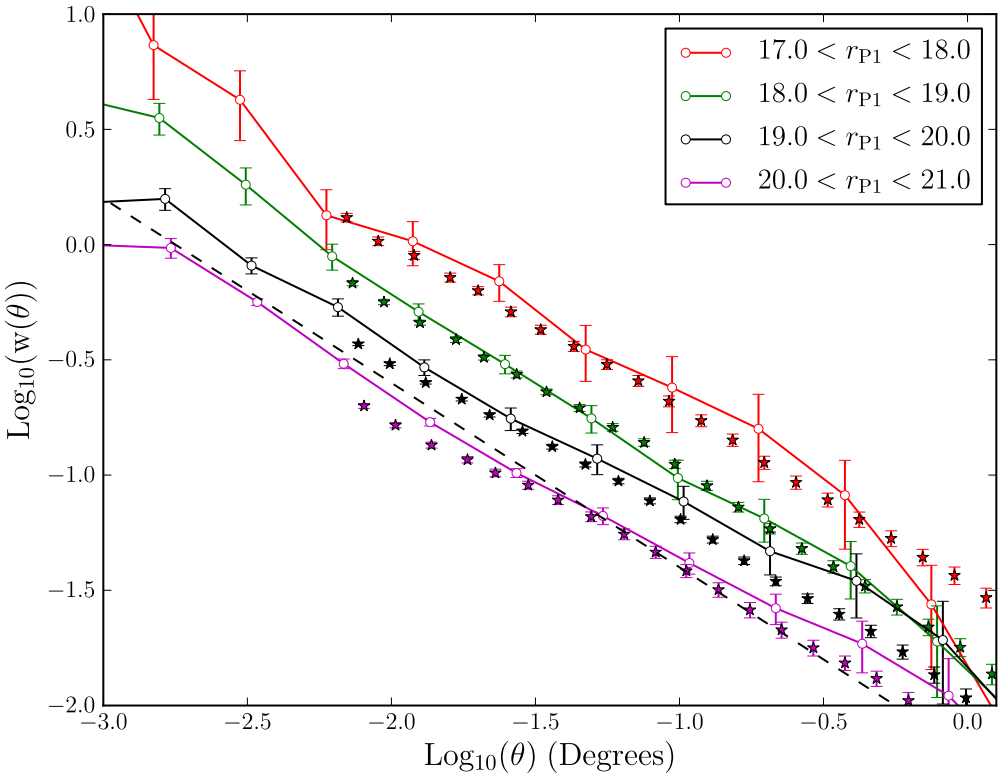

Figure 3.19: Angular clustering of galaxies over the full SAS2 area in PS1 (connected, open circles) and measurements from a much larger area of SDSS DR7 (filled stars) from Wang et al. 2013. The dashed line is the same reference power law as in Fig. 3.18. Different measurements have been offset horizontally for clarity, with the brightest PS1 and SDSS samples showing the positions of the true angular bins.

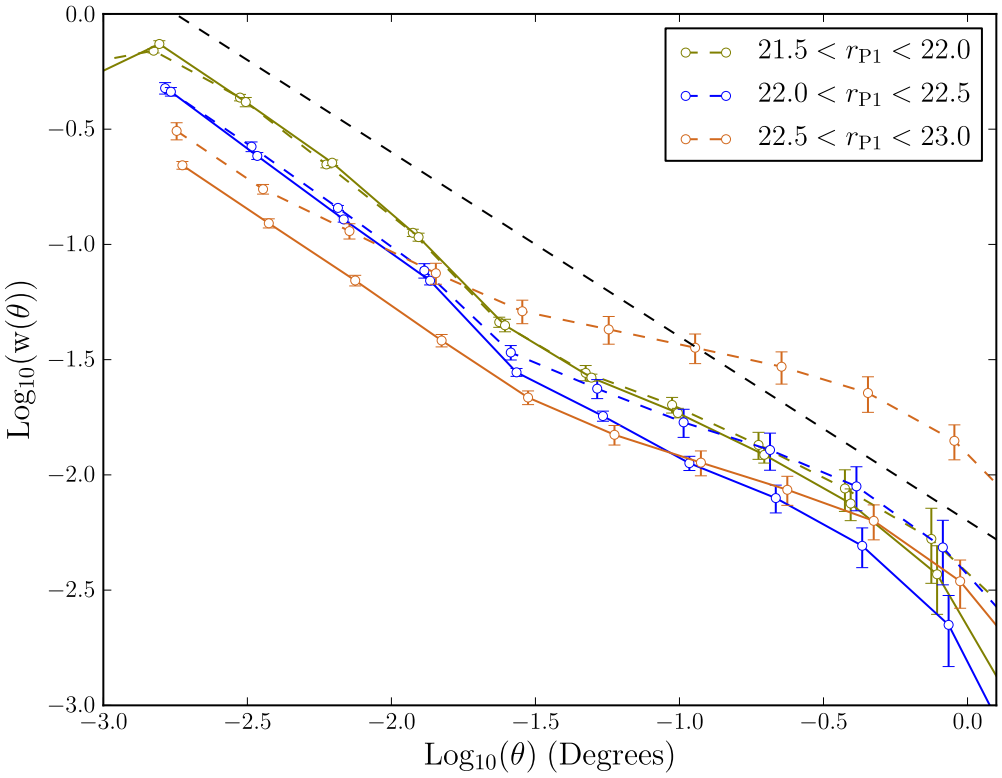

Figure 3.20: Angular clustering of faint galaxies before (dashed lines with points) and after (solid lines with points) applying our spatially varying depth correction. The dashed line is the same reference power law as Fig. 3.18. Different measurements have been offset horizontally for clarity. The uncorrected clustering of the brightest galaxy sample is at the true x-axis position for all of the measurements.

ing SDSS depth. Fainter than $r_{\mathrm{P1}} = 21.0$ the spatially varying depth will start to become important.

To see the effects of our depth correction we plot, in Fig. 3.20, the 2-point angular correlation function of galaxies before and after correcting the random catalogue for spatially varying depth. At $r_{\mathrm{P1}} = 22.0$ and $r_{\mathrm{P1}} = 23.0$, the edges of the brightest and faintest bins in Fig. 3.20, the average completeness is only 80% and 50% respectively. We see that without corrections clustering in the faintest two bins is enhanced by under-densities and over-densities caused by the spatially varying incompleteness. After correction the clustering strength is decreased, with the effect being more

marked for the faintest bin where one would expect the depth to be most spatially inhomogeneous. The largest correction occurs at large scales. Magnitude ranges brighter than $r_{\rm P1} < 22.0$ seem to need very little correction. The SAS2 region is likely to be more uniform than the full 3π data so the magnitudes at which the spatial depth variation correction becomes important may be slightly brighter for the full 3π survey.

As an alternate way of understanding our correction, we measure the angular correlation function of our spatial depth-corrected random catalogue, relative to an uncorrected, spatially uniform random catalogue. This gives us an estimate of the signal we remove from the faint magnitude bins. We see in Fig. 3.21 the clustering of the bright randoms is consistent with no clustering signal. Bright randoms have larger errors as there are fewer of them. For the faintest bin, where we see the strongest correction, the randoms are clustered. This type of clustering signal indicates the effect of variable depth on our measurements. We can infer that without correction clustering is enhanced on all scales at this depth. This effect will be particularly noticeable on larger scales where the intrinsic galaxy clustering is weak; this was seen in Fig. 3.20.

Qualitatively the correction appears to be doing a good job. To carry out a quantitative test we find the variance value which corresponds to some fiducial SNR at the faint edge of a magnitude bin, and mask spatial regions in the randoms and data that have a variance value higher than this. This limits our depth correction by removing data and randoms with fiducial SNR lower than some limit. The corrected clustering measurements for the range $22.0 < r_{\rm P1} < 22.5$ in Fig. 3.22 are robust to changes in the choice of the SNR limit, with more conservative cuts in SNR being in agreement with the more lenient cuts. To further emphasise this, we plot the clustering of $22.0 < r_{\rm P1} < 22.5$ galaxies with and without spatial depth corrections, in regions with SNR > 12.0 where the depth is fairly uniform. We see from these curves that using the full SAS2 region combined with a correction gives results in agreement with using a smaller region of uniform depth.

We plot in Fig. 3.23 the same tests for the faintest magnitude bin, $22.5 < r_{\rm P1} < 23.0$. The conservative SNR cuts in the faintest magnitude bin restrict the area of the

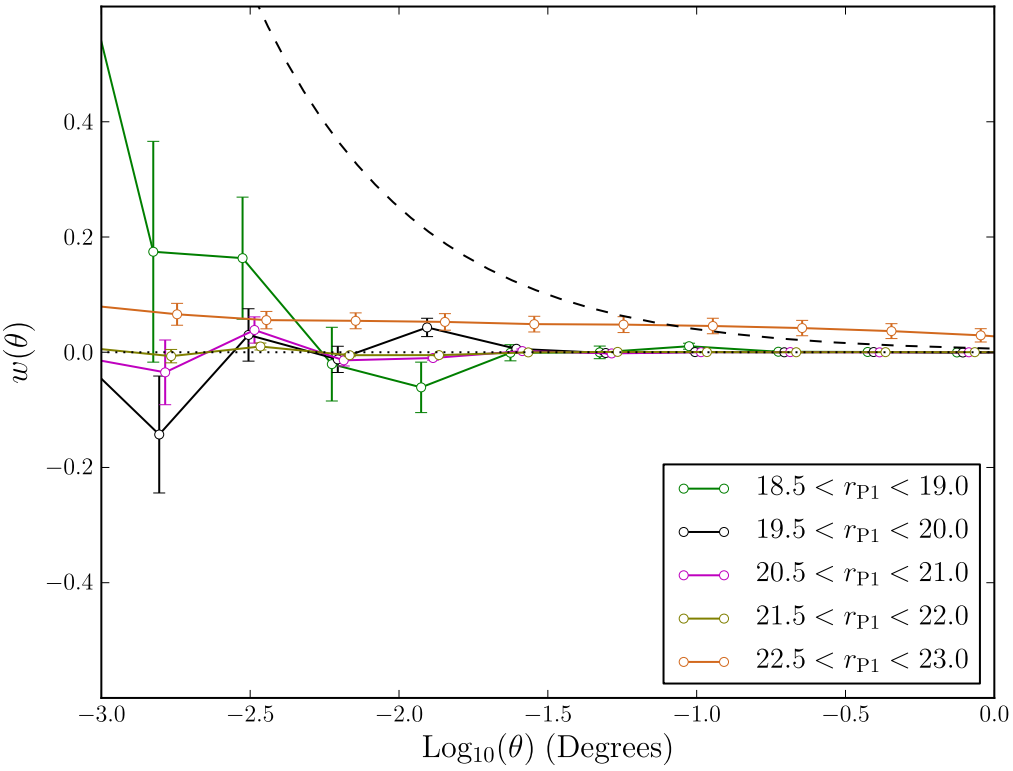

Figure 3.21: The angular correlation function of a random catalogue that has detection efficiency corrections applied to it, in effect measuring the clustering of the detection-weighted randoms relative to a uniform set of randoms. This gives an estimate of the clustering signal introduced into the data by the spatially varying depth. The clustering here is much weaker than the clustering of the galaxies, indeed for most magnitude bins there is no significant clustering. The faintest magnitude range shows a clear clustering signal, introduced by our modulation of the randoms to correct for spatially varying incompleteness. The dashed line is a reference power law added to all of our clustering plots, the dotted line marks no clustering.

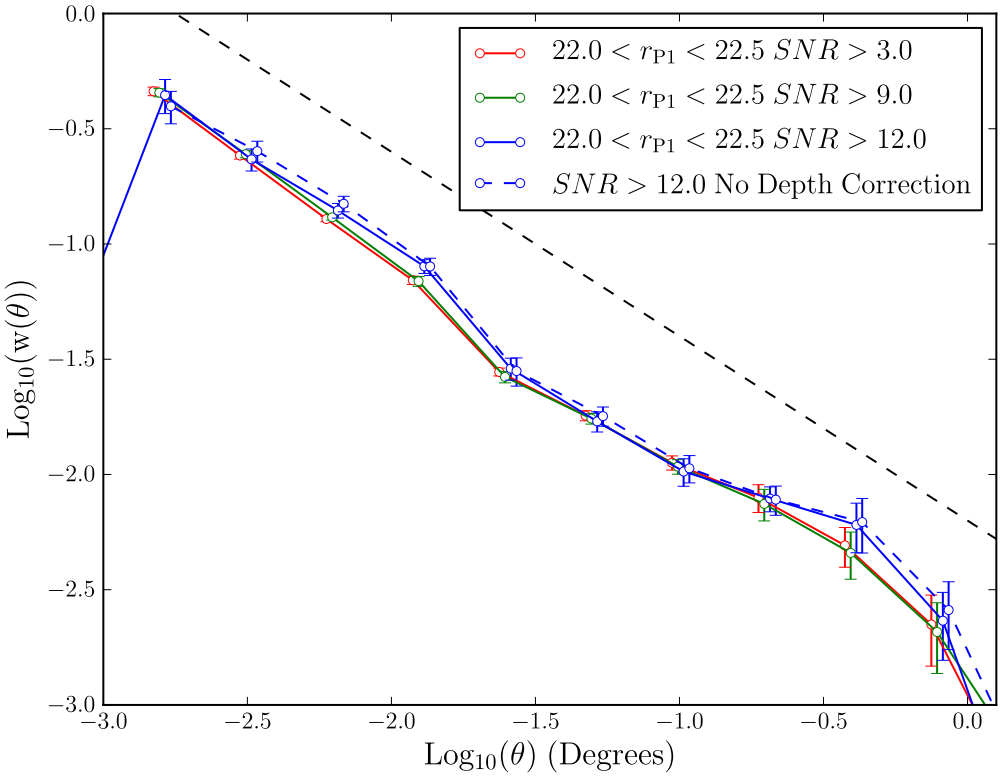

Figure 3.22: Angular clustering for $22.0 < r_{\rm P1} < 22.5$ galaxies in sub-areas satisfying different fiducial SNR cuts, as indicated in the key. We see that more conservative estimates of the clustering are in agreement with measures which use less deep data with a larger correction applied. For the brighter magnitude bin we also plot the clustering uncorrected for spatially varying depth from a region where the depth is fairly uniform. The points for the different curves have been artificially displaced along the x-axis for clearer viewing, the top curve in the legend shows the true x-axis position for all curves. The dashed grey line is a reference power law added to all of our clustering plots.

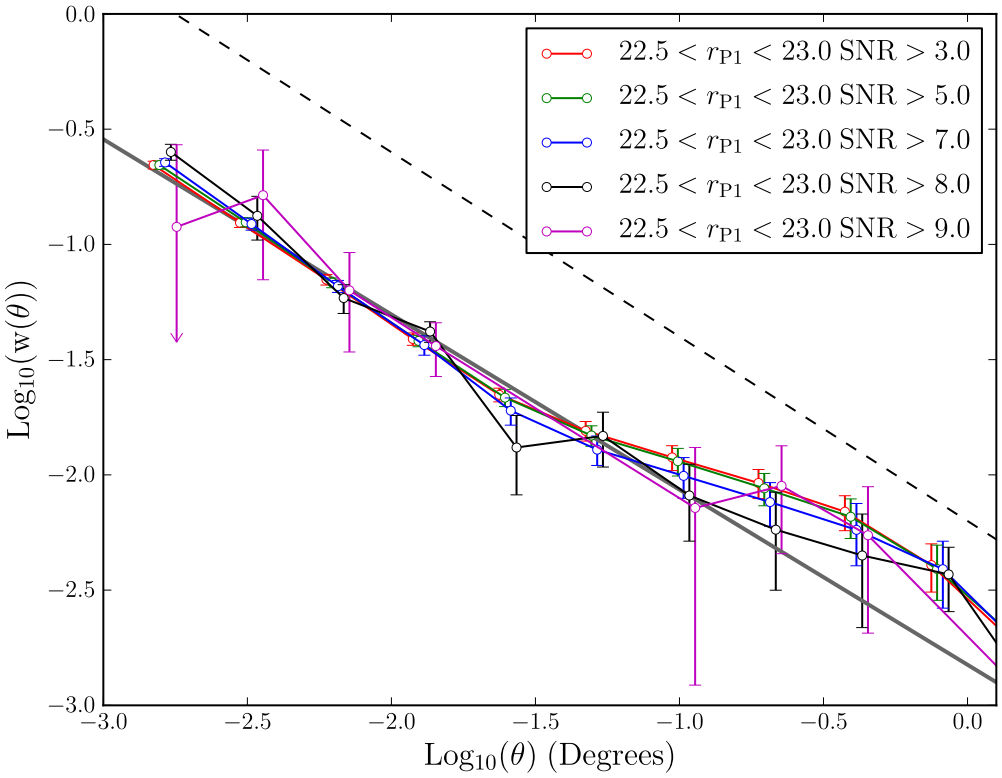

Figure 3.23: As in Fig. 3.22 but for $22.5 < r_{\rm P1} < 23.0$. The solid grey line is the power law we use to roughly estimate the effects of the integral constraint, which is necessary as the sub-areas in the faintest magnitude bin can be very small.

survey, and as such the integral constraint becomes important. We therefore correct clustering measurements in this plot for the integral constraint, using the power law fit plotted in grey. We do not show cuts more conservative than SNR > 9.0 as there are very little data beyond that cut in this magnitude range. Unfortunately the results of this test are less convincing, the different SNR cuts agree within error but there does appear to be a systematic trend for more conservative SNR cuts to measure a slightly weaker clustering signal on larger scales. This could suggest our correction is too small, though it could also be caused by other problems at very faint magnitudes such as false positives or stellar contamination. Remember that in this faintest magnitude bin our correction is extremely large and the data is very incomplete. Completeness is only around 50% at $r_{\rm P1} = 23.0$ (Paper I), so it is perhaps not surprising that the method is less successful in this regime.

In Fig. 3.24 we compare our measurements of clustering to those of Hudon & Lilly (1996), field "e" of Roche & Eales (1999) and Foucaud et al. (in preparation) for the magnitude range $19.0 < r_{\rm P1} < 23.0$. Note that the Roche & Eales (1999) sample is for $18.5 < R < 23.0$ measured in the Vega system, but despite these small differences it is still a useful comparison. The amplitudes of Hudon & Lilly (1996) and Roche & Eales (1999) have been corrected for stellar contamination using their estimate of the contamination fraction of $f = 0.29$ and $f = 0.11$ respectively. As introduced in Section 3.3.2 this correction involves boosting the amplitude by $(1 - f)^{-2}$ and is the same correction Hudon & Lilly (1996) and Roche & Eales (1999) apply to their own results. We estimate our contamination fraction, from the dashed red line in Fig. 3.9, to be $f = 0.07$ for this sample and we correct our amplitude accordingly. Foucaud et al. (in preparation) estimate their stellar contamination to be $f = 0.06$, so we also correct their clustering measurements.

In Fig. 3.24 we see our depth correction brings us closer to the other measurements of clustering. On smaller scales we show reasonable agreement with the literature measurements of Hudon & Lilly (1996) and Roche & Eales (1999). Across all scales we show a good agreement with the MD07 clustering measurements of Foucaud et al (in preparation). The scatter in the literature measurements is large due to the small sample sizes. As such, current available comparison data in the

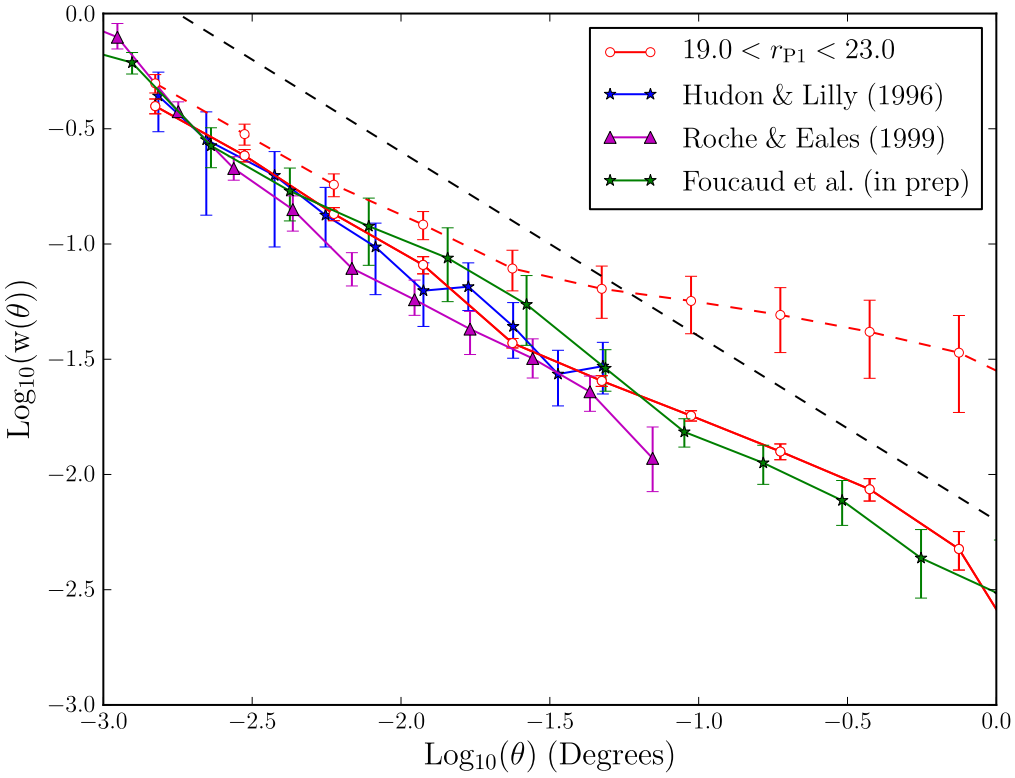

Figure 3.24: A comparison of our measurements (in red) to Hudon & Lilly (1996), Roche & Eales (1999) and the PS1 MD07 measurements of Foucaud et al (in preparation), before (dashed) and after (solid) our depth correction. The depth correction brings our results into closer agreement with the other measurements, which are from deeper and more uniform surveys than the PS1 SAS2 data. No attempt has been made to correct for the differences between the Hudon & Lilly (1996) or Roche & Eales (1999) R-band filters and our r_{P1}-band filter. Corrections for stellar contamination have been applied to all of the measurements. The dashed grey line is a reference power law added to all of our clustering plots.

r-band is limited by sample variance, restricting our ability to assess any remaining systematic errors. Our correction is very large for this sample, almost an order of magnitude on large scales; in practice, it is unlikely data with such a large correction will be used for science.

In Fig. 3.25 we show the angular correlation function measurements, using all the depth corrections described, down to $r_{\rm P1} = 22.5$ in 0.5 mag steps where we expect the clustering to still be reliable from Fig. 3.22. The angular clustering results from the whole of SDSS DR7 measured for Christodoulou et al. (2012), and measurements of the clustering of fainter galaxies from PS1 MD07 from Foucaud et al. (in preparation) are also shown. Again, our clustering measurements and those of Foucaud et al. (in preparation) have been corrected for stellar contamination.

The bright measurements are consistent within errors with the measurements made for Christodoulou et al. (2012). The fainter bins have power law shapes and lower amplitudes than the brighter bins, and agree with the MD07 measurements. Fig. 3.25 is a positive indication that PS1, combined with these depth corrections, can measure clustering to fainter magnitudes than existing wide field optical surveys.

3.5.3 Clustering of Stars and False Positives

As it is expected that some contamination of our galaxy sample will occur due to stars and false positives, we estimate their effect on clustering by measuring their correlation functions. We begin by looking at stars; Fig. 3.26 gives the clustering of objects classified as stars by our separator. We do not correct these objects for extinction in this plot, as it is unclear that this would be appropriate. We have so far assumed that stars are much less clustered than the galaxies, and so simply affect the amplitude of the galaxy clustering. The brighter stellar bins do indeed show a weaker signal than the galaxy samples, which is much less scale dependent than the galaxy clustering except on the largest scales.

Whilst we expect the clustering of stars to be weaker than that of the galaxies, we do not necessarily expect the stars to be unclustered. Stars appear in star clusters and gradients in stellar density exist due to the structure of the Milky Way. Measurements of the angular correlation function of stars have shown it to be flat

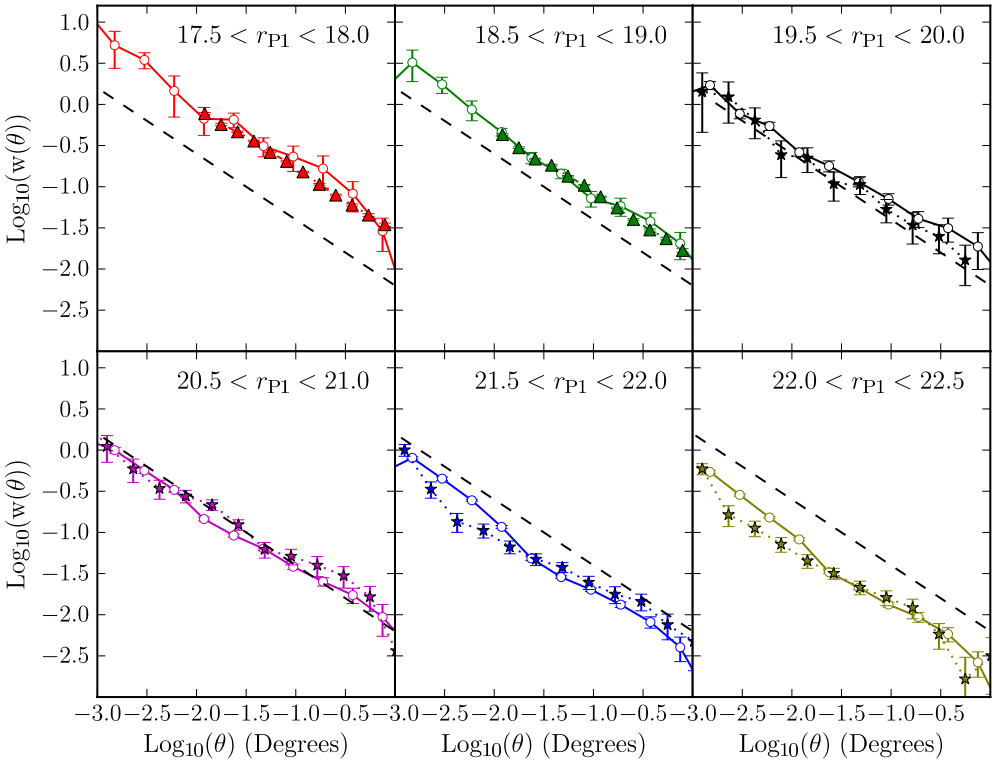

Figure 3.25: The lines and open points with error bars show the angular clustering of PS1 galaxies in the SAS2 region, for different magnitude ranges as indicated by the legend. Clustering measurements from Christodoulou et al. (2012). for similar magnitude ranges from the full area of SDSS DR7 are plotted as triangles. The stars with error bars are measurements of clustering from the MD07 fields for Foucaud et al. (in preparation). Error bars on our measurements are estimated with 9 jack-knife re-samplings. Our results and the Foucaud et al. (in preparation) have been corrected for stellar contamination. The Christodoulou et al. (2012) are assumed not to suffer from stellar contamination. The dashed line is a reference power law added to all of our clustering plots.

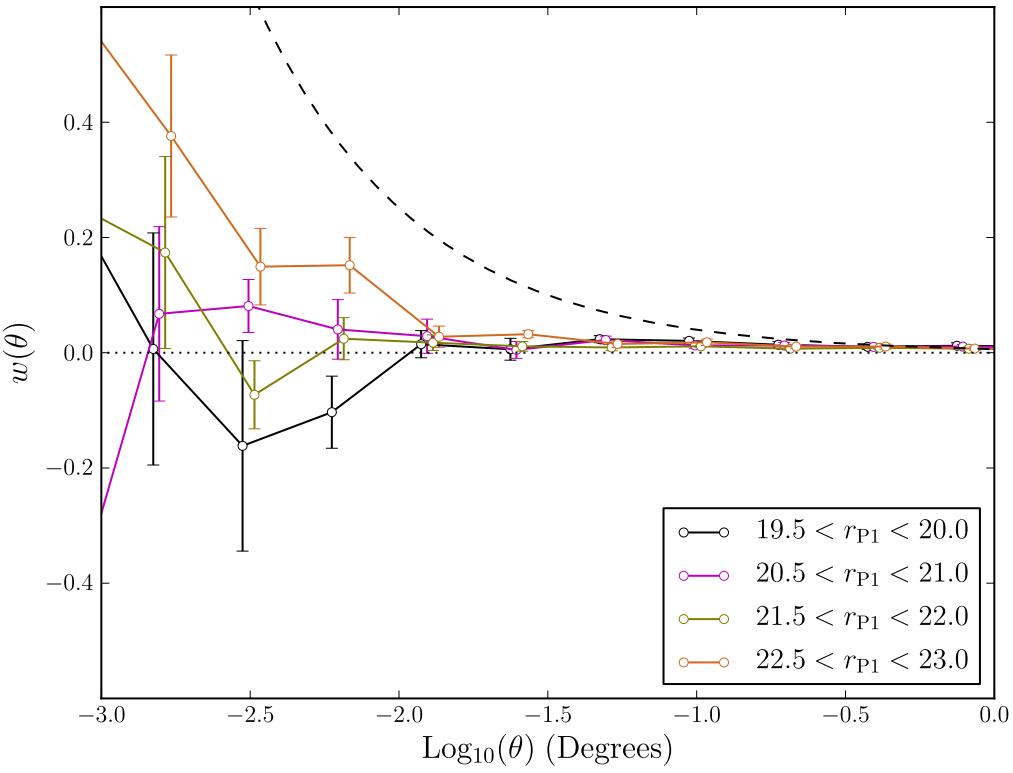

Figure 3.26: The angular correlation of objects classed as stars by our adopted star and galaxy separator, split by magnitude, as indicated by the key. The dashed line is a reference power law added to all of our clustering plots, the dotted line marks no clustering.

and non-zero on larger scales (e.g. Ross et al., 2011a; Myers et al., 2006). In Fig 3.27 we compare the clustering of galaxies in the range $22 < r_{\rm P1} < 22.5$ to that of stars. We detect clustering in the stars which is weaker than the galaxies on small scales but stronger than the galaxies on larger scales. As such, one could argue that the small scale clustering of stars is caused by contamination of the stellar sample by galaxies, whilst the large scale clustering of stars cannot be attributed to the galaxies. The clustering of stars in Fig 3.27 is fairly insensitive to detection efficiency corrections. In contrast, we find that extinction correcting the sample of stars enhances their clustering. This latter observation is concordant with the picture of stars having spatial density variations caused by the structure of the Milky Way. This is because one would expect dust to be correlated with the Milky Way's structure, and as such extinction correcting the stars would act to enhance spatial structure in the stellar sample. The enhancement of clustering signal after extinction correction is the opposite of what one would expect for galaxies. The flat angular correlation function we measure on larger scales for stars is in accord with the shape reported in the literature for brighter stellar samples (e.g. Ross et al., 2011a; Myers et al., 2006).

In Fig 3.28 we compare the clustering of a fainter sample of galaxies to that of stars. The clustering of stars in Fig 3.28 has a similar amplitude to that of the brighter stars in Fig. 3.27; the galaxy clustering is weaker however, such that the stars and galaxies have a similar amplitude of clustering on all scales. Again we do not believe the clustering in the star sample can be caused by galaxy contamination alone. This is because the clustering of galaxies in the stellar sample should be diluted by the stars in the sample and the resultant correlation function should have a lower amplitude than the galaxy sample. As in Fig 3.27, extinction correcting the stellar sample boosts its clustering, though the effect is smaller than for the brighter magnitude bin. Detection efficiency corrections also boost the clustering of the stellar sample in Fig 3.28. The likely cause of this is that the corrections are calibrated on galaxies which are harder to detect at these magnitudes, because they are extended. The combined effect of applying extinction corrections and detection efficiency corrections greatly boosts the clustering. This can be understood

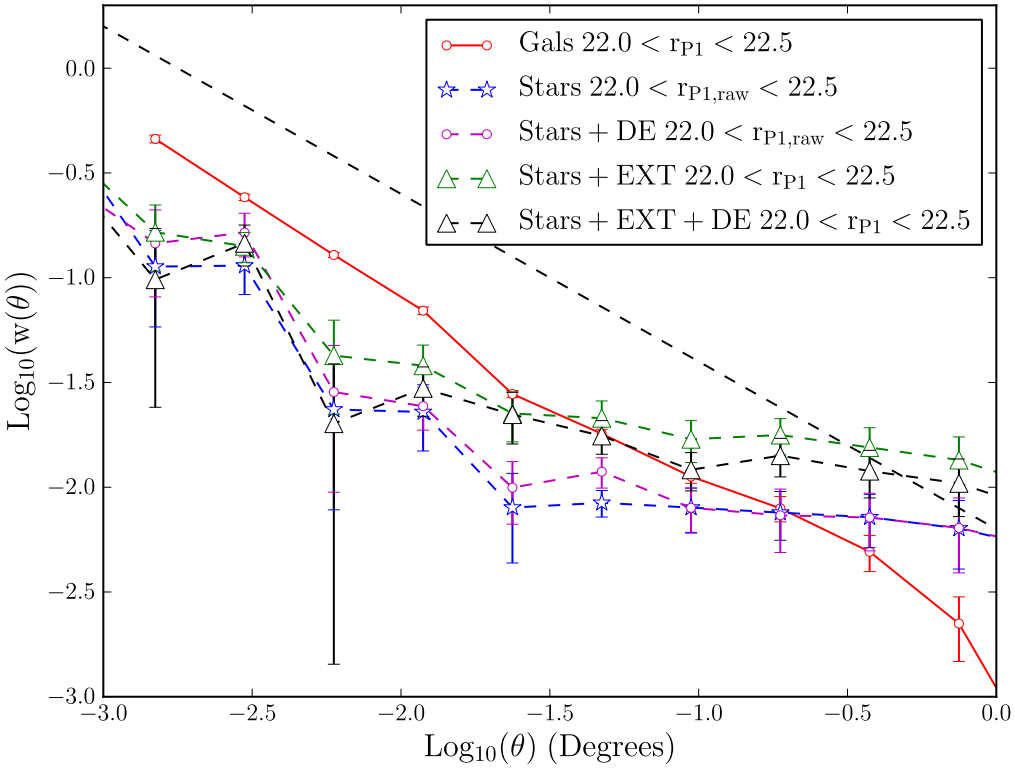

Figure 3.27: Measurements of the angular correlation function for the magnitude range indicated. Dashed lines show the clustering of objects classed as stars, for measurements with either extinction corrections (EXT), detection efficiency corrections (DE) or both (DE+EXT) applied as indicated in the legend. The solid line shows the clustering of galaxies, with detection efficiency corrections and extinction corrections applied. The straight, grey dashed line is the reference power law added to all of our clustering plots.

since their effect on the clustering will be compounded by the fact that extinction corrections bring objects with fainter observed magnitudes into the sample. These objects at fainter magnitudes have a larger detection efficiency correction and, since the detection efficiency corrections are based on galaxies, may artificially boost the stellar clustering further.

Clearly the clustering of stars and the effect of stellar contamination on galaxy clustering measurements will have to be further studied. For the full 3π survey measurements of the distribution of stars in the Milky Way could be used to attempt to model these effects. Cross correlating galaxy samples with stellar samples is also an important test we will carry out with the full 3π data, which will allow us to further study the effects of misclassification and stellar contamination. For this work, the clustering of stars and contamination of the galaxy sample could be boosting the estimates of the galaxy correlation function on large scales. This will be a larger effect for the fainter galaxy samples where the large scale clustering of stars has a higher amplitude than that of the galaxies and the stellar contamination fractions are larger. An expression relating the true angular correlation function of galaxies, $w_{\rm gg}$, to the measured correlation function, $w_{\rm measured}$, given the angular correlation function of stars, $w_{\rm ss}$, can be found in Myers et al. (2006),

$$w_{\rm measured}(\theta) = (1-f)^2 w_{\rm gg} + f^2 w_{\rm ss} - \epsilon(\theta) \tag{3.5.10}$$

where $\epsilon(\theta)$ is a very small cross term which is expected to be too small to influence our results. Eq. 3.5.10 was derived by Myers et al. (2006) for the Landy & Szalay (1993) estimator, but the Landy & Szalay (1993) gives very similar (much smaller than the error bars) results to the Hamilton (1993) estimator for our samples, so we can still use Eq. 3.5.10 to estimate the effect of stellar contamination. On small scales, where $w_{\rm ss} \ll w_{\rm gg}$, Eq. 3.5.10 reduces to the $(1-f)^2$ amplitude scaling we have used thus far. On larger scales and for fainter galaxy samples the star clustering can be stronger than the galaxy clustering. Using the measured clustering of the extinction and detection efficiency corrected star samples, which will be the clustering signal of stars mistakenly in the galaxy sample, we can estimate the effect of stars on the galaxy clustering. We do this by correcting the measured galaxy

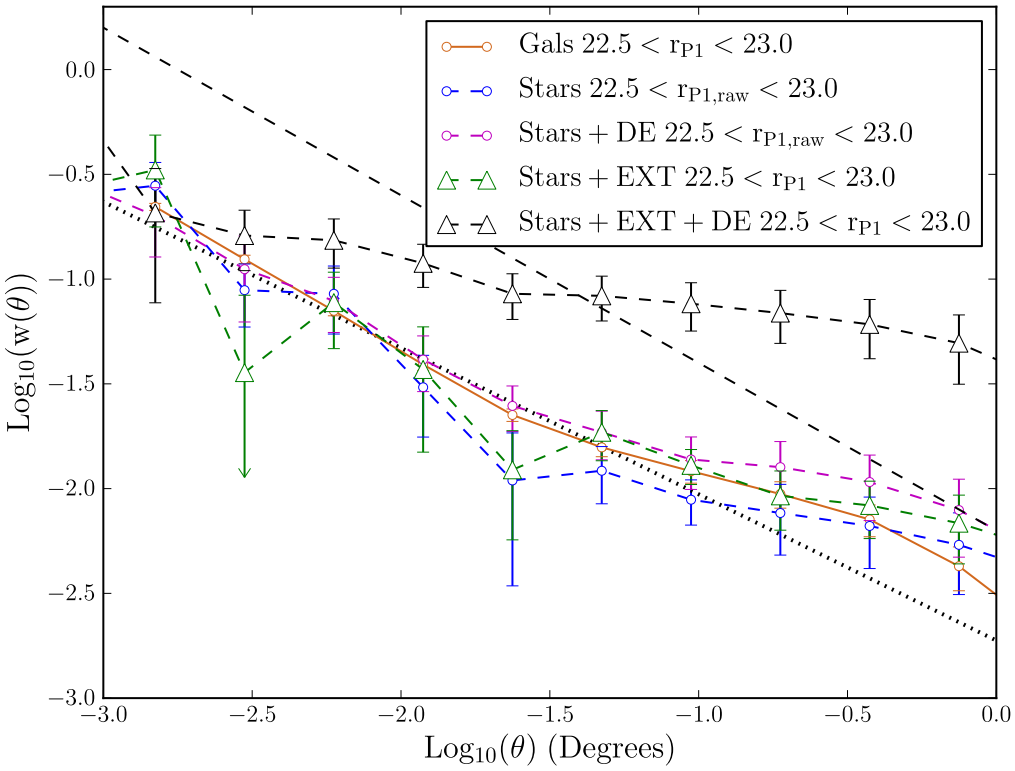

Figure 3.28: Measurements of the angular correlation function for the magnitude range indicated. Dashed lines show the clustering of objects classed as stars, for measurements with either extinction corrections (EXT), detection efficiency corrections (DE) or both (DE+EXT) applied as indicated in the legend. The solid line shows the clustering of galaxies, with detection efficiency corrections and extinction corrections applied. The dotted line gives the power law used to correct the clustering for the integral constraint. Extinction corrections and detection efficiency corrections combined greatly enhance the clustering, as the extinction correction results in a fainter apparent magnitude sample which receives greater detection efficiency corrections. These detection efficiency corrections enhance the clustering of stars as they are designed for galaxies, which are harder to detect.

clustering using Eq. 3.5.10 and comparing the result to using the simple $(1-f)^2$ correction we adopted. The faintest bin, $22.5 < r_{\rm P1} < 23.0$, has a contamination fraction of $f = 0.1$ (from Fig. 3.9) which leads to an enhancement of the galaxy clustering signal by clustered, stellar contaminants of 30% and 18% at 0.7 and 0.3 degrees respectively. For the brighter magnitude bin of $22.0 < r_{\rm P1} < 22.5$, with $f = 0.08$, this drops to 6% and 3% for 0.7 and 0.3 degrees respectively. All of these differences are smaller than the error bars, and as such adopting the $(1-f)^2$ for these data, instead of a more thorough modelling of stellar contamination, does not effect our conclusions. For the full 3π survey where clustering on larger spatial scales will be measured this issue will have to be revisited.

Fig. 3.29 gives the clustering of objects with extreme $\Delta_{\rm kron-psf}$, removed by our cut in Fig. 3.7, split into three magnitude bins. These objects are thought to be false positives. We see that, unfortunately, these objects have a strong clustering signal. This signal is well described by a power law that is steeper than the galaxy correlation functions. This is presumably because false positives tend to appear in clumps around image artifacts (see Paper I). Fortunately, for magnitude bins brighter than $r_{\rm P1} = 21.0$, false positives make up less than 1% of the data (Fig. 3.6) and are likely to have a negligable effect on clustering. For the fainter bins shown here, $r_{\rm P1} > 21.0$, clustering could be affected by the false positives which can be as prevalent as $8-10$% of the sources. Remember that Fig. 3.29 is measured from objects removed by our cut; false positives that evade this cut and so contaminate the galaxy sample could have different clustering. As we do not know if the false positives which evade our extreme $\Delta_{\rm kron-psf}$ have the same clustering as the objects in Fig. 3.29, Eq. 3.5.10 cannot be used to estimate their effect on clustering.

Improvements in the modelling of image artifacts will help ameliorate the problem of clustered false positives. Additionally, requiring detections in multiple bands can also be effective in eliminating false positives.

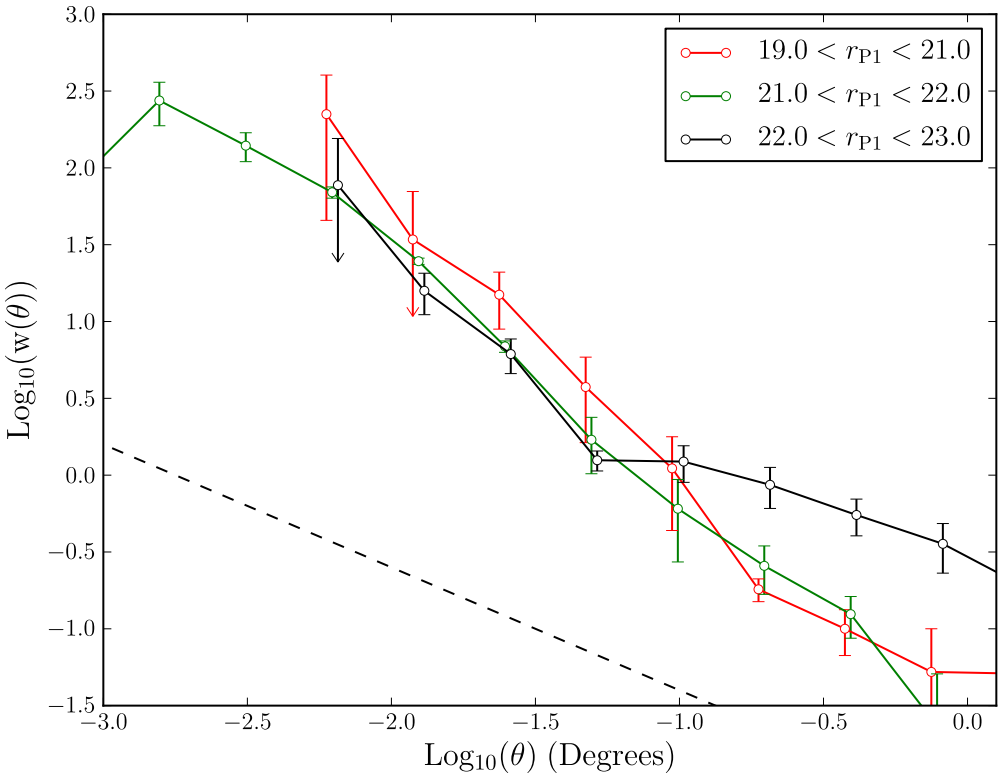

Figure 3.29: The angular correlation of objects cut by the extreme Kron minus PSF magnitude threshold given in Table 3.1, split by magnitude (see key). These objects are mostly false positives. Bins where one or more of the jack-knife regions have undefined clustering measurements, due to zero data-random or random-random pairs at that separation, have been omitted. The dashed line is a reference power law added to all of our clustering plots.

3.6 Discussion and Conclusions

We have presented methods of star and galaxy separation, angular masking and completeness corrections for PS1. Our star and galaxy separation approach uses fake images to identify cuts in $\Delta_{\mathrm{kron-psf}}$ that yield galaxy samples. Tests show our chosen separator is 91%-98% complete with less than around 10% stellar contamination down to a magnitude of $r_{\mathrm{P1}} < 23.0$. However, SAS2 has uniform properties, so before applying this to the full 3π data we need to test and calibrate the star/galaxy separator for different seeing and background noise. It is likely that the galaxy distribution in $\Delta_{\mathrm{kron-psf}}$ will depend on seeing. Changing the PSF of an image has a different effect on the surface brightness of stars and galaxies and this will drive a change in a galaxy's measured PSF magnitude. Ultimately a more sophisticated star and galaxy separator with better completeness and less contamination will need to be developed. Using the colours of galaxies (e.g Saglia et al., 2012) and other morphological measurements, such as galaxy size, are promising avenues to achieve this with PS1 data.

We present a method of generating angular masks for PS1 3π data, using a statistical approach to define the size of masked regions around bright stars. The relation between mask size and magnitude may vary across the much larger 3π field and as such the relation may need to be re-calibrated on the full data. We also present our binned-up variance maps, which we have used to develop a method of correcting PS1 measurements for spatially varying depth. A question left to address is what binning scale to choose for masks and maps of the whole survey. One has to balance accuracy with the computational costs of using large amounts of data. Ultimately the mask size will also depend on the science goals; BAO measurements for example will be less sensitive to small scale systematics than galaxy formation studies using small scale clustering.

Some further questions related to our depth corrections will have to be addressed in future work. Firstly, we need to test how well our SNR technique applies across a larger field with more variable PSFs and depths. One way to calibrate and test our method for the full survey would be to utilise the 10 PS1 Medium Deep fields, which are scattered across the sky. Using surveys in addition to Stripe 82, such as

the Medium Deep surveys, can also help remove the effects of false positives from our measurements of the probability of detection versus fiducial SNR. Additionally, our assumption that all galaxies have the same detection efficiency properties will have to be further explored, perhaps by studying clustering as a function of colour. Our comparisons of detection efficiency for red and blue Stripe 82 galaxies are a positive indication that this is a valid assumption. We can also gain more insight into our depth correction method by utilising our synthetic images to simulate more greatly varying PSFs and backgrounds.

One important test of our method is to exclude regions which fail to meet some SNR requirement and testing if clustering measurements from them agree with data with a less conservative cut. This test was demonstrated in Fig. 3.22 for SAS2 data but will have to be applied to the full 3π data. The application of this test to the full 3π data may be more fruitful as the much larger area will decrease the random errors on the measurement and make any systematics more apparent. Ultimately this SNR cut can be used as a free parameter in our method, which can be varied to ensure science results are not sensitive to its value.

By applying our methods to the SAS2 science verification data we show that measurements of clustering show reasonable agreement with literature data down to a magnitude of $r_{\rm P1} < 23.0$, though tests using regions with different fiducial SNR limits suggest perhaps a limit of $r_{\rm P1} < 22.5$ is more reliable. These limits may change as the PS1 survey matures. At bright magnitudes we show agreement with the published angular correlation function estimates of Christodoulou et al. (2012) and Wang et al. (2013), fainter than this our measurements show the decrease in amplitude expected. Our measurements agree with the measurements of Hudon & Lilly (1996), Roche & Eales (1999) and with Foucaud et al. (in preparation) for the threshold sample $r_{\rm P1} < 23.0$. Our magnitude bin samples also agree within error with Foucaud et al. (in preparation) down to a limit of $r_{\rm P1} < 22.5$. We also demonstrate our method yields sensible measurements of the number counts of galaxies, with $r_{\rm P1}$-band counts showing agreement with published data.

One difficulty with the literature comparisons is the relative deficit of faint r-band clustering measurements, especially from fields large enough to test the scales

where our correction is strongest. Future work will be able to further test our depth correction technique in several ways. Firstly, the extension of this work to different bands will allow a larger number of literature comparisons to be made. Additionally, combining the data across multiple bands will allow us to test the depth correction technique with more complex selection criteria, such as colour. Finally, using the full 3π data will greatly decrease the random errors in the SAS2 measurements, making systematics more apparent.

Clustered false positives are a potential limitation to measuring clustering, but these only affect the fainter magnitude bins and this problem should be improved by future efforts in understanding the instrumental signature of the PS1 camera. Additionally, matching between bands, which will be necessary for photometric redshifts, will go a long way in removing these false positives as image defects are very unlikely to be located in the same place in multiple bands.

Further issues not fully resolved in this work, but which will still have to be considered when utilising the full survey, also include how extinction corrections and stellar contamination affect the measured clustering signal. We have seen, for example, that stars have a larger clustering signal than galaxies on large scales. Issues such as these are common to many large galaxy surveys and there are approaches in the literature to deal with them (e.g. Myers et al., 2006; Ross et al., 2012; Wang et al., 2013).

We intend to apply these methods to the full survey, which is due to be completed by around January 2014, with data reduction complete by mid 2014 (Magnier et al. in preparation). If the techniques developed here are successfully applied, the PS1 3π survey will be able to push forward our understanding of cosmology and galaxy formation. One particularly exciting application will be to measure the Integrated Sachs-Wolfe effect by cross correlating PS1 galaxies with CMB data. The large area of 3π will be ideal for minimizing sample variance and false positives will be less of an issue as they are not likely to be correlated with the CMB.

Chapter 4

Projected Galaxy Clustering in GAMA

4.1 Introduction

We will now move on to measuring galaxy correlation functions with GAMA, which benefits from spectrocopic redshifts and a more mature calibration status. As introduced in Chapter 1, the two-point autocorrelation function of galaxies and its dependence on galaxy properties is well established, at low redshifts, by large area spectroscopic surveys such as SDSS (York et al., 2000) and 2dFRGS (Colless et al., 2001). The amplitude of the autocorrelation function of galaxies is seen to be strongly dependent on luminosity, stellar mass and colour. At low redshifts, brighter, redder and more massive galaxies have been observed to be more strongly clustered (e.g. Norberg et al., 2001, 2002; Li et al., 2006; Zehavi et al., 2011; Christodoulou et al., 2012).

In the higher redshift Universe, small ($< 1\text{deg.}^2$) but deep spectroscopic surveys have also measured the clustering of galaxies. The DEEP2 survey has been used to demonstrate that the colour dependence of galaxy clustering is already in place at $z \sim 1$, whilst within a red or blue sample of galaxies, clustering is insensitive to luminosity over the range $20.2 < M_B < 21.8$ (Coil et al., 2008). Compared with lower redshift SDSS data, the DEEP2 measurements of the clustering of brighter and more massive galaxies has a larger amplitude than expected from scaling the low

redshift measurements using linear theory (Coil et al., 2008; Li et al., 2012). This can be interpreted as evidence of significant bias evolution for these galaxies (Coil et al., 2008; Li et al., 2012). Another example of a small area, deep spectroscopic survey is the VIMOS-VLT Deep Survey (VVDS), which found a sharp increase in the amplitude of galaxy clustering around the characteristic magnitude of the sample's luminosity function, M_* (Pollo et al., 2006). VVDS also found, in agreement with DEEP2, that the clustering of massive galaxies, with stellar mass $> 10^{10.5}h^2\mathrm{M}_\odot$, at $z \sim 1$ can only be reconciled with lower redshift measurements if their bias evolves significantly (Meneux et al., 2008). More recent results from another small area, deep survey, zCOSMOS, show that this is true for galaxies more massive than $> 10^{10}h^2\mathrm{M}_\odot$ (Meneux et al., 2009). More recently, the VIPERS survey has found more luminous and more massive galaxies are more clustered at redshifts of $0.5 < z < 1.1$ than their fainter, less massive counterparts (de la Torre et al., 2013; Marulli et al., 2013).

The GAMA spectroscopic survey offers a new window onto the clustering of galaxies and its evolution with redshift. It is much larger than the smaller, deep surveys (180 deg^2) but has spectra of much fainter galaxies than large area surveys like SDSS. As such it complements both types of survey, by enabling clustering measurements at an intermediate epoch. In this chapter we study the projected two-point correlation function of galaxies as a function of their luminosity, stellar mass and colour, in three different redshift bins, in order to fully appreciate any redshift evolution. We compare our results to the semi-analytic galaxy formation model of Bower et al. (2006). This chapter is organised as follows. Section 4.2 introduces the GAMA data and the galaxy formation model we use, along with details of how we calculate luminosity, mass and rest-frame colour. Section 4.3 presents our method of generating a random catalogue and measuring clustering. In Section 4.4 we present our results, before discussing them and concluding in Section 4.5.

4.2 Data and theory

4.2.1 The Galaxy and Mass Assembly survey

The GAMA survey is a spectroscopic and multi-wavelength survey of galaxies carried out on the Anglo-Australian telescope (Driver et al., 2011). In this work we utilise GAMA-II NGP data, which consists of a highly complete ($> 98\%$) spectral catalogue of galaxies selected from the SDSS DR7 (Abazajian et al., 2009) to have $r_{\rm petro} < 19.8$. Details of the GAMA-I target selection are given in Baldry et al. (2010). Briefly, objects were targeted for spectroscopy based on the difference between their model and PSF magnitudes in SDSS DR7 data (i.e. similar to our separator in Chapter 3) and, where UKIDSS photometry is available, the object's optical and infrared colours. The data are split over three 12×5 deg^2 fields centered at 9^h (G09), 12^h (G12) and 14.5^h (G15) R.A. and approximately $\delta = 0$ degrees declination.

GAMA combines data from a large number of ground and space based telescopes and so has a very wide wavelength range, from X-ray to radio. In this work we use optical photometry from SDSS DR7 imaging data. To define luminosity samples we use SDSS Petrosian magnitudes (Petrosian, 1976), as the GAMA selection used Petrosian magnitudes. To define colours, and when estimating stellar mass, we use SDSS model magnitudes as these are often more suitable for colour terms (see the SDSS DR7 photometry webpage). We take all of the magnitude measurements from the GAMA Data Management Unit (DMU) TilingCatv40.

Redshifts for GAMA objects were measured as described in Driver et al. (2011), but we will briefly review the method here. For each object a redshift is automatically assigned using the software runz, before the spectra and runz fit are inspected manually. The astronomer assigns a subjective quality flag to the redshift assigned by the software. A large fraction of the galaxies were inspected multiple times, in order to assess the accuracy of each astronomer to produce a less subjective quality assessment for each galaxy: the normalised quality flag, nQ. We use a cut of $nQ \geq 3$ for this work, which corresponds to a probability of $>95\%$ that the redshift is correct (Driver et al., 2011). We use redshifts corrected to the CMB restframe from the DMU DistancesFramesv10.

In addition to the redshift quality cut, $nQ \leq 3$, we also only consider galaxies in regions with completeness greater than 75% using the GAMA angular completeness mask (Driver et al., 2011). We additionally only select objects with VIS_CLASS= 0, VIS_CLASS= 1 or VIS_CLASS= 255, which removes objects which upon visual inspection do not show any evidence of galaxy light or appear to be part of another galaxy (Baldry et al., 2010).

4.2.2 k-corrections and evolution corrections

The measured apparent magnitudes, m, need to be transformed to absolute magnitudes, M. As we look at galaxies at different redshifts using the same telescope filter, we look at different parts of each galaxy's rest-frame spectral energy distribution (SED). To correct for this, what is known as a k-correction is used, $k(z)$. The k-correction is reference redshift and filter specific. The luminosity of galaxies also evolves with time, and so in order to have a comparative sample of galaxies across different redshifts a correction for this is also often adopted. To compute absolute magnitudes we use the expression

$$M = m - k(z) + Q(z - z_{\rm ref}) - 5\log_{10}(D_L(z)) - 25 \tag{4.2.1}$$

where Q is the luminosity evolution parameter, D_L the luminosity distance in Mpc $\rm h^{-1}$ (see Chapter 1) and $z_{\rm ref}$ is a reference redshift, for which we adopt $z_{\rm ref} = 0.0$. Loveday et al. (2012) have fit evolving luminosity functions (i.e. with Q non-zero) to the GAMA-I data, which is a shallower version of the GAMA-II data with a limit of $r_{\rm petro} < 19.4$ in G09 and G15. However, using the values of Loveday et al. (2012) might not be appropriate for these data, we therefore find the best-fitting value for Q in Section 4.3.3.

At this stage we will also introduce a parameterisation of evolution common to luminosity function studies. The P parameter (e.g. Loveday et al., 2012, and references therein) parameterises the density evolution of a population of galaxies via

$$\phi^*(z) = \phi^*(z = 0)10^{0.4Pz} \tag{4.2.2}$$

where $\phi^*(z)$ is the number density of galaxies at redshift z. We will revisit this parameter in Section 4.3.3.

The k-corrections we use are derived from the GAMA DMU KCORR_Z00V03, which was produced using the method set out in Loveday et al. (2012). The Loveday et al. (2012) k-corrections are found by using the code KCORRECT_V4_2 (Blanton & Roweis, 2007) to fit each galaxy's u, g, r, i, and z-band SDSS model magnitudes with SED templates[1]. For many applications the maximum redshift at which an object fulfils the selection criteria of the survey, $z_{\rm max}$, is needed. For this the k-correction as a function of redshift is needed for each galaxy. To enable fast computation, Loveday et al. (2012) fit a 4th order polynomial to the k-correction of each galaxy as a function of redshift. The rms difference between the KCORRECT estimates of k-correction and the polynomial fits to them is less than 0.01 magnitudes for all bands (Loveday et al., 2012). We further speed up the k-correction process by producing average polynomials for galaxies in seven, $(g-r)$ rest frame colour bins, hereafter labelled $(g-r)_0$. To decide which colour bin to assign a galaxy to, we still utilize the individual k-correction polynomials.

4.2.3 Mock catalogues

We compare our observations to a semi-analytic galaxy formation model called GALFORM; specifically, we use the Bower et al. (2006) version. This model simulates galaxy formation by populating dark matter haloes in the Millennium Simulation (Springel et al., 2005). Recall from Chapter 1 that the Millennium Simulation uses an N-body code, with 2160^3 particles, to trace the evolution of dark matter from high redshifts to the present epoch. The positions and velocities of particles in the simulation are output at 64 different epochs logarithmically spaced in expansion factor. These outputs are called snapshots. Dark matter haloes are identified in the snapshots; these haloes and how they merge is tracked snapshot-to-snapshot. One limitation of the Millennium Simulation is that its value of σ_8 (see Section 1.5), of

[1]Following SDSS conventions, we will label model magnitudes using the letter associated with the bandpass in which the magnitude was measured.

$\sigma_8 = 0.9$ is too large compared to the current best estimate of $\sigma_8 = 0.83 \pm 0.01$ (Planck Collaboration et al., 2013). This could lead to too many large dark matter structures in the simulation. The haloes are occupied by mock galaxies, using physically motivated prescriptions for star formation, gas cooling and supernova feedback dependent upon each halo's mass and merger history. More information on semi-analytic models is given in Chapter 1, as well as in the papers which set out the GALFORM model (Cole et al., 2000; Baugh et al., 2005; Bower et al., 2006; Lagos et al., 2011, 2012).

The output from the Bower et al. (2006) model was converted into a mock catalogue using the lightcone code of Merson et al. (2013). This code converts the output from galaxy formation models into a mock catalogue by including a mock galaxy in the catalogue at the position and epoch when it enters into an observer's lightcone, i.e. when the light from the galaxy reaches the observer. Between snapshots, the positions of the mock galaxies are interpolated; particular care is taken when interpolating satellite galaxies to ensure the true small scale clustering of the model is represented in the lightcone mock. Other galaxy properties are not interpolated, as the interpolated values would not be representative of the stochastic nature of star formation in the model (Merson et al., 2013). For the analysis of mock catalogues, a median k-correction is applied to each simulated galaxy in order to estimate its "observed" magnitude. This median k-correction was taken as the median k-correction for SDSS galaxies. Currently, 9 mocks have been produced using the model of Bower et al. (2006), more mocks using different GALFORM models are still under production. These mocks have already been successfully utilised in other GAMA projects. For example, Robotham et al. (2011) have used these mocks to test algorithms that identify groups of galaxies.

The luminosity function of the mocks has been adjusted by abundance matching to the GAMA-I luminosity function split by redshift. This removes differences in the definitions of magnitudes (e.g. total versus Petrosian). This also ensures a sample of mock galaxies with the correct number density and radial selection function as compared to the data. The mock galaxy catalogue is cut to $r_{\rm petro} < 19.8$.

To define luminosity samples from the mock catalogue we use the apparent mag-

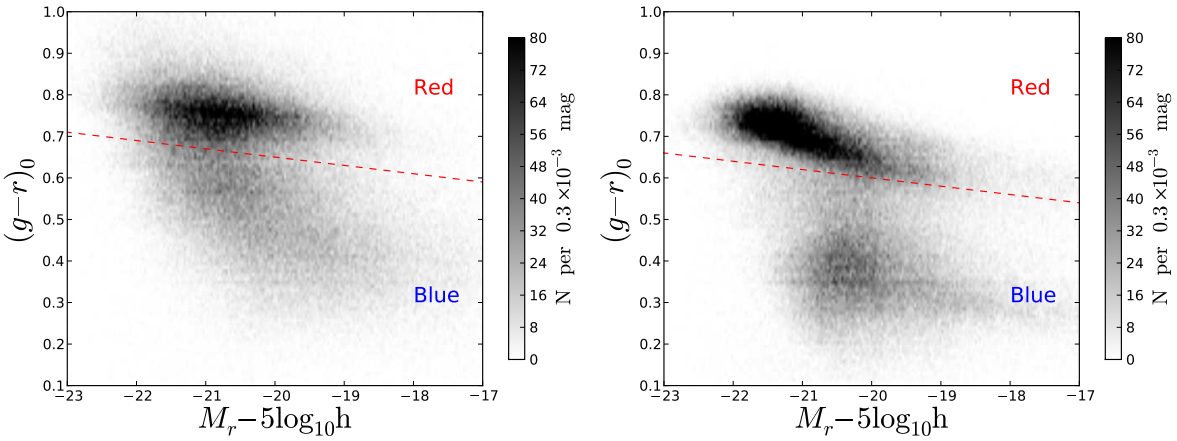

Figure 4.1: A restframe colour-magnitude diagram for the real GAMA galaxies (left) and for the mock galaxies (right). The red dashed line shows our cuts to define red and blue samples of galaxies.

nitudes defined above, converted to absolute magnitudes using Eq. 4.2.1. It is an interesting question as the whether the Q that best describes the mocks is the same as that of the data, we consider this in Section 4.3.3. Stellar mass and colour are both output by GALFORM and we use their values directly.

4.3 Methodology

4.3.1 Sample selection

We want to study the evolution of galaxy clustering with luminosity, mass, colour and redshift. One approach to do this is to use volume limited samples, which are characterised by a uniform detection probability across the survey volume. This is difficult to do for mass and colour, as there is not a direct relation between them and the Petrosian magnitude of a galaxy. Additionally, volume limited samples reduce the amount of data available for the analyses. We therefore do not use volume limited samples; instead we ensure the survey's radial selection function is properly dealt with by the random catalogue (see Section 4.3.2). We separate all of our mass, luminosity and colour samples into three redshift bins: low-z, $0.02 < z < 0.14$, intermediate-z, $0.14 < z < 0.24$ and high-z, $0.24 < z < 0.5$. These bins were

selected to have a roughly equal number of galaxies in each. The volumes of the low, medium and high redshift slices are 1.2×10^6 (Mpc/h)^3, 5.7×10^6 (Mpc/h)^3 and 4.3×10^7 (Mpc/h)^3 respectively. Luminosity samples are produced using Eq. 4.2.1 with the measured SDSS r-band DR7 Petrosian magnitude used to calculate the absolute magnitude in the r-band, M_r. In addition to luminosity samples, galaxies are divided into a red population and a blue population. The colour of a galaxy is often used as a rough proxy for the age of its stellar population, with galaxies undergoing star formation generally being expected to be bluer. It is therefore interesting to study how clustering differs as a function of colour. We use the colour cut of

$$(g-r) = -0.02(M_r - 5\log_{10}\mathrm{h}) + 0.25 \tag{4.3.3}$$

where $(g-r)$ is measured in the rest frame. A colour-magnitude plot, with this cut indicated in red, is shown in Fig. 4.1(left). With this cut 51% of galaxies are red and 49% are blue. In Fig. 4.1(right) we can see that the Bower et al. (2006) model reproduces the bimodality of galaxy colours, but arguably has a too well-defined blue cloud. The Bower et al. (2006) galaxies also have a clearer separation between the blue cloud and red sequence than the data. These findings are in accord with the Bower et al. (2006) comparisons of their model to data. To ensure we are looking at comparable samples of real galaxies and mock galaxies, we choose a colour cut on the mocks which results in the same red and blue fractions as in the real data, namely $(g-r) = -0.02M_r + 0.2$.

As well as luminosity and colour, we also want to use GAMA-II to measure clustering as a function of stellar mass. We use the relation between colour and stellar mass found for GAMA-I data by Taylor et al. (2011), namely

$$\log_{10}M_*/(\mathrm{M}_\odot h^{-2}) = 1.15 - 0.7(g-i) - 0.4(M_i - 5\log_{10}\mathrm{h}) \tag{4.3.4}$$

where M_i is the rest frame i-band absolute model magnitude and $(g-r)$ is, as before, measured in the rest frame. This relation was found by Taylor et al. (2011) from individual estimates of the stellar mass of GAMA-I galaxies. These individual estimates were produced from fitting stellar population synthesis models to the optical GAMA data; details are in Taylor et al. (2011). These mass estimates

should have a 1σ accuracy of around 0.1dex (Taylor et al., 2011).

Properties of our different samples are given in Table 4.1, 4.2 and 4.3. We see the median absolute magnitude of the low redshift red sample is a magnitude brighter than the blue sample; this difference decreases to 0.3 magnitudes in the high redshift sample. We also see that the more massive galaxies have brighter median magnitudes at all redshifts. Additionally, median redshifts in each sample tend to be slighter higher for brighter and more massive samples, while the more massive galaxies tend to be redder. The low and medium redshift ranges display a jump between typically blue $(g-r)$ colours to typically red $(g-r)$ colours between the lowest stellar mass and medium stellar mass samples. This information needs to be considered when trying to understand the clustering of different galaxy samples.

Comparing the number densities of the mock galaxy samples to those of the real data can tell us how successfully adjusting the magnitudes by abundance matching has been. It is also useful in indicating whether our results are sensitive to the mass estimates we adopt. Differences in the number density of mock and real galaxies in the same stellar mass range could be due to systematic differences in estimating mass, e.g. using the Taylor et al. (2011) relation versus using the GALFORM mass. Additionally, the number density of dark matter haloes can be related to the amplitude of their clustering (see Section 1.9 and references therein). If one expects that galaxy samples occupy dark matter haloes of a certain mass, then the number density of a sample of galaxies should relate to the amplitude of their clustering. Note that the quoted number density will be an underestimate of the true number density of samples which are incomplete. However, since the mock catalogue should have the same radial selection function of the data, the quoted real and mock galaxy number densities can be compared. In general the samples of mock galaxies have very similar number densities to those of the real galaxies, with the mock galaxy number density typically being a good match to that of the data, with a scatter of around 20%. This indicates one might expect the clustering of the mock galaxies to be a reasonable match to the amplitude of the real galaxy clustering.

In addition to the samples we have described, we also produce a sample with which to compare results to Zehavi et al. (2011). In order to make the comparison

Table 4.1: Different galaxy samples in the low redshift region ($0.02 < z < 0.14$), with their average number density, size and median properties.

Sample	$n\,(\mathrm{Mpc}/h)^3$	N_{gals}	$z_{\mathrm{med.}}$	$(M_r - 5\log_{10}\mathrm{h})_{\mathrm{med.}}$	$(\log_{10}M_*/(\mathrm{M}_\odot h^{-2}))_{\mathrm{med.}}$	$(g-r)_{0,\mathrm{med}}$
$-20.0 < M_r - 5\log_{10}h < -19.0$	2×10^{-2}	12030	0.11	-19.47	9.69	0.60
$-21.0 < M_r - 5\log_{10}h < -20.0$	6×10^{-3}	7262	0.12	-20.41	10.21	0.71
$-22.0 < M_r - 5\log_{10}h < -21.0$	2×10^{-3}	2048	0.12	-21.28	10.63	0.74
$8.5 < \log_{10}(M_*/(\mathrm{M}_\odot h^{-2})) < 9.5$	1×10^{-2}	18432	0.10	-18.50	9.07	0.44
$9.5 < \log_{10}(M_*/(\mathrm{M}_\odot h^{-2})) < 10.5$	1×10^{-2}	17271	0.11	-19.86	9.93	0.70
$10.5 < \log_{10}(M_*/(\mathrm{M}_\odot h^{-2})) < 11.5$	2×10^{-3}	2193	0.12	-21.25	10.65	0.76
Red	1×10^{-2}	15585	0.11	-19.73	9.99	0.73
Blue	2×10^{-2}	26276	0.10	-18.66	9.10	0.44

Table 4.2: Different galaxy samples in the medium redshift region ($0.14 < z < 0.24$), with their average number density, size and their median properties.

Sample	$n\,(\mathrm{Mpc}/h)^3$	N_{gals}	$z_{\mathrm{med.}}$	$(M_r - 5\log_{10}\mathrm{h})_{\mathrm{med.}}$	$(\log_{10}M_*/(\mathrm{M}_\odot h^{-2}))_{\mathrm{med.}}$	$(g-r)_{0,\mathrm{med}}$
$-20.0 < M_r - 5\log_{10}h < -19.0$	4×10^{-3}	23982	0.18	-19.64	9.71	0.57
$-21.0 < M_r - 5\log_{10}h < -20.0$	4×10^{-3}	25168	0.20	-20.41	10.20	0.70
$-22.0 < M_r - 5\log_{10}h < -21.0$	1×10^{-3}	7684	0.20	-21.30	10.64	0.74
$8.5 < \log_{10}(M_*/(\mathrm{M}_\odot h^{-2})) < 9.5$	1×10^{-3}	8459	0.17	-19.32	9.32	0.39
$9.5 < \log_{10}(M_*/(\mathrm{M}_\odot h^{-2})) < 10.5$	7×10^{-3}	42198	0.19	-20.11	10.04	0.67
$10.5 < \log_{10}(M_*/(\mathrm{M}_\odot h^{-2})) < 11.5$	2×10^{-3}	8572	0.20	-21.28	10.66	0.76
Red	5×10^{-3}	30493	0.19	-20.33	10.27	0.75
Blue	5×10^{-3}	28854	0.19	-19.89	9.72	0.50

Table 4.3: Different galaxy samples in the high redshift region ($0.24 < z < 0.5$), with their average number density, their size and their median properties.

Sample	$n\,(\mathrm{Mpc}/h)^3$	N_{gals}	$z_{\mathrm{med.}}$	$(M_r - 5\log_{10}\mathrm{h})_{\mathrm{med.}}$	$(\log_{10}M_*/(\mathrm{M}_\odot h^{-2}))_{\mathrm{med.}}$	$(g-r)_{0,\mathrm{med}}$
$-20.0 < M_r - 5\log_{10}h < -19.0$	1×10^{-5}	624	0.25	-19.93	9.60	0.37
$-21.0 < M_r - 5\log_{10}h < -20.0$	7×10^{-4}	31700	0.28	-20.65	10.30	0.65
$-22.0 < M_r - 5\log_{10}h < -21.0$	9×10^{-4}	38261	0.33	-21.42	10.71	0.72
$8.5 < \log_{10}(M_*/(\mathrm{M}_\odot h^{-2})) < 9.5$	1×10^{-5}	566	0.26	-20.06	9.41	0.28
$9.5 < \log_{10}(M_*/(\mathrm{M}_\odot h^{-2})) < 10.5$	8×10^{-4}	32304	0.28	-20.68	10.28	0.57
$10.5 < \log_{10}(M_*/(\mathrm{M}_\odot h^{-2})) < 11.5$	1×10^{-3}	44560	0.33	-21.49	10.76	0.75
Red	1×10^{-3}	44430	0.31	-21.27	10.72	0.77
Blue	8×10^{-4}	33535	0.30	-20.97	10.33	0.55

samples as similar as possible, we use magnitudes corrected to $z_{\rm ref} = 0.1$ and use the redshift cuts stipulated in Zehavi et al. (2011). Unfortunately, these redshifts cuts greatly restrict the volume of our survey. As such, only the Zehavi et al. (2011) magnitude bin sample of $-22.0 < M_r^{0.1} - 5\log_{10}h < -21.0$ has a large enough volume in GAMA-II for comparison.

4.3.2 Random catalogues

Recall from Chapter 3 that to measure clustering one needs a random set of points with the same radial and angular selection function as the data. We generate catalogues of random positions using the method set out in Cole (2011), which generates random catalogues from the real data in a way which is insensitive to large scale structure. For each galaxy in the catalogue the maximum volume of space over which it could be observed, $V_{\rm max}$, is calculated by finding $z_{\rm min}$ and $z_{\rm max}$, the redshift where a galaxy meets the bright and faint magnitude limits of GAMA-II. In order to account for density evolution, P, we artificially increase the volume as a function of redshift thus

$$V_{\rm max} = \int_{z_{\rm min}}^{z_{\rm max}} 10^{0.4Pz} \frac{{\rm d}V}{{\rm d}z} {\rm d}z. \tag{4.3.5}$$

It will become clear how this accounts for P later in this section. In addition to this, a density weighted maximum volume, $V_{\rm max,dc}$, is calculated as

$$V_{\rm max,dc} = \int_{z_{\rm min}}^{z_{\rm max}} \Delta(z) \frac{{\rm d}V}{{\rm d}z} {\rm d}z \tag{4.3.6}$$

where $\Delta(z)$ is the over-density as a function of redshift and dV/dz is the comoving volume element per redshift element. Given these volumes, every real galaxy in the catalogue is cloned n times, where n is given by

$$n = n_{\rm clones} \frac{V_{\rm max}}{V_{\rm max,dc}} \tag{4.3.7}$$

with $n_{\rm clones}$ being the total number of randoms you wish to produce divided by the number of galaxies in your sample. When cloning the galaxy, all of the intrinsic galaxy properties are also cloned, so that the random points have a stellar mass, an absolute magnitude and a colour. The cloned galaxies are randomly distributed

within the real galaxy's $V_{\rm max}$, with the GAMA angular mask used to ensure the angular selection function of the cloned galaxies matches that of the real galaxies.

This method requires the estimation of $\Delta(z)$, which is done using an iterative method. Initially it is assumed $\Delta(z) = 1$ everywhere such that each galaxy is cloned the same number of times. From this random catalogue, $\Delta(z)$ is estimated from the redshift distribution of the randoms, $n_{\rm r}(z)$, and the data, $n_{\rm g}(z)$, using

$$\Delta(z) = n_{\rm clones} \frac{n_{\rm g}(z)}{n_{\rm r}(z)} \,. \tag{4.3.8}$$

A new random catalogue is then produced with this new estimate of $\Delta(z)$, and the whole process repeated until $\Delta(z)$ converges. The redshift distributions and over-densities are measured in $\Delta z = 0.012$ bins; when solving Eq. 4.3.6 we use linear interpolation between these bins to allow much smaller bins, $\Delta z = 10^{-5}$, to be used for the numerical integration.

We show in Fig. 4.2(Top) the redshift distribution of the data and the randoms for different iterations of this process. We see that using the density-corrected maximum volume (green dashed line) only introduces subtle differences into the $n_{\rm r}(z)$ of the randoms, as compared to simply using $V_{\rm max}$ (red dashed line). The $n_{\rm r}(z)$ of the randoms seems like a good fit to the $n_{\rm g}(z)$ of the total sample; later we will check the random $n_{\rm r}(z)$ is appropriate for galaxies split into magnitude, colour and mass samples. In Fig. 4.2(Bottom) we plot the over-density estimate, Eq. 4.3.8, for successive iterations of our random catalogue generating method. As expected, the iterations act to slightly increase the over-density estimates, as the Cole (2011) method acts to remove their effect from the random catalogue. We can see from Fig. 4.2 that the random catalogue generating process has converged.

This method of generating randoms ameliorates the effects of large scale structure on the generation of a random catalogue, as over represented galaxies from over dense regions are cloned fewer times whilst under represented galaxies are cloned more times. Cole (2011) demonstrates how this scheme can produce a random catalogue unbiased by large scale structure. A strength of this approach to generating randoms is that the random catalogue comes with all of the properties of the galaxy catalogue. One can then apply the same selection to the random catalogues and the

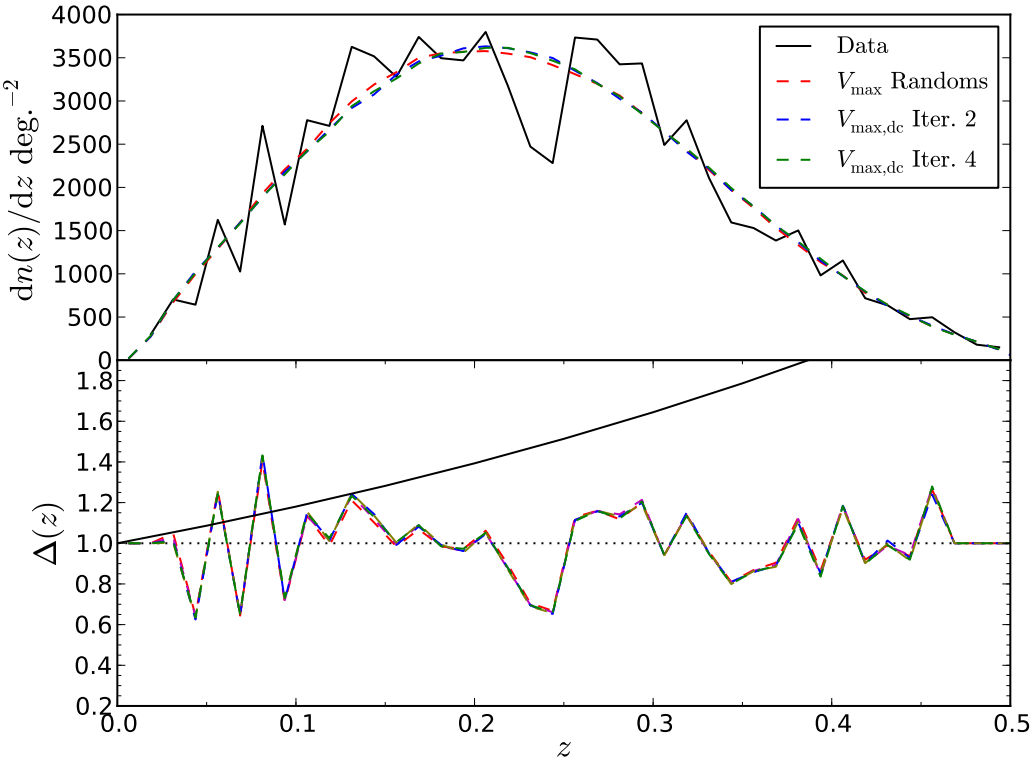

Figure 4.2: *(Top)* The redshift distribution of GAMA-II galaxies (solid) and our randoms (dashed) for multiple iterations of the Cole (2011) random catalogue generating approach, as explained in Section 4.3.2. The redshift distribution of the randoms is a good match to the data. *(Bottom)* Our estimates of the galaxy overdensity as a function of redshift, from the ratio of the galaxy and random redshift distributions. The solid, black line in the lower panel shows how the mean density increases with respect to $z = 0$, given a value of the density evolution parameter of $P = 1.6$, (i.e. it is $\phi^*(z)/\phi^*(z = 0)$).

galaxy catalogues so that the random catalogue has the correct angular and radial distribution.

4.3.3 Finding P and Q

With our random catalogues we can attempt to find the best values of the evolution parameters P and Q. Recall that the density evolution, P, affects the $n(z)$ of the randoms by modifying the size of the volume over which they are distributed, whilst the luminosity evolution, Q, modifies the random $n(z)$ by changing the $V_{\rm max}$ values of the galaxies (Section 4.3.2). To do this we create random catalogues for different values of Q and P on a grid with a spacing of 0.2 in Q and P. For each random catalogue we check to see if the inferred $\Delta(z)$ (see Fig. 4.2(Bottom)) is consistent with unity, within some estimate of the expected variance, σ^2_Δ. As galaxies are clustered, one needs to be careful when estimating this expected variance. Adapting the expression in Cole (2011) to our redshift bins gives

$$\sigma^2_\Delta(z) = \frac{1 + 4\pi J_3 \rho(z)}{\bar{n}_{\rm r}(z)} \tag{4.3.9}$$

where $J_3 = \int \xi(r) r^2 {\rm d}r$ (Peebles, 1980), $\bar{n}_{\rm r}(z) = n_{\rm r}(z)/n_{\rm clones}$ and $\rho(z)$ is the galaxy number density at z, predicted by dividing the $\bar{n}_r(z)$ with the volume in that redshift bin. The value $4\pi J_3 \rho(z)$ gives the typical number of galaxies in an over-density (Peebles, 1980); it is used here to account for how large scale structure can boost σ^2_Δ above Poisson noise (Cole, 2011). We estimate J_3 using a Zehavi et al. (2011) power law fit to their clustering measurements. We took their threshold sample $M_r^{0.1} < -21$, as a rough estimate of how GAMA galaxies should cluster. Zehavi et al. (2011) measure clustering out to around 12 Mpc h^{-1}, and it would be inappropriate to extrapolate their power law out to scales larger than this; we therefore use an upper limit of 12 Mpc h^{-1} when integrating the power law correlation function to find J_3. We find that $4\pi J_3 = 3900$ (Mpc/h)^3. We will show that our conclusions are insensitive to reasonable deviations from this value, caused, for example, by our choice of upper limit or by the clustering measurement we chose as a rough estimate of the GAMA galaxy clustering. From these estimates of variance, we find the χ^2

of the deviation of $\Delta(z)$ from unity, i.e.

$$\chi^2 = \sum_{z_i} \frac{(\Delta(z_i) - 1)^2}{\sigma^2_\Delta(z_i)}. \tag{4.3.10}$$

This in effect gives the χ^2 of the deviation of the data from the randoms, taking into account the expected variations due to large scale structure. Note that the χ^2 we estimate here ignores covariance between the redshift bins in the data, so is likely an underestimate. In Fig. 4.3 we plot the reduced χ^2 for randoms generated for the GAMA-II galaxies. We can see that the estimates of Q and P are very degenerate, with a diagonal feature within which the randoms are a statistically equally good fit. Our definition of a good fit is a little loose here, as our reduced χ^2 values do not account for covariance in the data and we only have a rough estimate of J_3. Nonetheless it is clear that a diagonal region of Q and P values is favoured for these data. This degeneracy was also seen by Cole (2011), when testing a conceptually similar method to the one presented here. We could simply adopt a fiducial value for P or Q and use Fig. 4.3 to pick an appropriate value for the other parameter. This would yield a random $n_\mathrm{r}(z)$ which would be a good fit to the data. However, the value of Q we adopt affects our estimates of magnitude, so finding the best value of Q is important. In the absence of a method to break the P and Q degeneracy, we adopt the (Loveday et al., 2012) values of $Q = 0.7$ and $P = 1.8$. These values were found by fitting the GAMA-I data set, as such they may not be the correct values for the deeper GAMA-II data. However, we also see these values fall in the low reduced χ^2 region, as indicated by the star in Fig. 4.3. We also need to generate a random catalogue for the mock catalogue. The luminosity function of the mock catalogues has been adjusted to match that of the data as a function of redshift, so we might expect the redshift distribution to be the very similar. However, it is less clear whether the same values of P and Q will be appropriate, as the luminosity of the mock galaxies may vary differently with redshift. We therefore repeated our method of constraining P and Q on the mock catalogues. We plot the results in Fig. 4.4. We once again see a strong degeneracy between P and Q. The value we adopted for the data does not seem to be the best fit to the mock catalogue; we must therefore choose better values. We choose to keep the same value of Q, such

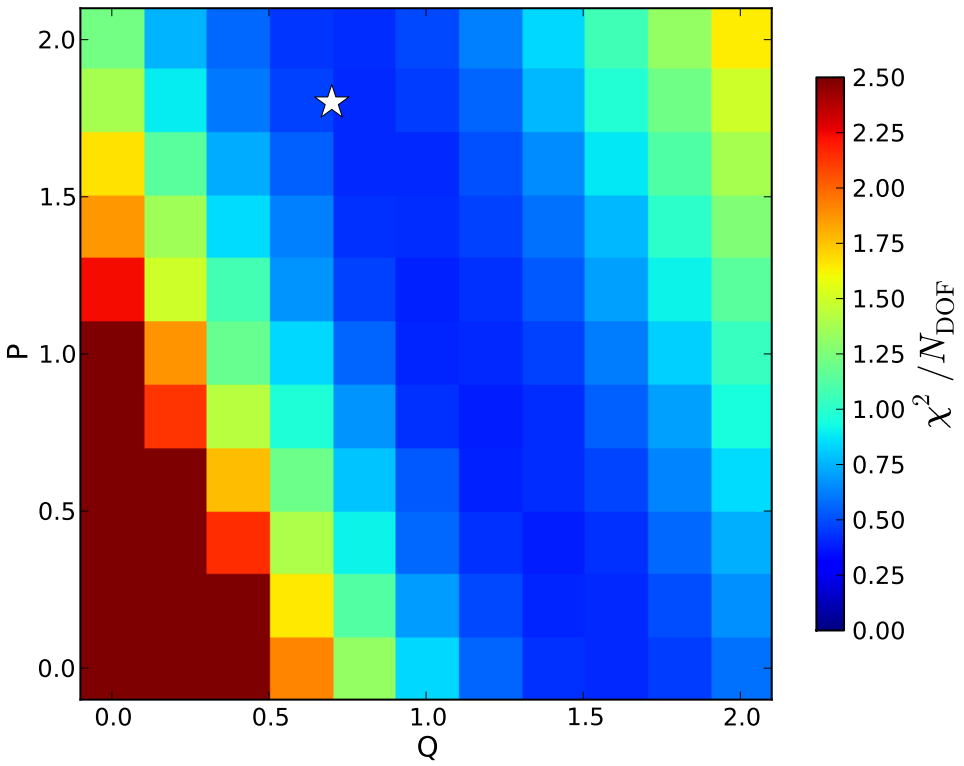

Figure 4.3: The reduced χ^2 of the random catalogue $n_{\rm r}(z)$, given the data. The star indicates the Loveday et al. (2012) value of P and Q for GAMA-I data. The χ^2 we estimated here ignores covariance between the redshift bins in the data, so is likely an underestimate. Nonetheless, we can still see a clear degeneracy between Q and P.

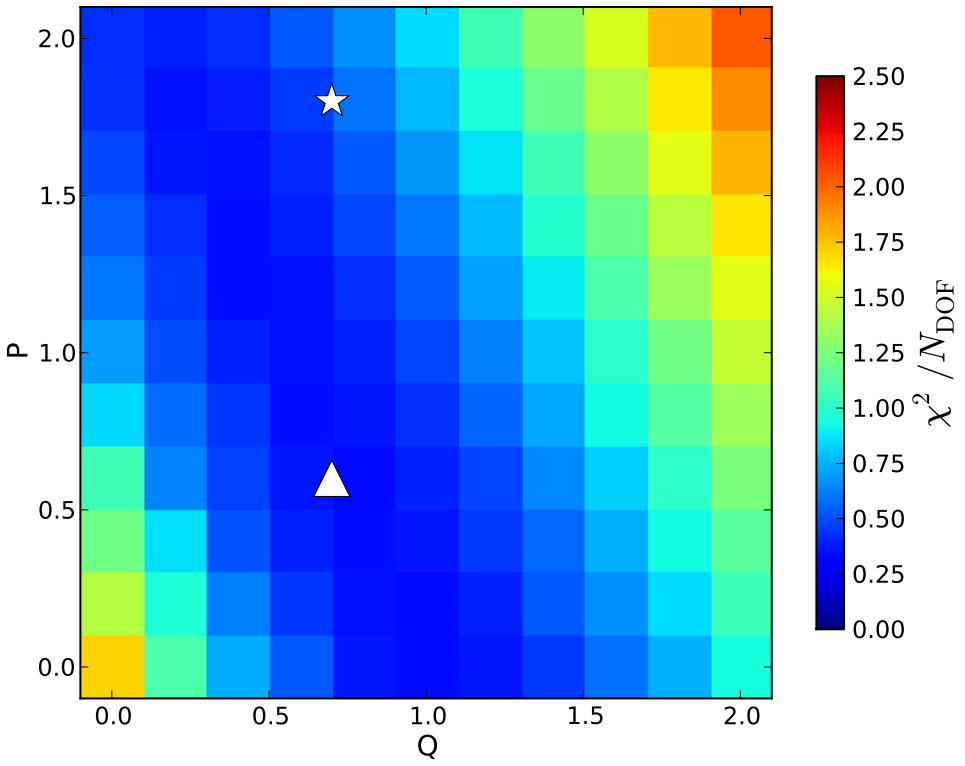

Figure 4.4: The reduced χ^2 of the random catalogue $n_{\rm r}(z)$, given the mock. The star indicates the Loveday et al. (2012) value of P and Q for GAMA-I data. The triangle indicates the Q and P adopted to produce randoms for the mock catalogue. The χ^2 we estimated here ignores covariance in the data, so is likely an underestimate.

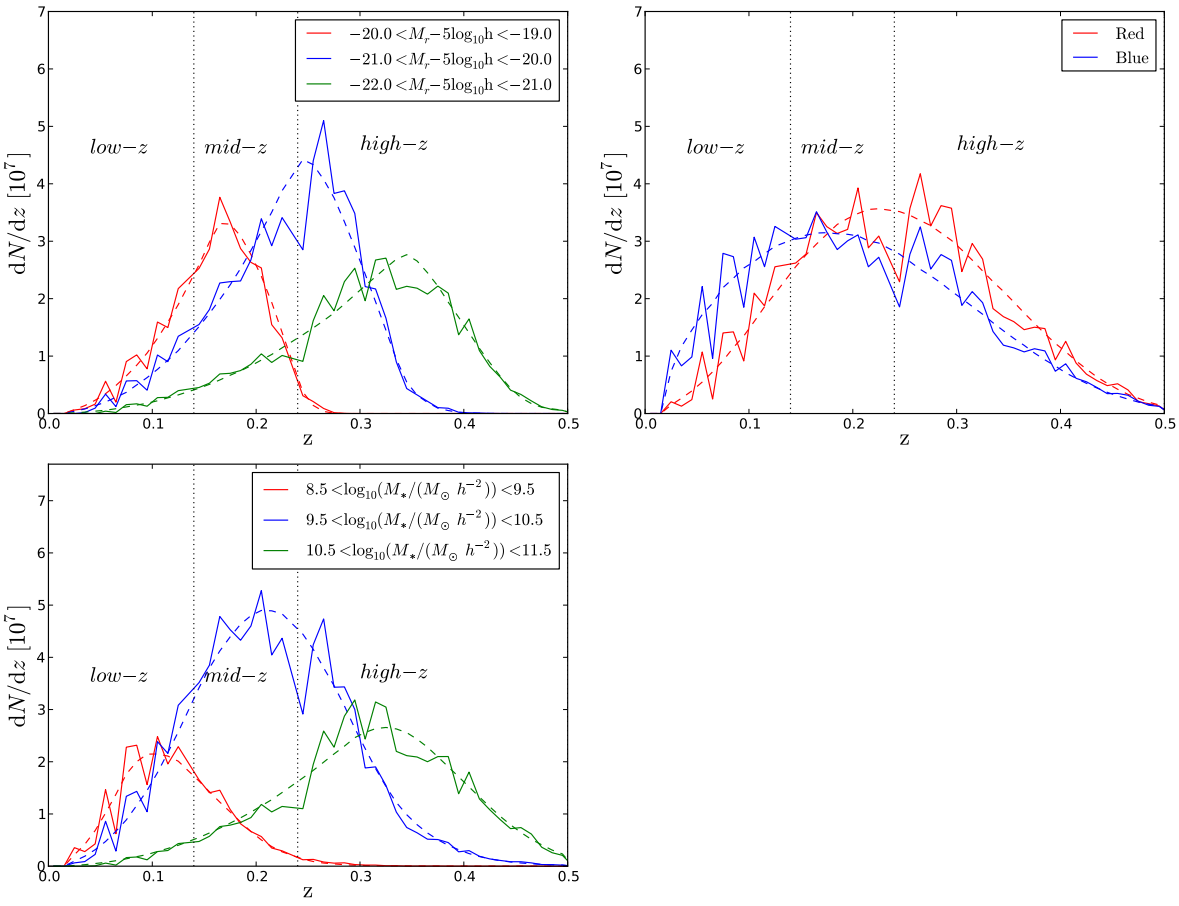

Figure 4.5: The redshift distribution of the data (solid lines) compared to the redshift distribution of the randoms (dashed lines), for different samples as indicated in the legend. Vertical dotted lines mark the positions of our redshift cuts. The randoms provide an excellent fit to the data.

that the magnitudes between mock and real galaxies are consistent, and use a lower value of $P = 0.6$.

In Fig. 4.5 and Fig. 4.6 we show the redshift distribution of randoms and data, for the real catalogue and mock catalogue respectively. We see for the luminosity, mass and colour samples we study, the random redshift distribution is an excellent fit to the data. Interestingly, the red and blue galaxies have a similar $n(z)$ in both the mocks and the data. This suggests using the same luminosity evolution parameter for them has not biased our results. It also means the integrals of their luminosity functions up to the detection limit must be similar across the redshift range we study.

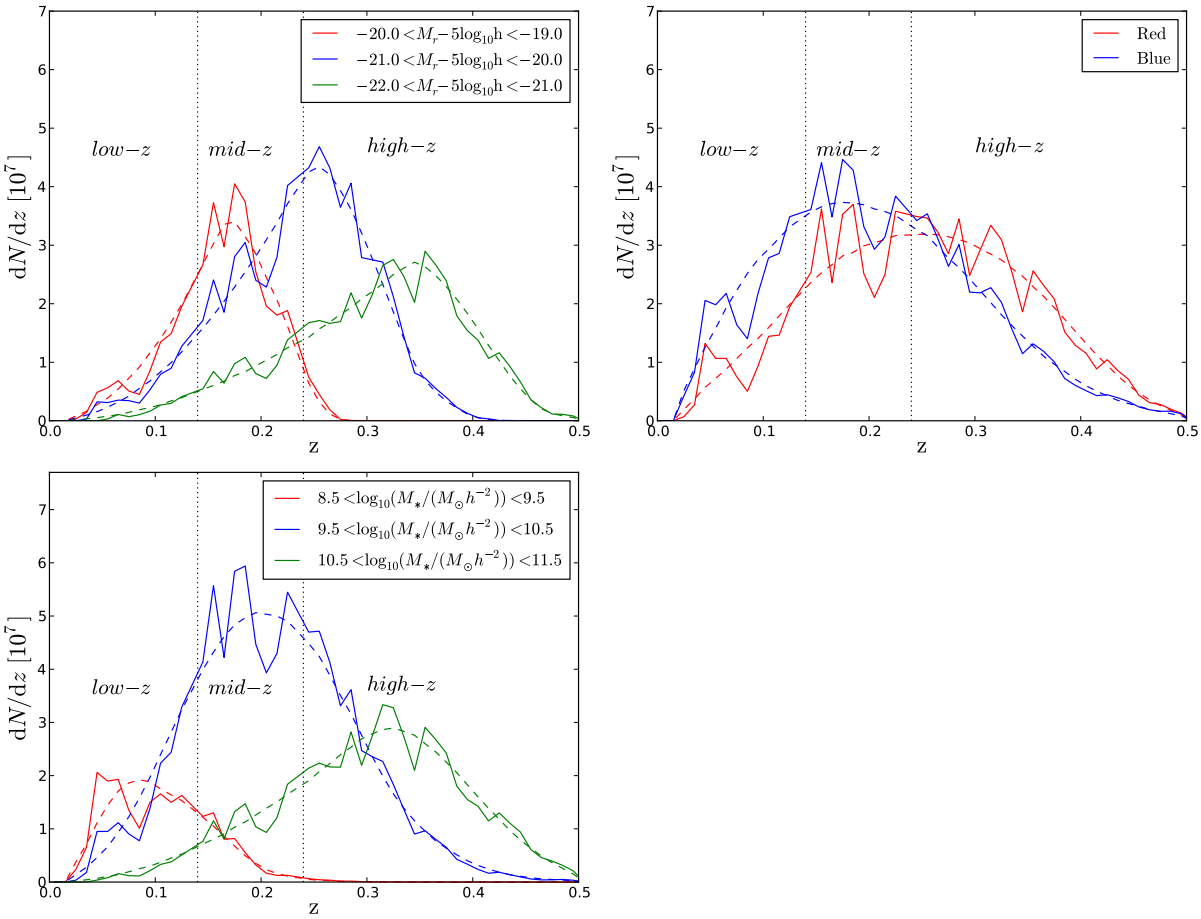

Figure 4.6: The redshift distribution of the mock catalogue (solid lines) compared to the redshift distribution of the randoms (dashed lines), for different samples as indicated in the legend. Vertical dotted lines mark the positions of our redshift cuts. The randoms provide an excellent fit to the mock data.

For the Zehavi et al. (2011) comparison sample we choose a luminosity evolution that is as close as possible to the luminosity evolution adopted for that paper. We find that $Q = 1.6$ gives a good approximation to the complicated polynomial luminosity evolution Zehavi et al. (2011) adopted. For this luminosity evolution we adopt $z_{\rm ref} = 0.1$. For the redshift range we study the difference between our $Q = 1.6$ luminosity evolution and the Zehavi et al. (2011) polynomial luminosity evolution is less than 0.05 magnitudes. We use a value of $P = 0.0$ with this value of Q, as this is required to still be in the best fitting region in Fig. 4.3.

4.3.4 Projected clustering

We measure the 2-point correlation function of galaxies in 2D using pairs of galaxies and randoms with the Landy & Szalay (1993) estimator. Following the standard approach adopted in the literature (e.g. Coil et al., 2008) we measure pair separations parallel, π, and transverse, r_P, to the line of sight for each pair. These are computed by first converting the angular position and redshift of each object to a vector, $\mathbf{r}$. We then define a line of sight direction to a pair as $\mathbf{l} = 0.5(\mathbf{r_1} + \mathbf{r_2})$, where $\mathbf{r_1}$ and $\mathbf{r_2}$ are the positions of the two pair members. The parallel to the line of sight distance, π, is the projection of the separation, $\mathbf{s} = \mathbf{r_2} - \mathbf{r_1}$, onto the line of sight

$$\pi = \frac{\mathbf{s} \cdot \mathbf{l}}{|\mathbf{l}|}. \tag{4.3.11}$$

The separation transverse to the line of sight is then

$$r_p = \sqrt{|s|^2 - \pi^2}. \tag{4.3.12}$$

Pairs are binned onto a grid of π and r_p. In order to maximise SNR we use a mixed linear and logarithmic binning scheme. At small separations, where it is expected that there is a large amount of clustering signal, the binning is linear with a bin size of 0.5 Mpc h^{-1}. At a scale of 2.5 Mpc h^{-1}, in π and r_p, logarithmic binning is adopted, with a bin size of 1.2 dex, so that the bin size grows for larger separations, where there is a weaker clustering signal. We use $n_{\rm sets}$ times more randoms than data. Tests of our choice of binning and $n_{\rm sets}$ are shown in Section 4.3.5.

Fig. 4.7 gives an example of 2D correlation functions of galaxies, $\xi(r_p, \pi)$, as measured from our red and blue galaxy samples. It is well known that this measured

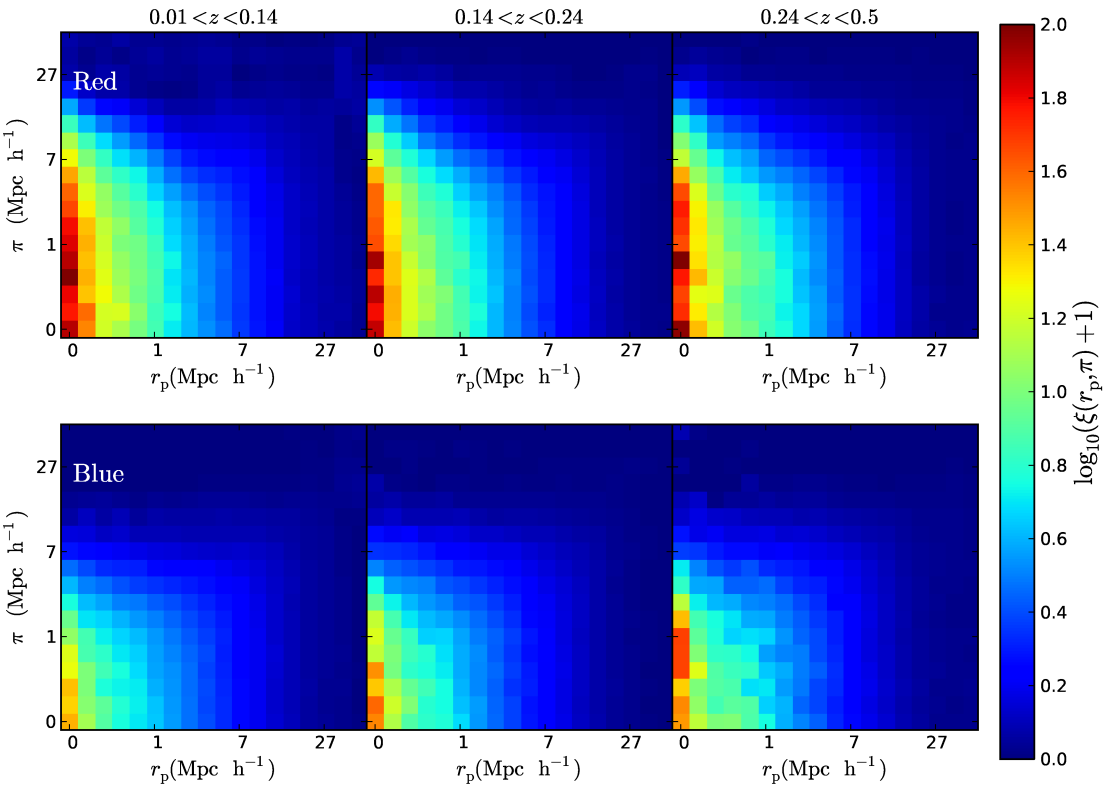

Figure 4.7: The 2-point correlation function of red (top row) and blue (bottom row) galaxies, for the redshift slices indicated. The elongation of the correlation function on small scales, caused by redshift space distortions, can be seen more clearly in the red sample, as one might expect since these galaxies tend to be in clusters.

correlation function is distorted by the peculiar velocities of galaxies. On larger scales the infall of galaxies squash the observed correlation function in the line of sight direction (Kaiser, 1987). On small scales the virial motions of galaxies within clusters can elongate the correlation function along the line of sight (Jackson, 1972). This elongation can be seen in the red galaxy samples of Fig. 4.7. These distortions have been studied in the GAMA data by Christodoulou & et al. (2013) and Blake et al. (2013); in this work we focus instead on the projected correlation function, $w_p(r_p)$. The projected correlation function is a standard approach to dealing with redshift space distortions, which involves integrating $\xi(r_p, \pi)$ along the π direction to minimize their effects, thus

$$w_p(r_p) = 2 \int_0^{\pi_{\rm max}} \xi(r_p, \pi) {\rm d}\pi. \tag{4.3.13}$$

In practice this integral is carried out numerically using our $\xi(r_p, \pi)$ grid. The choice of $\pi_{\rm max}$ warrants careful consideration. Ideally, one would use the largest possible value of $\pi_{\rm max}$ as it includes the most amount of the 2D clustering signal, and because theoretically the effects of redshift space distortions are only removed if you integrate out to infinity. Unfortunately, in real surveys noise affects the measurements, and measurements for large values of $\pi_{\rm max}$ can be particularly noisy. We decide on a value of $\pi_{\rm max}$ in Section 4.3.5.

The results of Eq. 4.3.13, with $\pi_{\rm max} = \infty$, can be calculated analytically for a circularly symmetric power law correlation function, $\xi(r_p) = (r_p/r_0)^\gamma$, where r_0 and γ are constants. The result is

$$w_p(r_{\rm p}) = r_p \left(\frac{r_0}{r_{\rm p}}\right)^\gamma \frac{\Gamma(1/2)\Gamma((\gamma-1)/2)}{\Gamma(\gamma/2)} \tag{4.3.14}$$

where Γ is the Gamma function. We will fit Eq. 4.3.14 to some of our samples in Section 4.5 in order to measure r_0.

To compute error bars on our clustering measurements, 27 jack-knife samples (e.g. Norberg et al., 2009), 9 per region, are formed by rejecting roughly equal area regions of data. When plotting clustering, we often include a reference power law line or divide through by this reference power law, $w_{\rm ref}$, to allow easier comparison between plots. We use the Zehavi et al. (2011) power law fit to their $-21.0 < M_r^{0.1} - 5{\rm log}_{10}h < -20.0$ sample, $r_0 = 5.33$ Mpc h^{-1} and $\gamma = 1.81$, for this purpose.

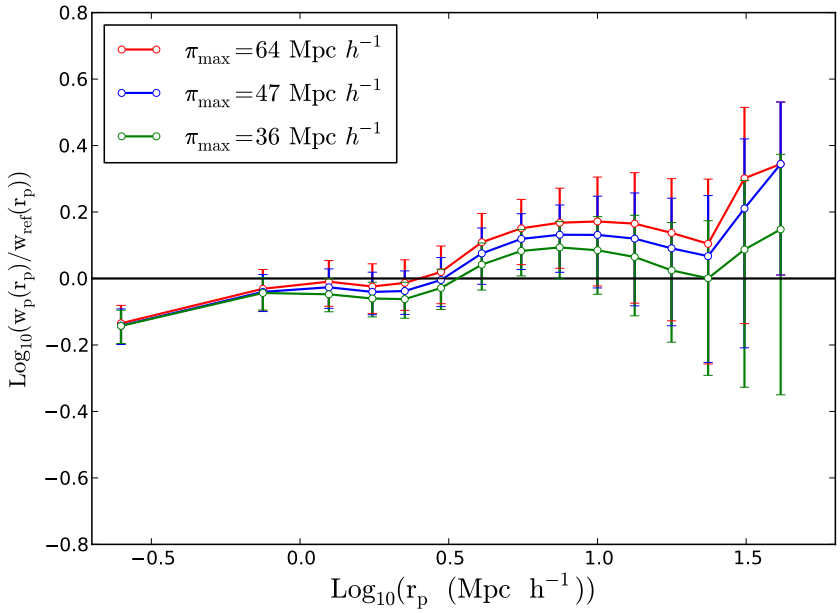

Figure 4.8: The projected two point correlation function of our low redshift, $-20 < M_r - 5\log_{10}h < -19$ galaxy sample, for different values of $\pi_{\rm max}$, as indicated in the legend. Adjacent measurements have been offset by 0.01 dex along the x-axis, with the highest $\pi_{\rm max}$ in its original position. The measurements are divided by the reference power law defined in Section 4.3.4.

4.3.5 Integration tests

In this section we determine suitable values for $n_{\rm sets}$ and $\pi_{\rm max}$, as well as testing if our results are sensitive to the binning we adopted for the 2D correlation function.

We tested different values of $n_{\rm sets}$, using the Zehavi et al. (2011) comparison sample as it is the smallest we consider, so most convenient for computing correlation functions with large values of $n_{\rm sets}$. We found that the clustering results for $n_{\rm sets} = 30$ and $n_{\rm sets} = 16$ were almost identical, with differences being far smaller than the size of the error bars. The $n_{\rm sets} = 8$ measurements had a larger error for the smallest separation of $r_{\rm p} = 0.25$ Mpc h^{-1}. We therefore adopt a value of $n_{\rm sets} = 16$.

In addition we tested different values of $\pi_{\rm max}$ using our $-20 < M_r - 5\log_{10}h < -19$ low redshift sample, the results are shown in Fig. 4.8. This small volume sample is likely to suffer from the largest amount of sample variance, as it has few pairs it

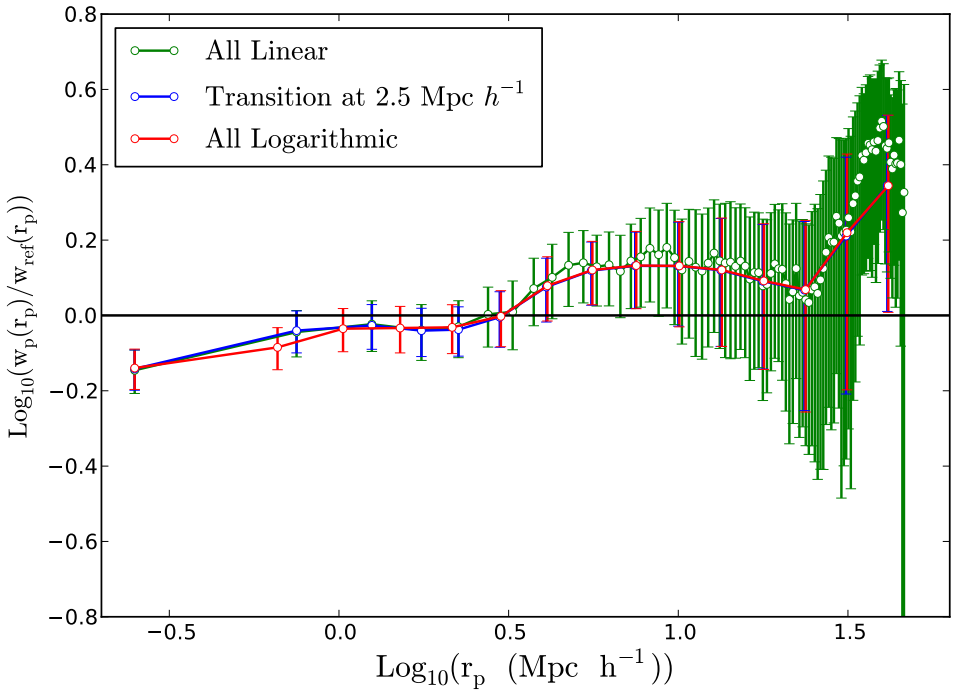

Figure 4.9: The projected two point correlation function of our low redshift, $-20 < M_r - 5\log_{10}h < -19$ galaxy sample, for different approaches to binning the 2D correlation function, as indicated in the legend. Adjacent measurements have been offset by 0.01 dex along the x-axis, with the linear binning line in its original position. The measurements are divided by the reference power law defined in Section 4.3.4.

is also likely to be noisy. Clustering measurements in this section are divided by the reference power law defined in Section 4.3.4, in order to allow easier comparison of the results. We see as we increase π_{max} the correlation function rises on larger scales. However, this is an effect much smaller than the error bars. We adopt a limit of $\pi_{\mathrm{max}} = 47$ Mpc h^{-1}, as using larger values has little effect on the results. We also tested different approaches to binning the 2D correlation function. We tried entirely linear, entirely logarithmic binning and binning which swaps from linear to logarithmic at 2.5 Mpc h^{-1}. As previously, we used our low redshift, $-20 < M_r - 5\log_{10}h < -19$ sample for these tests. In Fig. 4.9 we see no evidence of any systematic differences between the different binning methods. We therefore adopt the mixed binning scheme, as it appears to be slightly less noisy than pure

linear binning

Carrying out these tests on small and noisy samples can be troublesome, as the random errors could mask any small systematics. Work to test our integration on larger samples, which will take longer, is ongoing.

4.4 Results

4.4.1 Comparison to literature results

In this section we compare our measurements to those of Zehavi et al. (2011), which come from the SDSS. This comparison acts as a test that our methods for k-correcting galaxies, producing randoms and measuring clustering give reasonable results. We can also use the large area of the SDSS to gauge if the GAMA-II volume is unusual, i.e. particularly under-dense or over-dense. Ultimately, the large area of SDSS can be used to constrain the absolute bias (Section 1.9) of the GAMA-II volume, but we will leave this for future work.

In order to facilitate these comparisons we k-correct and evolution correct our magnitudes to $z_{\rm ref} = 0.1$, which is the reference redshift used by Zehavi et al. (2011). We wish to compare to the volume limited, luminosity binned samples using the same redshift cuts as Zehavi et al. (2011). Unfortunately it is only really sensible to compare to the magnitude bin sample of $-22.0 < M_r^{0.1} - 5\log_{10}h < -21.0$, as the redshift cuts for the fainter magnitude bins result in small volumes in GAMA-II (around 1.2×10^6 (Mpc/h)-3), whilst the brighter bin of $-23.0 < M_r^{0.1} - 5\log_{10}h < -22.0$ only contains 304 galaxies. Our comparison is plotted in Fig. 4.10. We see the measurements agree on small scales, but appear to be slightly above the Zehavi et al. (2011) data for scales larger than around 3 Mpc h^{-1}. The difference is small considering the error bars and so the deviation could simply be the result of sample variance. To test this hypothesis we will now test how well our jack-knife errors represent the true sample variance.

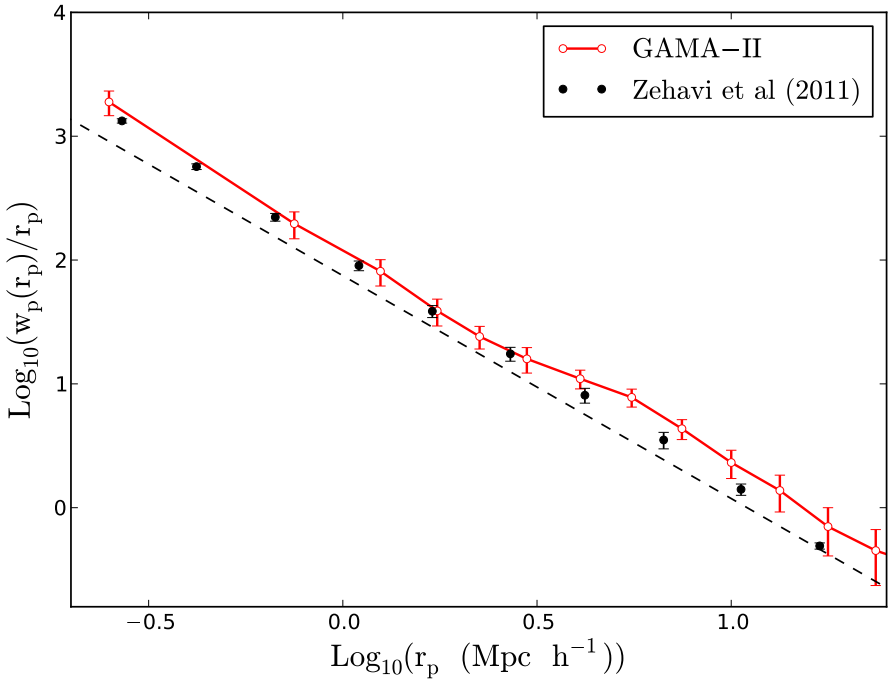

Figure 4.10: The $-22.0 < M_r^{0.1} - 5\log_{10}h < -21.0$ clustering measurement from Zehavi et al.(2011) (black), along with our measurement of clustering for the same magnitude and redshift cuts. The dashed line is the reference power law defined in Section 4.3.4.

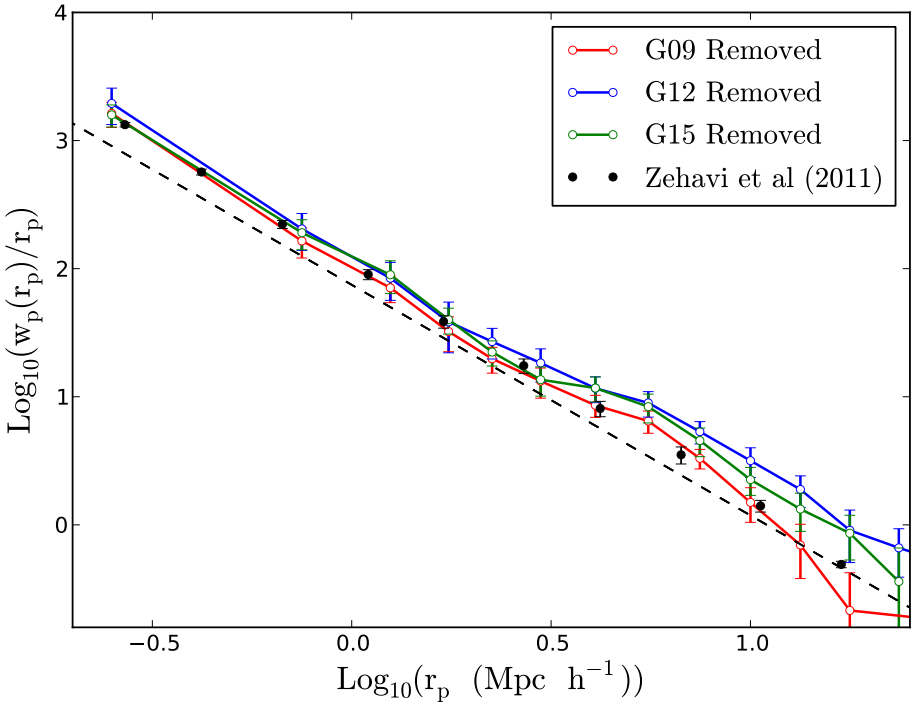

Figure 4.11: The $-22.0 < M_r^{0.1} - 5\log_{10}h < -21.0$ clustering measurement from Zehavi et al.(2011) (black), along with our measurement of clustering for the same magnitude and redshift cuts. The different coloured lines indicate measurements from excluding different GAMA regions, as indicated in the legend. The dashed line is the reference power law defined in Section 4.3.4.

4.4.2 Tests of jack-knife error estimates

We use a standard approach to calculate errors in this chapter: the jack-knife method. To test these error estimates we study how the correlation function is modified by removing individual GAMA-II regions (i.e. G09, G12 or G15). This is the jack knife method, but carried out by excluding entire GAMA-II regions rather than smaller sub regions. Error bars for these measurements were calculated by further splitting the unexcluded regions into 18 jack-knife samples. In Fig. 4.11 we show the results of this test. On smaller scales the different measurements agree, but on larger scales the G09 measurements and the G12 measurements appear slightly discrepant given the errors. This could suggest the jack-knife errors from the 27 sub-regions are slight underestimates of the true error. We can also see from Fig. 4.11 how correlated the bins are, with the whole correlation function changing amplitude when excluding different GAMA regions. From these observations, it seems likely that our measurements are consistent with those of Zehavi et al. (2011), with the differences in Fig. 4.10 being the result of sample variance.

As well as the mock catalogue we are using in this chapter, several other GAMA-mock catalogues were produced. These lightcones are produced by orientating the virtual observer towards different directions of the simulation box. By comparing these mock catalogues, we have another means with which to estimate sample variance. Fig. 4.12 gives the clustering of galaxies in our low-redshift, red colour sample, for the real data and three different mock catalogues. We will defer comparisons between the data and mock catalogues to the next section, and simply focus on the difference between the different mock catalogues. We can see the scatter between the mock realisations is larger than expected given the jack-knife error bars, with the mock we use for this work having stronger clustering at $< 3\mathrm{Mpc}\ h^{-1}$ than the other two. This is further evidence that our jack-knife errors are underestimates of the true error.

One way of gaining accurate error estimates could be to utilise many more mock catalogues. As new mock catalogues with different cosmologies and galaxy formation models are under production, we will defer this to later work, and continue using jack-knife errors derived from the 27 regions. It is important to note, however, that

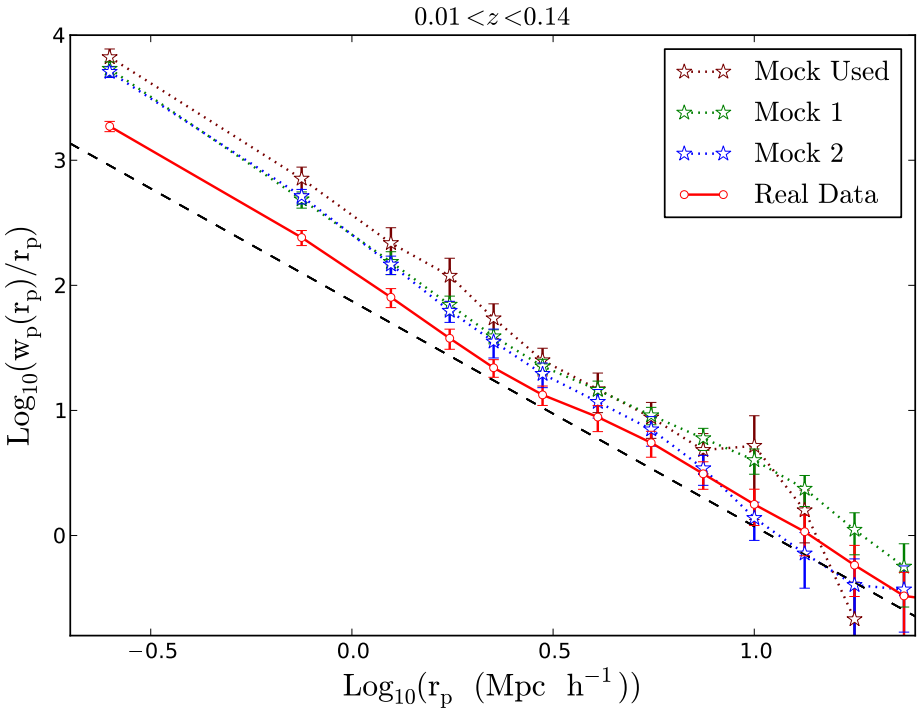

Figure 4.12: The projected clustering of real red galaxies (red solid line) and mock red galaxies for multiple different mock catalogues, as indicated by the legend, for our low redshift slice. We see considerable scatter between the different mock catalogues. The dashed line is the reference power law defined in Section 4.3.4.

the work in this section suggests the standard approach of using jack-knife error bars underestimates the true sample variance.

4.4.3 Colour dependent clustering

Fig. 4.13 shows the clustering of our red and blue galaxy samples (with solid lines). In all of the redshift intervals we probe, red galaxies are more clustered than blue galaxies. We also note that the red galaxy correlation functions are steeper on small scales, with the lowest redshift, red galaxy correlation function showing an inflection before a steepening of slope at around 2 Mpc h^{-1}. This can be interpreted as red galaxies predominantly being in larger haloes with more satellite galaxies (see Chapter 1).

The mock galaxies show the same segregation of clustering strength with colour in Fig. 4.13 (dotted lines). The red mock galaxies also have steeper correlation functions than the blue mock galaxies. The mock galaxies do well at matching the clustering of the real blue galaxy samples, and the red galaxy samples in the high redshift region. For the two lower redshift slices the mock red galaxies have a higher amplitude correlation function than that of the real data. This effect seems larger on smaller scales. Note that even though the low redshift slice suffers from considerable sample variance, Fig. 4.12 shows that two different mock catalogues also have stronger small scale clustering than the data. This combined with the fact that in the much larger volume of the intermediate redshift slice the mock galaxies are also too clustered on small scales, suggests that this difference is not due to sample variance. The disagreement on smaller scales could imply the mock red galaxy sample contains too many satellites, and so has too large a one halo term (see Chapter 1). To quantify the differences between the clustering of our red and blue galaxy sample, we consider the relative bias. In Section 1.9 we introduced the concept of bias, here we calculate the relative bias between the red galaxy projected correlation function $w_{\rm p,red}(r_{\rm p})$ and the blue galaxy projected correlation function $w_{\rm p,blue}(r_{\rm p})$ thus

$$b_{\rm rel}(r_{\rm p}) = \sqrt{\frac{w_{\rm p,red}(r_{\rm p})}{w_{\rm p,blue}(r_{\rm p})}}. \tag{4.4.15}$$

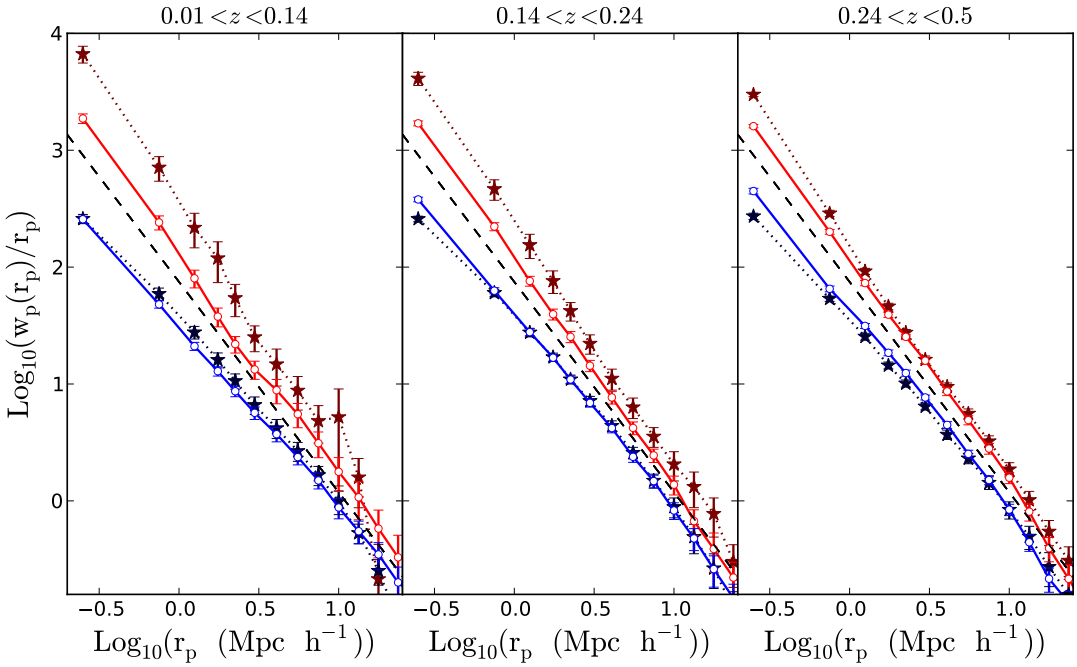

Figure 4.13: The projected correlation function of red galaxies (red solid lines and circles) and blue galaxies (blue solid lines and circles) in different redshift slices. Also shown is the clustering of mock galaxies from the Bower et al. (2006) model (stars and dotted lines with darker shades of blue and red). The Bower et al. (2006) model does a good job reproducing the clustering of blue galaxies but is less successful in reproducing the clustering of red galaxies, particularly on smaller scales. The dashed line is the reference power law defined in Section 4.3.4.

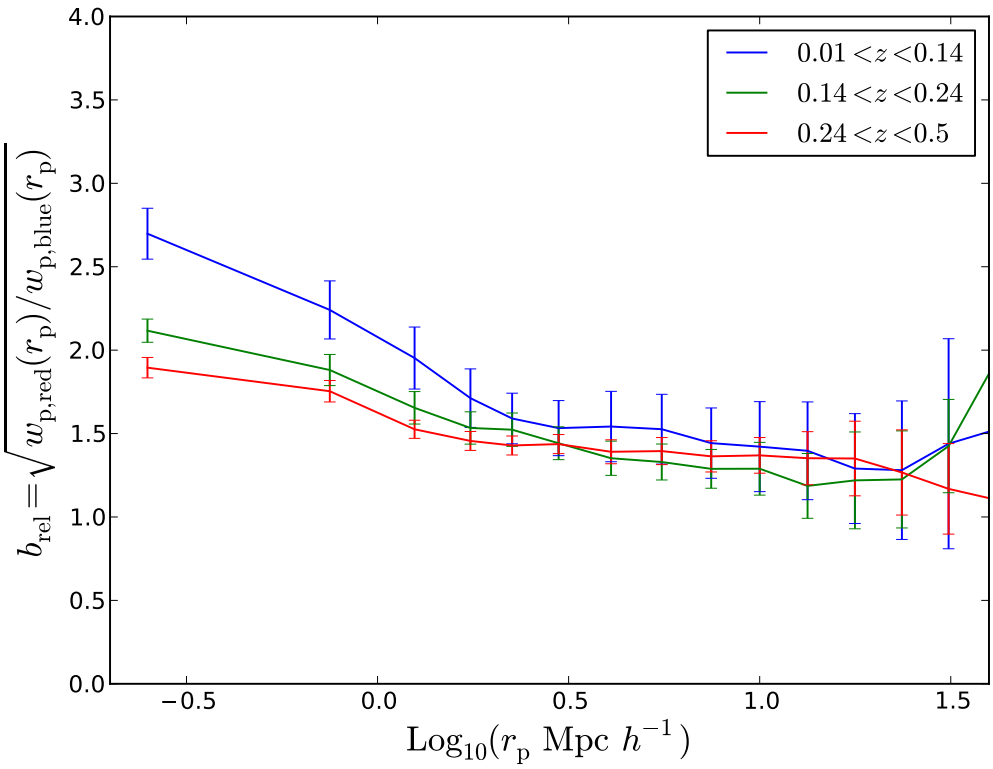

Figure 4.14: The relative bias of the red and blue galaxy samples, for different redshift slices as indicated in the legend.

We show this quantity for our different redshift slices in Fig. 4.14. We can see that relative bias increases for the low and intermediate redshift slices at around 2 Mpc h^{-1}. This could mark the transition to the one-halo term, where one might expect stronger clustering for red galaxies which are more likely to be satellites. We can see that the relative bias is around 1.6 on scales larger than 2 Mpc h^{-1}. Table 1 of Coil et al. (2008) gives estimates for the relative bias of red and blue galaxies, based on their own study using DEEP2 and based on other galaxy surveys. Our value of this relative bias seems to be in agreement with the Zehavi et al. (2002) low redshift ($z \approx 0.1$) SDSS value given in this table of ≈ 1.6, but is slightly higher than the Coil et al. (2008) value of 1.23 ± 0.09 at $z \approx 1$. This could suggest that the bias is evolving, though one has to be careful when interpreting this as different authors measure bias over different scales. The Coil et al. (2008) value was measured for scales of 1 - 15 Mpc h^{-1}, which is comparable to our work, whilst the Zehavi et al. (2002) value, as given in Coil et al. (2008), is simply derived from power law fits to the samples. In our different samples the errors are too large to draw any strong conclusions about bias evolution between the different redshift slices, though it does look like there is tentative evidence that small scale (< 2 Mpc h^{-1}) bias decreases with redshift.

The relative bias, and its evolution of redshift can act as a test of galaxy formation physics, by comparisons to mock catalogues. In Fig. 4.15 we show the relative bias of red and blue galaxies in the mock. As one might expect from Fig. 4.13, the relative bias in the mocks is higher than that of the data on small scales but in reasonable agreement on larger scales. Redshift evolution on scales less than 2 Mpc h^{-1} is more clear in the mock catalogue than in the data, with the small scale bias showing a decrease with redshift in each sample.

4.4.4 Luminosity dependent clustering

In Fig. 4.16 we show the clustering of galaxies as a function of luminosity and redshift, divided by our reference power law. Dividing by a reference power law in this way means our measurements show the square of the galaxy bias, relative to the fiducial power law. For all of the redshift intervals we notice segregation between the

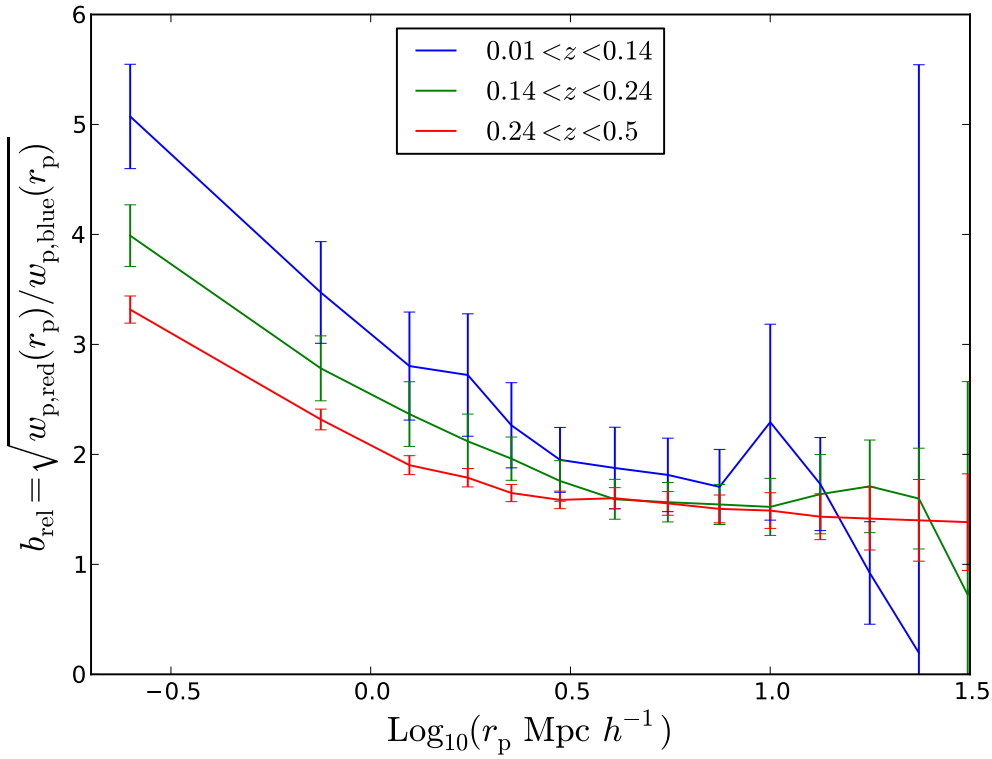

Figure 4.15: The relative bias of the red and blue mock galaxy samples, for different redshift slices as indicated in the legend.

faint and bright samples, with brighter galaxies being more clustered. This trend is reproduced in the measurements from the mock catalogue. As has been previously reported for other redshift ranges, this supports the theory that brighter galaxies lie in more massive dark matter haloes.

The real galaxy samples have amplitudes which slightly decrease with redshift. The only exception is the brightest sample, which has a fairly constant amplitude between the intermediate and high redshift bins. The trends of clustering between different redshift ranges is less clear for the mock galaxies. For the intermediate magnitude sample, the mock galaxies have decreasing clustering with redshift, as in the data. In contrast, for the faintest sample, the clustering actually increases between the low and intermediate redshift bins. Note, however, that the small volume of the low redshift slice is quite sensitive to sample variance (see Fig. 4.12). At the brightest magnitudes the mocks, like the data, have correlation functions with a fairly constant amplitude between the high and intermediate redshift slices.

The detailed shape of the clustering of the mock galaxies and real galaxies disagrees. In the intermediate redshift range there is a trend for the mock galaxies to be slightly more clustered than the real sample; the amplitude offset is small and comparable to the size of the errors however. In the highest redshift slice the shapes of the mock and real galaxy correlation functions are remarkably similar, though the brightest mock galaxies are more clustered on smaller scales. However, to fully quantify the extent of these disagreements would require a better understanding of sample variance. We will address this in future work once the new mock catalogues are produced.

The low redshift, real galaxy sample shows the same increase of clustering strength for scales larger than 3 Mpc h^{-1} seen in the Zehavi et al. (2011) comparison sample. This is likely caused by the same large scale structure that caused the upturn in the Zehavi et al. (2011) comparison sample, as the redshift ranges are very similar.

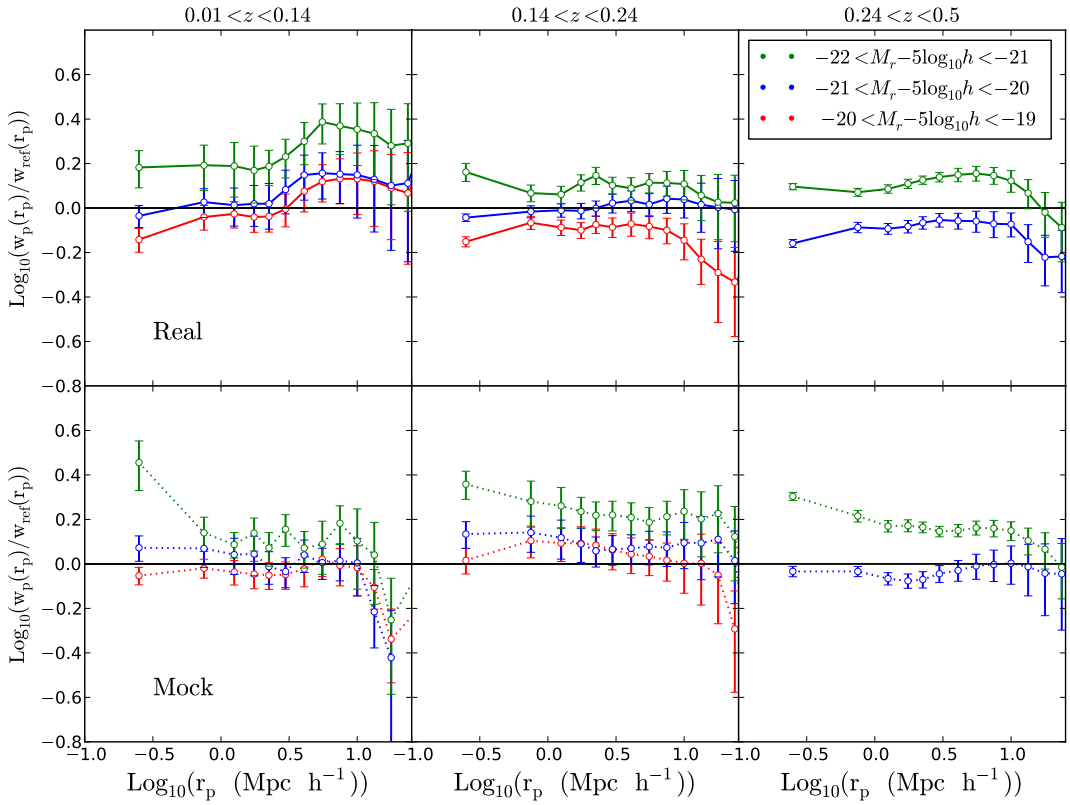

Figure 4.16: The projected two-point correlation function of real (top) and mock (bottom) galaxies as a function of redshift (different columns) and luminosity (different colours, as indicated in the legend). The measurements are divided by the reference power law defined in Section 4.3.4.

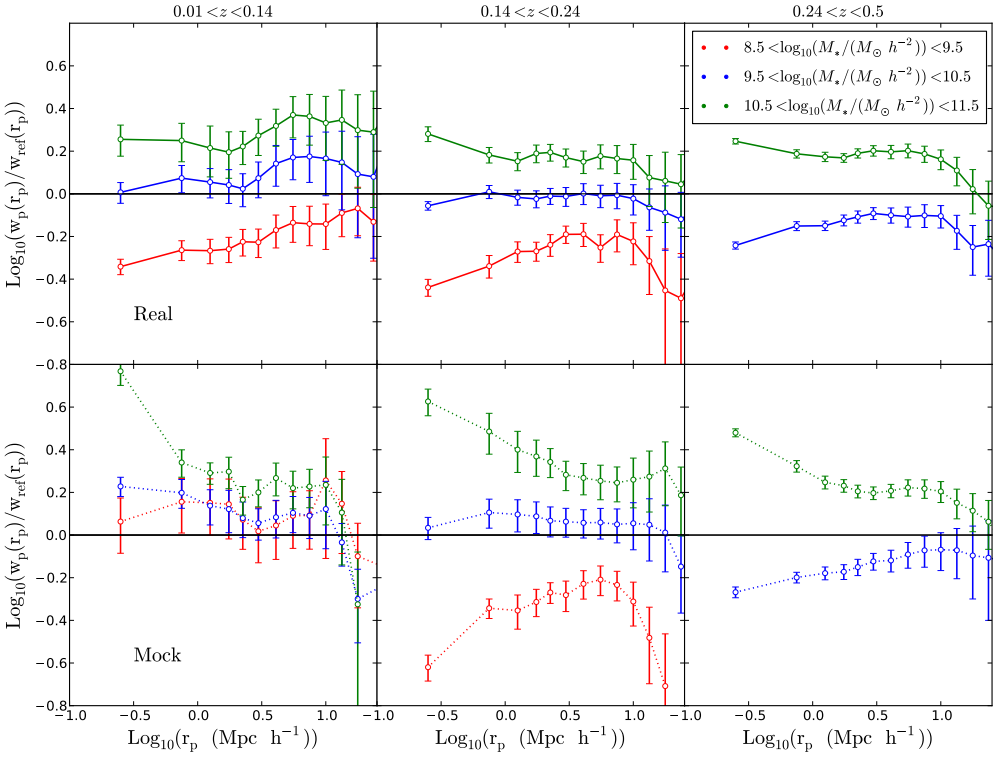

Figure 4.17: The projected two-point correlation function of real (top) and mock (bottom) galaxies as a function of redshift (different columns) and stellar mass (different colours, as indicated in the legend). The measurements are divided by the reference power law defined in Section 4.3.4.

4.4.5 Stellar mass dependent clustering

In Fig. 4.17 we show the clustering of galaxies as a function of mass. We see that more massive galaxies are more clustered than less massive ones, in all of the redshift intervals. As was the case for clustering as a function of luminosity, this trend is successfully reproduced by the mock catalogues, except in the low redshift region where the clustering of the mock galaxies is very similar for the two least massive samples. As we have already seen, the low redshift slice suffers from considerable sample variance, it is quite possible that this is the explanation for the unusual clustering of the mock here. Indeed, the redshift distribution of the least massive mock galaxies, shown in Fig. 4.6, does show a large over-density at around $z = 0.05$. We will study the mass evolution of clustering more quantitatively in the intermediate and high redshift slices, where sample variance is less of an

issue. On scales between 3.2 Mpc h^{-1} and 10 Mpc h^{-1} the square of the bias, relative to the fiducial power law, is different by a factor of around 0.2 dex between the intermediate mass and high mass samples. The correlation function of the mock galaxies are also separated by around 0.2 dex for these two samples. At higher redshift the intermediate and high mass samples are separated by 0.3 dex, in both the data and the mock catalogue. This suggests the relative bias of the high mass, $10.5 < \log_{10}(M_*/(\mathrm{M}_\odot h^{-2})) < 11.5$ sample to the intermediate mass, $9.5 < \log_{10}(M_*/(\mathrm{M}_\odot h^{-2})) < 10.5$ sample increases with redshift. The agreement between the mock catalogue and the data suggests that the Bower et al. (2006) model is assigning galaxies to dark matter haloes with the correct relative bias.

The amplitude of the mock galaxy correlation function is too high in the intermediate redshift sample; in contrast, the clustering of galaxies at high redshift is very closely matched by the mocks, except at scales less than 1 Mpc h^{-1} where the most massive sample has excess clustering. The most massive mock galaxies also show excessive small scale clustering in the other redshift slices. One explanation for the most massive mock galaxies being too clustered on these small scales is that the simulation has too many galaxy clusters and groups. This could be a result of the value of σ_8 used in the Millennium Simulation, which is larger than the true value (see Section 4.2.3). We will discuss this further in Section 4.5.

The clustering of the mocks and the data both show evolutionary trends with redshift. The clustering amplitude of the $9.5 < \log_{10}(M_*/(\mathrm{M}_\odot h^{-2})) < 10.5$ sample decreases with redshift between the low redshift slice and the high redshift slice. The mock galaxies of this mass also show a decreasing clustering amplitude between the intermediate and high redshift slices. There is a lack of clustering evolution between the low redshift slice and the intermediate redshift slice for the mock catalogue, though this could easily be due to sample variance in the low redshift slice. In both the mocks and the data the more massive $10.5 < \log_{10}(M_*/(\mathrm{M}_\odot h^{-2})) < 11.5$ galaxy sample shows less evolution with redshift. The evolution of clustering with redshift can be used to probe how the galaxy bias evolves with time, which can be a useful constraint on the physics of galaxy formation. We will compare our clustering amplitudes to literature results in the next section.

4.5 Discussion and Conclusions

We have studied the projected two point correlation function of galaxies in GAMA-II. To do this we used the Cole (2011) approach to generate random catalogues; this method resulted in a set of random points with all of the properties of the real galaxies. This allowed sample selection cuts to be applied to both the data and the random catalogue, allowing the measurement of galaxy clustering as a function of diverse galaxy properties.

We have confirmed that more luminous, more massive and redder galaxies are more strongly clustered, in three redshift slices between $z = 0$ and $z = 0.5$. This is in agreement with previous measurements that show these trends exist at different redshift ranges to our data (e.g. Zehavi et al., 2011; Christodoulou et al., 2012; Li et al., 2012; de la Torre et al., 2013; Marulli et al., 2013). We also find that red galaxies have steeper correlation functions in all of our redshift slices, again in agreement with clustering measured at higher (e.g. Coil et al., 2008) and lower (e.g. Zehavi et al., 2011) redshifts. We do note from Table 4.1, 4.2 and 4.3 however, that the more massive galaxies tend to be red and more luminous. In order to decide which of these galaxy properties is most important for driving these clustering trends, future work could study the clustering of samples of galaxies with cuts in multiple parameters, e.g. red, massive galaxies versus red, low mass galaxies.

We detect redshift evolution of the clustering in some of the samples of real galaxies. To summarise these results, and compare our findings to those at high redshifts we plot our values of r_0 for the two mass samples for which we have clustering measurements in each of our redshift slices. We find these values of r_0 from fitting Eq. 4.3.14 to the full r_p range of our data. We compare our findings to the high redshift measurements from VIPERS in Marulli et al. (2013), who fit a power law over the scales $0.2 < r_\mathrm{p}\,\mathrm{Mpc}\,h^{-1} < 20.0$. The range over which this work and Marulli et al. (2013) fit power laws includes the one-halo and two-halo terms of the clustering, so our results should be comparable. We show our measurements of r_0 (stars) and the Marulli et al. (2013) measurements (circles) as a function of each sample's median redshift in Fig. 4.5. We see that our estimates of r_0 at $z \approx 0.3$ agree with the measurements of Marulli et al. (2013) at $0.6 < z < 1.0$, suggesting little

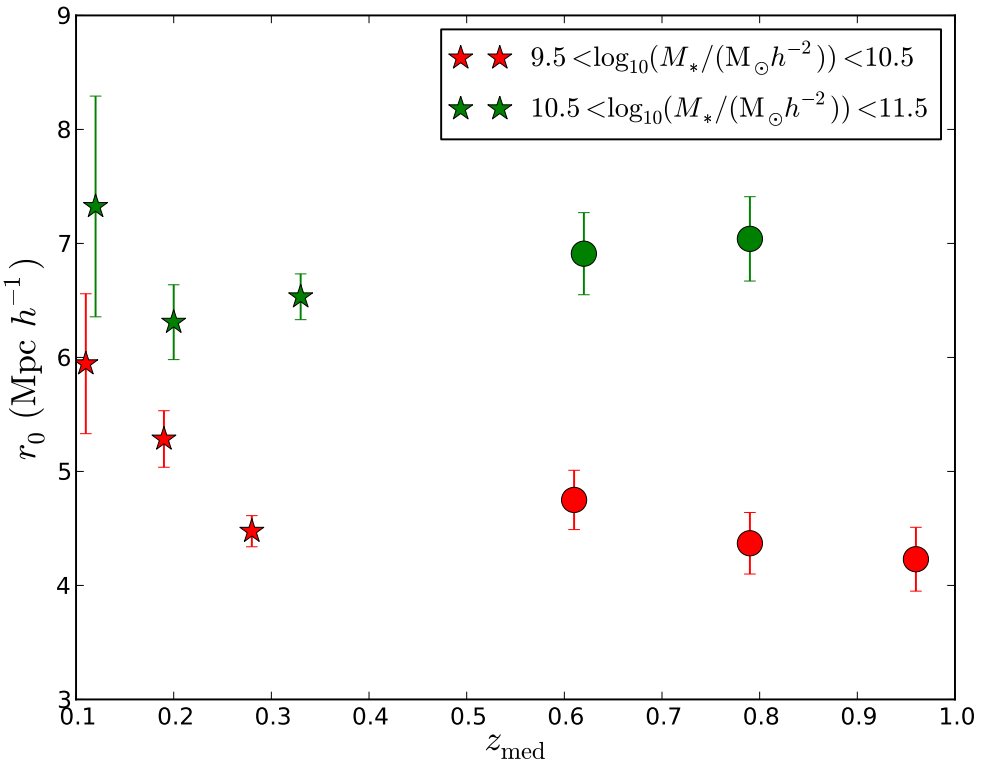

Figure 4.18: Measurements of the correlation length, r_0, for galaxy samples of different mass as indicated in the legend. The stars show our measurements, while the circles show measurements from the VIPERS survey from Marulli et al. (2013). Values are plotted at the median redshift of each sample.

evolution occurred between the two redshift ranges of our survey. One has to be careful with this interpretation however, as different methods of estimating stellar mass and sample variance could lead to systematic offsets. We do see evidence of redshift evolution in the $9.5 < \log_{10}(M_*/(\mathrm{M}_\odot h^{-2})) < 10.5$ sample across our redshift slices. In contrast we see no evidence of redshift evolution in galaxies more massive than $10^{10.5}\,\mathrm{M}_\odot\,h^{-2}$. Meneux et al. (2008) also found that galaxies more massive than this limit showed less clustering evolution between $z \approx 1$ to $z \approx 0.15$ than their less massive counterparts. They demonstrated this implies that these more massive galaxies have faster bias evolution.

The trend with luminosity, mass and colour observed in the real galaxies is reproduced in the mock galaxies, except in the low redshift slice which suffers from considerable sample variance. The mock galaxies are particularly successful in reproducing the relative bias of $9.5 < \log_{10}(M_*/(\mathrm{M}_\odot h^{-2})) < 10.5$ to $10.5 < \log_{10}(M_*/(\mathrm{M}_\odot h^{-2})) < 11.5$ galaxies. This is a positive indication that the Bower et al. (2006) galaxy formation model is assigning galaxies to the correct dark matter haloes.

Disagreements do exist between the mocks and the data, however, and these disagreements could indicate that key pieces of galaxy formation physics are neglected or incorrectly realised in the model. We find that the mock galaxies tend to be more clustered on scales smaller than $1 - 3$ Mpc h^{-1} than the data. In the red galaxy sample this could be associated with an excess of satellite galaxies. Previous publications have also found this result, and their suggestions for new galaxy formation physics involve processes which remove satellite galaxies (see Chapter 1 and references therein). For the most massive and most luminous mock galaxies, this excess on small scales could be down to the value of σ_8 used in the Millennium Simulation. Whilst typically clustering on small scales is more related to galaxy formation physics than cosmology, the overly large value of σ_8 used for the mocks could result in more massive dark matter haloes, which in turn, would result in dark matter correlation functions which are steeper on small (non-linear) scales.

Interestingly, how well the clustering of the mock galaxies agrees with that of the data varies with redshift. The agreement between mocks and data is better for the

high redshift region, $0.24 < z < 0.5$, than for the intermediate redshift region, where the amplitude of the clustering of the mocks tends to be too high (see Fig. 4.13 to Fig. 4.17). This demonstrates that our results, as a function of redshift, can act as a new test for galaxy formation models. Indeed, mock catalogues with different values of σ_8 and different implementations of galaxy physics (e.g. Lagos et al., 2012) are currently under production, comparing their clustering to these results could yield new information on galaxy formation and cosmology.

When testing galaxy formation and galaxy models against our results there are two main limitations. Firstly, our jack-knife resampling likely underestimates the true variance for some of the samples. In order to overcome this we will derive new error estimates based on measurements from mock catalogues, or from larger jack-knife regions. Secondly, our low redshift slice has a small volume and so is prone to sample variance. However, for trends of clustering with colour, mass and luminosity, SDSS already provides highly accurate clustering statistics in the low redshift Universe.

Chapter 5

Conclusions

This thesis has presented results from two, very different, galaxy surveys. We first presented the tests and preparations which were carried out to exploit PS1 for galaxy clustering and cosmology. After this, we used the GAMA-II survey to make measurements of galaxy clustering that can be used as new constraints when developing galaxy formation models. In this chapter we shall review our key findings before suggesting future developments to this research.

5.1 Pan-STARRS1

The software of PS1 has been tested to ensure that the magnitude measurements it makes can be used for science. We found that the PS1 IPP software can measure Kron magnitudes for stars and galaxies, with little evidence of a magnitude dependent bias. Furthermore, we show, using synthetic images, that the stacking and warping processes preserve the magnitudes of sources. We also demonstrate with our synthetic images that the stacking procedure increases depth by the expected amount.

The image backgrounds of PS1 were also studied by measuring the pixel power spectrum. The pixel power spectrum of PS1 images has features within it related to the time varying bias of different pixel rows on the CCD detector. We also found that the PS1 image background power spectra has more large scale power relative to SDSS at scales of $k \approxeq 1$ arcseconds^{-1} , which corresponds to wavelengths

greater than 6 arcseconds. We have shown using synthetic images that unresolved sources alone cannot account for this excess power. It is possible that the source of this noise is related to the electronics of the CCD camera, perhaps, for example, a result of the time varying bias of the rows of pixels. To test this, power spectra of images that have undergone different stages of the IPP processing, from raw data to detrended exposures, could be produced by the IPP team and their power spectra analysed. Testing if there is any dependence of the shape of the power spectrum on the detrending methods used by IPP, such as the order of the polynomial fit used in the row-by-row bias correction (Section 2.3), will also illuminate this issue.

We additionally found that the rms scatter of the sum of the background in apertures on empty regions of PS1 images increases with aperture size more than it would for white noise. For a 4 arcsecond aperture, Fig. 2.16 implies a 0.13 magnitude increase in magnitude scatter. We attribute this to the large scale upturn in the power spectrum. The large scale noise will have to be accounted for if one wants to predict the magnitude error on measurements from apertures. This quantity is important as it is used when fitting SED templates to photometry, which is an important step in determining photometric redshifts.

We also presented preparations for measuring galaxy clustering in PS1. Using a region of science verification data we developed a star/galaxy separator that is 91%-98% complete. We also developed a method of accounting for the variable depth of the PS1 survey. Using these techniques, we demonstrated our ability to measure angular clustering with PS1, by comparing to literature measurements from deeper and more homogeneous surveys. We found that the presence of false detections is a concern for galaxy clustering studies, as false detections in PS1 can have a strong clustering signal. One method which could be developed to remove these false positives is using the final 3π stacked data to detect and mask image artifacts in the individual warps, before restacking these newly cleaned warps. Additionally, false detections make up only a small fraction of the sample in SAS2 data. We demonstrated that reliable clustering in SAS2 can be measured to a limit of $r_{\rm P1} = 22.5$.

PS1 should finish observations in January 2014, and the data should be reduced

by mid 2014 (Magnier et al. in preparation). In order to fully utilise this data set, our depth correction method and a method of star/galaxy separation needs to be rolled out across the full survey. This presents a large number of challenges. Firstly, the PSF FWHM of SAS2 is very uniform, the finished 3π data will have far greater variations in PSF FWHM. Both star/galaxy separation and detection efficiency depend on the PSF FWHM. The synthetic images we developed for this thesis can be utilised towards understanding how to adapt our methods for more variable seeing. For example, synthetic images with a range of different PSFs could be generated in order to determine the scaling between PSF parameters, like width and ellipticity, to detection efficiency and star/galaxy separation cuts. The synthetic images can also be used to test how well our methods work on data with more variable image backgrounds.

A further challenge is related to how to scale our techniques from the 68 deg.^{2} area of SAS2 to the 31,000 deg.^{2} of the full 3π. Note that, in practice, the galactic disk may limit the area of sky of interest to extra-galactic astronomers. Computer memory is unlikely to be a major issue, as our binned-up variance maps are around 600MB in size, so a binned up, 3π variance map to the same resolution would be a manageable 275GB in size. The challenges arise with computing and utilising these masks. The PS1 IPP is currently producing binned up variance maps in order to apply our methods to the whole survey.

Potential applications of the finished PS1 3π data set include searching for the Integrated Sachs Wolfe (ISW) effect. This effect, as explained in Chapter 1, is an increase in the temperature of CMB photons, caused by them travelling through a gravitational potential well that is decaying due to the accelerated expansion of the Universe. It can act as an important probe of the dynamics of dark energy. Another application is generating catalogues of galaxy clusters. In both cases the large area of PS1 could give it an edge over its competitors. The detection of the ISW effect in PS1 could arise from cross correlating the distribution of galaxies with the CMB. Our method could correct for spatial depth variations in the galaxy field, allowing for the use of 3π data to a fainter magnitude limit than what would be required for homogeneous depth. The fast computation of the depth as a function of position

will also be a useful input into cluster finding software, allowing it to differentiate between genuine over-densities of galaxies and changes in depth.

5.2 GAMA-II

We have utilised the GAMA-II survey to measure the projected two point correlation function across the redshift range $0.0 < z < 0.5$. We find in intermediate, $0.14 < z < 0.24$ and high, $0.24 < z < 0.5$, redshift slices both real GAMA galaxies and mock galaxies from the Bower et al. (2006) semi-analytic model show increasing clustering with mass and luminosity. We additionally find red galaxies have steeper, higher amplitude correlation functions than blue galaxies in both the mocks and the data, and in all of the redshift slices.

The clustering of real and mock galaxies shows some intriguing differences. The red mock galaxies have a larger correlation function amplitude than the data, a difference that is more marked for scales less than $1 - 3$ Mpc h^{-1}. This excess of small scale clustering supports the idea that the Bower et al. (2006) model produces too many satellite galaxies. An idea that has been raised by other authors, who suggest mechanisms for removing satellite galaxies from dark matter haloes (see references in Chapter 1). In addition, the most massive and most luminous mock galaxies tend to also have too much small scale clustering; this could be an effect of the σ_8 value adopted in the Millennium Simulation, which is larger than the current best estimates (e.g. Planck Collaboration et al., 2013). Interestingly, the difference between the clustering of real galaxies and mock galaxies changes between different redshift bins.

We also detect redshift evolution in the clustering amplitude of our real galaxies. Notably our intermediate luminosity, $-21.0 < M_r - 5\log_{10}h < -20.0$, and our intermediate mass, $9.5 < \log_{10}(M_*/(\mathrm{M}_\odot h^{-2})) < 10.5$, samples show a clustering amplitude that decreases between $z = 0.0$ and $z = 0.5$. Comparing our values of r_0 to those measured at $z \approx 1$ by Marulli et al. (2013) indicates little evolution of r_0 between $z = 0.5$ and $z \approx 1$.

The clustering measured in the GAMA-II survey can act as a powerful new test

of galaxy formation models. Comparing these results to a simulation with a different value of σ_8 and different GALFORM models is an obvious first step. Additionally, better estimates of the sample variance of clustering measurements need to be developed. One approach to do this is to compare results from multiple mock catalogues. Also, future work could estimate the bias of our galaxy clustering measurements, relative to models of dark matter. A redshift dependent bias could then be derived which could be compared to predictions from models. Finally, HOD fitting techniques could be applied to the clustering measurements to find what the data imply about the occupation statistics of dark matter haloes.

As the galaxies in the random catalogues we developed have all of the properties of the genuine galaxies, clustering in GAMA can be studied as a function of more exotic galaxy properties. For example, the multi-wavelength nature of GAMA could allow the measurement of the dependence of galaxy clustering on 21cm radio luminosity. This emission is an indicator of molecular gas, the main ingredient for star formation. The dependence of clustering on star formation rate (SFR) can also be probed. GAMA has spectra of galaxies which could allow the estimation of SFR from Hα emission. In addition, SFR could also be estimated in GAMA via the ultra-violet or infra-red emission of galaxies, or SED fits to optical photometry. Estimating SFR in multiple ways allows added redundancy in the measurements. As models such as GALFORM make predictions for clustering as a function of SFR and molecular gas content, the GAMA data has the potential to test the galaxy formation physics in these models.

5.3 Future Prospects

There are many upcoming imaging surveys which will also help constrain galaxy formation and cosmology. Our research in understanding the systematics affecting large surveys, such as stellar contamination and the effects of incompleteness, will be valuable to these. We will now highlight a few other interesting future surveys.

The Large Synoptic Survey Telescope (LSST; Ivezic et al., 2008) would be a prime candidate for the application of the spatially varying depth correction method. Like

PS1, the LSST will be made up of a large number of stacked exposures and as such is likely to suffer from the same spatial depth variations. After 10 years the LSST is expected to reach a depth of $r = 27.5$ (Ivezic et al., 2008), far deeper than PS1. LSST will be able to measure BAOs at higher redshifts, to further constrain the equation of state of dark energy. It is also expected to be an excellent tool for weak gravitational lensing studies, where the distortion of galaxy light by mass is used to probe dark matter. The angular clustering of LSST galaxies could also be used to make comparisons against the predictions of models, like GALFORM, at higher redshifts.

The Dark Energy Survey (DES; The Dark Energy Survey Collaboration, 2005) have already begun gathering data. DES will measure multi-band photometry over 5 years for 5000 deg.^{2} down to a 10σ limit of $r = 24.1$ (The Dark Energy Survey Collaboration, 2005). DES will also be able to measure BAO in photometric redshift slices, as well as measuring weak gravitational lensing and the ISW effect (The Dark Energy Survey Collaboration, 2005). A possible systematic in DES angular clustering measurements is understanding the galaxy bias, which could affect measurements of the BAO peak (e.g. The Dark Energy Survey Collaboration, 2005). The measurements made for this thesis could be used to improve galaxy formation models, and so increase our understanding of galaxy bias. As before, the angular clustering of DES galaxies as a function and colour, stellar mass and photometric redshift could also act as new constraints on galaxy formation models.

The VST-ATLAS survey is also being carried out. VST-ATLAS is a survey of 4500 deg.^{2} of southern sky to SDSS depths[1]. Follow-up spectroscopy of LRGs and quasars in VST-ATLAS is expected to yield new measurements of the galaxy correlation function and BAOs at unprobed redshifts. Another major spectroscopic survey aiming to measure BAOs is the Dark Energy Spectroscopic Instrument (DESI; Levi et al., 2013). This will measure the BAO peak in 35 redshift bins, allowing a highly accurate measurement of the expansion history of the Universe. PS1 data overlaps with the DESI footprint and so could provide additional photometry.

[1]http://astro.dur.ac.uk/Cosmology/vstatlas/, accessed 17/12/13

Perhaps the most exciting upcoming project is Euclid, which involves launching a satellite to carry out 15,000 deg.^{2} of deep imaging (in their visible band down to 24.5 mag.) with a small PSF FWHM (less than 0.2 arcseconds in the visible band; Laureijs et al., 2011). Combined with this it will carry out a spectroscopic survey of 50 million galaxies down to $z \sim 2$. It will combine BAO measurements from the spectroscopic data, to weak lensing measurements from the visible data (Laureijs et al., 2011). Their aim is to measure w to a 1σ error of 0.01, to put a very strong constraint on the nature of dark energy (Laureijs et al., 2011). As with DESI, PS1 could provide further visible photometry for this survey.

Overall, the work in this thesis contributes to our understanding of galaxy formation and galaxy surveys. The latter of which are becoming ever more ambitious in their attempts to understand the nature of dark energy and dark matter.

Bibliography

Abazajian K. N. et al., 2009, ApJS, 182, 543

Anderson L. et al., 2012, ArXiv e-prints 1203.6594

Annis J. et al., 2011, ArXiv e-prints 1111.6619

Baldry I. K. et al., 2010, MNRAS, 404, 86

Bard D., Bellis M., Allen M. T., Yepremyan H., Kratochvil J. M., 2012, ccogs: Cosmological Calculations on the GPU. Astrophysics Source Code Library

Baugh C. M., Lacey C. G., Frenk C. S., Granato G. L., Silva L., Bressan A., Benson A. J., Cole S., 2005, MNRAS, 356, 1191

Benson A. J., Frenk C. S., Baugh C. M., Cole S., Lacey C. G., 2001, MNRAS, 327, 1041

Berlind A. A., Weinberg D. H., 2002, ApJ, 575, 587

Bertin E., Arnouts S., 1996, A&AS, 117, 393

Blake C. et al., 2013, ArXiv e-prints 1309.5556

Blanton M. R. et al., 2001, AJ, 121, 2358

Blanton M. R., Roweis S., 2007, AJ, 133, 734

Bond J. R., Cole S., Efstathiou G., Kaiser N., 1991, ApJ, 379, 440

Bottini D. et al., 2005, PASP, 117, 996

Bower R. G., Benson A. J., Malbon R., Helly J. C., Frenk C. S., Baugh C. M., Cole S., Lacey C. G., 2006, MNRAS, 370, 645

Cabré A., Fosalba P., Gaztañaga E., Manera M., 2007, MNRAS, 381, 1347

Christodoulou L. et al., 2012, MNRAS, 425, 1527

Christodoulou L., et al., 2013, MNRAS submitted

Coil A. L. et al., 2008, ApJ, 672, 153

Cole S., 2011, MNRAS, 416, 739

Cole S., Aragon-Salamanca A., Frenk C. S., Navarro J. F., Zepf S. E., 1994, MNRAS, 271, 781

Cole S., Kaiser N., 1989, MNRAS, 237, 1127

Cole S., Lacey C. G., Baugh C. M., Frenk C. S., 2000, MNRAS, 319, 168

Cole S. et al., 2005, MNRAS, 362, 505

Coles P., Lucchin F., 2002, Cosmology: The Origin and Evolution of Cosmic Structure, Second Edition

Colless M. et al., 2001, MNRAS, 328, 1039

Creasey P., Theuns T., Bower R. G., 2013, MNRAS, 429, 1922

de Bernardis P. et al., 2000, Nature, 404, 955

de la Torre S. et al., 2013, A&A, 557, A54

De Lucia G., Blaizot J., 2007, MNRAS, 375, 2

de Vaucouleurs G., 1948, Annales d'Astrophysique, 11, 247

Driver S. P. et al., 2011, MNRAS, 413, 971

Dutton A. A. et al., 2011, MNRAS, 410, 1660

Eisenstein D. J., Seo H.-J., White M., 2007, ApJ, 664, 660

Eisenstein D. J. et al., 2005, ApJ, 633, 560

Farrow D. J. et al., 2014, MNRAS, 437, 748

Ferrarese L. et al., 2006, ApJS, 164, 334

Finlator K. et al., 2000, AJ, 120, 2615

Fixsen D. J., 2009, ApJ, 707, 916

Fixsen D. J., Cheng E. S., Gales J. M., Mather J. C., Shafer R. A., Wright E. L., 1996, ApJ, 473, 576

Font A. S. et al., 2008, MNRAS, 389, 1619

Foster J., Nightingale J. D., 1995, A Short Course in General Relativity

Freedman W. L. et al., 2001, ApJ, 553, 47

Freedman W. L., Madore B. F., Scowcroft V., Burns C., Monson A., Persson S. E., Seibert M., Rigby J., 2012, ApJ, 758, 24

Frenk C. S., White S. D. M., 2012, Annalen der Physik, 524, 507

Frigo M., Johnson S. G., 2005, Proceedings of the IEEE, 93, 216, special issue on "Program Generation, Optimization, and Platform Adaptation"

Giannantonio T., Crittenden R., Nichol R., Ross A. J., 2012, MNRAS, 426, 2581

Gonzalez-Perez V., Baugh C. M., Lacey C. G., Kim J.-W., 2011, MNRAS, 417, 517

Goto T., Szapudi I., Granett B. R., 2012, MNRAS, 422, L77

Graham A. W., Driver S. P., 2005, Publications of the Astronomical Society of Australia, 22, 118

Guth A. H., 1981, Phys. Rev. D, 23, 347

Hamilton A. J. S., 1993, ApJ, 417, 19

Hodapp K. W. et al., 2004, Astronomische Nachrichten, 325, 636

Hogg D. W., 1999, ArXiv Astrophysics e-prints

Hu W., Dodelson S., 2002, ARA&A, 40, 171

Hu W., Eisenstein D. J., Tegmark M., 1998, Phys. Rev. Lett., 80, 5255

Huang J.-S. et al., 2001, A&A, 368, 787

Hubble E., 1929, Proceedings of the National Academy of Science, 15, 168

Hudon J. D., Lilly S. J., 1996, ApJ, 469, 519

Ilbert O. et al., 2005, A&A, 439, 863

Ivezic Z. et al., 2008, ArXiv e-prints

Jackson J. C., 1972, MNRAS, 156, 1P

Jian H.-Y. et al., 2013, ArXiv e-prints 1305.1891

Kaiser N., 1987, MNRAS, 227, 1

Kaiser N. et al., 2002, in Society of Photo-Optical Instrumentation Engineers (SPIE) Conference Series, Vol. 4836, Society of Photo-Optical Instrumentation Engineers (SPIE) Conference Series, Tyson J. A., Wolff S., eds., pp. 154–164

Kashikawa N. et al., 2004, PASJ, 56, 1011

Kauffmann G., White S. D. M., Guiderdoni B., 1993, MNRAS, 264, 201

Kim H.-S., Baugh C. M., Cole S., Frenk C. S., Benson A. J., 2009, MNRAS, 400, 1527

Kovács A., Szapudi I., Granett B. R., Frei Z., 2013, MNRAS, 431, L28

Kron R. G., 1980, ApJS, 43, 305

Lagos C. d. P., Bayet E., Baugh C. M., Lacey C. G., Bell T. A., Fanidakis N., Geach J. E., 2012, MNRAS, 426, 2142

Lagos C. D. P., Lacey C. G., Baugh C. M., Bower R. G., Benson A. J., 2011, MNRAS, 416, 1566

Landy S. D., Szalay A. S., 1993, ApJ, 412, 64

Laureijs R. et al., 2011, ArXiv e-prints

Le Fèvre O. et al., 2005, A&A, 439, 845

Levi M. et al., 2013, ArXiv e-prints

Lewis A., Bridle S., 2002, Phys. Rev., D66, 103511

Li C., Kauffmann G., Jing Y. P., White S. D. M., Börner G., Cheng F. Z., 2006, MNRAS, 368, 21

Li C. et al., 2012, MNRAS, 419, 1557

Liddle A., 2003, An Introduction to Modern Cosmology, Second Edition

Loveday J. et al., 2012, Galaxy and Mass Assembly (GAMA): ugriz galaxy luminosity functions

Lupton R. H., Gunn J. E., Szalay A. S., 1999, AJ, 118, 1406

Madgwick D. S. et al., 2003, MNRAS, 344, 847

Magnier E., 2006, in The Advanced Maui Optical and Space Surveillance Technologies Conference

Magnier E. A. et al., 2013, ApJS, 205, 20

Martin N. F. et al., 2013, ApJ, 772, 15

Marulli F. et al., 2013, A&A, 557, A17

McCracken H. J. et al., 2003, A&A, 410, 17

Meneux B. et al., 2009, A&A, 505, 463

Meneux B. et al., 2008, A&A, 478, 299

Merson A. I. et al., 2013, MNRAS, 429, 556

Metcalfe N. et al., 2013, MNRAS, 435, 1825

Mo H., van den Bosch F. C., White S., 2010, Galaxy Formation and Evolution

Myers A. D. et al., 2006, ApJ, 638, 622

Norberg P., Baugh C. M., Gaztañaga E., Croton D. J., 2009, MNRAS, 396, 19

Norberg P. et al., 2002, MNRAS, 332, 827

Norberg P. et al., 2001, MNRAS, 328, 64

Padilla N. D., Strauss M. A., 2008, MNRAS, 388, 1321

Parkinson D. et al., 2012, Phys. Rev. D, 86, 103518

Peacock J. A., 1999, Cosmological Physics

Peacock J. A., 2013, ArXiv e-prints 1301.7286

Peacock J. A., Smith R. E., 2000, MNRAS, 318, 1144

Peebles P. J. E., 1980, The large-scale structure of the universe

Penzias A. A., Wilson R. W., 1965, ApJ, 142, 419

Percival W. J. et al., 2010, MNRAS, 401, 2148

Percival W. J. et al., 2002, MNRAS, 337, 1068

Perlmutter S. et al., 1999, ApJ, 517, 565

Petrosian V., 1976, ApJ, 209, L1

Planck Collaboration et al., 2013, ArXiv e-prints 1303.5076

Pollo A. et al., 2006, A&A, 451, 409

Press W. H., Schechter P., 1974, ApJ, 187, 425

Riess A. G. et al., 1998, AJ, 116, 1009

Riess A. G. et al., 2011, ApJ, 730, 119

Robotham A. S. G. et al., 2011, MNRAS, 416, 2640

Roche N., Eales S. A., 1999, MNRAS, 307, 703

Ross A. J. et al., 2011a, MNRAS, 417, 1350

Ross A. J. et al., 2012, MNRAS, 424, 564

Ross A. J., Tojeiro R., Percival W. J., 2011b, MNRAS, 413, 2078

Rubin V. C., Ford, Jr. W. K., 1970, ApJ, 159, 379

Saglia R. P. et al., 2012, ApJ, 746, 128

Schlafly E. F. et al., 2012, ApJ, 756, 158

Sérsic J. L., 1963, Boletin de la Asociacion Argentina de Astronomia La Plata Argentina, 6, 41

Shane C. D., Wirtanen C. A., 1967, Pub. Lick Obs., 22

Shen S., Mo H. J., White S. D. M., Blanton M. R., Kauffmann G., Voges W., Brinkmann J., Csabai I., 2003, MNRAS, 343, 978

Simard L., Mendel J. T., Patton D. R., Ellison S. L., McConnachie A. W., 2011, ApJS, 196, 11

Slipher V. M., 1917, Proceedings of the American Philosophical Society, 56, 403

Springel V. et al., 2005, Nature, 435, 629

Strauss M. A. et al., 2002, AJ, 124, 1810

Suzuki N. et al., 2012, ApJ, 746, 85

Taylor E. N. et al., 2011, MNRAS, 418, 1587

Tegmark M., Zaldarriaga M., 2002, Phys. Rev. D, 66, 103508

The Dark Energy Survey Collaboration, 2005, ArXiv Astrophysics e-prints

Tonry J. L., Burke B. E., Isani S., Onaka P. M., Cooper M. J., 2008, in Society of Photo-Optical Instrumentation Engineers (SPIE) Conference Series, Vol. 7021, Society of Photo-Optical Instrumentation Engineers (SPIE) Conference Series

Tonry J. L. et al., 2012, ApJ, 750, 99

Valenti S. et al., 2010, The Astronomer's Telegram, 2773, 1

Vogelsberger M., Genel S., Sijacki D., Torrey P., Springel V., Hernquist L., 2013, ArXiv e-prints 1305.2913

Wang Y., Brunner R. J., Dolence J. C., 2013, MNRAS, 432, 1961

Ward M. J., Hutton S., Mattila S., Kotak R., 2011, in American Astronomical Society Meeting Abstracts #218

White S. D. M., Frenk C. S., 1991, ApJ, 379, 52

White S. D. M., Rees M. J., 1978, MNRAS, 183, 341

Yasuda N. et al., 2001, AJ, 122, 1104

York D. G. et al., 2000, AJ, 120, 1579

Zacharias N., Finch C. T., Girard T. M., Henden A., Bartlett J. L., Monet D. G., Zacharias M. I., 2013, AJ, 145, 44

Zehavi I. et al., 2002, ApJ, 571, 172

Zehavi I. et al., 2011, ApJ, 736, 59

Zeilik M., Gregory S., 1998, Introductory Astronomy and Astrophysics. Harcourt College Publishers

Zheng Z. et al., 2005, ApJ, 633, 791

Zwicky F., 1933, Helvetica Physica Acta, 6, 110